Geophysical Exploration of the Campi Flegrei (Southern Italy) Caldera' Interiors: Data, Methods and Results

Edited by

Aldo Zollo
Paolo Capuano
Margherita Corciulo

Geophysical Exploration of the Campi Flegrei (Southern Italy) Caldera' Interiors: Data, Methods and Results

Edited by

Aldo Zollo

Dipartimento di Scienze Fisiche, Università Federico II, Napoli, Italy

Paolo Capuano

Dipartimento di Scienze e Tecnologie per l'Ambiente ed il Territorio, Università del Molise, Isernia, Italy

Osservatorio Vesuviano, INGV, Napoli, Italy

Margherita Corciulo

Dipartimento di Scienze Fisiche, Università Federico II, Napoli, Italy

Coordinamento editoriale
doppiavoce
www.doppiavoce.it

ISBN-10: 88-89972-04-1
ISBN-13: 978-88-89972-04-5

Contents

Preface 7

Introduction 9

1 Study of the Campi Flegrei volcanic structure based on earthquake database 13

1.1 1984 Campi Flegrei seismic waveforms compilation 15
P. Capuano, G. Russo, T. Vanorio, R. Prevete, E. Auger, M. Bonagura, G. Caielli, V. Convertito, N. Damiano, L. D'Auria, A. Emolo, L. Lovisa, M. Moretti

1.2 A rock physics and seismic tomography study to characterize the structure of the Campi Flegrei caldera 25
T. Vanorio, J. Virieux, A. Zollo, P. Capuano, G. Russo

1.3 The Vp and Vp/Vs structure of the Campi Flegrei caldera 34
C. Chiarabba, M. Moretti, P. De Gori

1.4 A 3D velocity model for earthquake location in Campi Flegrei area: application to the 1982-84 uplift event 38
C. Satriano, A. Zollo, P. Capuano, G. Russo, T. Vanorio, G. Caielli, L. Lovisa, M. Moretti

2 The Campi Flegrei blind test 51

2.1 Model construction and forward modelling 53
P. Klinc, E. Priolo, L. D'Auria, A. Zollo, G. Seriani, A. Vuan

2.2 Tomographic inversion 62
L. Lovisa, E. Priolo, A. Michelini, J. Virieux, G. Bohm, G. Rossi, F. Gentile, T. Vanorio, B. Monteiller, L. Got, S. Gautier

3 Study of the Campi Flegrei volcanic structure based on active seismic data 77

3.1 Campi Flegrei active seismic experiments waveforms compilation 79
P. Capuano, A. Zollo, E. Auger, G. Caielli, C. Chiarabba, V. Convertito, L. D'Auria, R. de Franco, A. Emolo, S. Judenherc, L. Lovisa, J. Makris, A. Michelini, M. Moretti, E. Priolo, G. Russo, J. Virieux

3.2 Structure of Campi Flegrei caldera: new insights from the inversion of first P-arrival times of Serapis experiment 88
A. Zollo, D. Dello Iacono, S. Judenherc

3.3 2-D P velocity models and development of refraction data imaging techniques 100
R. de Franco, G. Caielli, R. Tondi

4 Techniques for volcanic structure study 105

4.1 Joint 3D seismo-gravity inversion (theoretical development) 107
R. de Franco, R. Tondi, T. Vanorio, J. Virieux

4.2 Thermo-mechanical modeling of the Campi Flegrei volcanic area (Italy) 113
G. Giberti, G. Russo, T. Vanorio, B. Yven, M. Zamora

4.3 Mechanical properties of volcanic rocks and their relations to transport properties 119
M.L. Bernard, M. Zamora

4.4 Three dimensional QP and QS tomographic images of the Campi Flegrei caldera 129
S. de Lorenzo, A. Zollo, M. Trabace, T. Vanorio

4.5 Full-waveform modelling in 3D visco-elastic structures 143
P. Klinc, G. Seriani, E. Priolo

4.6 Full-wave simulation of a Serapis seismic section 153
P. Klinc, E. Priolo

4.7 Morphology and depth of reflectors from 2D non-linear inversion of seismic data 157
M. Vassallo, V. Nisii, A. Zollo, G. Iannaccone

4.8 Database on laboratory measured data on physical properties of rocks of Campi Flegrei volcanic area (Italy) 179
G. Giberti, B. Yven, M. Zamora, T. Vanorio

Conclusive remarks and future research perspectives 193
Aldo Zollo

Appendix 199

A 1984 Campi Flegrei P- and S- phase picking 201
G. Russo, T. Vanorio, P. Capuano, E. Auger, M. Bonagura, G. Caielli, V. Convertito, N. Damiano, L. D'Auria, A. Emolo, L. Lovisa, M. Moretti

B P-phase picking of Serapis experiment 202
J. Battaglia, D. Dello Iacono, S. Judenherc

Colour reproduction of selected figures 203

Preface

The National Group of Volcanology (GNV) of INGV (Istituto Nazionale di Geofisica e Volcanology) has launched and coordinated in 1999 a Framework Program prepared by an ad hoc Committee of the Italian Department of Civil Protection. The latter was also the organization financially supporting the Program and the main end user.
The objective of the Program was to improve, through coordinated innovative research projects, the basic knowledge of the structure and dynamics of Italian active volcanoes and of the methods for monitoring the activity and assessing the hazard. The Program aimed also at enhancing the high quality experimental data collected in the latest years on Italian volcanoes, re-processing them with modern methodologies and integrating them in multi-facets models. Finally it wanted to promote innovative methods and technologies to allow a quality improvement of the information relevant for risk mitigation on Italian volcanoes. A call was issued for projects on the following themes:
– improvement of monitoring methods;
– eruptive scenarios and hazard assessment;
– risk assessment, alert levels and land use planning;
– development and application of Remote sensing;
– innovative and integrated methods to study the deep structure of volcanoes;
– investigation of submerged parts of Italian active volcanoes;
– Campi Flegrei.

These objectives were pursued through 19 Research Projects carried out by 135 Research Groups from Italian Universities and Research Organizations. 12 Research Groups were from non Italian Research Organizations (mostly French, English and German). The projects have been selected and continuously monitored by an International Evaluation Committee.
One of the most successful projects of the whole Program was related to the line: Innovative and integrated methods to study the deep structure of volcanoes and was applied to the Campi Flegrei caldera, one of the areas with the highest volcanic risk in the world. The Project involved 9 Research Units, produced several high quality deliverables and was very effective in combining the development of innovative methodologies and its application to the analysis of high quality local earthquake data collected during the 1983-84 seismic cri-

sis in the Phlegraean areas combined with those from a high resolution offshore reflection survey (SERAPIS Project). with gravity and with laboratory rock physics data.
The Evaluation Committee ranked this Project among those which met or exceeded the expected objectives. It further stressed out that this project shows how modern geophysical methodologies can be developed and used toward a better imaging of the internal structure of a volcano and an improved understanding of its functioning. This volume collects all the contributions given from this project; the accompanying CD furnishes the collection of experimental field and laboratory data used in the Project.
Campi Flegrei is a resurgent caldera with strong similarities to other far away areas (e.g. Yellowstone and Long Valley in Western United States). GNV hopes that this volume can be an useful addition to the understanding of the dynamics and the structural control of the phenomena occurring in this type of volcanoes.

Paolo Gasparini
Director of GNV

Introduction

Arrival times and waveforms of first and secondary arrivals (reflected and converted waves) produced by active sources (on land and offshore explosions) and/or natural sources (microearthquakes), can provide significant seismic information about the smooth variations of the velocity and attenuation of seismic waves and about the morphology of the most important reflectors. The project "Integrated seismic methods applied to the investigation of the active volcano structure: an application to the Campi Flegrei caldera" aimed both at developing and using advanced techniques in order to model active and passive seismic data recorded in the Campi Flegrei region, and at the comparison of the obtained velocity and attenuation measurements with laboratory data. In particular, spatial variation of the elastic (P and S velocity values) and anelastic (P and S quality factors) properties, jointly with recent information about the caldera thermal state, can provide parameters necessary to a preliminary thermo-mechanical modeling of the active physical processes.

Structural complexity of the upper crust in volcanic regions is due to mechanisms of magma feeding and volcanic structure building. Moreover, variations in rocks rheology and elastic parameters of the propagation medium can be produced by an anomalous thermal field. Thus, a reliable model representing the distribution of elastic/anelastic properties in the propagation medium is needed both to understand and to reproduce the mechanisms which drive the magma rising up and to monitor accurately and continuously the seismic activity occurring during eruptive quiescence periods and crisis episodes. Complexities of seismograms recorded in volcanic regions are usually produced by strong heterogeneities of the propagation medium, sometimes jointly to seismic source complexity (e.g. volcanic tremor, low frequency earthquakes), and by the small depth and magnitude of the seismic events. Since '80s, the availability of digital, reliable and dense seismic networks enable to record high quality data in volcanic regions, allows to interpret the seismograms complexities. Arrival times, amplitudes, polarisations and waveforms of the most important seismic phases can be analysed to discriminate source and propagation effects.

From a methodological point of view, since the early '80s, travel time tomography of P and S first arrivals from local earthquakes has provided new information on the active volcanoes structure. In the last '80s-early '90s, the joint analysis of active (explosive sources located in boreholes) and passive (local

microearthquakes) seismic data has been introduced in order to better resolve the strongly non-linear inverse problem of the joint determination of the propagation medium (seismic waves velocity in a 3D-grid nodes) and hypocentral parameters (earthquake location and origin time).
The project has concerned the development and implementation of innovative techniques of analysis and interpretation of active/passive seismic data recorded in the Campi Flegrei. Thanks to bradisismic crisis occurred in the early '80s, the scientific background and the general geological/geophysical knowledge are improved. The main goals of the project was the definition of a 3D detailed crustal model of the volcanic region and the identification and detection of the possible deep reservoir of magma feeding.
The project was based on the analysis and interpretation of different seismic data set. The first one was a data set of several hundreds of microearthquakes recorded during the last bradiseismic crisis occured on 1984. The second was the DSS (Deep Seismic Soundings) seismic refraction data acquired during the surveys conducted on 1980 and 1985 in the region. The latest was a data set acquired in the framework of the MareVes97 offshore seismic survey, an experiment devoted to the definition of the structure of the Somma-Vesuvio volcanic complex.
Moreover, during the project development has been planned and carried out a new experiment (called SERAPIS, **SE**ismic **R**eflection/Refraction **A**cquisition **P**roject for **I**maging complex volcanic **S**tructures) based on off-shore seismic energization and data acquisition on the sea-bottom. The experiment was performed in September, 2001 during which the vessel NADIR of IFREMER (equipped with 12, 16-liters airgun) produced more than 5000 air gun shots recorded at a sea-bottom seismograph array of 62 OBS and 50 station installed on-land. The data set acquired during the SERAPIS experiment integrated the above mentioned data set and has been successfully used to infer 3D images of the volcanic structures of Campi Flegrei and Neapolitan bay.
The importance of studying the structure of Campi Flegrei is related to the high volcanic risk associated even to a minor eruption because CF is one of the main unrest calderas in the world where several hundred thousands people live within its borders.
In the past the structure of the caldera has been mainly investigated by a few km deep drillings, earthquake seismic tomography, gravity and magnetic surveys and sporadic observations of teleseismic and wide angle seismic data.
The whole geophysical information indicate the following features: a) the evidence of sharp temperature gradients at shallow depths (450 degrees measured at 3km depth) b) the presence of a few km thick, inner basin characterized by low Vp, high Vp/Vs and high Qp; c) the shape of this basin is consistent with the gravity low anomaly and appear to be the site where most of deformation is concentrated during the recent ground uplift episodes; d) the possible occurrence of a magmatic reservoir at about 4-5 km depth from teleseismic observations and extrapolation of thermal data. Relevant open que-

stions still remained to be answered, mainly concerning the depth and lateral extension of the shallow magmatic reservoir and the possible existence of intra-crustal magmatic sill as it has been found in the nearby Mt.Vesuvius.
The main objective of the project was the detailed reconstruction of the 3D structure of the Campi Flegrei caldera through the inversion of passive and active data sets and the understanding of the relationship between the elastic/anelastic properties and the physical, mechanical and thermal properties of rocks forming the caldera edifice.
In the enclosed CD-Rom you will find appendixes A and B.

The Editors

1

Study of the Campi Flegrei volcanic structure based on earthquake database

During the last rapid uplift episode occurred in the Campi Flegrei caldera in 1983-1984, University of Wisconsin jointly with Osservatorio Vesuviano deployed a portable digital seismic network from January to June 1984, to record the intense microearthquake activity. The whole earthquakes data-set has been recovered and organized in a database of 3-component waveforms containing several hundreds microearthquakes. This dataset, representing actually the unique digital data-base acquired during an unrest episode at Campi Flegrei caldera, is strongly increased respect to that used by previous authors and have been completely re-picked. The waveforms archive assembled is formed by more than 1,000 events recorded by 3-C stations, in particular about 850 events are recorded at more than 3 stations. About 4600 P-phase pickings and about 3300 S-phase pickings have been produced.
This passive seismic database has been used to infer an image of the Campi Flegrei caldera in terms of P- and S-wave velocity model, using different tomographic approach. Selected seismic data were modeled by using a tomographic method based on an accurate finite-difference travel-time computation which simultaneously inverts P-wave and S-wave first-arrival times for both velocity model parameters and hypocenter locations. A different approach using double difference algorithm has been used for a simultaneous inversion for earthquake hypocenters and velocity parameters, merging passive data with active data produced by the Serapis project.
Starting from the results of tomography studies obtained by active seismic data, a 3D P-wave velocity model for earthquakes location in Campi Flegrei area has been developed, validate and used to locate the seismicity of the 1982-1984 uplift episode. This model taking into account the strong 3D structural variations characterizing the volcanic area, can contribute to obtain reliable earthquakes location very helpful in the surveillance activity.
The reconstructed passive dataset represents a valuable reference to be used for seismic hazard analyses during future crises.

1984 Campi Flegrei seismic waveforms compilation

P. Capuano[1,2], G. Russo[3], T. Vanorio[4], R. Prevete[3], E. Auger[3], M. Bonagura[3], G. Caielli[5], V. Convertito[3], N. Damiano[2], L. D'Auria[3], A. Emolo[3], L. Lovisa[6], M. Moretti[7]

[1] *Dipartimento di Scienze e Tecnologie per l'Ambiente ed il Territorio, Università del Molise, Isernia, Italy*

[2] *Osservatorio Vesuviano, INGV, Napoli, Italy*

[3] *Dipartimento di Scienze Fisiche, Università Federico II, Napoli, Italy*

[4] *Géosciences Azur, CNRS, Université de Nice, Sophie Antinopolies, Valbonne, France*

[5] *Istituto per la Dinamica dei Processi Ambientali, CNR, Milano, Italy*

[6] *Istituto Nazionale di Oceanografia e Geofisica Sperimentale, Trieste, Italy*

[7] *Centro Nazionale Terremoti, INGV, Roma, Italy*

Abstract: The whole earthquake waveform data-set acquired by University of Wisconsin during the 1984 acquisition experiment, performed in the Campi Flegrei caldera, has been recovered, formatted and organized in a easy-accessible data archive. This archive represents a complete database of 3-component waveforms containing several hundreds microearthquakes recorded at Campi Flegrei, during the last bradiseismic crisis in the 1983-84.

In addition to its relevance for earthquake location and velocity structure investigations this is actually the unique, digital data-base acquired during an unrest episode at Campi Flegrei caldera and it represents a valuable reference data set to be used for seismic hazard analyses during future crises.

The whole waveform data base has been re-picked. This is because the data set has been strongly incremented, respect to the previous one, with the new recovered data, and possible heterogeneities of new with previous picks could bias the tomographic inversion results.

This database can be used to better understand Campi Flegrei structure applying updated technique of analysis. It has been used to perform a tomographic analysis using an increased P- and S-phase dataset, with a re-location of some hundreds of earthquakes.

Introduction

One of the tasks of the project "Integrated seismic methods applied to the investigation of the active volcano structure: an application to the Campi Flegrei caldera", concerns the recovering of previous active and passive sei-

smic data acquired in the Campi Flegrei area. A "seismic crisis" occurred in the Campi Flegrei caldera area (Southern Italy) in 1983-1984, when rapid uplift was detected and microearthquake activity increased dramatically. A temporary network of University of Wisconsin (Madison, USA) portable digital seismic recorders with 3-component sensors was deployed, in co-operation with Osservatorio Vesuviano, in the vicinity of the Campi Flegrei caldera from January to June 1984 (Figure 1).

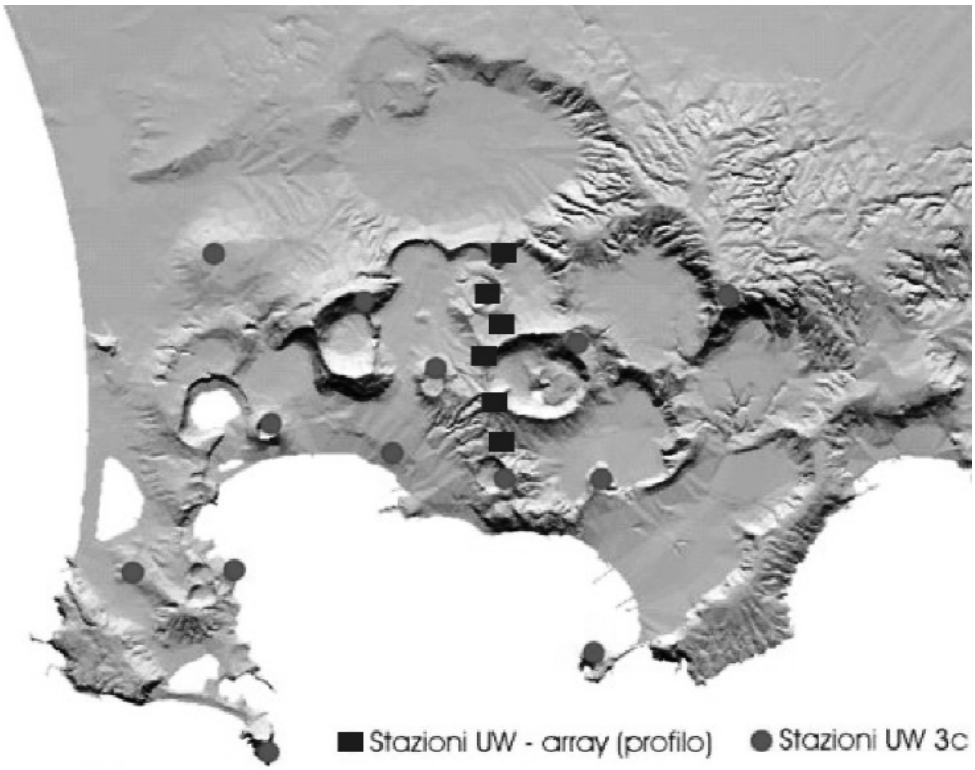

Fig. 1. Location of stations belonging to the Campi Flegrei caldera array. Dots show sites occupied from January to May, 1984; squares show sites occupied during the Natural Event Profile (NEP) (June 2 to June 6, 1984).

The seismicity associated to this ground uplift episode reached a maximum during March-April 1984 including a large earthquakes swarm on 1 April, 1984. Data were recorded in triggered mode for all stations. Table 1 presents the station coordinates.

The general objective of the task is the implementation of a complete three-component seismic waveform archive containing data from several hundreds microearthquakes occurred on 1983-1984 at Campi Flegrei. A part of these

Tab. 1. List of coordinates of all UW temporary network site locations

Id	Latitude North (°,')		Longitude East (°,')		Elevation (m)	Name
W01	40	50.91	14	8.99	62.0	ASTRONI A
W02	40	49.52	14	8.40	100.0	SOLFATARA A
W03	40	50.77	14	9.17	35.0	ASTRONI_B
W04	40	50.11	14	5.03	70.0	MT.NUOVO
W05	40	51.42	14	11.58	457.0	CAMALDOLI
W06	40	48.59	14	3.63	45.0	CAPPELLA
W07	40	51.58	14	5.74	170.0	MT. RUSCELLO
W08	40	51.70	14	3.87	11.0	MT. RUSCELLO
W09	40	52.00	14	4.30	135.0	MT. RUSCELLO
W10	40	46.69	14	5.37	50.0	CAPOMISENO
W11	40	49.26	14	7.25	40.0	DARSENA (POZZUOLI)
W12	40	49.60	14	8.66	180.0	SOLFATARA B
W13	40	48.58	14	4.96	20.0	BAIA CASTELLO
W14	40	47.78	14	9.90	40.0	NISIDA
W15	40	49.51	14	9.84	150.0	MT.SPINA
W16	40	49.63	14	6.23	80.0	PIRELLI
W17	40	49.84	14	7.78	84.0	DA MARIO
W18	40	49.30	14	8.20	90.0	MADONNA
W19	40	49.54	14	7.54	37.0	ANFITEATRO
W20	40	51.14	14	5.89	306.0	MT.S.ANGELO
W21	40	50.47	14	7.67	175.0	FONDI DI CIGLIANO
W31N	40	50.08	14	8.32	195.0	P1 (north)
W31C	40	49.99	14	8.35	195.0	P1 (central)
W31S	40	49.90	14	8.38	185.0	P1 (south)
W32N	40	50.40	14	8.25	236.0	P2 (north)
W32C	40	50.32	14	8.27	245.0	P2 (central)
W32S	40	50.26	14	8.28	233.0	P2 (south)
W33N	40	50.85	14	8.23	190.0	P3 (north)
W33C	40	50.77	14	8.17	184.0	P3 (central)
W33S	40	50.68	14	8.15	192.0	P3 (south)
W34N	40	51.18	14	8.04	155.0	P4 (north)
W34C	40	51.10	14	8.11	159.0	P4 (central)
W34S	40	51.01	14	8.18	175.0	P4 (south)
W35N	40	51.38	14	7.94	140.0	P5 (north)
W35C	40	51.34	14	7.80	120.0	P5 (central)
W35S	40	51.25	14	7.75	85.0	P5 (south)
W37N	40	52.00	14	8.72	94.0	P7 (north)
W37C	40	51.87	14	8.62	94.0	P7 (central)
W37S	40	51.78	14	8.55	94.0	P7 (south)

data were available at Osservatorio Vesuviano and part of them were still available at the University of Wisconsin laboratories. The task activity concerns the retrieval, formatting and archiving of the whole data set, which is accomplished in co-operation with personnel of the University of Wisconsin. Once the waveforms dataset was reconstructed we realize P- and S-phase picking over all the event recording, including events recorded at less then 3 stations.

Seismic Instrumentation

First of all we retrieved all the information concerning the seismic stations and sites (station geographical co-ordinates, sensors characteristics, running periods, gain tables). The University of Wisconsin (UW) portable digital seismic recorders are wide dynamic-range instruments (106 dB) designed for recording seismic waves from earthquakes or explosions (Powell, 1983). Data from 1-Hz Geotech S-13 and Hall-Sears HS-10-1 geophones were recorded at 100- or 200-Hz sampling rates, with a 4-pole Butterworth antialiasing filter at 24 and 48 Hz, respectively. A 13.6 kHz Omega receiver, incorporated in each seismograph, recorded time data from the worldwide Omega network concurrently with seismic signals. A timing-correction process developed for application to the UW seismic recorders provides 1/4 sample RMS time error relative to Universal Time (Schneider et al., 1987). Ground motion may be estimated from an average value for voltage sensitivity of 150 V/m/s for the UW Hall-Sears geophones. S-13 geophones were deployed at stations W11 and W13 (200 Hz). Table 2 reports more detail on the instrument characteristics.

Seismic waveforms

The activity related to recover information about the seismic acquisition conducted in the 1984 jointly by Osservatorio Vesuviano (OV) and University of Wisconsin, that deployed in Campi Flegrei caldera 13 digital stations occupying about 20 sites, is consisted in re-read about 30 digital tapes, available in the OV archive. The re-analysis of old magnetic tapes evidenced that some tapes and some parts of tapes show problems on reading due to the wearing of the tape surface. The time schedule of instrument installation and operation has been recognised and the part of data retrievable at OV has been defined. Codes for tape reading, clock correction and format translation of raw data in SAC (Seismic Analysis Code) format, that was selected as final format for the reconstructed archive, was developed. File name contain all information regarding the complete date, time up to milliseconds of the first sample, station name and component. The SAC header was used to connect the available information to all single trace (Station name, station coordinates, time of first sample, number of sample, sampling frequency, etc.).
Data span from January to May, with some hole due to the cited reading problems. Each retrieved file corresponds to one trigger and is about 40-60s long. An example of recordings is shown in Figure 2.
Due to the high seismic activity level some trigger can contain more than one event, as shown in Figure 3.
Following step was separate out seismic events from 'false' clustering of trigger times due to non-seismic activity, by removing noisy trace and trace cor-

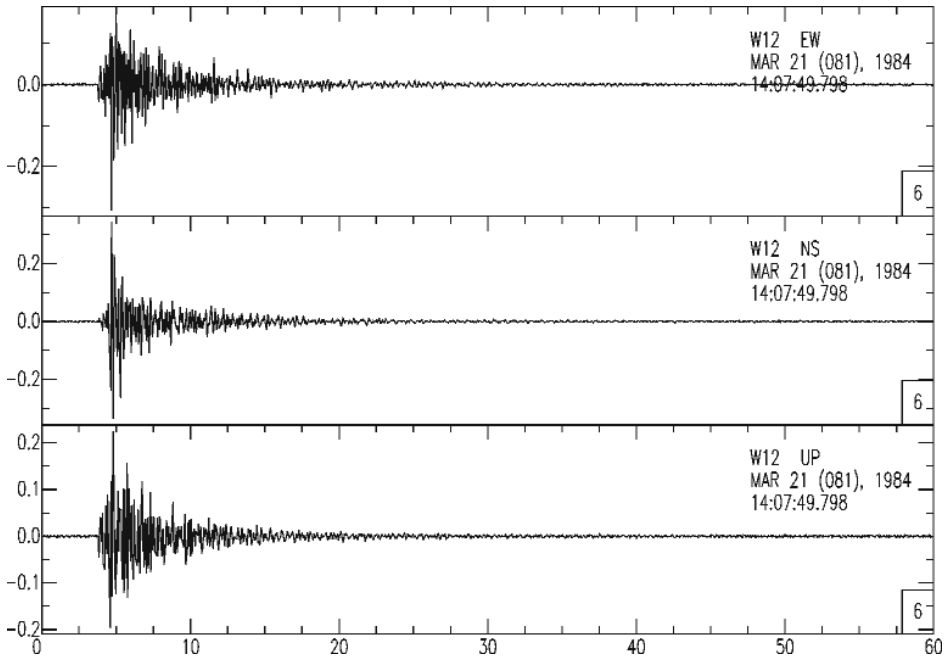

Fig. 2. Example of 3-C recordings of a Phlegrean earthquake.

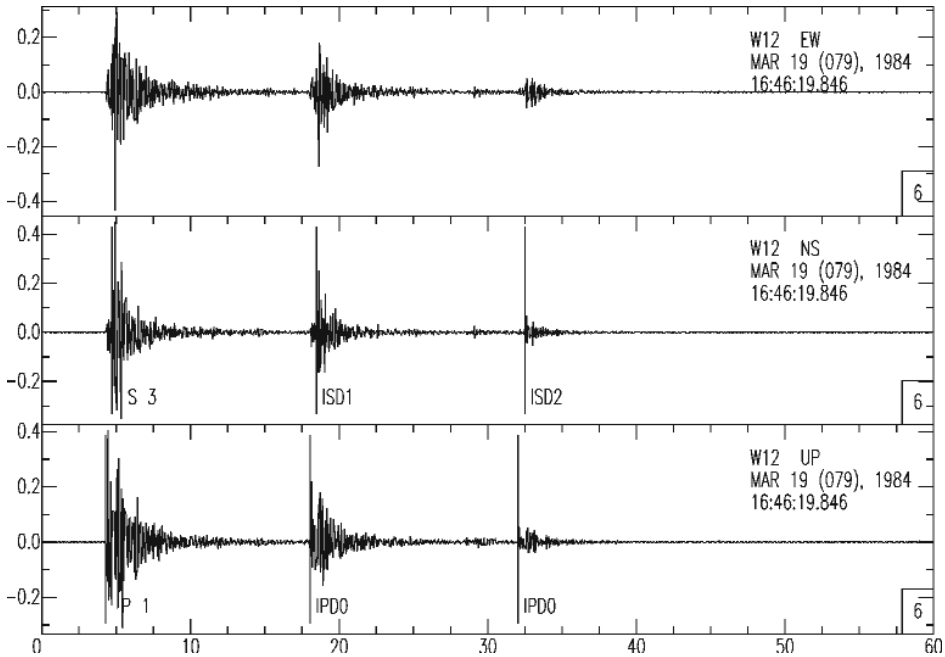

Fig. 3. Example of multiple events recording in a single trigger file.

responding to midnight check, a system used to monitor station functionality. Finally, we obtain the archive of seismic waveform available at OV center.
Afterwards, in co-operation with the University of Wisconsin we arrange to complete the analysis regarding the part of the experiment retrievable in the United States, where the original field tape were still existing. This analysis regarded the recover of data no more readable in Italy, the checking of the consistency of data read independently by the two groups, the retrieve of data belonging to the period mid-April mid-June, never available in Italy.
Figure 4 shows an example of NEP recording during the period June 2-June 6, in which the stations were deployed in 1-C configuration.
The waveforms archive assembled is formed by more than 1,000 events recorded by 3-C stations, in particular about 850 events are recorded at more than 3 stations, as detailed in Table 2. Due to seismic quiescence of the Campi Flegrei caldera in the last 20 years, interrupted only by very few earthquakes, this archive represents an unique collection of waveforms produced by seismic sources in a complex volcanic area that can be very useful to better understand caldera dynamic.

Tab. 2. Number of events/station recordings

N. of events	N. of stations
240	4
160	5
162	6
115	7
72	8
46	9
31	10
18	11

After the verification of some inconsistency with previous phase pickings, the project group decided to re-pick the all dataset as described in the next paragraph. Thus, we obtain 4583 P-phase pickings and 3321 S-phase pickings. We define the picking weight p *(0-4)*, taking into account the reading time error (picking accuracy is in the range 0.02-0.05 s for P- and 0.02-0.10 s for S-waves), to give an idea of picking quality. We obtain 80% of P-picking with $p \leq 1$ and 70% of S-picking with $p \leq 2$. Finally, the pickings were arranged using HYPO71 format.

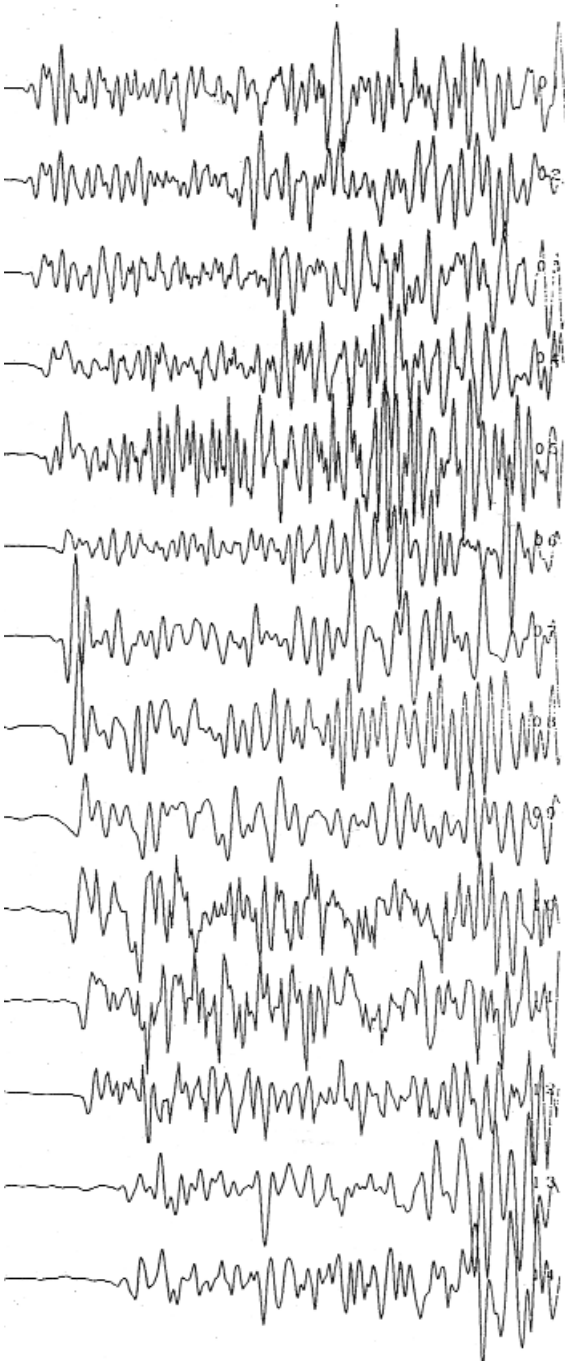

Fig. 4. Example of recording by the NEP array.

Picking check and validation

Some of the retrieved data have never been used for any seismic analysis, so it was necessary to perform the picking of P and S arrival times. To make the picking dataset homogeneous we re-pick also data already used in previous paper (Aster and Mayer, 1988; 1989). The obtained triggers were then divided into four parts, each distributed to one Research Unit involved in seismic modelling. This implies that the pickers for each part were different, moreover many Research Units involved more than one picker in the analysis of their part of database.
The parts in which the database has been divided do not overlap. Given the fact that many different pickers were involved in picking, there was the needed to set up a criterion to check the homogeneity of the pickings.
Let us consider a homogeneous half space in which an earthquake occurs. Considering a pair of stations *i* and *j*, we can compute the difference between the P arrival times and between the S arrival times:

$$T_{Si} - T_{Sj} = \frac{V_P}{V_S}\left(T_{Pi} - T_{Pj}\right)$$

Plotting the S arrival time difference versus the P arrival time difference for each pair of stations, we obtain a line passing through the origin whose slope is the Vp/Vs ratio. Obviously, the real velocity structure is not homogeneous, but, assuming that the pickings are consistent, we expect to find the same degree of complexity if we plot the formula above for each part of the database. In Figure 5, we show these plots.

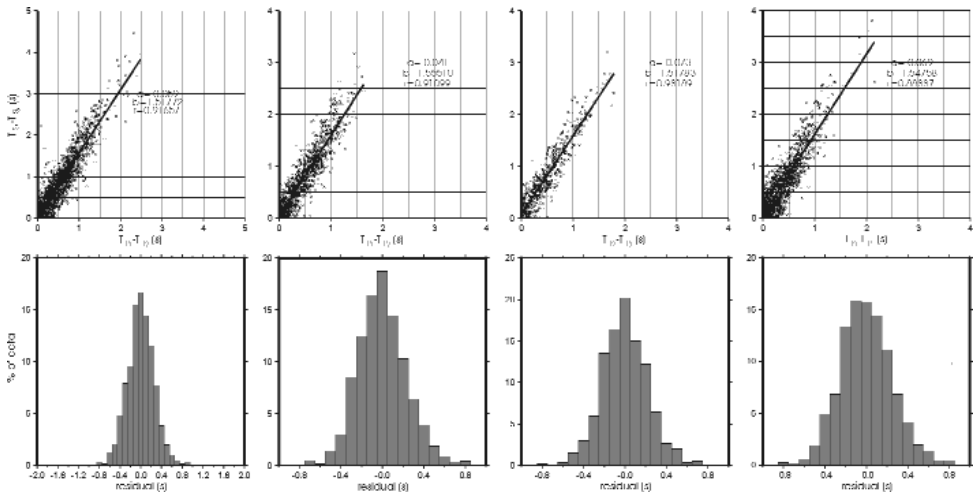

Fig. 5. Plot of the S arrival time difference versus the P arrival time difference for each pair of stations, with best fit line (upper part). Distributions of residuals around the best fit lines (lower part). Plots are related to each subset in which data were divided.

Tab. 3. General specifications, University of Wisconsin-Madison digital 3-component recorders

DATA STORAGE	5" reel 1/4" tape, 1800 feet
CAPACITY	20 Mbyte
FORMAT	4-track; 3-channel + error correction multi-stream packet
DYNAMIC RANGE	106 dB Noise = 0.25 mV P-P Clipping = 0.05 V P-P
CALIBRATION	Random binary sequence and step current applied to seismometer coils through a bridge (at programmed start times)
PASSBAND	Low end: 2 poles at 0.09 Hz High end: 4-pole Butterworth at (0.25 * sample rate)
SAMPLE RATE	25, 50, 100, 200, 400 samples/second
PRE-EVENT DELAY	512, 1024, 2048 samples/channel
MODES	Programmed and/or multiple-mode triggered
RUN TIMES	Programmable to 1000 minutes in 1 sec steps with optional programmed limits on total recording time for each mode
TRIGGER HARDWARE	STA/delayed LTA ratio; broadband or teleseismic filtered
TRIGGER SOFTWARE	Three frequency band Walsh transform filter to discriminate teleseismic, regional, and noise; with independent run times
STATUS REVIEW	Omega signal, time, configuration, schedules, number of events recorded and time used for each mode, times of last 500 events, seismometer period and damping
TIMING INTERNAL	1 mHz TCXO, $\pm 1 \times 10^{-6}$ over temperature range
EXTERNAL	13.6 kHz Omega VLF phase recorded with seismic data; Worldwide coverage (except Antarctica and central Greenland)
POWER	12.5 V DC +/- 20%
DIMENSIONS	56 x 33 x 40 cm
WEIGHT	22 kg

The most evident thing shown by the plots is that they have a marked linear trend, even if data are quite spread along this trend, as could be expected. So, it makes sense to perform a linear fitting of data. The resulting best fit lines have compatible values of intercept and slope (a and b in figure). The correlation coefficients (r in figure) do not show important variations. Also, the distributions of residuals around the best fit lines (lower part of the figure) are similar, all showing a standard deviations of about 0.27 s. This demonstrates that the pickings are compatible since different pickers have produced similar distributions of arrival times. Even if this test shown that the picking could safely be mixed to build the database, before doing that all of them were revised by only two pickers to ensure even more homogeneity of the data.

Data analysis

Aster and Meyer (1988, 1989) determined hypocenter locations and velocity structure of the caldera using a segment of the data from mid-March to mid-

May, including about 220 events. Our enriched dataset make possible a more confident re-analysis of velocity structure and location. Moreover, we were able to retrieve phase pickings of events recorded by permanent OV network and by temporary network deployed by AGIP-Aquater in the framework of geothermal exploration. Thus we perform a tomographic study (Vanorio et al., 2005) including 1209 earthquakes occurred from January to mid-April, which provide 7264 P- and 3121 S- arrival time reading.
The new enriched dataset was used also to re-locate the earthquakes in the new three-dimensional velocity model obtained by the tomography from P and S microearthquake travel times (Vanorio et al, 2005) and by active data tomography (Zollo et al, 2003).

Acknowledgments

Authors are grateful to the University of Wisconsin, particularly C. Thurber and B. Lutter, for their invaluable help in recover part of dataset. Authors would also like to thank all people that participate to the picking and related activity.

References

Aster R. C., Meyer R. P. (1988). Three-dimensional velocity structure and hypocenter distribution in the Campi Flegrei caldera, Italy. *Tectonophysics*, 149, 195-218.

Aster R. C., Meyer R. P. (1989). Determination of shear- and compressional-wave velocity variations and hypocenter locations in a rapidly inflating caldera: the Campi Flegrei. *Phys. Earth Planet. Inter.*, 55, 313-25.

Powell L. A. (1983). Engineering Description of the U.W. Portable Digital Seismograph, Proceedings of the Committee on Controlled Source Seismology (CCSS). *Workshop on Portable Digital Seismograph Development*, Los Altos, California, 121-122.

Schneider J. F., Aster R. C., Powell L. A., Meyer R. P. (1987). Timing of portable seismographs from Omega navigation signals. *Bull. Seism. Soc. Am.*, 77, 1457-78.

Vanorio T., Virieux J., Capuano P., Russo G. (2005). Three-dimensional seismic tomography from P wave and S wave microearthquake travel times and rock physics characterization of the Campi Flegrei Caldera. *J. Geophys. Res.*, 110, B03201, doi:10.1029/2004JB003102.

Zollo A., Judenherc S., Virieux J., Makris J., Auger E., Capuano P., Chiarabba C., de Franco R., Michelini A., Musacchio G. (2003). Evidence for the buried rim of Campi Flegrei caldera from 3-d active seismic imaging. *Geophys. Res. Lett.*, 30(19), doi:10.1029/2003GL018173.

A rock physics and seismic tomography study to characterize the structure of the Campi Flegrei caldera

T. Vanorio[1], J. Virieux[1], A. Zollo[2], P. Capuano[3,4], G. Russo[2]

[1] *Géosciences Azur, CNRS, Université de Nice, Sophie Antinopolies, Valbonne, France*

[2] *Dipartimento di Scienze Fisiche, Università degli Studi di Napoli "Federico II", Italy*

[3] *Dipartimento di Scienze e Tecnologie per l'Ambiente e il Territorio, Università del Molise*

[4] *Osservatorio Vesuviano, INGV, Napoli*

Abstract: The Campi Flegrei (CF) caldera experiences dramatic ground deformations unsurpassed anywhere in the world. The source responsible for this phenomenon is still debated. With the aim of exploring the structure of the caldera as well as the role of hydrothermal fluids on velocity changes, a multidisciplinary approach dealing with 3-D delay-time tomography and rock physics characterization has been followed. Selected seismic data were modeled by using a tomographic method based on an accurate finite-difference travel-time computation which simultaneously inverts P-wave and S-wave first-arrival times for both velocity model parameters and hypocenter locations.

The retrieved P-wave and S-wave velocity images as well as the deduced Vp/Vs images were interpreted by using experimental measurements of rock physical properties on CF samples, to take into account steam/water phase transition mechanisms affecting P-wave and S-wave velocities. Also, modelling of petrophysical properties for site-relevant rocks constrains the role of over-pressured fluids on velocity. A flat and low Vp/Vs anomaly lies at 4 km depth under the city of Pozzuoli. Earthquakes are located at the top of this anomaly. This anomaly implies the presence of fractured over-pressured gas-bearing formations and excludes the presence of melted rocks. At shallow depth, a high Vp/Vs anomaly located at 1 km suggests the presence of rocks containing fluids in the liquid phase. Finally, maps of the Vp*Vs product show a high Vp*Vs horse-shoe shaped anomaly located at 2 km depth. It is consistent with gravity data and well data and might constitute the on-land remainder of the caldera rim, detected below sea level by tomography using active source seismic data. For a more exhaustive description of the utilized methodologies, of synthetic tests for spatial resolution and uncertainty assessment and, the interpretation of results, the reader may refer to the paper Vanorio et al. (2005).

INTRODUCTION

As with many calderas, CF periodically experiences notable unrest episodes which include ground deformations, seismic swarms and increases in the degassing activity (Barberi et al., 1984). However, unlike other calderas, ground deformations in CF may reach values unsurpassed anywhere in the world (Newhall and Dzurisin, 1988). Based on historical records, the uplift phase may precede a new eruptive event as occurred in 1538 (Dvorak and Gasparini, 1991). Nevertheless, short uplift phases may also interrupt the secular subsidence as occurred in 1970-1972, 1982-1984, 1989, 1994 and, 2000 without culminating in an eruption. Mechanisms accounting for these phenomena have generally involved pressure generation exerted either from a magma chamber (Bianchi et al., 1987; Bonafede, 1986) or from hydrothermal reservoirs (Oliveri del Castillo and Quagliariello, 1969; Casertano et al., 1976; Bonafede, 1991). Modelling of ground deformation data shows that any of the possible sources responsible for the recurrent uplift and subsidence has to be placed between 1.5 and 4 km depth, in order to fit both the magnitude and the narrow bell-shape of the recorded displacement (Bianchi et al., 1987; Bonafede, 1991). The presence of a magmatic reservoir underneath the CF caldera has been proposed as a possible interpretation of both P-S converted phases at 4 km depth (Ferrucci et al., 1992) and temperature data inferred by Qp models (de Lorenzo et al., 2001). However, no evidence for magma bodies having volumes larger than 1 km^3 has been found down to 4-5 km by the recent 3-D P- wave tomography performed in the Gulf of Naples and Pozzuoli (Zollo et al., 2003). Furthermore, no variation of isotopic ratios of magma-derived species has been found in fumaroles during the 1982-1984 unrest that could serve as evidence for the magmatic origin of the crisis (Allard et al., 1991).

The possibility that hydrothermal fluids play a fundamental role in triggering activity at CF often attracts attention because a correlation between ground displacement and gas emission rate has been found (Barberi et al., 1984; Chiodini et al., 2003). No signatures indicating cap-rock formations, which are required to build up pore fluid pressure within reservoirs, have yet been detected. Under the hypothesis of pore fluid pressure generation, the assessment of cap-rock formations constitutes evidence constraining the depth of the triggering source. Thus, many questions still remain unresolved and mechanisms responsible for the CF activity not well constrained.

The Rationale of this work

Why a new Seismic Tomography in the CF from micro-earthquake travel times?

Local Earthquake Tomography constitutes a basic tool to assess the 3-D velocity structure in seismically active areas (Thurber, 1992). Although, velocity images from the inversion of passive data (earthquakes) may suffer from a lower resolution in very shallow layers compared to that of active data (shots), Local Earthquake Tomography both shows the advantage of imaging the velocity structure during a seismic crisis and of providing also an S- wave field. The assessment of a reliable S wave velocity structure is crucial, especially in a geothermal field, to overcome ambiguities deriving from the interpretation of the P-wave velocity field alone. In the CF area, a previous joint tomographic and earthquake location study using Micro-earthquake travel-times was performed by Aster and Meyer (1988) who used 228 events occurring during the 1982-1984 crisis. They reported both a high Vp/Vs ratio at 1 km depth that was interpreted as a region of highly water saturated fractured rocks and a cessation of seismicity at approximately 4 km. In this new seismic tomographic study, the 1982-1984 dataset from January 1st through April 15th, 1984 has been upgraded and entirely re-picked so largely increasing the number of P-wave and S-wave time readings compared to the previous study (Aster and Meyer, 1988). The picking of the waveforms from the temporary network (21, 3-component digital short-period seismometers) deployed by the University of Wisconsin (WS) was operated by some URs participating to the project: UR1, UR3, UR4 and UR5. However, the analysis of this distributed and collective picking showed us that a homogeneous re-picking was necessary to achieve the resolution we wanted. Consequently, the UR6 has performed together with G. Russo (UR1) a new and more accurate picking and checked its consistency by Wadati diagram analysis. Also, during the same period, two networks were complementing the WS one: the network maintained by the Vesuvian Observatory (VO) and by AGIP (Azienda Generale Italiana Petroli, AG) consisting of 25 vertical seismic stations. Consequently, the UR6 has performed together with G. Russo (UR1) a new and more accurate picking and checked its consistency by Wadati diagram analysis. We added P- picking data coming from the VO and AGIP database, verifying consistency (see Figure 2 for the network configuration).

The dataset consists of 1209 micro-earthquakes occurring from January 1st through April 15th 1984 which provided 7,264 P- and 3,121 S- arrival time readings. Arrival times measured from digitized seismograms were estimated to be accurate in the range of 0.02-0.05 s for P- and 0.02-0.1 s for S- waves. A preliminary hypocenter location was determined by using the 1-D P velocity model resulting from the active seismic experiment performed in the Bay of Pozzuoli (Zollo et al., 2003). From the initial data set, we selected earth-

quakes that had at least 6 P- and 4 S- phases read, azimuthal gaps smaller than 180° and RMS time residuals smaller than 0.5 s. This selection provided a final database consisting of 462 events with a number of P- and S- readings of 3,447 and 2,289, respectively.

Why Rock Physic Characterization in the CF caldera?

The anomalies of the P-wave and S-wave velocity structure need to be interpreted on a physics base. Rock Physics plays the role of connecting the inferred changes in seismological parameters to properties and conditions occurring at depth. Therefore, to improve the interpretation of the retrieved anomalies, we modelled the role of hydrothermal fluids on P-wave and S-wave velocities via effective medium modelling.
Both laboratory measurements on site-relevant lithologies under controlled conditions of pressure (Vanorio et al., 2002; Vanorio, 2003) and the comparison with results obtained on other lithologies under pressure and temperature conditions (Ito et al., 1979; Wang and Nur, 1989) constrained the modelling results. The combined approach afforded in this study brings new clues useful to assessing the CF caldera structure and, in turn, its activity.

Methods

The inversion strategy

We used a linearized, iterative tomographic approach as proposed by many authors (Spakman and Nolet, 1988; Aster and Meyer, 1988; Hole, 2000; Benz et al., 1996; Latorre et al., 2004, among others) in which P- and S- first arrival times are simultaneously inverted for both earthquake locations and velocity model parameters at each step of the inversion procedure. The importance of coupling earthquake hypocenter parameters (locations and origin time) on the one hand and velocities on the other has been discussed by Thurber (1992) who emphasized that all required parameters should be mutually consistent to avoid significant bias in the derived models.
Inherently, the final solution of a tomographic inversion depends strongly on the a priori choice of the 1-D reference model (Kissling et al., 1994). As a first approach, we used the 1-D P-wave velocity model resulting from the tomographic inversion of 77,000 first P wave arrival times collected during the active seismic experiment performed in the CF caldera (Zollo et al., 2003). The initial S- velocity model was derived from the P- velocity model using a Vp/Vs ratio of 1.7 estimated from Wadati diagrams. However, due to the inherent difference in the geometry of the passive and active experiments and to the elapsed time between the acquisition of the two datasets (~20 years), we veri-

fied the accordance between the initial 1-D velocity model (Zollo et al., 2003) and earthquake data. The elapsed time is a significant factor because of changes occurring in geothermal systems. A statistical study based on RMS time residuals was inferred from 400 initial 1-D models, randomly generated within two extreme 1-D velocity bounds. The upper and lower velocity bounds were chosen to have the 1-D reference model of Zollo et al. (2003) as average. The outcome of this procedure indicated that the mach between earthquake data on the one hand and the 1-D velocity model on the other, revealed an overestimation of the reference 1-D velocity. This could affect velocity estimates in the final models. On account of that, we made a more restrictive selection on the 1-D reference model by choosing, as a reference model, the average one resulting from the initial models showing the lowest RMS residuals (< 0.2 s). This selection provided a final 3-D solution showing a lower RMS (0.07 s) (which means a reduction of 46% from the initial RMS value of 0.13) and a zero-centered distribution of travel time residuals.

The rock physics modelling

We theoretically reproduced the effect of higher temperatures and pressures on Vp/Vs via modelling as proposed by Dvorkin and Nur (1996). Since our intention was to model sediments with a non-zero stiffness of the dry matrix, we used the upper Hashin-Shtrikman bound to appropriately model the elastic moduli. Once the moduli and density of the dry matrix are computed (Dvorkin and Nur, 1996 and Dvorkin et al., 1999a GRL for details), the computation in the low-frequency domain (i.e. fluid and solid motions are in phase) of the bulk and shear moduli of the saturated sediment come from Gassmann's equation (Gassmann, 1951). In the reported modelling, pore fluid is described by a mixture of water and carbon dioxide (20% of carbon dioxide and 80% of water) whose bulk modulus and density were computed (Batzle and Wang, 1992) for a constant temperature of 350°C and by only varying pressure conditions. Modelling computed the variation of Vp/Vs as a function of pore fluid pressure: the modelled rock bears a lithostatic pressure of 70 MPa (c.a. 4 km depth) and a pore fluid pressure varying from 5 MPa to 45 MPa. The results of modelling (Figure 1) showed that the increase of pore fluid pressure leads to a decrease in pore fluid compressibility (i.e. vapour-liquid transition is simulated) and, as a consequence, the Vp/Vs ratio increases.
Figure 1 also shows the expected variation in Vp/Vs in the case where an increase of pore fluid pressure leads the bulk rock porosity to increase by 5% (Φ=25%, dashed black line in the figure). The line connecting rock models having different porosity describes the result of computation by slightly increasing porosity by steps of 1%. Figure 1 shows that in gas-bearing rocks, crack opening leads the Vp/Vs ratio to decrease as a function of pore pressure.

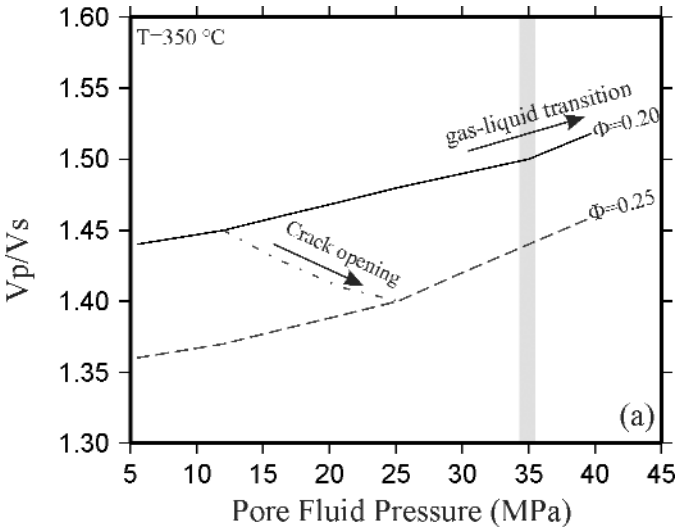

Fig. 1. Theoretical modeling of pore pressure effects on Vp/Vs ratios in a tuffite at 350° C.

RESULTS

- At shallow depth, we found similar velocity trends to those reported in the previous tomographic study of Aster and Meyer (1988). However, our augmented database allowed an improved resolution of the tomographic images at depths between 4 km and 5 km where we found an anomalously low Vp/Vs ratio (Figure 2).
- Several P-wave and S-wave velocity logs have been extracted from the 3-D model that indicate reversal trends (Figure 2) (e.g. velocity values decrease with depth) which weaken moving radially away from the center of the caldera (the city of Pozzuoli and Solfatara zone) towards more external sites (Agnano, Arco Felice, Montagna Spaccata Quarto). This result marks departures of the effective stress from normal compaction trends.
- The modelling of rock physical properties as well as the reversal trends led us to interpret the low Vp/Vs anomaly at 4 km depth as the top of formations enriched in gas under pressure. Transient fluid pressure events induced by episodical self-sealing processes (Batzle and Simmons, 1977) represent a significant mechanism in hydrothermal environments which have been noted in other inflating calderas as Long Valley Caldera (Farrar et al., 1995; Sanders et al., 1995; Hill et al., 1990) and Yellowstone (Husen et al., 2004). In CF, reversal trends gather in the center of the caldera and imply a localized pressure source as suggested by the narrow bell shape of the recorded displacement. The signature of a low Vp/Vs ratio at 4 km depth excludes the presence of melted rocks at 4 km whose assessment

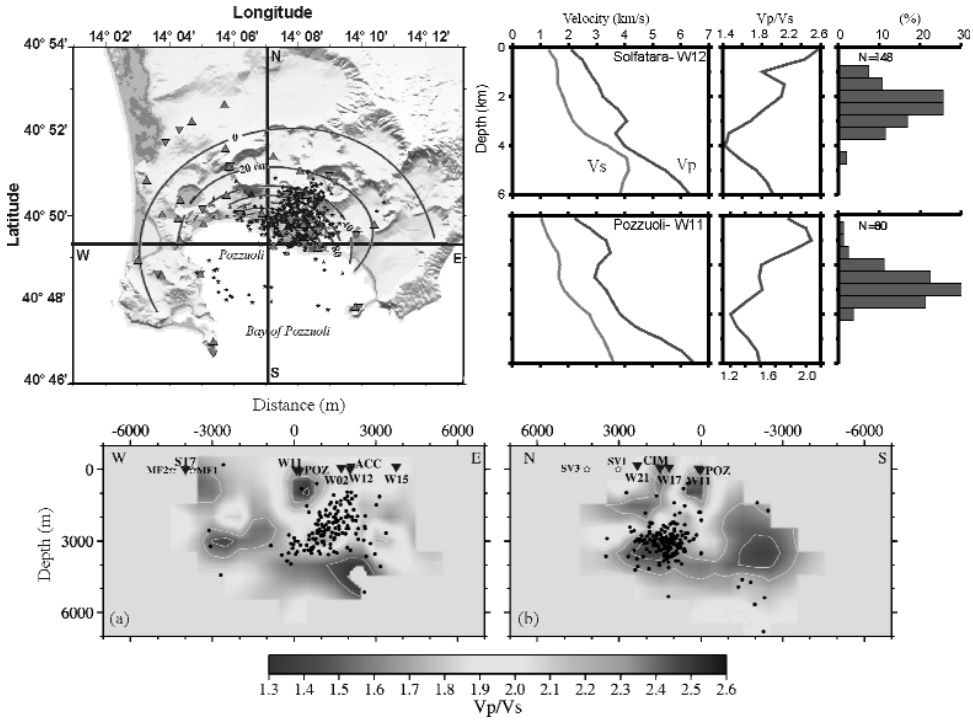

Fig. 2. *Top left panel* – Map of the CF caldera showing seismometer stations (triangles) and final earthquake locations (stars). The map also reports the elevation contours (black lines) for the 1982-1984 uplift. *Top right panel* – Reversal trends on vertical velocity profiles, Vp/Vs and, histograms showing earthquake distribution along profiles (radius equal to 0.5 km). *Bottom* – Vp/Vs vertical cross-sections and earthquake distribution (black points) along the directions reported in the map. Stars and triangles indicate wells and stations, respectively.
You can see this figure in color on page 205.

would instead require high Vp/Vs ratios. The absence of melt formations down to 4-5 km depth is also in accordance with the results reported in Zollo et al. (2003).

– Earthquake locations are mostly distributed on the top of velocity reversals and within the low Vp/Vs anomaly. Our results from the CF caldera suggest that storage of supercritical fluids at depth has to be tracked to monitor the caldera activity and to prevent risks.

REFERENCES

Allard P., Maiorani A., Tedesco A., Cortecci G., Turi B. (1999). Isotopic study of the origin of sulfur and carbon in Solfatara fumaroles, Campi Flegrei caldera. *J. Volcanol. Geotherm. Res.*, 48, 139-59.

Aster R. C., Meyer R. P. (1988). Three-dimensional velocity structure and hypocenter distribution in the Campi Flegrei caldera, Italy. *Tectonophysics*, 149, 195-218.

Barberi F., Corrado G., Innocenti G., Luongo G. (1984). Phlegraen Fields 1982-1984: Brief chronicle of a volcano emergency in a sensely populated area. *Bull. Volcanol.*, 47, 175-85.

Batzle M. L., Simmons G. (1997). Geothermal systems: Rocks, fluids, fractures, in The Earth's Crust: Its Nature and Physical Properties. *Geophys. Monogr. Ser.*, 20, 233-42, edited by Heacock JC, AGU, Washington, D.C.

Batzle M. L., Wang Z. W. (1992). Seismic properties of pore fluids. *Geophysics*, 57, 1396-1408.

Benz H. M., Chouet B. A., Dawson P. B., Lahr J. C., Page R. A., Hole J. A. (1996). Three-dimensional P and S wave velocity structure of Redoubt Volcano, Alaska. *J. Geophys. Res.*, 101, 8111-28.

Bianchi R., Coradini A., Federico C., Giberti G., Lanciano P., Pozzi J. P., Sartoris G., Scandone R. (1987). Modeling of surface deformations in volcanic areas: The 1970-1972 and 1982-1984 crises at Campi Flegrei, Italy. *J. Geophys. Res.*, 92, 14139-50.

Bonafede M., Dragoni M., Quareni F. (1986). Displacement and stress field produced by a centre of dilation and by a pressure source in a viscoelastic half-space: Application to the study of ground deformation and seismic activity at Campi Flegrei. *Geophys. J. R. Astron. Soc.*, 87, 455-85.

Bonafede M. (1991). Hot fluid migration: An efficient source of ground deformation: Application to the 1982-1985 crisis at Campi Flegrei-Italy. *J. Volcanol. Geotherm. Res.*, 48, 187-98.

Capuano P., Achauer U. (2003). Gravity field modeling in the Vesuvius and Campanian area, in *The TomoVes Seismic Project: Looking Inside Mt. Vesuvius*, edited by A. Zollo et al., Cuen, Naples, Italy.

Casertano L., Oliveri A., Quagliariello M. T. (1976). Hydrodynamics and geodynamics in the Phlegraean Fields area of Italy. *Nature*, 264, 1614.

Chiodini G., Frondini F., Cardellini C., Granieri D., Marini L., Ventura G. (2001). CO2 degassing and energy release at Solfatara Volcano, Campi Flegrei, Italy. *J. Geophys. Res.*, 106, 16213-21.

Chiodini G., Todesco M., Caliro S., Del Gaudio C., Macedonio G., Russo M. (2003). Magma degassing as a trigger of bradyseismic events: The case of Phlegrean Fields (Italy). *Geophys. Res. Lett.*, 30(8), 1434, doi:10.1029/2002GL016790.

de Lorenzo S., Zollo A., Mongelli F. (2001). Source parameters and 3-D attenuation structure from the inversion of microearthquake pulse width data: Qp imaging and inferences on the thermal state of the Campi Flegrei Caldera. *J. Geophys. Res.*, 106, 16265-86.

Dvorak J. J., Gasparini P. (1991). History of earthquakes and vertical ground movement in Campi Flegrei caldera, southern Italy: Comparison of precursory event to the A.D. eruption of Monte Nuovo and activity since 1968. *J. Volcanol. Geotherm. Res.*, 48, 77-92.

Dvorkin J., Nur A. (1996). Elasticity of high-porosity sandstones: Theory for two North Sea datasets, *Geophysics*. 61, 1363-70.

Dvorkin J., Prasad M., Sakai A., Lavoie D. (1999). Elasticity of marine sediments: Rock physics modeling. *Geophys. Res. Lett.*, 26, 1781-4.

Farrar C. D., Sorey M. L., Evans W. C., Howle J. F., Kerr B. D., Kennedy B. M., King C. Y., Southon J. R. (1995). Forest-killing diffuse CO2 emission at Mammoth Mountain as a sign of magmatic unrest. *Nature*, 376, 675-8.

Ferrucci F., Hirn A., Virieux J., De Natale G., Mirabile L. (1992). P-SV conversions at a shallow boundary beneath Campi Flegrei Caldera (Naples, Italy): Evidence for the magma chamber. *J. Geophys. Res.*, 97, 15351-9.

Gassmann F. (1951). Elastic wave through a packing of spheres. *Geophysics*, 16, 673-85.

Hill D. P., Ellsworth W. L., Johnston M. J. S., Langbein J. O., Oppenheimer D. H., Pitt A. M., Reasenberg P. A., Sorey M. L., McNutt S. R. (1990). The 1989 earthquake swarm beneath Mammoth Mountain, California: An initial look at the 4 May through 30 September activity. *Bull. Seismol. Soc. Am.*, 80, 325-39.

Hole J. A., Brocher T. M., Klemperer S. L., Parsons T., Benz H. M., Furlong K. P. (2000). Three-dimensional seismic velocity structure of the San Francisco Bay area. *J. Geophys. Res.*, 105, 13859-74.

Husen S., Smith R. B., Waite G. P. (2004). Evidence for gas and magmatic sources beneath the Yellowstone volcanic field from seismic tomographic imaging. *J. Volcanol. Geotherm. Res.*, 131, 397-410.

Ito H., DeVilbiss J., Nur A. (1979). Compressional and shear waves in saturated rock during water-steam transition. *J. Geophys. Res.*, 84, 4731-5.

Kissling E., Ellsworth W. L., Eberhart-Phillips D., Kradolfer U. (1994). Initial reference models in local earthquake tomography. *J. Geophys. Res.*, 99, 19635-46.

Latorre D., Virieux J., Monfret T., Monteiller V., Vanorio T., Got J.-L., Lyon-Caen H. (2004). A new seismic tomography of Aigion area (Gulf of Corinth-Greece) from a 1991 dataset. *Geophys. J. Int.*, 159, 1013-31.

Newhall C. G., Dzurisin D. (1988). Historical unrest at large calderas of the world. *U.S. Geol. Surv. Bull. B*, 1855(1-2), 1108.

Oliveri del Castillo A., Quagliariello M. T. (1969). Sulla genesi del bradisismo flegreo. *Atti Assoc. Geofis. Ital.*, 4, 1-4.

Sanders C. O., Ponko S. C., Nixon L. D., Schwartz E. A. (1995). Seismological evidence for magmatic and hydrothermal structure in Long Valley caldera from local earthquake attenuation and velocity tomography. *J. Geophys. Res.*, 100, 8311-26.

Spakman W., Nolet G. (1988). Imaging algorithms, accuracy and resolution, in *Mathematical Geophysics*, edited by N. Vlaar, pp. 155-87, Springer, New York.

Thurber C. H. (1992). Hypocenter-velocity structure coupling in local earthquake tomography. *Phys. Earth Planet. Inter.*, 75, 55-62.

Vanorio T., Prasad M., Nur A., Patella D. (2002). Ultrasonic velocity measurements in volcanic rocks: Correlation with microtexture. *Geophys. J. Int.*, 149, 22-36.

Vanorio T. (2003). Physical properties of volcanic rocks from the Campanian Plain. *TOMOVES: The Internal Structure of Mt. Vesuvius: A Seismic Tomography Investigation*. Edited by P. Capuano et al., Liguori Editore, 553-580.

Wang Z. W., Nur A. (1989). Effect of CO2 flooding on wave velocities in rocks and hydrocarbons. *Soc. Pet. Eng. Res. Eng.*, 3, 429-39.

Zollo A., Judenherc S., Auger E., D'Auria L., Virieux J., Capuano P., Chiarabba C., de Franco R., Makris J., Michelini A., Musacchio G. (2003). Evidence for the buried rim of Campi Flegrei caldera from 3-d active seismic imaging. *Geophys. Res. Lett.*, 30(19), 2002, doi:10.1029/2003GL018173.

The Vp and Vp/Vs structure of the Campi Flegrei caldera

C. Chiarabba, M. Moretti, P. De Gori
Istituto Nazionale di Geofisica e Vulcanologia, CNT, (Rome)

Abstract: In this study we computed the shallow structure of the Phlegrean Fields caldera by the integration of active and passive seismic data. P-wave arrivals from airguns shots (Serapis project, 2001) and P- and S-wave arrival times re-elaborated from the last seismic swarm at the volcano are used to define Vp and Vp/Vs tomographic images of the upper crust beneath the caldera. We used the TomoDD inversion code that consists of a simultaneous inversion for earthquake hypocenters (with a double difference algorithm) and velocity parameters. The high resolution of the model allows us to identify the caldera fault bordering a high Vp, high Vp/Vs ring anomaly both inland and off-shore. No features of a significant magma accumulation are revealed in the upper 4 km. A dramatic Vp/Vs decrease at 3-4 km below the center of the caldera.

Seismic data

During 2001, a two weeks long active seismic experiment has been executed. A total of about 77000 waveforms from 5000 airguns shots at a 2D array of 134 stations has been analysed and used by Zollo et al. (2003).
From the huge dataset, we selected 500 shots for which more than 50 arrivals at OBS and on-land stations were available. Most of the data (see Figure 1) sample the off-shore region of the caldera and the Pozzuoli Gulf. The fast distance stations, 10-20 km, allows to investigate the upper 1-2 km of the crust, with most of the crossing at 1 km depth.
P-wave and S-P arrivals for 400 local earthquakes of the 1984 seismic swarm have been re-picked on digital re-analysed waveforms. Reading errors are improved with smaller uncertainties of about 0.02 s. A total of 19,200 phases at 81 stations is used in the inversion.

Tomographic modeling

Active and passive data have been inverted with the double difference inversion algorithm (TomoDD) by Zhang and Thurber, 2003.

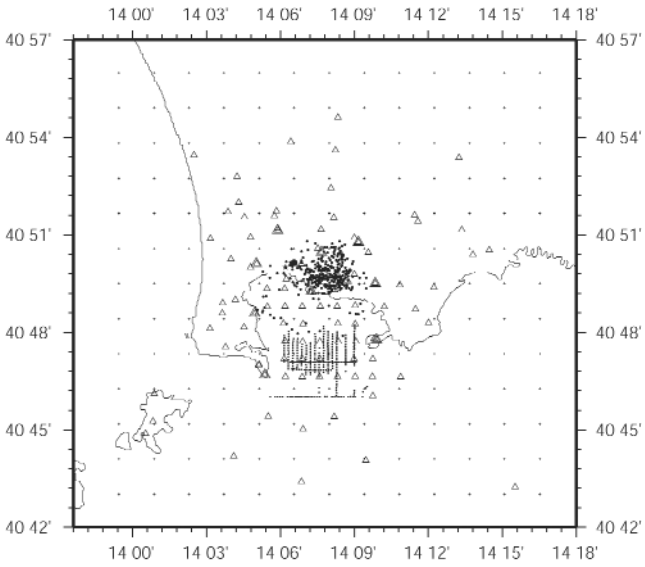

Fig. 1. Map distribution of seismic stations (on land and OBS) shots and local earthquakes. Crosses are the nodes used in the inversion.

In our approach, we first inverted shots data for the uppermost (0-2 km) structure. Then, we used the model computed with shots data as the starting model for the inversion of local earthquakes. Vp/Vs parameters were only inverted in this run, by using a starting value of 1.76 derived from Wadati diagram of the data set. Final rms is 0.07 s.

Resolution of the model has been verified with synthetic tests.

Figure 2a shows the Vp model in the inverted layers. At 0 km depth, a central low Vp anomaly is present beneath the caldera, mostly centered in the Pozzuoli Gulf (Vp<2.5 km/s), indicating the sedimentary fillings of the caldera. A clear high Vp ring of anomalies defines the caldera rim at 0 and 1 km depth. Vp ranges from 4.0 to 2.8 km/s with maxima located at the nortwestern limit of the caldera in correspondance of more competent lava beds. At 2 km depth, the low Vp anomaly is centered a few kms to the east of the main shallow low Vp, between Pozzuoli and Procida.

Vertical section shows the details of the caldera structure (Figure 2b). The caldera ring faults are defined by strong velocity gradients between the high Vp caldera rim and the low Vp sedimentary fillings.

The collapsed regions are characterized by a shallow and broad low Vp anomaly down to 1 km depth and a deeper and narrow low Vp volume down to 3 km depth, nested within the upper anomaly. At surface, high Vp/Vs anomalies are observed around the caldera rim, suggesting the presence of diffuse cold fluid circulation along the caldera rim faults. At depth, a significant low Vp/Vs anomaly is observed consistent with a gas enriched volume.

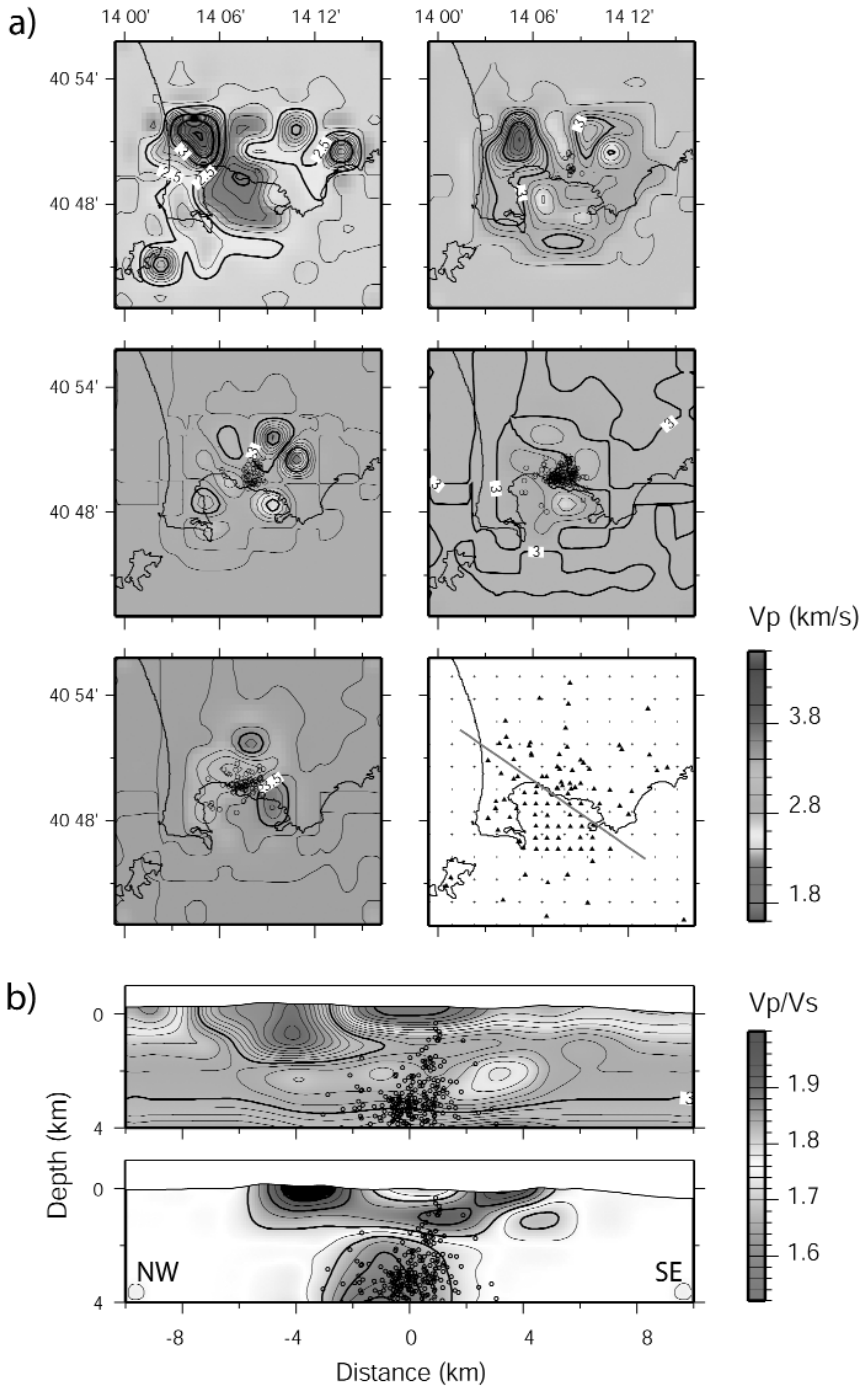

Fig. 2. (a) P wave velocity model in the five layers. (b) Vertical sections across the caldera of Vp (top) and Vp/Vs (bottom) models. Relocated earthquakes are plotted on sections.
You can see this figure in color on page 206.

Discussion and conclusion

Vp and Vp/Vs models help to constrain the structure and physics of the Phlegrean Fields plumbing system. The main results of this inversion is the low Vp/Vs anomaly located beneath caldera between 2 and 4 km that is interpreted as an over-pressured gas volume. The lack of high Vp/Vs anomaly interpretable as magma fluids in this depth range suggests that the magma chamber responsible for the heat is located below the target volume.
The more likely model of unrest is the fluctuation of gas over-pressure within the reservoir located at 2 to 4 km beneath the caldera identified by pronounced high Vs, low Vp/Vs anomaly.

References

Zhang H., Thurber C. H. (2003). Double-difference tomography: the method and its application to the Hayward fault, California. *Bull. Seism. Soc. Am.*, 93, 1875-89.

Zollo A., Judenherc S., Auger E., D'Auria L., Virieux J., Capuano P., Chiarabba C., de Franco R., Makris J., Michelini A., Musacchio G. (2003). Evidence for the buried rim of Campi Flegrei caldera from 3-d active seismic imaging. *Geophys. Res. Lett.*, 30(19), 2002, doi:10.1029/2003GL018173.

A 3D velocity model for earthquake location in Campi Flegrei area: application to the 1982-84 uplift event

C. Satriano[1], A. Zollo[1], P. Capuano[2,3], G. Russo[1], T. Vanorio[4], G. Caielli[5], L. Lovisa[6], M. Moretti[7]

[1] *Dipartimento di Scienze Fisiche, Università Federico II, Napoli, Italy*

[2] *Dipartimento di Scienze e Tecnologie per l'Ambiente ed il Territorio, Università del Molise, Isernia, Italy*

[3] *Osservatorio Vesuviano, INGV, Napoli, Italy*

[4] *Géosciences Azur, CNRS, Université de Nice, Sophie Antinopolies, Valbonne, France*

[5] *Istituto per la Dinamica dei Processi Ambientali, CNR, Milano, Italy*

[6] *Istituto Nazionale di Oceanografia e Geofisica Sperimentale, Trieste, Italy*

[7] *Centro Nazionale Terremoti, INGV, Roma, Italy*

Abstract: The uplift crisis of the 1982-1984 in the Campi Flegrei area underlined the importance of seismic surveillance for this volcanic caldera. One of the key elements for an effective seismic network is to make use of a reliable velocity model for earthquake location.
In the present work we will discuss criteria for the construction and validation of a new 3D P-wave velocity model for earthquake location in the Campi Flegrei area built from the integration of two high-resolution 3D tomographic images of the region.
The model is used for locating a group of earthquakes from the uplift event of the 1982-1984.

Introduction

The Campi Flegrei (CF) caldera is an active volcanic system located at the west of the city of Naples. Like other calderas, CF periodically experiences significant unrest episodes which include ground deformations and seismic swarms. Nevertheless ground deformations in CF may reach values without equal in the world. Two marked ground uplift took place in the area in the periods 1970-1972 and 1982-1984. The last one, began in the second half of 1982 and was characterized by a total vertical displacement of 1.8 m (Barberi et al., 1984), together with a seismic swarm of more that 15,000 shallow microearthquakes with a maximum duration magnitude of 4.0 (Zollo and De Natale, 1986).

Aster and Mayer (1988) first made a joint tomographic and earthquake location study, using 228 events occurred during the 1982-1984 crisis. Recently (Capuano et al., this issue) a database of 3C waveforms containing several hundreds microearthquakes have been reconstructed and the whole waveform data base have been re-picked.
Vanorio et al. (2005) upgraded the original dataset by using 1209 earthquakes and performed a new joint inversion of earthquake location and P and S velocity model. They interpreted the resulting velocity model by using experimental measurements of rock physical properties.
The SERAPIS experiment (Zollo et al., 2002) has given a new insight into the structure of the CF area. Zollo et al. (2003) and Judenherc and Zollo (2004) obtained high-resolution 3D P wave velocity images from the inversion of the active seismic data (~90,000 P wave first arrival times), evidencing several volcanic structures like the buried rim of the Campi Flegrei caldera.
One of the most important components of volcanic surveillance is the recording and analysis of seismic activity. Due to the strong 3D structural variations generally characterizing the volcanic areas, in order to obtain reliable earthquake locations it is important not only to have a dense network with a good azimuthal coverage deployed on the area but also a valid velocity model.
In this paper, starting from the results of tomographic studies, we have developed and validated a 3D P-wave velocity model for earthquake location in CF area. This model have been used to locate the seismicity of the 1982-1984 uplift episode.

Construction of the model

We constructed a 16 x 20 x 8 km 3D P-wave model for the CF area and surroundings, centered on the Bay of Pozzuoli, starting from two 3D tomographic images. The first is a 250m-cell P wave tomography of the Bay of Pozzuoli obtained by Zollo et al. (2003); the second is a 1000m-cell image of the Gulf of Naples obtained by Judenherc and Zollo (2004).
Due to the resolution of the tomographic procedure, both the starting models have cells where the velocity value is not defined. However, for event location, the velocity model must be defined everywhere in the search volume so that the location algorithm can look for all the possible ray paths.
In order to define a complete velocity model for the CF area we proceed as follows.
First we select the interested area, then the large scale model (1000m) is re-sampled at 250m, finally the two model are merged together using the values of the large scale model where the 250m values were not defined. Then, for the cells which still remained undefined, we use a mean value for that particular depth.
The resulting model was filtered using a cosine filter with one cell width (250m), in order to avoid abrupt changes in velocity from a cell to another and,

therefore, unrealistic reflections in ray paths, especially for those areas where different kind of information were combined.
Finally, the model was extended above the sea level, using the mean velocity value of the shallowest layer.
The resulting model is shown in Figure 1. P-wave velocity values go from 1.12 km/s at the surface to about 7 km/s for the deepest layers.
As already evidenced by Zollo et al. (2003), the most important feature of the model is the presence of an arc-like, high P-velocity anomaly (Vp = 3.5-4.0 km/s) delineating the southern border of the gulf of Pozzuoli, presenting a pattern almost concentric to the coastal line. The top of this body is at about 800m depth and it extends down to about 2000m depth. Its location and annular shape indicate that it represents the image of the buried rim of the CF caldera.

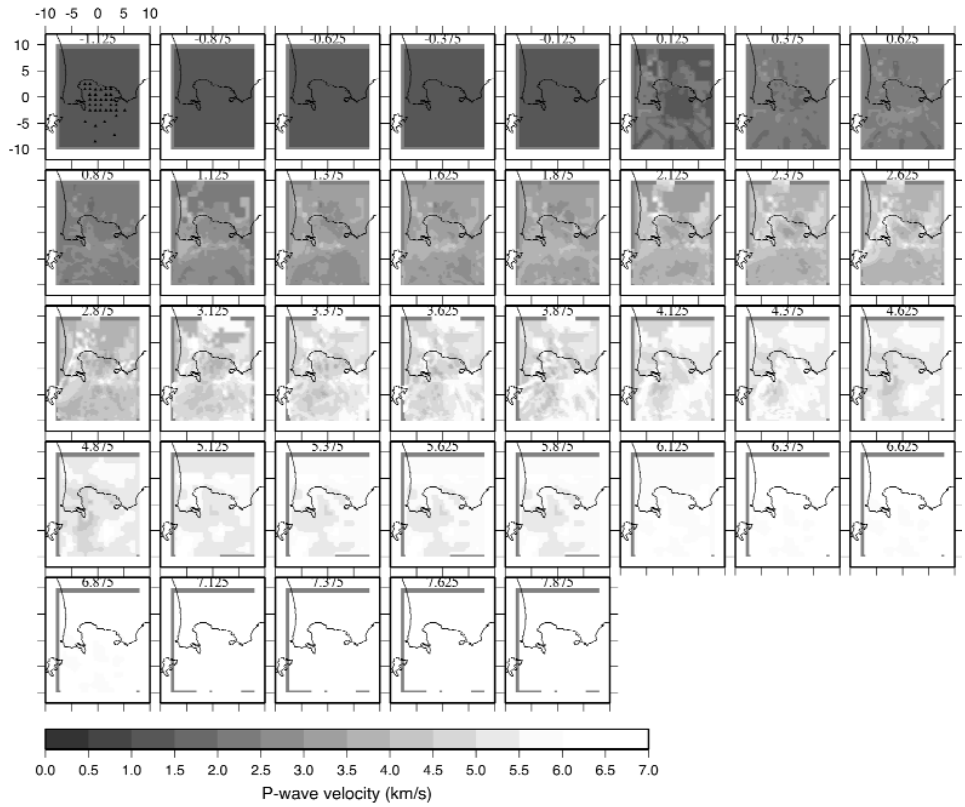

Fig. 1. 3D P-wave velocity filtered model resulting from the integration of two tomographic images of the CF area from the SERAPIS experiment (Zollo et al., 2003; Judenherc and Zollo, 2004). The first slice also shows the position of the OBS used for the location of the SERAPIS shots in the Pozzuoli bay.
You can see this figure in color on page 207.

The Italian Oil Agency (AGIP) drilled five 2-3 km deep boreholes on the landside of the caldera for geothermal exploration purposes (AGIP, 1987). Lithostratigrafic and sonic log data indicate that the caldera rim is formed by a sequence of compacted tuffs, tuffs with interbedded lavas and thermo metamorphic rocks, the latter of which are encountered at about 2-2.5 km depth. P-wave log velocities show a variation with depth (2.7-3 km/s at 0.8-1 km depth, 3.6-4.2 km/s at 2-2.2 km depth) which is consistent with our velocity model in the same depth range.

Verification of the 3D velocity model

We evaluated the quality of the constructed velocity model looking at the differences between observed and calculated travel times for the shots in the Pozzuoli bay from the SERAPIS experiment (Zollo et al., 2002); then we tried to locate the shots using the proposed model.
The travel times are calculated using a method based on the finite difference solution of the eikonal equation (Podvin and Lecomte, 1991), which is valid for a 3D heterogeneous medium.
Figure 2 shows the distribution of the differences between observed and calculated travel times using different models. We make a comparison between a 1D model, obtained calculating the mean value of each layer, the 3D velocity model obtained by Vanorio et al. (2005), our proposed 3D unfiltered model and the 3D filtered model.
Both the 1D model and the Vanorio model present a highly spread distribution of time residuals and a very large mean value (-0.37s and 0.23s, respectively). The 3D unfiltered model still present a bias (-0.05s), but the distribution of residual is very narrow, which indicates that actual travel times are better reproduced. The 3D filtered model presents a worse bias (-0.11s), but a similar distribution.
We verify the consistency of our model also by comparing the location of the SERAPIS shots using these four models computed by NonLinLoc program (Lomax et al., 2000) to obtain probabilistic location using a non-linear global search methods. The results of location are shown in Figure 3. The black stars are the located events; the grey dots show the actual position of the shots.
Figure 3a shows the location obtained using the 1D model. The shots path is quite well reproduced but there is a shift in horizontal position that becomes larger moving inward the Pozzuoli bay. All the events are located around 1 km depth with a little dispersion. Nevertheless we are locating very shallow events (in Figure 3 we show the mean event depth which is around 10 meters).
Figure 3b shows the location obtained with the 3D Vanorio model. The shots path is only vaguely reproduced. Events are very scattered in depth without showing an evident mean value. A great quantity of events (21%) is located above the sea level.

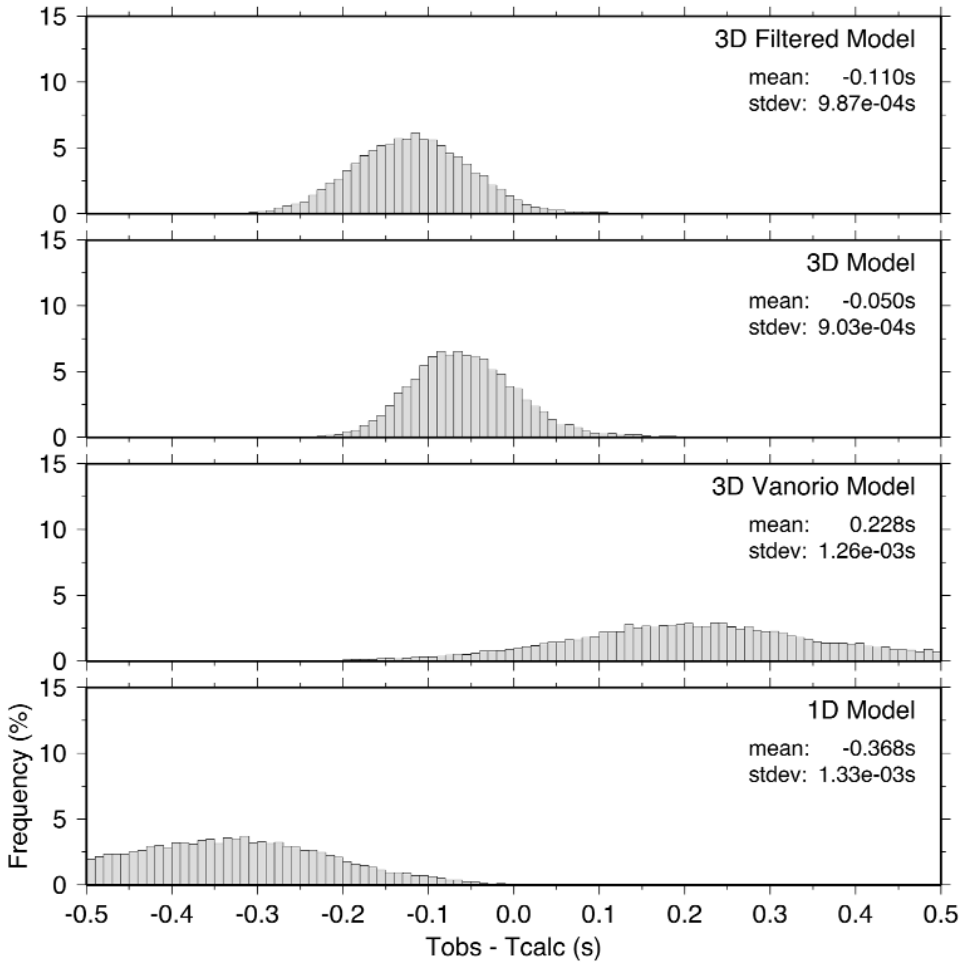

Fig. 2. Distribution of the differences between observed and calculated travel times at the Pozzuoli OBS for different velocity models: (a) 1D velocity model obtained using a mean velocity value for each layer, (b) 3D velocity model from Vanorio et al. (2005), (c) proposed 3D unfiltered model and (d) proposed 3D filtered model.

The third location is obtained using our 3D unfiltered model (Figure 3c). The horizontal view shows a good agreement between observed and actual shots position, even if there is still a little shift. The events are distributed in depth mainly along three levels, as one can clearly see from WE projection, and become deeper moving outside the bay. The events located in the northern part of the figure have a mean depth which is closer to the actual one, but with a dispersion which makes a number of events to lie above the sea level. The events in the central and southern part of the figure are placed at an unrealistic depth (the maximum depth of the bay in that area is

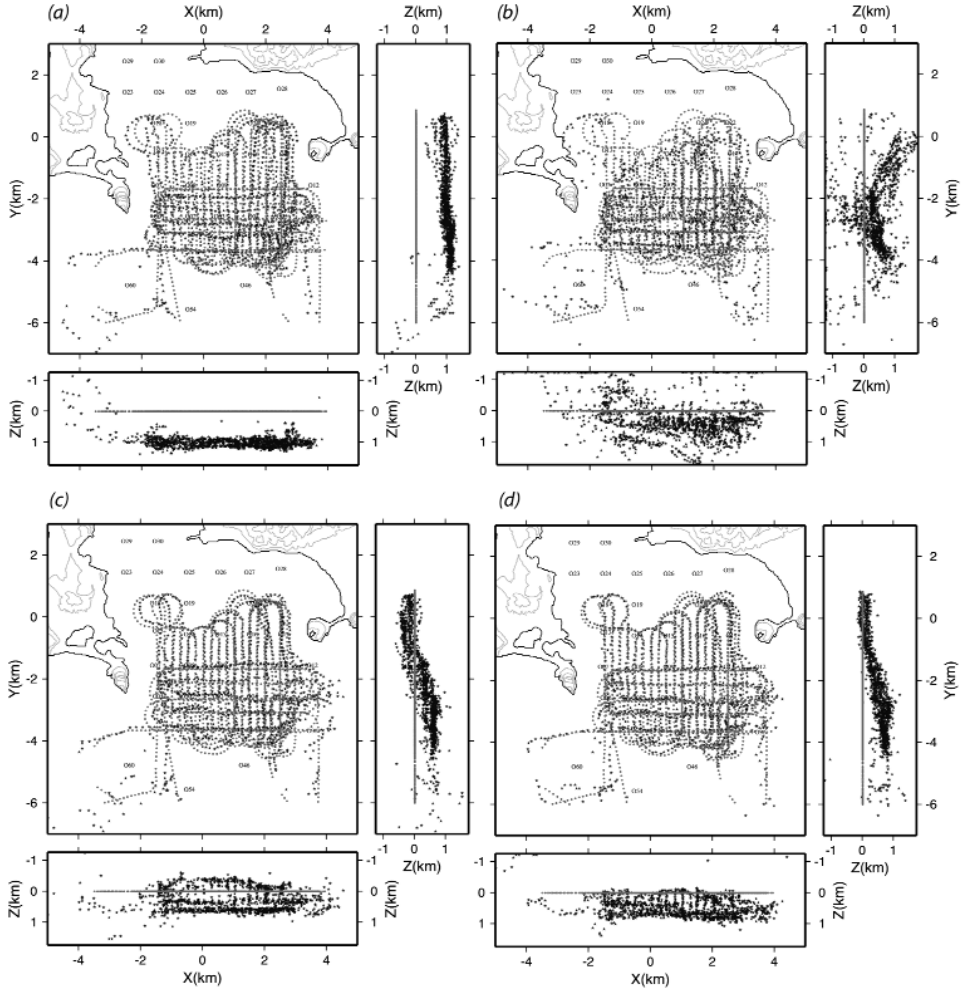

Fig. 3. SERAPIS shots locations using the four models described in Figure 2: 1D (a), Vanorio (b), 3D unfiltered (c), 3D filtered (d). The grey dots show the actual shot positions in the plane view, while they indicate a mean depth in the vertical views. The black stars are the located shots.

around 300m). This is probably due to the lower density of OBS in this area (as one can see from Figure 1), which implies a bad quality of the location in terms of the 68% confidence ellipsoid major semi-axis length (Lomax et al., 2001).

Figure 3d shows the location results using the 3D filtered model. The horizontal pattern is accurately reproduced; the dispersion in depth is strongly reduced with many events around the actual mean depth in the area where the location is more accurate. Again, as we move outward the bay, the quality of the location decreases and the depth estimate gets worse.

Figure 4 shows the distribution of the values of the 68% confidence ellipsoid major semi-axis length as a function of the position along the N-S direction. One can see how, for both the unfiltered and the filtered model, the quality of the location improves moving inward the bay (highest values of Y).

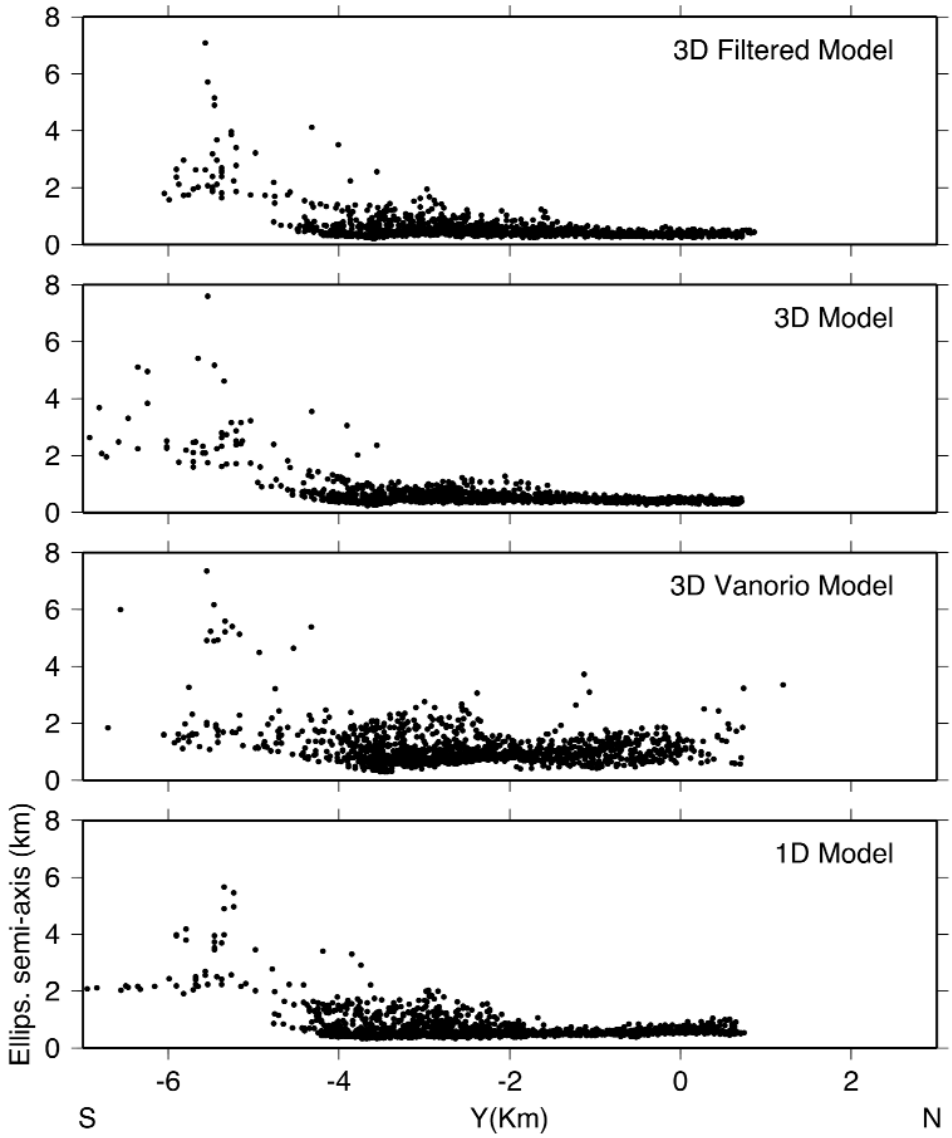

Fig. 4. Length of the major semi-axis of the 68% confidence ellipsoid as a function of the Y (N-S) position for the four models described in Figure 2.

Figure 5 shows the final residuals after the shots location. The filtered model gives better residuals than the unfiltered one, confirming the above discussion. After the analysis of the results of the described comparison, we may conclude that the 3D filtered velocity is highly consistent with the shots location and the observed P-wave arrival times, thus it may represent a more detailed P velocity model for locating earthquakes. We use this model to locate microearthquakes from the 1982-84 uplift event.

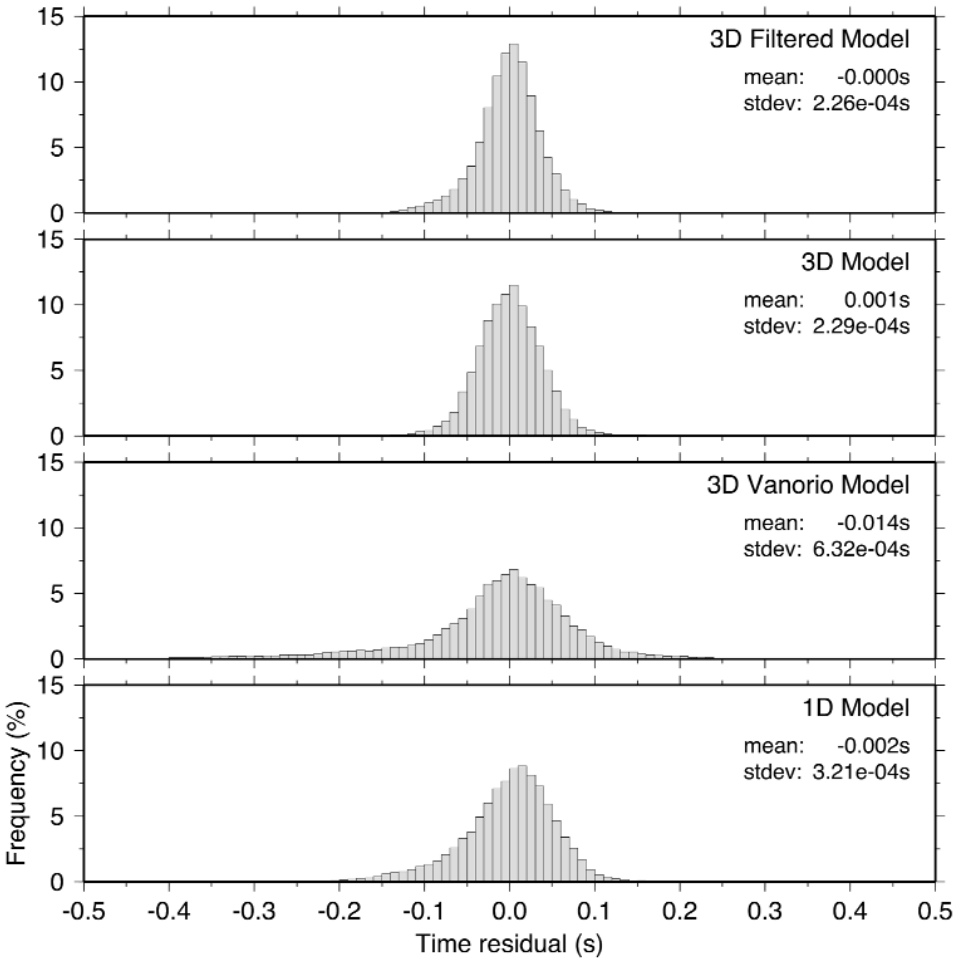

Fig. 5. Distribution of time residuals after the location of Pozzuoli shots for the four models described in Figure 2.

Location of the earthquakes from the 1982-84 uplift event

As a contribute to monitor the seismic activity accompanying the 1982-1984 crisis, the University of Wisconsin began a field experiment deploying a temporary network consisting of 21 three-component digital short-period seismometers. Data were recorded at 100 or 200 Hz sampling rates and 1 Hz geophones were used (Aster and Meyer, 1988). The seismic monitoring network recorded more than 15,000 events. Events were clustered in time, mainly concentrated in the Pozzuoli-Solfatara area and had maximum duration magnitudes of 4.0 (De Natale and Zollo, 1986).
After the reconstruction of waveforms database and phase pickings (Capuano et al., this issue), Vanorio et al. (2005) used these database joint with the seismicity occurred in the previous period, recorded by the Osservatorio Vesuviano seismic network, to produce tomographic maps.
We started from a dataset of 726 events from January 1st trough April 15th 1984, with a total number of 4237 P and 2837 S readings. For the location we used a fixed Vp/Vs ratio of 1.68; this is a reasonably good mean value for the inferred Vp/Vs ratio distribution in the area (Vanorio et al, 2005). A more consistent investigation of Vp/Vs ratio will be dealt in an upcoming study.
After the first location, we calculated the station corrections as the mean residual value for each station. We iterated this process two times. Figure 6 shows station residuals for P and S readings before applying station corrections (a) and after the last iteration (b). It is evident that the station residuals are highly reduced, except for two stations (W06, W08) for which, anyway, there are very few readings (13 and 8, respectively).
Figure 7 shows the final location result. We selected for plotting only the events with a maximum 68 per cent confidence ellipsoid semi-axis length of 1.5 km (319 earthquakes). The events are located within a small area in the Solfatara zone. Most of the hypocenters are clustered around a depth between 2 and 3 km. These results are in good accordance with the localization obtained by Vanorio et al. (2005) but events appear less scattered, especially in the W-E direction.

Discussion

We have constructed a 3D velocity model (Figure 1) for earthquake location in CF area and surroundings starting from two high-resolution tomographic images obtained after the SERAPIS seismic experiment.
We confirm that the 3D velocity model reproduce P waves travel times and location for the SERAPIS shots, also comparing with results obtained using a 1D mean model and the 3D tomographic model proposed by Vanorio et al. (2005).
This new 3D velocity model has been used to obtain non-linear global search earthquakes locations selecting 726 earthquakes from the 1982-1984 CF uplift

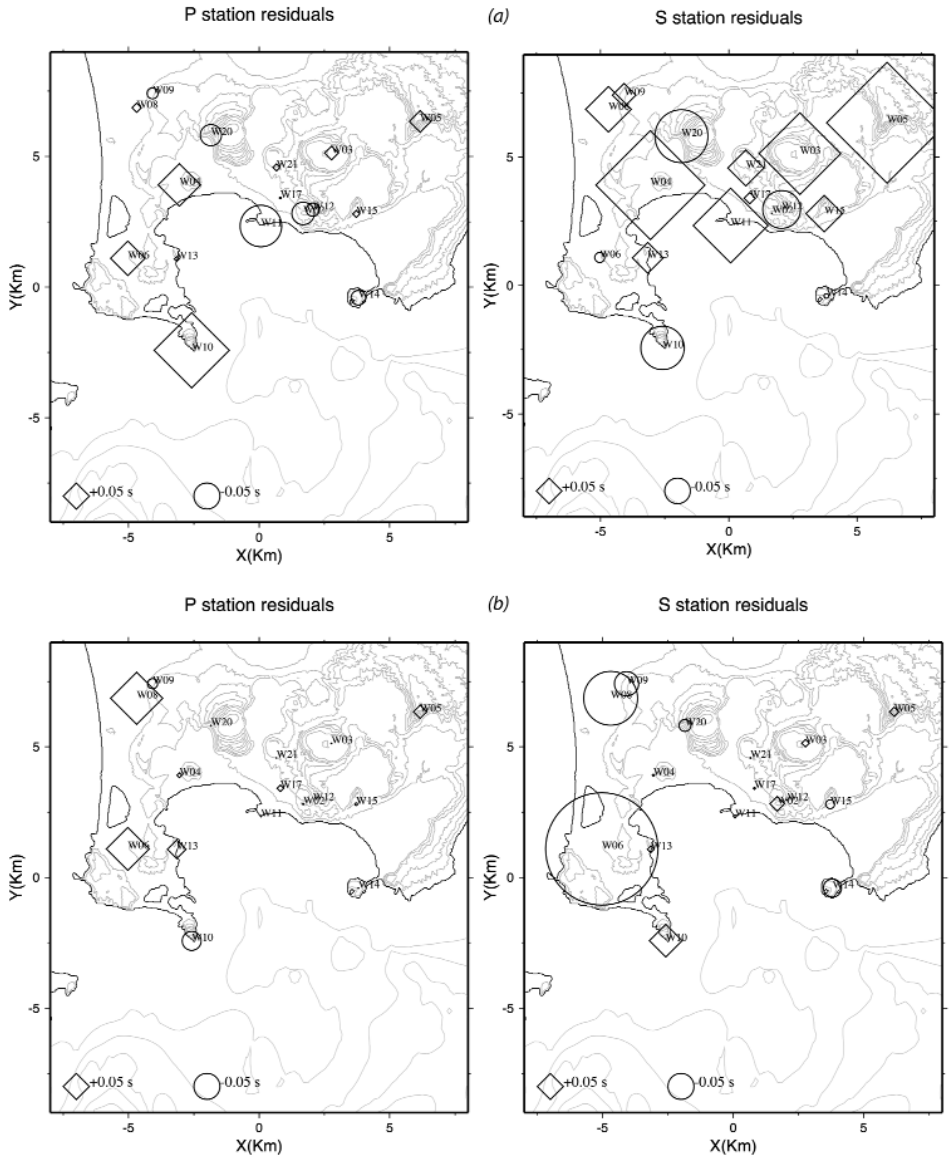

Fig. 6. P and S residuals for the Wisconsin stations (Aster and Meyer, 1988) before (a) and after (b) applying station corrections.

event obtaining locations in good accordance with previous studies (Aster and Mayer, 1988; Vanorio et al., 2005), but based on a larger and more robust database.

The earthquake locations obtained with the new 3D model are probably most representative of the true locations since this model is derived from shot data

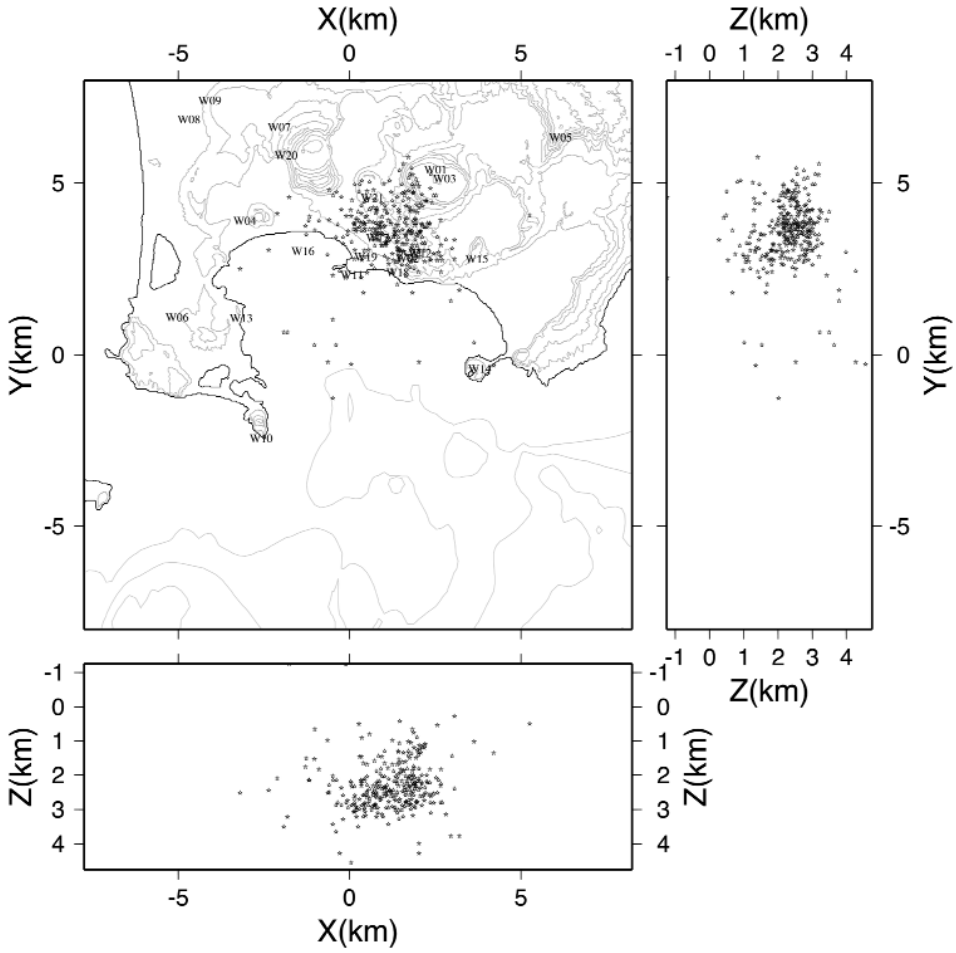

Fig. 7. Final location of 726 earthquakes from the 1982-84 uplift event. We selected for plotting only the events with a maximum 68% confidence ellipsoid semi-axis length of 1.5 km (319 earthquakes). The events are located within a small area in the Solfatara zone. Most of the hypocenters are clustered around a depth between 2 and 3 km.

with known source locations and origin times. Finally, we believe that the new 3D model can give more realistic images of earthquake distribution than a 1D model because of the high heterogeneity of the area (Judenherc and Zollo, 2004) and it will improve the accuracy of earthquake location and depth estimate in the volcano monitoring.

A successive study to verify Vp/Vs ratio and compute more reliable focal mechanism, will contribute to a better understanding of shallow structure at CF caldera.

REFERENCES

AGIP (1987). Geologia e Geofisica del Sistema Geotermico dei Campi Flegrei. *Servizi Centrali per l'Esplorazione*, SERG-MMESG, San Donato.

Aster R. C., Meyer R. P. (1988). Three-dimensional velocity structure and hypocenter distribution in the Campi Flegrei caldera, Italy. *Tectonophysics*, 149, 195-218.

Barberi F., Corrado G., Innocenti F., Luongo G. (1984). Phlegraen Fields 1982-1984: Brief chronicle of a volcano emergency in a densely populated area. *Bull. Volcanol.*, 47, 175-85.

Capuano P., Russo G., Vanorio T., Prevete R., Auger E., Bonagura M., Caielli G., Convertito V., Damiano N., D'Auria L., Emolo A., Lovisa L., Moretti M. (2006). 1984 Campi Flegrei seismic waveforms compilation, in *Geophysical Exploration of the Campi Flegrei (Southern Italy) Caldera' Interiors: Data, Methods and Results*, edited by A. Zollo, P. Capuano, M. Corciulo, pp. 15-24 , doppiavoce, Naples, Italy.

De Natale G., Zollo A. (1986). Statistical analysis and clustering features of the Phlegraean Fields earthquake sequence. *Bull. Seismol. Soc. Am.*, 76(3), 801-14.

Judenherc S., Zollo A. (2004). The Bay of Naples (southern Italy): Constraints on the volcanic structures inferred from a dense seismic survey. *J. Geophys. Res.*, 109, B10312, doi:10.1029/2003JB002876.

Lomax A. J., Virieux P., Volant & Berge C. (2000). Probabilistic earthquake location in 3D and layered models: introduction of a Metropolis-Gibbs method and comparison with linear locations, in *Advances in Seismic Event Location*, edited by C.H. Thurber & N. Rabinowitz, pp. 101-34, Kluwer, Amsterdam.

Lomax A., Zollo A., Capuano P., Virieux J. (2001). Precise, absolute earthquake location under Somma-Vesuvius volcano using a new three-dimensional velocity model. *Geophys. J. Int.*, 146, 313-31.

Podvin P., Lecomte I. (1991). Finite difference computations of traveltimes in very contrasted velocity models: a massively parallel approach and its associated tools. *Geophys. J. Int.*, 105, 271-84.

Vanorio T., Virieux J., Capuano P., Russo G. (2005). Three-dimensional seismic tomography from P wave and S wave microearthquake travel times and rock physics characterization of the Campi Flegrei Caldera. *J. Geophys. Res.*, 110(B03), doi:10.1029/2004JB003102.

Zollo A., Virieux J., Makris J., Auger E., Boschi L., Capuano P., Chiarabba C., D'Auria L., De Franco R., Judenherc S., Michelini A., Musacchio G. (2002). High resolution seismic imaging of the Campi Flegrei caldera, Southern Italy. *Eos Trans. AGU,* 83(47).

Zollo A., Judenherc S., Auger E., D'Auria L., Virieux J., Capuano P., Chiarabba C., de Franco R., Makris J., Michelini A., Musacchio G. (2003). Evidence for the buried rim of Campi Flegrei caldera from 3-d active seismic imaging. *Geophys. Res. Lett.*, 30(19), 2002, doi:10.1029/2003GL018173.

2

The Campi Flegrei blind test

A numerical blind test has been built-up and carried out to estimate the actual resolution power of the "Wisconsin" microearthquakes data-set acquired during the 1982-1984 seismic crisis. To this aim, a model representing the 3D structure of the caldera beneath Campi Flegrei area has been built-up, and a synthetic data-set of waveforms and time arrivals has been computed using a 3D staggered Fourier pseudo-spectral full-wave method and a 3D finite-difference solution of the eikonal equation, respectively. The geometry of stations and earthquakes reproduces the main features of that of the 1982-1984 data-set. The synthetic data-set consists of about 36,000 three-component seismograms and P- and S-time arrivals, computed at about thirty stations for a set of about 1200 earthquakes.

The tomographic inversion has been performed by four independent teams using different methods. The teams had no knowledge of either the input velocity model and earthquake hypocentres used to create the synthetic data-set. The results obtained by the different groups have been compared and analyzed in the light of the true model.

This work provide a thorough analysis of the earthquake tomography potential of the Wisconsin (1984) data-set. It shows that all the tested earthquake tomography methods provide reliable low-resolution images of the background velocity field of the Campi Flegrei area. However none of them succeeds in the main goal, that is in detecting the presence of either the magmatic chamber beneath 4 km of depth or the smaller, isolated bodies which represent possible magmatic chimneys and intrusions in the synthetic model.

The fact that the target is represented by fluid magma, and can be detected by an S-velocity anomaly, rather than a P-velocity one, is indeed a major difficulty for tomographic approaches, since direct S-phases are imbedded within complex waveforms and S-delays can easily be missed or misunderstood among converted phases. The synthetic data-sets of full waveforms and time arrivals clearly show that this might be a quite recurrent situation for the Winsconsin (1982-1984) waveforms data-set, thus suggesting that 1) a careful analysis of the waveform should be performed in the future, and 2) only a waveform inversion approach will likely improve the image of the magmatic chamber beneath.

Model construction and forward modelling

P. Klinc[1], E. Priolo[1], L. D'Auria[2], A. Zollo[2], G. Seriani[1], A. Vuan[1]

[1] *Istituto Nazionale di Oceanografia e Geofisica Sperimentale, Trieste, Italy*

[2] *Dipartimento di Scienze Fisiche, Università Federico II, Napoli, Italy*

Introduction

Several microearthquake waveforms were recorded in the Campi Flegrei area during the 1983-84 seismic swarms caused by an episode of bradisism. The data were acquired by a portable digital network deployed by Univ. of Wisconsin and Vesuvius Observatory and collected into a data-set (Aster and Meyer, 1988).

In order to reproduce a synthetic equivalent of that data-set, a 3-D digital model of the structure beneath the Campi Flegrei area has been build-up. The model reproduces the likely, but still hypothetical, velocity structure of the caldera and simulates the presence of the magmatic chamber at the bottom and some isolated bodies representing magmatic chimneys within the model. Being filled by fluid magma, these structural units are opaque to S-waves propagation (i.e. the S-wave velocity approaches to zero).

The ultimate goal of this study is to build-up a synthetic data-set of waveforms and arrival times to be used as an input by earthquake tomography methods to estimate the actual resolution power of the "Winsconsin" microearthquake data-set. The computation of such a data-set involves a number of difficulties, such as the design and definition of the 3D digital geo-model, the input preparation and execution of the numerical simulations of seismic full-wave propagation in a 3D complex structure, and the estimation of P- and S-arrival times. In particular, the main difficulty of the last point was that the arrival times should have been picked from a data-set of several thousands of complex waveforms manually. To overcome this problem, we have chosen to compute the theoretical travel times by an independent method.

The model design and input preparation tasks have been performed using the Gocad© software tools, whereas the data-set of full-waveforms has been computed using the 3-D Fourier staggered pseudo-spectral method originally developed within this project. Finally, the data-set of P- and S-arrival times has been computed using a numerical solution of the eikonal equation (Podvine and Lecomte, 1991) and NonLinLoc software (Lomax, 1999).

Model construction

The model represents a hypothetical structure of the caldera and the surrounding Earth's structure in a box with size 12 km × 14 km × 8 km, in the directions North, East and depth, respectively. The origin point is ($40^0$47'N, $14^0$02'E) and it is located at sea level (Figure 1).

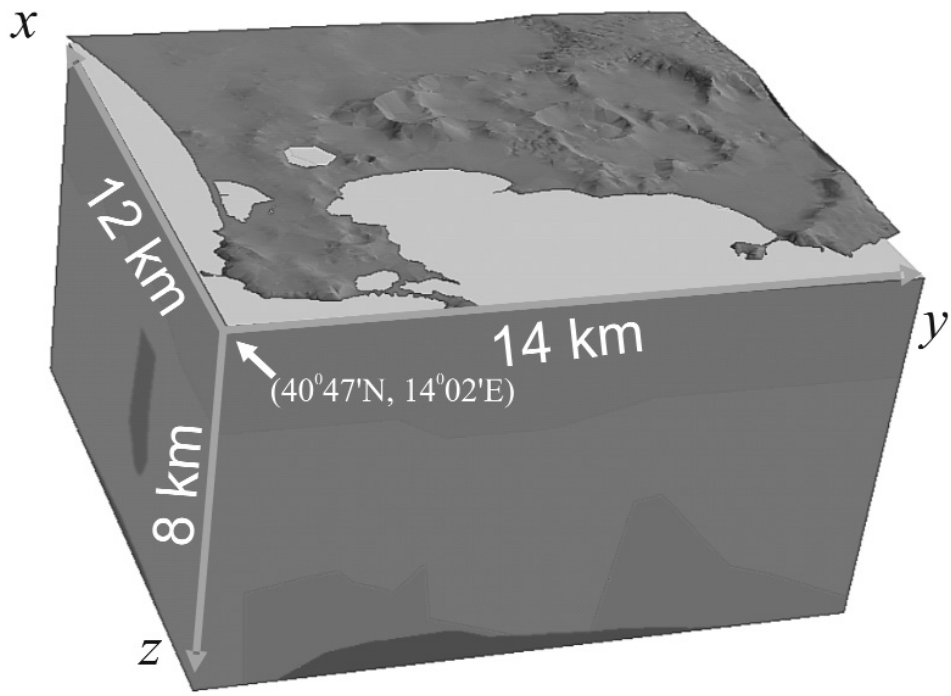

Fig. 1. The box containing the hypothetical model of the Campi Flegrei caldera. The arrow indicates the origin point.

The model has been defined using the Gocad® software. It does not include either topography or sea water layer, as well as it does not take into account the Earth's surface curvature. Regions are defined by their external boundaries and internal physical properties. The physical properties of each region are: velocity of compressional waves V_P, velocity of shear waves V_S, density ρ, attenuation Q. For this set of simulations, the attenuation has been defined according to Graves (2000). According to this formalism, the same attenuation value is used for P- and S-waves. Within regions, the physical parameters are

either constant or vary as a function of depth z. The model regions have been associated to six lithological units having the values of the physical properties defined in Table 1.

Table 1. Physical properties associated to the structural units in the hypothetical model

Unit	Vp (m/s)	Vp/Vs	kg/m^3	Q
Fluid Magma	2800	∞	2500	100
Carbonates	5500 + 250*(z(km)-4)	1.75	2600	200
Solid Magma	2500	1.8	2650	200
Met. Tuffs	4000 + 400* (z(km)-3)	1.8	2650	100
Tuffs	2000 + 500*z(km)	1.85	2400	80
Incoherent Soils	1000 + 500*z(km)	2.0	1500	50

In detail, the hypothetical structure of the Campi Flegrei simulates the presence of the magmatic chamber, filled by fluid magma at the bottom of the model. In addition, some intrusions of fluid magma is present in the upper layers (red body in Figure 2a). The first layer above the fluid magma is the carbonate unit (green layer in Figure 2b). Some solidified magma bodies (purple) is distributed in the northern part of the volume (Figure 2c). The remaining volume is filled by metamorphized tuffs (dark brown in Figure 2d) in the lower part and yellow tuffs in the upper part (light brown in Figure 2e). At the surface, the model features some shallow layers of unconsolidated material (grey in Figure 2f). The result of the construction of the model is a set of vector GoCad structures, which can be easily managed and modified.

Synthetic dataset construction

In order to perform the numerical simulations of seismic wave propagation, the information contained in the model need to be extracted from the digital GoCad data structures and formatted appropriately. Since the pseudo-spectral method uses regular (or structured) grids, this operation is performed by means of the Gocad® "Voxet" object. The result is a regular 3D rectangular grid of nodes, with desired spacing, on which the values of the physical properties are computed by local interpolation of the vector values defined within each region. The output is a binary file which contains the information about the physical parameters at each grid point. For this study, the model has been discretized with a spatial step of 50 m in all the directions. The resulting grid consists of 280 × 240 × 160 nodes, which corresponds to a total amount of 168 MB to store the four parameters by real type data (4 bytes).

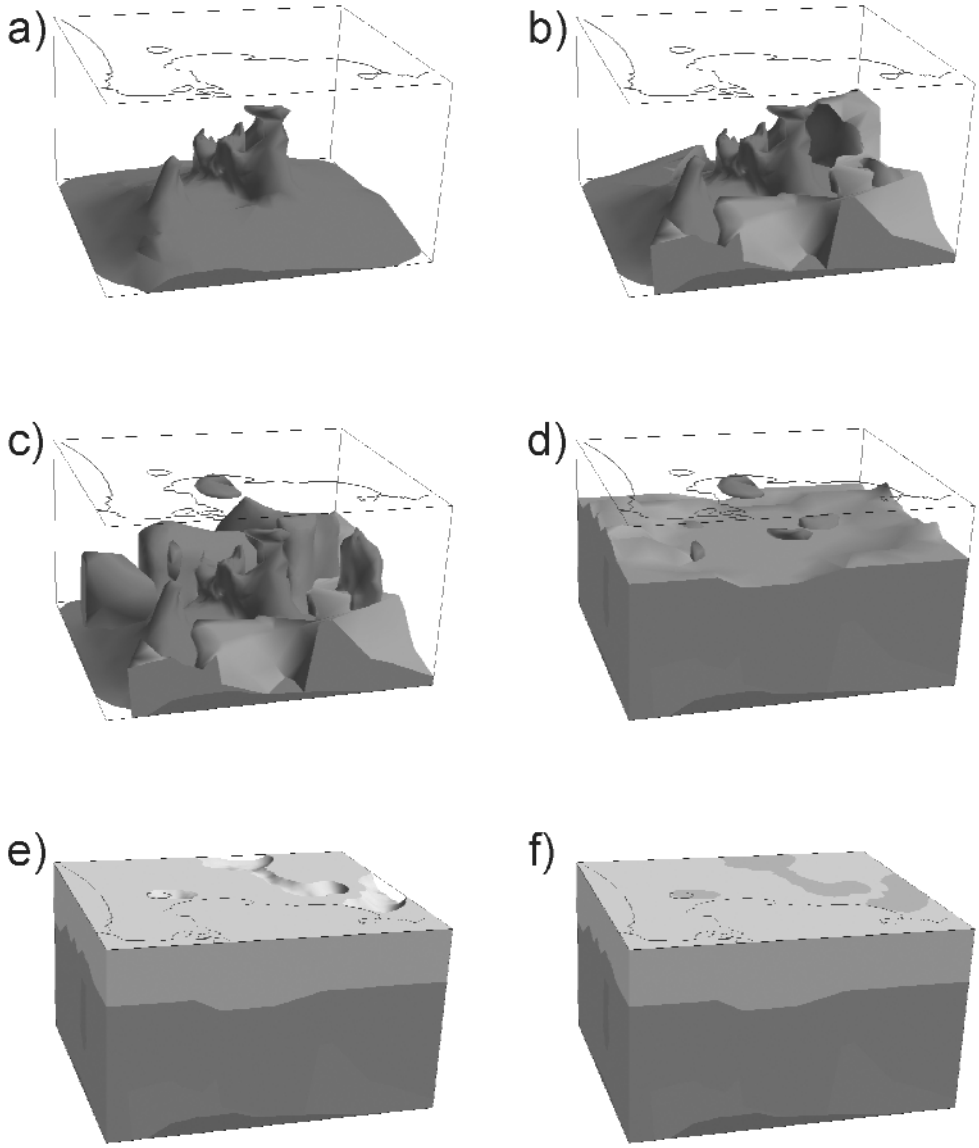

Fig. 2. Structure of the digital model.
You can see this figure in color on page 208.

The synthetic data-set of three-component waveforms has been computed for 14 receiver locations (Table 2 and Figure 3) corresponding to those of the 1982-1984 acquisition and a swarm of 1200 microearthquakes, located within a volume similar to that of the past seismic sequence. However, to better eva-

Table 2. Coordinates of the receivers used in the blind-test

Station	Lon.	Lat.
W03	40.8462	14.1528
W04	40.8352	14.0838
W05	40.8570	14.1930
W09	40.8667	14.0717
W11	40.8210	14.1208
W12	40.8267	14.1443
W13	40.8097	14.0827
W14	40.7963	14.1650
W15	40.8252	14.1640
W17	40.8307	14.1297
W18	40.8217	14.1367
W19	40.8257	14.1257
W20	40.8523	14.0982

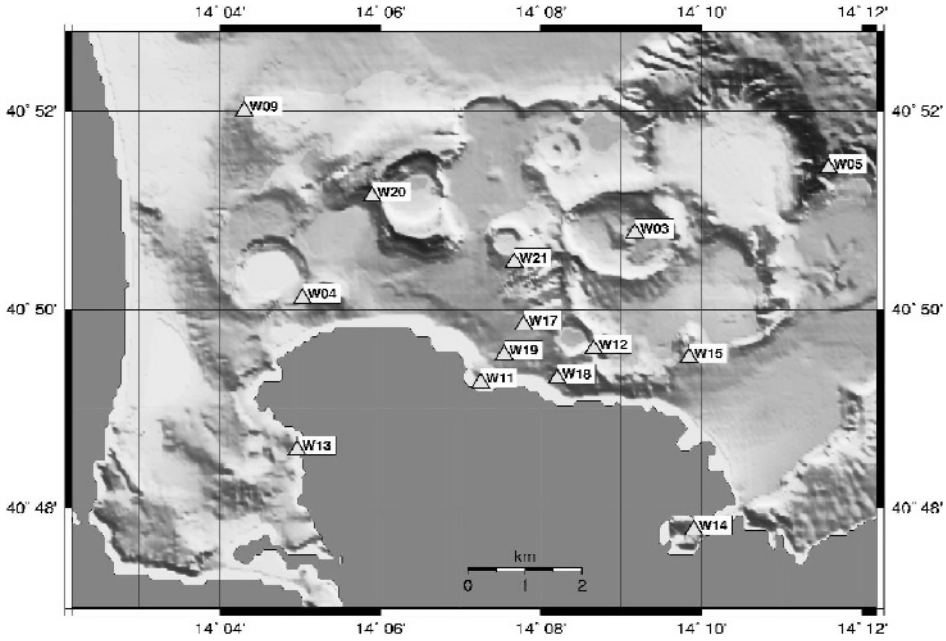

Fig. 3. Distribution of receiver locations for the numerical simulations.

luate the accuracy of the tomographic methods in locating earthquakes, the hypocenters have been aligned along five fault planes with different orientation (Figure 4).

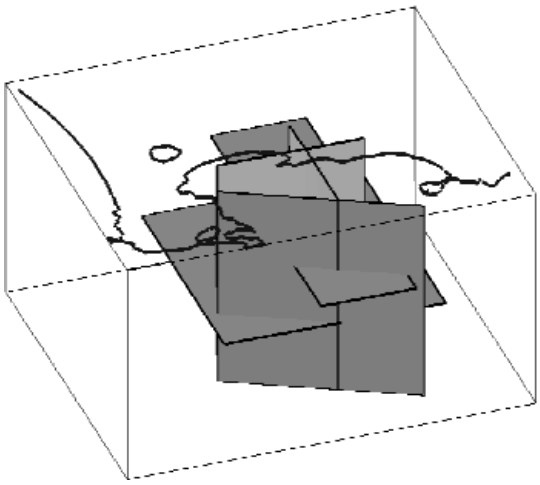

Fig. 4. The five alignments of the earthquake hypocenters used for the blind-test.

Arrival time computations

The synthetic dataset of P and S-wave arrival times has been computed using the numerical solution of the eikonal equation developed by Podvin and Lecomte (1991). This method is implemented in the NonLinLoc software package developed by Lomax (2001). The input model used in the computations is the same grid model, with spatial step 50 m, used to compute the full-wave propagation. The final data-set consists of about 15,600 P- and S-wave arrival times, respectively. Only a subset of this dataset corresponding to about 550 earthquakes has been used for the tomographic blind test.

Waveform computations

The data-set of full waveforms has been computed using an improved version (see Chapter 4.5) of the staggered Fourier pseudo-spectral method (Seriani et al., 2002). This data-set includes waveforms due to micro-earthquakes corresponding to the propagation through 3D model previously described. Since the Fourier pseudo-spectral method has very high accuracy, a minimum number of grid points for wavelength ($G \cong 2$) has been used to discretize the model. The highest resolved frequency of the simulations is 5 Hz.
Since the number of receivers is much smaller than those of the sources, we have applied the reciprocity principle (Eisner and Clayton, 2001), to reduce the overall computational time. Considering that, for simulating 10 s of wave propagation in the considered model, about 6 h of parallel computations on 32

processors of the IBM-SP4 computer are required, the whole set of simulations required about 700 h of computations on the same computer.
The comparison of the computed arrival times with the computed waveforms reveals that for a number of cases the direct S-phases are imbedded within complex waveforms and direct S-arrival times can easily be missed or misunderstood. We show here some examples. Figure 5 shows three waveforms computed at receiver W12 (Figure 3) for three different sources. In panel a, the P- and S-arrival times predicted theoretically fit those that would have been estimated manually from the full waveforms. Panel b shows a strong converted phase which anticipates the directs S-wave. As a result the S-arrival time picked manually from the waveforms, would anticipate the true one. Finally, in panel c, the theoretical S-wave arrival time seems to be quite uncorrelated with the computed waveform.

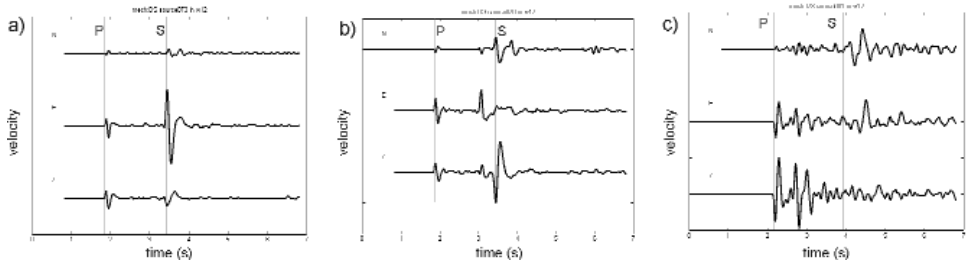

Fig. 5. Comparison between the computed arrival times and the computed waveforms in the receiver W12 for a dip slip point source in three different locations.

Figure 6 shows a set of waveforms computed at receiver W03 for a set of sources aligned horizontally (Z = 5 km). Receiver W03 is located at the surface of incoherent pyroclastic material. The theoretical arrival times are superimposed. The P-wave arrival times fit accurately the P-wave onset, whereas no S-wave corresponds to the predicted S-arrival times. A preliminary interpretation of this fact is that in the direction of receiver W03 the direct S-wave radiation is weak, whereas the seismograms clearly feature the effect of medium heterogeneity, and in particular the presence of both PS converted phases, at about the arrival time of the direct S wave, and surface waves at later times.

Conclusions

A hypothetical digital 3D complex structural model of has been constructed, and a synthetic database of arrival times has been computed for a set of sour-

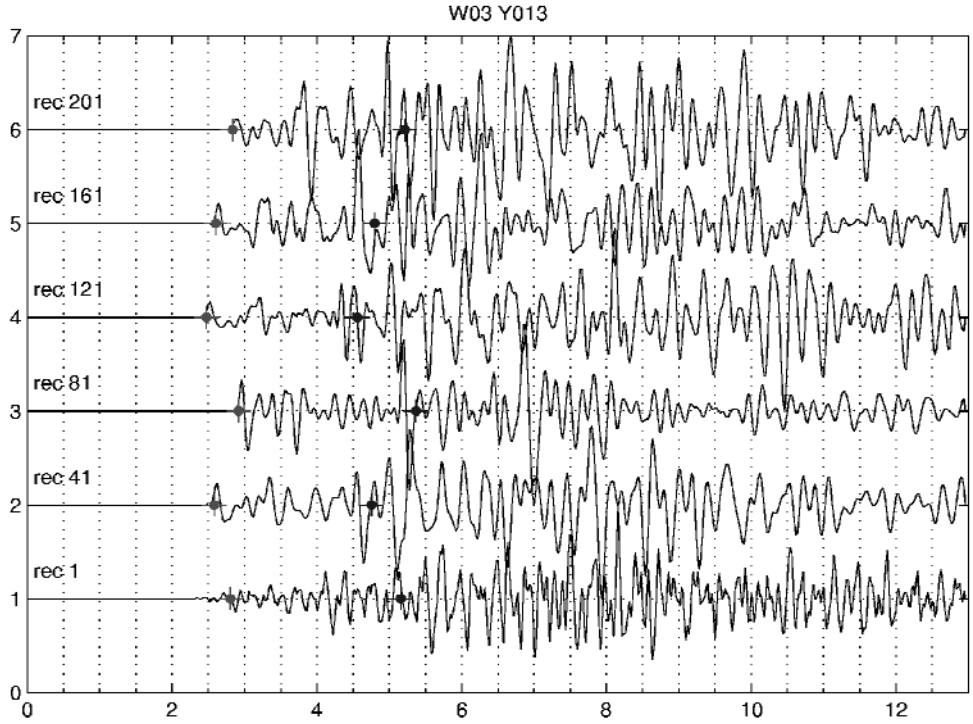

Fig. 6. Waveforms (vertical component) computed at receiver W03 for a set of six sources aligned along a straight, horizontal, N-S oriented line at 5 km of depth. The theoretical arrival times are superimposed the first circle indicates the P-arrival and the second the S-arrival.

ces simulating the 1982-1984 seismic swarm. A procedure for the seismic waveforms computation in detailed complex 3D velocity models has been developed and used to compute full waveform seismograms with for this specific 3D model.

Two synthetic data-sets of full waveforms and theoretical arrival times have been computed with the purpose of using them as an input of earthquake tomography methods to estimate the actual resolution power of the "Winsconsin" microearthquake data-set. This work represents a useful tool for improving the interpretation of the structure beneath the Campi Flegrei area. The 3D hypothetical model in digital GoCad format can be re-used and easily improved in the future.

The procedure for the computation of seismic waveforms in 3D complex visco-elastic media developed within this project opens new possibilities of validating hypothetical 3D structures, as well as forward and inverse modelling methods through waveform fitting.

REFERENCES

Aster R. C., Meyer R. P. (1988). Three-dimensional velocity structure and hypocenter distribution in the Campi Flegrei caldera, Italy. *Tectonophysics*, 149, 195-218.

Burridge R., Knopoff L. (1964). Body force equivalents for seismic dislocations. *Bull. Seis. Soc. Am.*, 54, 1875-88.

Eisner L., Clayton R. W. (2001). A reciprocity method for multiple-source simulations. *Bull. Seis. Soc. Am.*, 91, 553-60.

Graves R. W. (1996). Simulating seismic wave propagation in 3D elastic media using staggered-grid finite-differences. *Bull. Seism. Soc. Am.*, 86, 1091-106.

Lomax A. (2001). NonLinLoc Home Page, *http://alomax.free.fr/nlloc/soft2.30/*.

Podvin P., Lecomte I. (1991). Finite difference computation of traveltimes in very contrasted velocity models: a massively parallel approach and its associated tools. *Geophys. J. Int.*, 105, 271-84.

Seriani G., Vuan A., Priolo E., Carcione. Development and validation of a 3D staggered Fourier pseudo-spectral method for wave modelling. EGS 2002, XXVII General Assembly, Nice (France), April 21-26, 2002. Poster Session.

Tomographic inversion

L. Lovisa[1], E. Priolo[1], A. Michelini[1,3], J. Virieux[2], G. Bohm[1], G. Rossi[1], F. Gentile[1], T. Vanorio[2], B. Monteiller[2], L. Got[2], S. Gautier[2]

[1] *Istituto Nazionale di Oceanografia e Geofisica Sperimentale, Trieste, Italy*

[2] *Géosciences Azur, CNRS, Université de Nice, Sophie Antinopolies, Valbonne, France*

[3] *Istituto Nazionale di Geofisica e Vulcanologia, Roma, Italy*

Introduction

The second part of the blind-test work concerns the tomographic inversion of the synthetic data-set. Four different methods have been used to perform the inversion of the same data-set, and the results are here compared and analyzed in the light of the true model.
The blind-test data-set was distributed to participants, with no information about either the synthetic model or source location. The groups performed the tomographic inversion independently each other; they started from different initial models and had nearly no exchange of information about the ongoing activity.
This chapter is organized in the following way. The first paragraph describes the main features of the synthetic, input data-set. The second paragraphs provides details about both the theoretical methodology of each tomographic approach and the strategy used by each group to solve the problem, respectively. In the final paragraph the blind-test results are compared each other and with the input model. Some general conclusions is eventually drawn.

The synthetic data-set

The synthetic velocity model has already been described in the previous chapter. We just emphasize that the structural model defined for the blind-test represents only one, although probably the best, of the possible conjectures based on the data available at the beginning of the project. The receiver geometry reproduces closely that of the stations operating during the 1984 Wisconsin field acquisition. The 1982-84 seismicity was mostly concentrated in a volume beneath the Pozzuoli Bay at depth shallower than 4 Km. The data-set of synthetic sources spans about the same volume, but hypocenters are aligned along five different planes (three vertical and two horizontal, respecti-

vely). This geometry has been chosen in order to better evaluate the accuracy of the tomographic methods in locating earthquakes.
The synthetic data-set used for the tomographic blind-test is a sub-set of 550 earthquakes, randomly chosen within the full data-set computed in the previous chapter. Figure 1 shows the location of the hypocenters sources, respectively, used to produce the synthetic data-set. Some of these alignments can be clearly recognized. 145 earthquakes out of 550 are deeper than 4 Km with a maximum hypocentral depth of 7.55 Km.
The data-set of arrival times consists of 3830 P-phases and 2056 S-phases. In order to make the synthetic data-set more realistic, the computed arrival times have been contaminated by a random error, with an average value of 0.05 s.
As a result of the blind-test tomographic inversion, each group has been asked to provide the data-sets of earthquake locations and the (Vp, Vs) inverted values for a grid with a spatial step of 200 m.

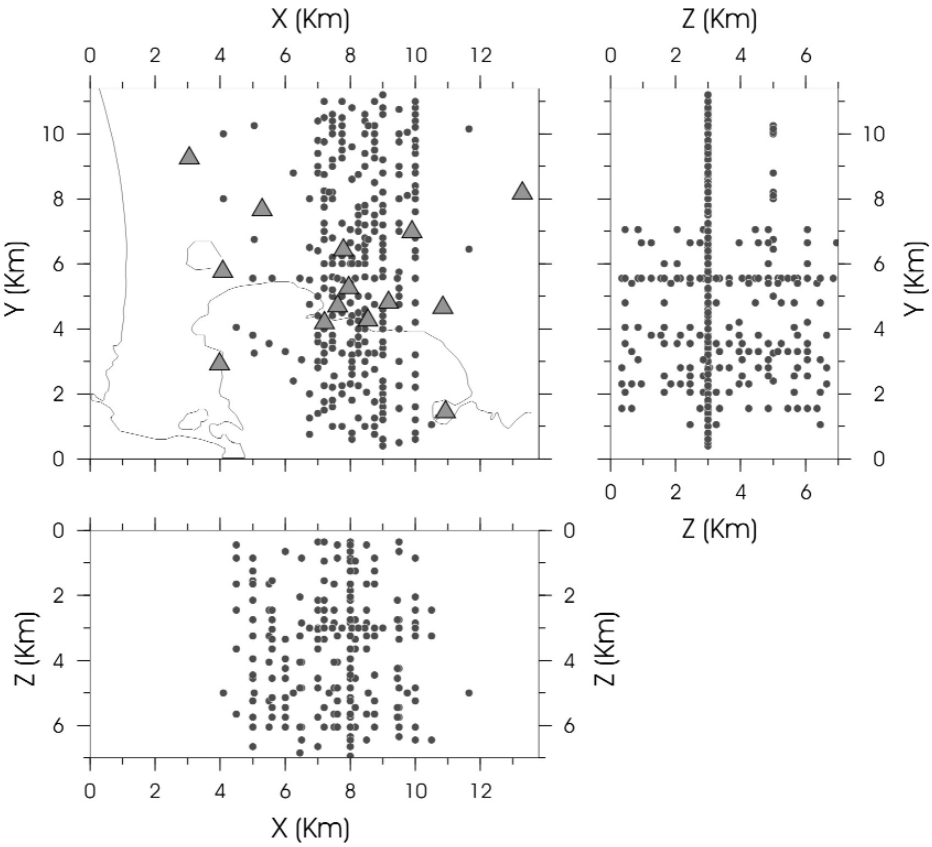

Fig. 1. Location of the synthetic hypocenters.

DISJOINT INVERSION AND INTEGRATED ANALYSIS USING CAT3D TOMOGRAPHIC SOFTWARE AND NLLOC SOFTWARE EARTHQUAKE LOCATION

In this analysis we invert the travel times associated to a subset of the synthetic data-set consisting of those events for which the localization was well constrained and with low error. A total of 3338 P arrivals and 1909 S arrivals were examinated.
We apply an iterative procedure which includes the earthquake location and the travel time inversion in separated, sequential steps. The procedure starts with the definition of the initial velocity model: a simple vertical velocity gradient with a constant values of Vp/Vs ratio (1.8 Km/sec). The first location produces the output file containing the position of the localized earthquakes and the definition of the starting times. This file is used as an input for the travel time inversion. The new velocity volume, obtained by the tomography, is the input velocity field for a new earthquake location.
Earthquake localizations are performed using NonLinLoc software (Lomax, 2001 version). It performs non linear search technique to define the maximum-likelihood hypocenter among a set of nodes distributed on a regular grid P- and S-travel times are inverted separately, with no weight associated. No constraint is applied to the Vp/Vs ratio value.
Each iteration consists of two steps, i.e. earthquake re-location and tomographic inversion. Before each new location, travel times affected by high residuals are excluded from the input data. The final inversion has been obtained after a total of five iterations.
In order to increase the resolution of the tomographic image, with no loss of reliability, we apply the staggered grid method in the inversion procedure (Vesnaver and Bohm, 2000). It takes advantage of low-resolution grids (whose inversion is fast and stable) to obtain high-resolution inversion. It uses a number of different grids by just shifting them rigidly in the space. By averaging the velocity fields, obtained by the inversion of each grid, we can get a composite image where the influence of each single grid is reduced and the boundaries of velocity anomalies can be described by a much finer and more complex representation (Figure 2).
The null space map is considered as indicator of the reliability of the tomographic results, which is based on the singular value decomposition of the tomographic matrix (Bohm and Vesnaver, 1996).
In this test, the null space analysis shows a distribution of the high reliability area not very large in depth. This is due to the different spatial distribution of the earthquake with respect of the position of the stations. The usable area doesn't cover enough the low velocity anomalies present in the true model, which can not be resolved by the earthquake-station couples used in this experiment.

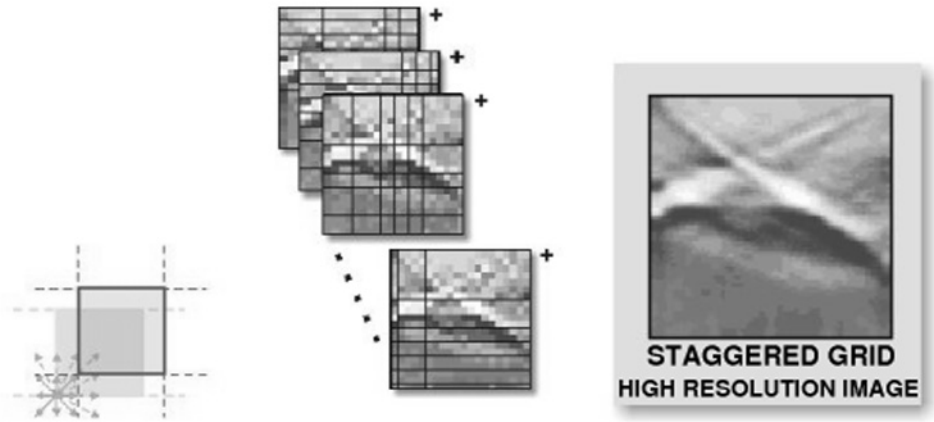

Fig. 2. Scheme of the staggered grid method applied in the inversion procedure.

TOMOGRAPHIC ANALYSIS USING SIMULPS14

Simulps14 (Haslinger, 1999) is a program that performs simultaneous inversion of Vp, Vp/Vs and hypocenter locations. The code is based on Simulps13q (Thurber, 1993; Evans et al., 1990), but it has been extended to use a full 3-D shooting ray tracer. The new ray tracer has been developed by J. Virieux and V. Farra and it is based on Hamiltonian perturbation theory and paraxial ray tracing.

The unknowns of the inversion procedure are both the velocities computed at a structured (non-regular) grid of nodes and the hypocenters locations. At each point of the volume analyzed, the velocity field is determined by linear interpolation of the velocity values at the eight nearest nodes.

The nodes are distributed on a rectangular (but not regular) grids that consist of 11 x 11 x 6 = 726

nodes with a spacing variable between 1 Km and 3 Km.

The 1-D initial P velocity model was constrained from results of previous studies (Finetti and Morelli, 1974; Aster and Meyer, 1988; De Matteis et al., 2000) assuming a velocity field variable only along depth axis. The S velocity field was obtained from Vp, by keeping a constant value of the Vp/Vs ratio equal to 1.80, as inferred from the $\delta P/\delta S$ diagram that, being based on the determination of the differences between P and S arrival phases at different stations, can be directly derived from the Wadati diagram (Lay and Wallace, 1995).

The first localization was computed using Hypo71 (Lee and Lhar, 1972) and the result was used as an input of the tomographic inversion.

In the inversion we excluded the events whose localization was poorly constrained or produced high residuals in the first location. As a result, 510 earth-

quakes of a set of 550 have been used, and 3575 P and 1934 S arrivals were eventually examined.
The procedure performed to find the best velocity field consists of the following steps. Firstly, keeping fixed the Vp/Vs ratio, we determine the damping value for the P-inversion by choosing the best value of the trade-off curve in the model-variance-vs.-data-variance diagram. Then, using the damping value found (Figure 3), the P velocity inversion is performed and the Vp field obtained is used to determine the damping value for the Vp/Vs inversion, with similar procedure adopted for the P inversion. Finally, the ultimate inversion-localization step is performed by inverting Vp and Vp/Vs jointly.
The inversion results show that the quality of the solution was estimated by computing the resolution matrix for all velocity model nodes. Low values of resolution (close to zero) indicate that little or no information is coming from the data, and the velocity solution in the damped least-squares inversion remains close to the initial model. The high resolution areas are located in the middle of the model (i.e. at depth 2, 3, 4 and partially 5 Km), while the shallowest and deepest layer (i.e. 1 and 6 Km) are poorly solved as a result of the poor coverage provided by the overall geometry of stations and hypocenters. On average, the obtained Vp and Vp/Vs fields are shifted 800 m upwards compared to the synthetic ones. This is probably due to the poor accuracy of the initial velocity models. In addition, low velocity intrusions have not been solved, and we explain that with the fact that 1) only few hypocenters are located beneath these bodies, and 2) these bodies have a too small size for being solved by the method.

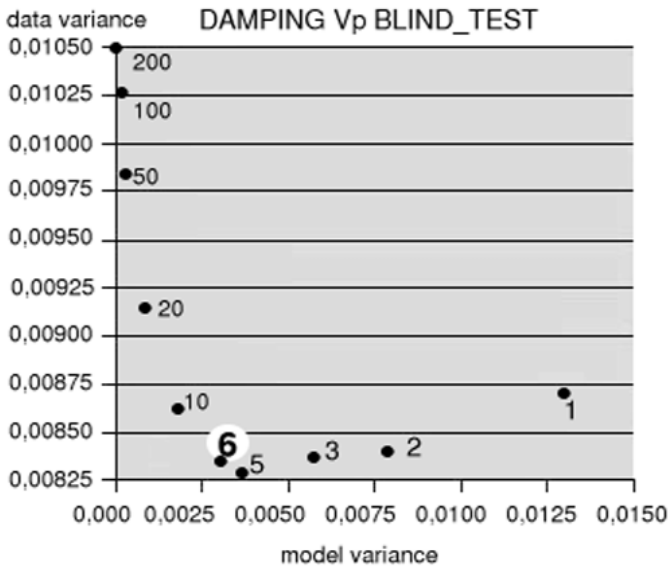

Fig. 3. Damping test for P-velocity. Chosen value highlighted.

TOMOGRAPHIC ANALYSIS USING SIM28 (3D INTERPOLATION WITH CUBIC-SPLINES)

Sim28 (Michelini and McEvilly, 1991) is a tomographic software based on the simultaneous inversion for velocity structure and earthquake location algorithm introduced by Thurber (1983). Sim28 adopts cubic B-splines basis function for interpolation and uses the LSQR sparse matrix solver for the inversion.

The model grid set for the inversion consists of 20x20x6=2400 nodes for a total of 4800 inversion nodes (i.e., 2400 P- and 2400 S-wave velocity parameters).

The inversion data set was composed by events having more that 10 arrival phases. This totals to 248 earthquakes used for the inversion out of 550 events provided initially. In particular, 1960 P phases and 1294 S phases were used. Once the simultaneous inversion was performed, all the remaining earthquakes have been relocated.

Great emphasis has been given to resolve the best fitting 1-D velocity model that it was then used as initial model for the 3-D inversion (Figure 4) . The model resolved features a final weighted root mean square (RMS) of the residual times of 0.056 s (P and S combined).

Five iterations have been performed for the 3-D velocity inversion. The final RMS of the residual times is of 0.039 s for a reduction of about 31 per cent (P and S combined). However, similar reduction were already obtained at the 2nd iteration indicating that, probably owing to the complexity of the true model, the initial model is difficult to perturb within a linearized iterative inversion scheme.

The robustness of the inversion results has been tested against a number of different discretizations of the model. For example the velocity model was shifted along depth and different layers of nodes were used. The resolved models, however, have been found consistent among each other. In order to visualize the better resolved parts of the velocity model, we have summed up and normalized the partial derivatives at each grid node (it is analogous to the calculation of the hit-counts). As expected, the inner parts of the velocity model are those better resolved.

The results of this inversion show little lateral variations of the resolved models. This shows that either the true velocity model is homogeneous or that the velocity model chosen for the tests combined with the imposed source-receiver geometry is just impossible to resolve with the type of data available. On one side this owes to the limited resolving power of the phase data themselves while, on the other, to the location of the anomalies when compared to the "illuminated" parts of the model.

It is important to note, however, that the procedure/technique used here is capable to relocate well the events (i.e., the horizontal and vertical streaks can be identified) and that the mean value of the model (both P and S) are reasonably close to the true ones.

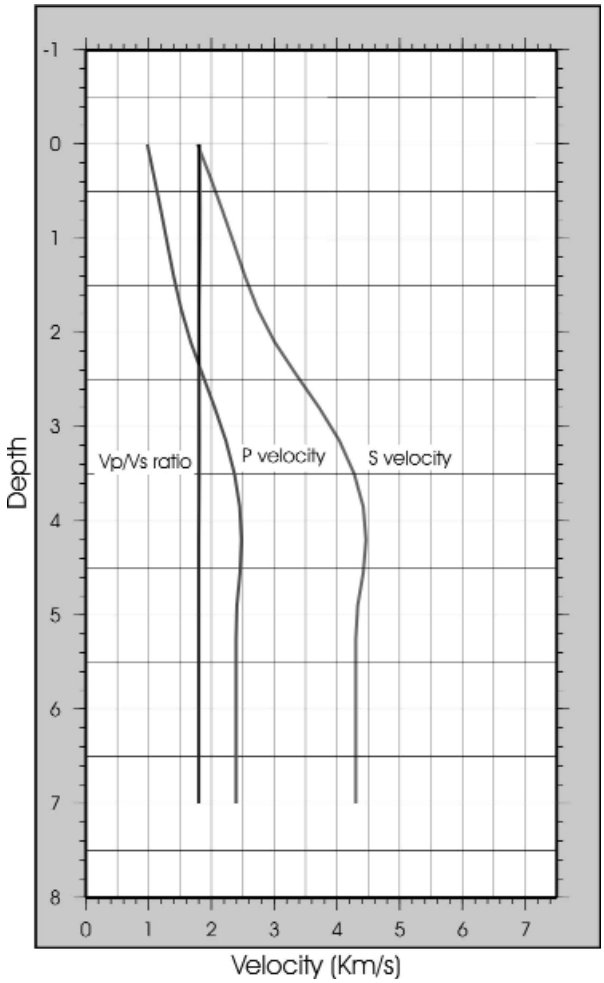

Fig. 4. Initial velocity model along the vertical direction.

The Vp/Vs ratio, in particular, is a good indicator of the robustness of the results and in these inversions it has been found that down to 3 km depth the results are very consistent to those of the true model. In general, however, the data set lacks of resolving power at depth, and there is little it can be done with any technique to compensate this deficit.

Tomographic analysis using TLR3 (Tomography, location and relocation version 3)

The applied tomographic technique is a linearized technique based on reducing delayed times between observed first-arrival times (both P and S) and

synthetic first-arrival times. Two main steps are required for constructing the linear system to be solved. The first requires the sampling of the 3D medium by rays. By using a Finite Difference solver of the Eikonal equation, one may reconstruct first-arrival times at each node of a fine grid for a given station. Ray tracing from the source back to the station using local steepest descent over this time grid defines 1D line between each station and each source. These lines are stored and the first step is concluded.

The second step computes again travel times through the integral of the slowness with the desired accuracy for tomography. Effects of errors in the ray itself are reduced in these newly travel times. The second-member of the linear system is constructed as differences between observed time and synthetic time at each station.

Simultaneously, partial derivatives are computed for velocities while computing along the ray. Hypocenter parameters partial derivatives are added. These different values are stored in a sparse matrix. This concludes the second step and the system is ready to be solved.

Preconditioning is important before proceeding to the inversion. One has to perform normalisation and scaling between different sets of parameters. We invert the preconditioning new linear system by LSQR technique (Paige and Saunders, 1982).

Both scaling and normalization are adapted using synthetic datasets in order to recover true parameter values. Source/station distributions are key elements of such preconditioning. New values of parameters as velocity perturbations and earthquake new positions will be used as initial values for another iteration. We may repeat until the maximum of iterations or until a criterion of convergence has been reached. We usually performed around 15-20 iterations and, by a post analysis, we conclude what is the optimal iteration we should have used.

The model grid set for the 1D initial model and for the inversion has 71 nodes in the X direction related to longitudinal direction, 71 nodes in the Y direction related to latitude direction and 46 nodes in the vertical direction. The spacing is regular and identical for these three directions and is 200 m.

The model size is consequently 14 km in horizontal directions and 9 km in vertical direction.

The blind test has provided us picked data and stations coordinates: one has first to define a first initial model for locating earthquakes. We have used HYPO71 software and we have proceeded by trial and error for obtaining the best quality localisations of earthquakes by changing the P wave velocity structure and the constant ratio of P and S velocities. The 1D structure starts with a velocity of 1.86 km/s at the zero altitude and reaches 6.6 km/s at the depth of 8 km. The velocity ratio was found to be optimal for 1.85. The quality of locations is mainly B with few locations with C and D and none with quality A.

The discretisation of the HYPO71 first 1D model has been recast in ten regularly spaced layers of 200 m thickness. The velocity variation inside each layer

has an amplitude of 400 m/s around the HYPO71 value. A random distribution of 200 models has been performed which keeps a positive gradient as we go deeper and a constant velocity ratio.
For each of these initial models, we have computed initial residuals as well as final ones for an inversion on a coarse grid of 1 km. Initial residuals are between 0.14 s up to 0.18 s while final ones are inside a quite narrow interval of [0.056 s-0.057 s]. From these results, one may wonder if we have performed an enough extensive sampling test of the initial 1D velocity structure and we must agree that the number of trial models should go higher than 3000 for adequate sampling.
We have selected the best 20 media and we have computed the 1D averaged medium from the initial structures of these 20 media. Consequently, velocity ratio stays the same for the initiation of the inversion. Averaging on the final media would have left a heterogeneous velocity ratio for the initial model.
The inversion scheme starts with an initial rms value of 0.1150 s and reaches a final rms of 0.0345 s at the end of the process.
Results show that heterogeneities are very weak especially for superficial structures. One may wonder possible problems of illuminations. Because any biased superficial estimation will have a dramatic effect on deep features of velocity anomalies, a more extensive investigation should be performed for superficial layers. Unfortunately, the small number of stations prevents such investigation.
Either we have a rather stratified medium or we may have missed superficial features because of lacks of events. One expects contrasted velocity structures from geological argumentations. Therefore, the first layer of 1 km is unable to find the strong heterogeneity of the real model.
Layers at 2 km and 3 km are the best constrained because of the number of events.
Low velocity zones are partially recovered. Success at the layer 4 km is more limited because the number of events decreases quite rapidly while the true model increase its complexity. This is the inherent limitation of the first-arrival delayed time tomography and one has to investigate reflections for going deeper in the reconstruction of the velocity structure.
Below that layer, it is difficult to assess any correlation between the true model and the inverted one, even the average velocity value.
Hypocenter localisations are better located and, although ambiguity between depth and origin time has made events more superficial they should, the horizontal structure is recovered quite nicely and one may wonder what will be the effect of a double difference technique. By locating better events respectively one to each other, the low content of the velocity structure might be recovered and, therefore, a better localisation and so on.

Discussion of the results and conclusions

In this subsection we compare the results obtained from the application of the four different inversion approaches.
The quality of the accuracy of the localizations has also been analyzed by estimating the shift of the hypocenter distributions along the three cartesian axes with respect to the true locations, and the correlated standard deviation (Table 1). TLR3 and Sim28 methods provides the lowest shifts and errors. Note however that both TLR3 and Cat3D+NLLoc tend to over-estimate the source depth (i.e. estimated hypocenters are shallower than the true ones) of about 300 m and 500 m, respectively. If we consider that Cat3D performs the location and tomographic inversion disjointly, the quality of the results achieved by this method is surprisingly good. On the other hand, Simulps14 estimates a good hypocentral average value but individual locations are usually affected by quite high errors.

Table 1. Average shift and standard deviation of the hypocenter distributions retrieved. Unit in km.

Cat3d+NLLoc	Simulps14	Sim28	TLR3
ΔX_{med}=0.088	ΔX_{med}=0.001	ΔX_{med}=0.034	ΔX_{med}=0.018
St.dev=0.424	St.dev=0.537	St.dev=0.276	St.dev=0.292
ΔY_{med}=0.296	ΔY_{med}=0.335	ΔY_{med}=0.058	ΔY_{med}=0.028
St.dev=0.651	St.dev=0.963	St.dev=0.526	St.dev=0.565
ΔZ_{med}=0.488	ΔZ_{med}=-0.095	ΔZ_{med}=-0.073	ΔZ_{med}=0.334
St.dev=0.794	St.dev=1.029	St.dev=0.502	St.dev=0.470

In the analysis of the velocity structures inverted by earthquake tomography, we examine two different features, i.e. 1) how the background velocity field has been imaged, and 2) how the anomalous bodies, such as magmatic chamber and chimneys, have been recovered.
About the first aspect, Figure 5 shows the mean difference between the true and inverted models at increasing depths. All methods reproduce the Vp and Vs background fields reasonably well down to depth of about 5 km. At that depth the accuracy decreases for the progressive reduction of the number of sources. The Vp/Vs error has a similar trend, i.e. it increases at depth larger than 3 Km.
Note that the reliability of the inversion is disregarded in this analysis, i.e. errors are calculated for each point independently of the local resolution value.

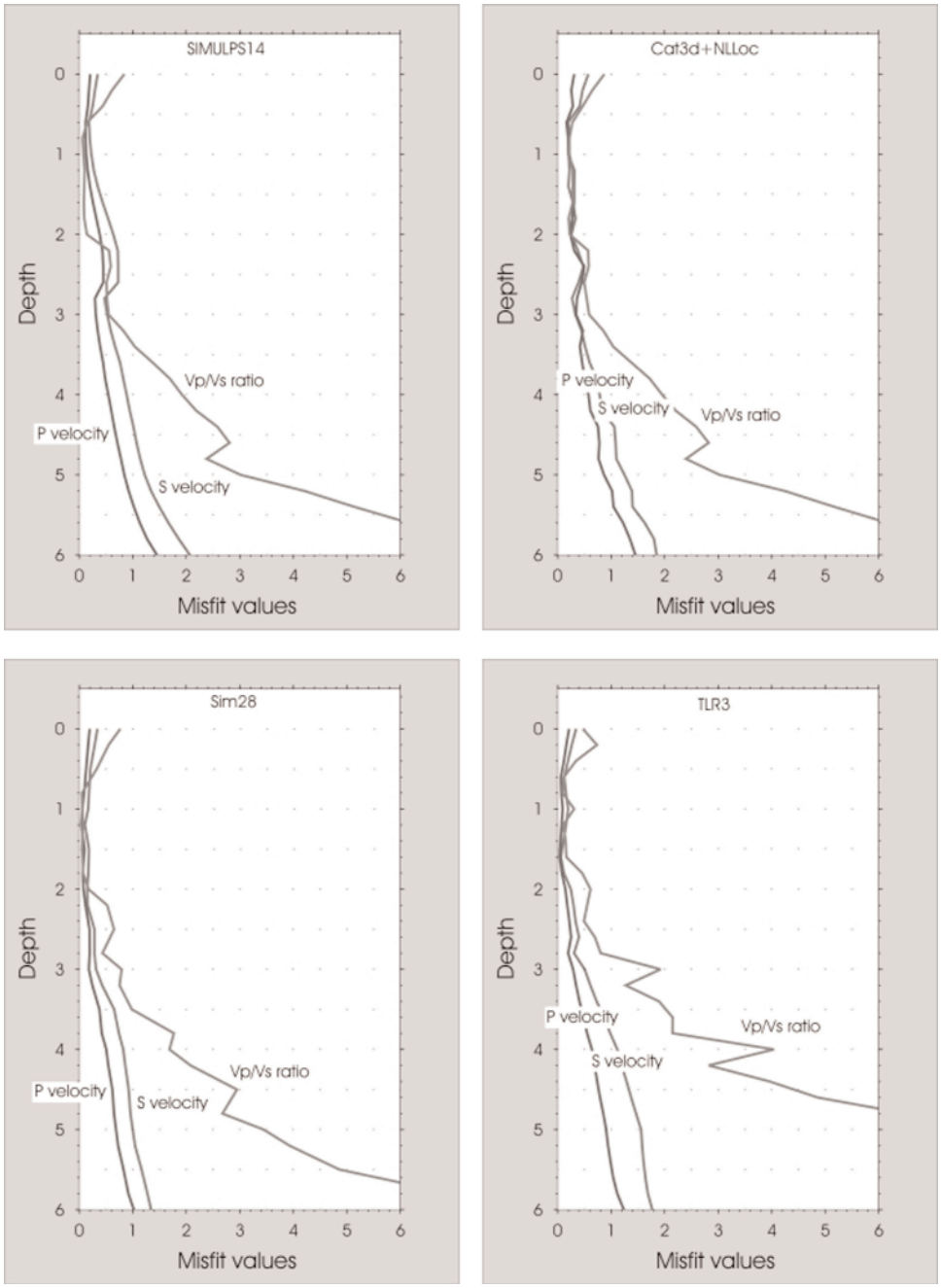

Fig. 5. Vp, Vs, and Vp/Vs mean difference between the synthetic model and the tomographies as a function of the depth.

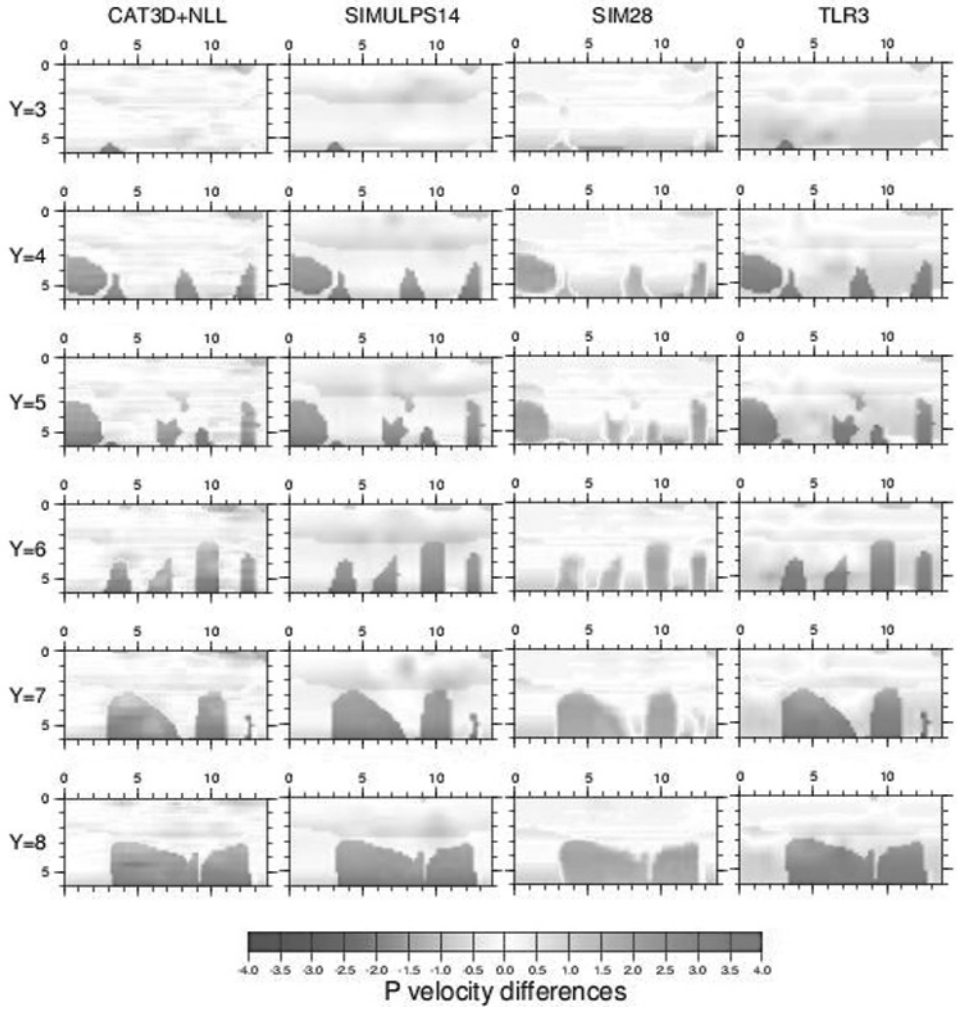

Fig. 6. Difference between Vp synthetic and inverted models along Y sections. Blue/red areas indicate negative/positive misfit. White areas correspond to good fit.
You can see this figure in color on page 209.

About the second aspect, we plot the tomographical results and the synthetic model using the same color palette (a complete set of pictures is included in the full report (Priolo and Lovisa, 2004).
The best results are obtained by Sim28, although it is clear that all methods fail in resolving the anomalous bodies.
Although this blind-test differ from the real situation in a number of features – the real model features a lower value of Vp/Vs ratio than defined in our model; the synthetic data-set of hypocenters reproduces the overall volume but not each single distribution – we think that the results here obtained do

provide a thorough analysis of the earthquake tomography potential of the Winsconsin (1984) data-set. As a general conclusion, this study shows that all the tested earthquake tomography methods provide reliable low-resolution images of the background velocity field of the Campi Flegrei area. However none of them succeeds in the main goal, that is in detecting the presence of either the magmatic chamber beneath 4 km of depth or the smaller, isolated bodies which represent possible magmatic chimneys and intrusions in our model.

This failure can be attributed to a number of reasons, some pertinent to the specific study case and others more general. First, the poor coverage resulting from the overall geometry of stations and hypocenters. Most earthquakes are shallow ($z < 4$ km) and, as a result, most ray-paths do not go through the low S-velocity anomalies of the magma chamber. Second, transmission tomography solves smooth changes of velocity and it cannot solve sharp changes such as interfaces: as a result, the time delay due to the presence of an isolated low S-velocity body is spread over a larger volume of the model. The fact that the target is represented by an S-velocity anomaly, rather than a P-velocity one, is indeed a major difficulty for tomographic approaches, since direct S-phases are imbedded within complex waveforms and S-delays can easily be missed or misunderstood among converted phases. The data-sets of 3D full waveforms and arrival times computed in previous chapter clearly show that this might be a quite recurrent situation for the Winsconsin (1984) waveform data-set, thus suggesting that 1) a careful analysis of the waveforms should be performed in the future, and 2) only a waveform inversion approach will likely improve the image of the magmatic chamber beneath.

References

Bohm G., Vesnaver A. (1996). Relying on a grid. *J. Seismic Expl.*, 5, 169-84.

Bohm G., Vesnaver A. (1999). Minimum time ray-tracing for 3-D irregular grids. *J. Seismic Expl.*, 8, 117-31.

Bruno P. P. G., Rapolla A., Di Fiore V. (2003). Structural setting of the Bay of Naples (Italy) seismic reflection data: implications for Campanian volcanism. *Tectonophysics*, 372, 193-213.

De Matteis R., Latorre D., Zollo A., Virieux J. (2000). 1-D P-velocity models of Mt. Vesuvius volcano from the inversion of TomoVes96 first arrival time data. *Pure and Applied Geophysics*, 157, 1643-61.

Evans J. R., Eberhart-Phillips D., Thurber C. H. (1994). User's manual for simulps12 for imaging vp and vp/vs: a derivative of the Thurber tomographic inversion simul3 for local earthquakes locations and explosions. *U.S.Geol. Surv. Open File Report*, 7 pp.

Finetti I, Morelli C. (1974). Esplorazione sismica a riflessione dei Golfi di Napoli e Pozzuoli. *Boll. Geof. Teor. Appl.*, 16, 175-222.

Haslinger F. (1998). Velocity Structure, Seismicity and Seismotectonics of Northwestern Greece Between the Gulf of Arta and Zakynthos. *Diss. ETH* No. 12966.

Herring T. A., Dong D., King R.W. (1991). Sub-milliarcsecond determination of pole position using Global Positioning System data. *Geophys. Res. Lett.*, 18, 1893-6.

Latorre D., Virieux J., Monfret T., Monteiller V., Vanorio T., Got J.-L., Lyon-Caen H. (2004). A new seismic tomography of Aigion area (Gulf of Corinth, Greece) from a 1991 dataset. *Geophys. J. Int.*, 159, 1013, doi:10.1111/j.1365-246X.2004.02412.x.

Le Meur H., Virieux J., Podvin P. (1997). Seismic tomography of the Gulf of Corinth: a comparison of methods. *Ann. Geophys.*, XL, 1-25.

Lomax A. (2001). NonLinLoc Home Page, *http://alomax.free.fr/nlloc/soft2.30/*.

Priolo E., Lovisa L. (2004). The Campi Flegrei blind-test. *Gruppo Nazionale di Vulcanologia, Open File Report*: OFR_ISMACF_A5.1, 93 pp.

Michelini A., McEvilly T. V. (1991). Seismological Studies at Parkfield. I. Simultaneous Inversion For Velocity Structure And Hypocenters Using Cubic B-Splines Parametrization. *Bull. Seis. Soc. Am.*, 81, 524-52.

Monteiller V., Got J.-L., Virieux J., Okubo P. Double-difference tomography and localisation in heterogeneous media: method and application to Kilauea South flank. *In preparation.*

Stewart R. (1993). Exploration Seismic Tomography: Fundamentals. *SEG Society of exploration Geophysicists. Course Notes Series*, Volume 3. S.N. Domenico, Ed.

Paige C. C., Saunders M. A. (1982). LSQR: sparse linear equations and least squares problems. *ACM Trans. Math. Softw.*, 8, 195-209.

Podvin P., Lecomte I. (1991). Finite difference computation of traveltimes in very contrasted velocity models: a massively parallel approach and its associated tools. *Geophys. J. Int.*, 105, 271-295.

Thurber C. H. (1983). Earthquake locations and three-dimensional crustal structure in the Coyote Lake area, central California. *J. Geophys. Res.*, 88, 8226-36.

Thurber C. H. (1993). Local earthquake tomography: velocities and Vp/Vs-theory, in *Seismic Tomography: Theory and Practice*, edited by H.M. Iyer, K. Hiahara, Chapman & Hall, London.

Vesnaver A., Bohm G. (2000). Staggered or adapted grids for seismic tomography? *The Leading Edge*. 9, 944-50.

Waldhauser F., Ellsworth W. L. (2000). A double difference earthquake location algorithm: method and application to the northern Hayward fault, CA. *Bull. Seismol. Soc. Am.*, 90, 1353-68.

Zhang H., Thurber C. H. (2003). Double-difference tomography: the method and its application to the Hayward fault, California. *Bull. Seismol. Soc. Am.*, 93, 1875-89.

3

Study of the Campi Flegrei volcanic structure based on active seismic data

A new experiment called SERAPIS (**SE**ismic **R**eflection/Refraction **A**cquisition **P**roject for *I*maging complex volcanic **S**tructures) has been planned and carried out, based on off-shore seismic energization and data acquisition on land and on sea-bottom. A typical acquisition lay-out of industrial surveys for oil research has been performed. Serapis experiment provided a 3D seismic coverage of the Gulf of Pozzuoli and of the Campi Flegrei land area, as well as a partial reacquisition of the Gulf of Naples. This project provided a database of more than 92,000 traces, recorded from 72 OBS positioned in the Gulfs of Naples and Pozzuoli, and from 62 3-component land stations in the Campi Flegrei. The shots were totally about 5,000 at 125 m distances, and they were produced with the 16 airguns mounted on the Nadir oceanographic ship of Ifremer, which covered a total of 620 km along dense grid-lines oriented N-S and E-W in the Gulf of Pozzuoli, and along a few grid-lines in the Gulf of Naples. A dataset for the seismic waveforms and related P-picks (more than 90000 data) has been realized.

In addition, active seismic refraction DSS (Deep Seismic Soundings) acquired during the surveys conducted in 1980 and 1985 were recovered jointly with seismic data acquired in the Campi Flegrei area in the framework of the MareVes97 offshore survey.

The data set acquired during the SERAPIS experiment, extended with MareVes97 dataset, has been successfully used to infer 3D images of the volcanic structures underneath the Campi Flegrei and Neapolitan bay, allowing to compute the most comprehensive 3D P-wave velocity model in the bay of Naples, down to about 6 Km depth, including a small scale, high resolution model of the Campi Flegrei area. The three-dimensional image of the top of Mesozoic carbonate basement is reconstructed underneath the bay of Naples and the Mt. Vesuvius area. Its morphology is very complex due to the occurrence of fault escarpments and depressions, whose link with the volcanic activity is still to be fully understood.

Different inversion code of refraction data imaging techniques have been applied to obtain 2D P-wave velocity model of the bay of Naples and Pozzuoli, allowing to define the morphology and the depth of the Mesozoic carbonate basement.

Campi Flegrei active seismic experiments waveforms compilation

P. Capuano[1,2], A. Zollo[3], E. Auger[3], G. Caielli[5], C. Chiarabba[7], V. Convertito[3], L. D'Auria[3], R. de Franco[5], A. Emolo[3], S. Judenherc[3], L. Lovisa[6], J. Makris[8], A. Michelini[7], M. Moretti[7], E. Priolo[6], G. Russo[3], J. Virieux[4]

[1] *Dipartimento di Scienze e Tecnologie per l'Ambiente ed il Territorio, Università del Molise, Isernia, Italy*

[2] *Osservatorio Vesuviano, INGV, Napoli, Italy*

[3] *Dipartimento di Scienze Fisiche, Università Federico II, Napoli, Italy*

[4] *Géosciences Azur, CNRS, Université de Nice, Sophie Antinopolies, Valbonne, France*

[5] *Istituto per la Dinamica dei Processi Ambientali, CNR, Milano, Italy*

[6] *Istituto Nazionale di Oceanografia e Geofisica Sperimentale, Trieste, Italy*

[7] *Centro Nazionale Terremoti, INGV, Roma, Italy*

[8] *University of Hamburg, Hamburg, Germany*

Abstract: A new experiment called SERAPIS (**SE**ismic **R**eflection/Refraction **A**cquisition **P**roject for **I**maging complex volcanic **S**tructures) has been planned and carried out, based on off-shore seismic energization and data acquisition on land and on sea-bottom. The experiment was performed in September, 2001 during which the vessel NADIR of IFREMER (equipped with 12, 16-liters air-gun) produced more than 5000 air gun shots recorded at a sea-bottom seismograph array of 72 OBS and 62 stations installed on-land. Active seismic refraction DSS (Deep Seismic Soundings) acquired during the surveys conducted in 1980 and 1985 were recovered jointly with seismic data acquired in the Campi Flegrei area in the framework of the MareVes97 (an experiment devoted to the definition of the structure of the Somma-Vesuvio complex) offshore survey. The data set acquired during the SERAPIS experiment has been successfully used to infer 3D images of the volcanic structures of Campi Flegrei and Neapolitan bay. Active seismic waveforms and related P-picks (more than 90000 data) from the SERAPIS experiment are also available in the project data server.

INTRODUCTION

One of the tasks of the project "Integrated seismic methods applied to the investigation of the active volcano structure: an application to the Campi

Flegrei caldera", concerns the recovering of previous active seismic data acquired in the Campi Flegrei area.

In particular we refer to the Deep Seismic Soundings (DSS) performed in the Thyrrenian sea. We perform the recovery and homogenisation of old data of DSS seismic experiment, available at Istituto di Ricerca sul Rischio Sismico (now department of Istituto Nazionale di Geofisica e Vulcanologia). In particular, the Deep Seismic Sounding data, acquired in the 1985 during a Campi Flegrei micro-array sub-experiment, were digitised and archived.

In addition, with the aim to provide new insight on the caldera structure and to investigate its feeding system, a dense and extended marine active seismic survey called "SERAPIS" has been performed during September, 2001 in the gulfs of Naples and Pozzuoli. SERAPIS provided a dense 3D seismic coverage of the Gulf of Pozzuoli, the coastal part of the Campi Flegrei caldera, as well as a partial reacquisition of the western sector of the Gulf of Naples. During the field operation about 5000 shots, at 125 m distances, produced by a battery of 12, 16-liters synchronized air-guns mounted on the oceanographic vessel NADIR (IFREMER), have been recorded at a network of 72 sea bottom receivers and 62 3-component on shore seismographs. The oceanographic ship covered a total of 620 km along dense grid-lines oriented N-S and E-W in the Gulf of Pozzuoli, and along a few grid-lines in the Gulf of Naples The SERAPIS experiment provided an additional (and originally not expected) active seismic data-base, consisting of more than 92,000 traces, whose structural informative potential has been partially explored during the project, which essentially used the first P-pick data set.

Merging the Serapis 2001 and MareVes 1997 data-sets allows for the covering of the whole gulf of Naples from the Sorrento peninsula at East to the Ischia and Procida islands at west. The whole data set consists of more than 650000, three component records, acquired by 72 sea-bottom seismographs and 84 onland stations installed in the Campi Flegrei and Mt. Vesuvius volcanic areas. First P-arrival times have been manually picked on pre-processed common receiver sections. The used P-picks for seismic tomography consist of about 65000 data relative to sea-bottom stations and 25000 data from on-land stations. The data base has been integrated with re-picking of the MareVes seismic section (5000 pickings)

SERAPIS PROJECT

SERAPIS experiment, carried out in September 2001, consisted in to record at dense submarine and on land 3C seismic network, installed in the bays of Naples and Pozzuoli (Figure 1), the waves radiated by a battery of 12, 16-liters synchronized air-gun sources mounted on the ship NADIR, owned by the French company Ifremer. The source and receiver arrays cover an area of more than 50x50 km^2. 62 three-component stations have been installed on-land in

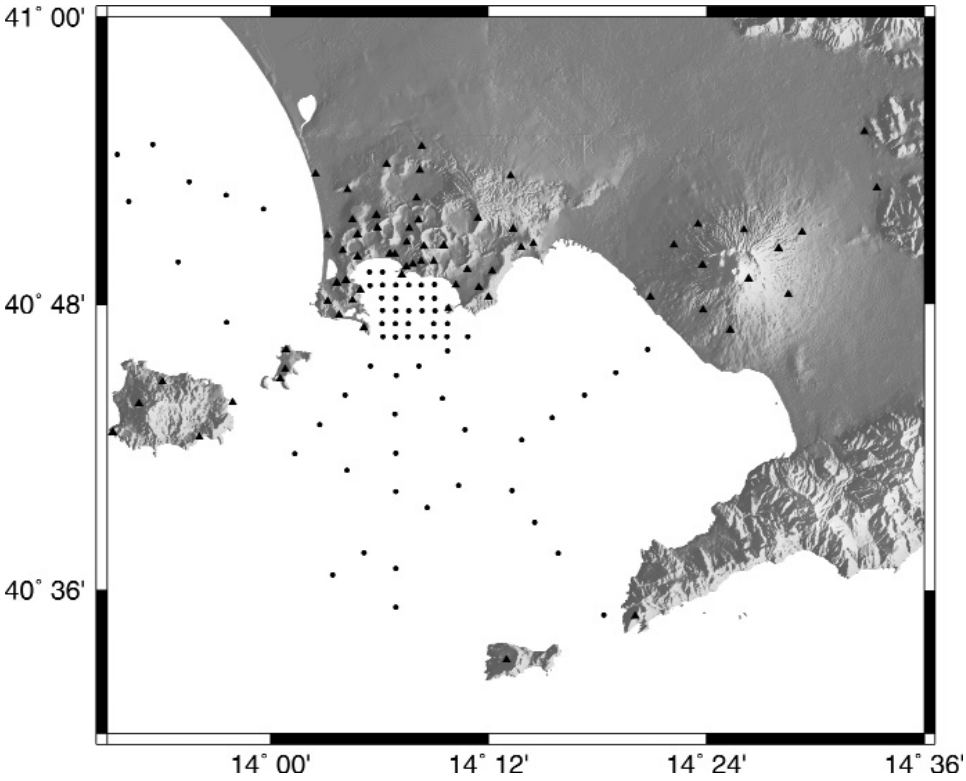

Fig. 1. Map of the area investigated during the SERAPIS experiment. Black lines traces the path of the vessel during the campaign. Red and blue circles display the position of OBS and seismograph during the experiment.
You can see this figure in color on page 210.

the areas of Campi Flegrei, Mt. Vesuvius and on the islands of Ischia and Procida. 72 sea bottom seismographs (OBS) have been installed in the gulfs of Naples and Pozzuoli by the University of Hamburg with the logistic support of private companies Geopro (Germany) and Geolab (Italy). The OBS were equipped with 4.5 Hz 3C sensor and a continuous recording device, while almost all on land station were equipped with 1 Hz 3C sensor. The permanent stations of Osservatorio Vesuviano were also set to record the experiment. A denser 2D network of 35 OBSs has been deployed in the bay of Pozzuoli aimed at detecting and modeling reflected/converted waves from the possible shallow to deep discontinuities beneath the Campi Flegrei caldera.

Over a two week period a total number of about 5000 air gun shots have been fired during the experiment, with an average spatial spacing of 125 m, for a total ship travel path of 620 km. All of the seismic lines were re-sampled at

least twice, using a staggered configuration, which results in a smaller source spacing (less than 65 m). The acquisition layout was designed to provide a very high data density in Pozzuoli Bay (about 2500 shot were performed inside the Bay) for an explored surface of 5x5 km^2. The other shots were performed in the Bay of Naples along some 10-20 km long profiles.
The horizontal OBS ray sampling of the area investigated in the present study is shown in the Figure 2. This corresponds to more than 40000 ray paths.

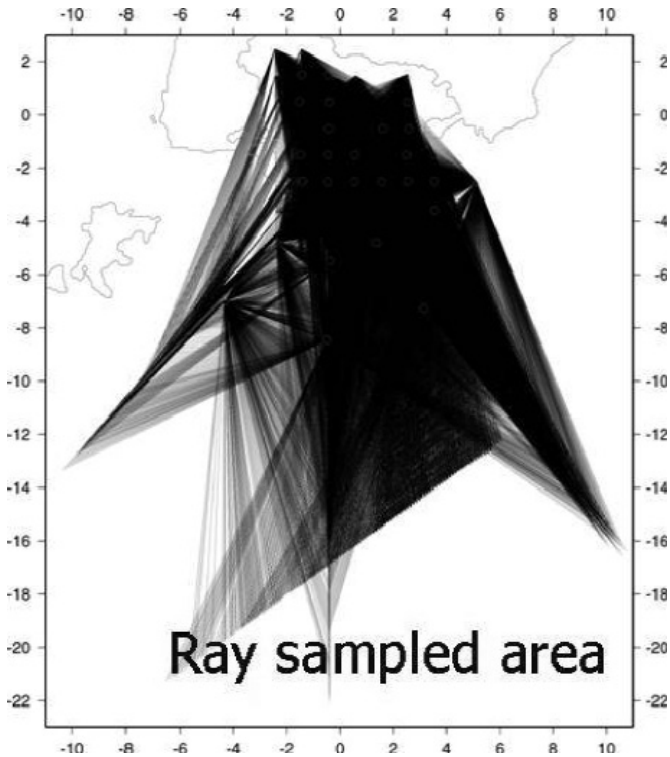

Fig. 2. Horizontal ray sampling of the area investigated during the SERAPIS experiment.

Due to dense urbanization of the area and the night time selected to perform shots trying to reduce noise problem, only six air-guns were operated near the coastline and in the Pozzuoli Bay, while offshore all 12 air-guns were used. The latter allowed the recordings of high energy P waves at distance of > 40 km. An example of recorded data bandpass filtered (5-15 Hz), amplitude equalized (AGC window of 1 s) and plotted in a time reduced scale, using a reduction velocity of 6 km/s, is shown in Figure 3.

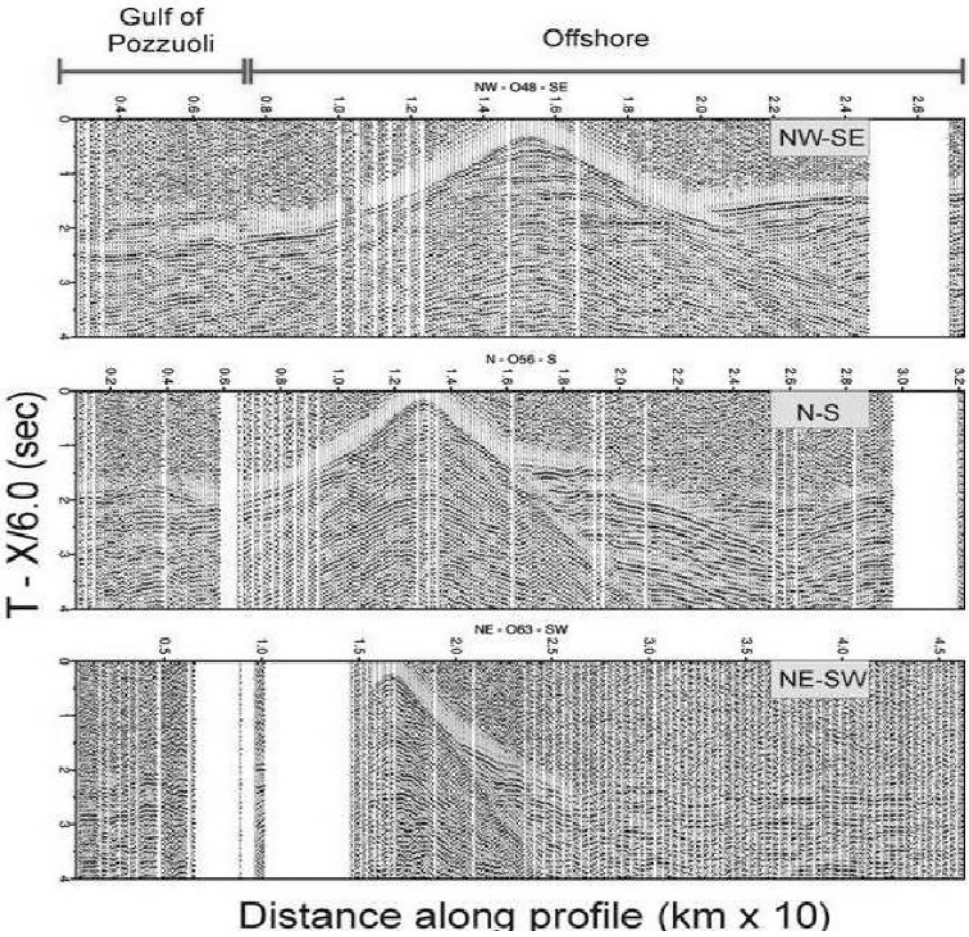

Fig. 3. Examples of common receiver seismic section along NW-SE (upper), NS (centre) and NE-SW (bottom) direction, through the Bay of Pozzuoli towards offshore.

All the recorded traces were arranged in a complete three-component seismic waveform archive, distributed to all participants to the project. This seismic waveform archive joint to a similar one containing data from several hundreds microearthquakes occurred on 1983-1984 at Campi Flegrei (Capuano et al., this issue) represent an unique collection of waveforms produced by passive and active seismic sources in a complex volcanic area, recorded on land and on the sea bottom, that can be very useful to better understand caldera structure.
Once the SERAPIS waveforms dataset was realized, manual reading of the first P wave arrivals has been performed. All the waveforms were band-pass filtered between 5 and 15 Hz in order to work in the frequency range were the phase and amplitude response of the instruments deployed were the same. Picking

was performed on the pre-processed traces, arranged as common receiver gathers (CRG). The SERAPIS data set processing consisted of examining 300,000 OBS waveforms and 400,000 waveforms from stations on land, providing 65,000 and 25,000 P wave first arrival times, respectively. The number of high-quality waveforms recorded by land stations was rather low as compared to the OBS due to the high cultural noise level in the studied area. In all, and considering also the integration of the data from the MareVes97 investigations, the dataset used included ca. 95,000 picks of P-wave first arrivals.
Aster and Meyer (1988, 1989) determined hypocenter location and velocity structure of the caldera using a segment of the passive data recorded in 1984. Vanorio et al., 2005, using the new passive dataset performed a more confident re-analysis of velocity structure and location. SERAPIS data allowed the realization of 3D tomographic images that cover also the Bay of Pozzuoli and part of the Gulf of Naples, evidencing the buried rim of the Campi Flegrei caldera, as shown in Figure 4 (Zollo et al., 2003; Judenherc and Zollo, 2004).

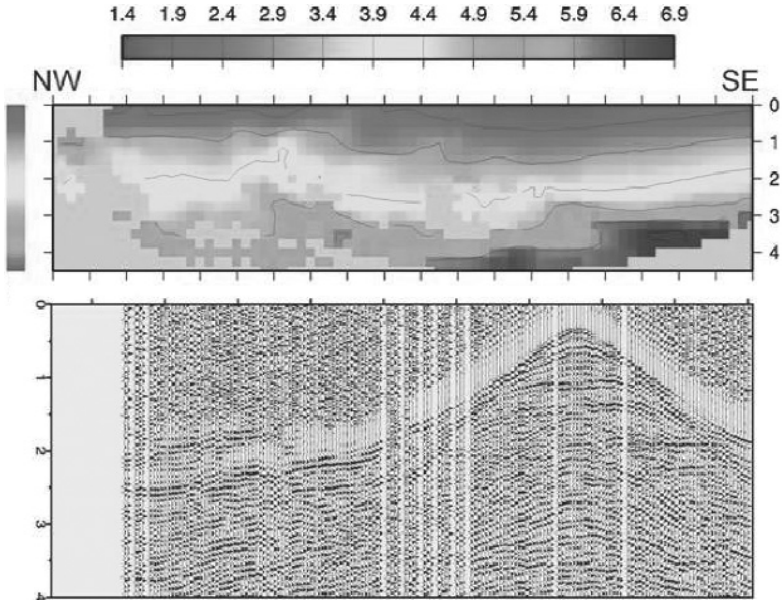

Fig. 4. Example of P-velocity depth section in the Campi Flegrei bay area.
You can see this figure in color on page 210.

DSS WAVEFORMS

We perform the recovery and homogenisation of IRRS old data of DSS seismic experiment. In particular, the Deep Seismic Sounding data, acquired in

the 1985 during a Campi Flegrei micro-array sub-experiment, were digitised and archived. The data were acquired using sea shots (Figure 5) and deploying 20 analog stations along a dense micro-array (about 100 m spacing, length 2.5 km) in the Caldera area (Figure 5 panel inset).

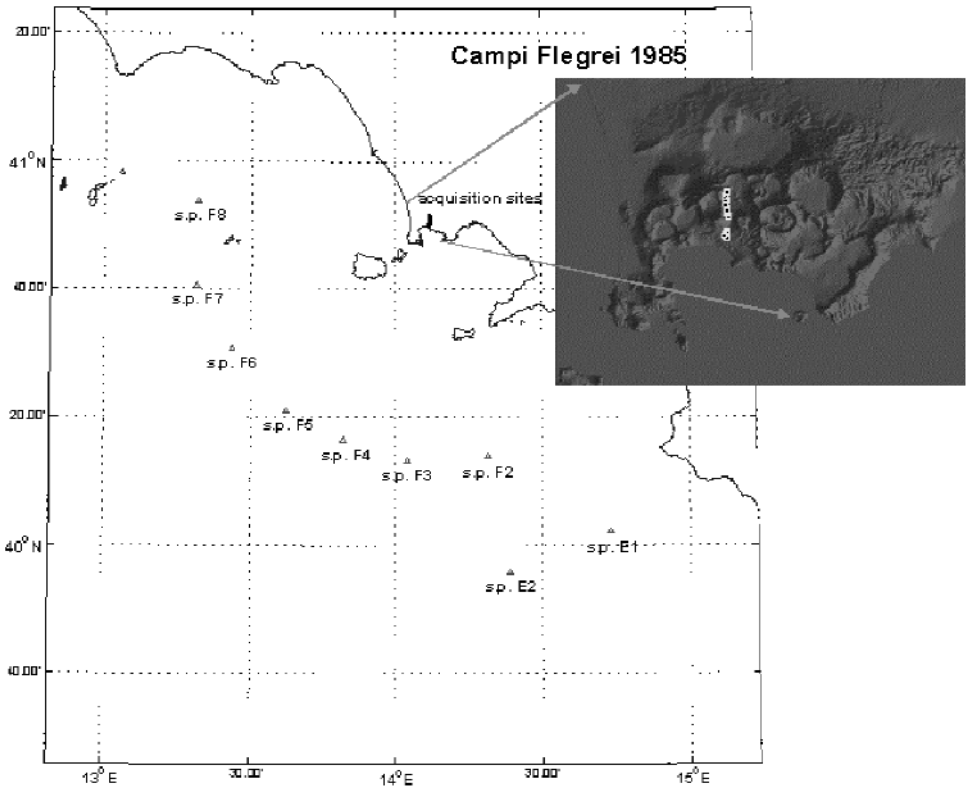

Fig. 5. Campi Flegrei 1985 DSS microarray experiment.

This data constitute a sub dataset of the 1985 experiment which were unpublished and which were never processed in previous studies (Ferrucci et al., 1989). This sub data set constitutes an useful information also in order to compare with the SERAPIS 2001 seismic experiment. Recording examples of the recovered data are shown in Figures 6a and 6b.

The activity product consists of a data compilation report. The data were transferred to the Napoli data base center and, in the future, the homogenisation and integration with the other data of the 1985 experiment will be performed.

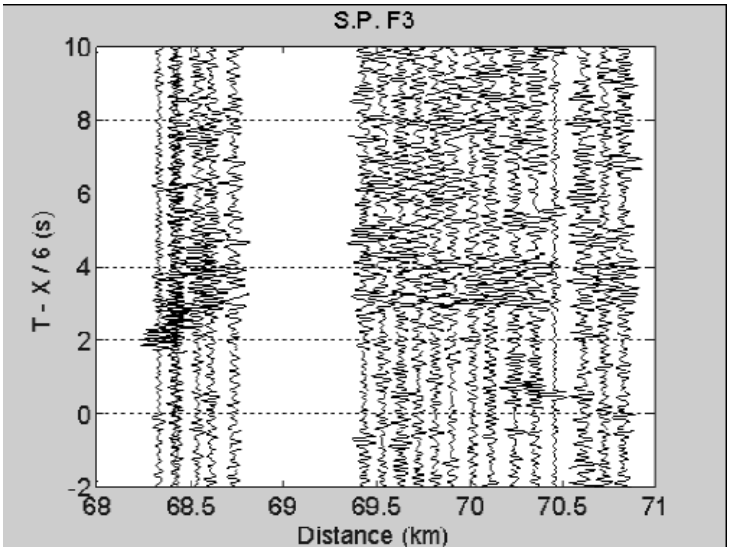

Fig. 6a. Microarray data S.P. F3, vertical Component. Filtered 2-10 Hz. Profile configuration.

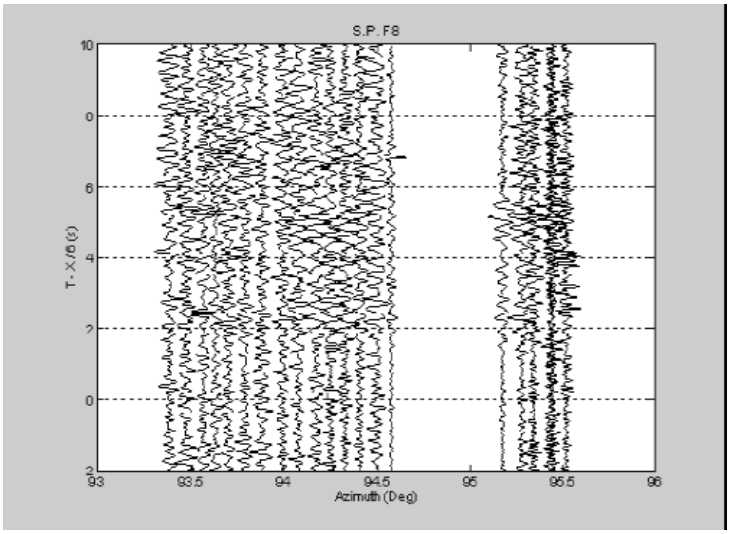

Fig. 6b. Microarray data S.P. F8, vertical Component. Filtered 2-10 hz. Fan configuration.

Conclusion

A typical acquisition lay-out of industrial surveys for oil research has been performed during SERAPIS experiment. The high quality and density of acquired seismic information suggest the experiment design can be exported to

investigate the structure of other coastal volcanoes. An advanced array of sea-bottom instruments has been installed and operated during three week, demonstrating that sub-marine seismic monitoring of volcanic activity is feasible and should be implemented in the future with permanent systems, linked to the on-shore monitoring networks.
The Serapis experiment provided a valuable P-wave arrival time data set allowing for the 3-D tomographic reconstruction of the sub-surface structure underneath the whole bays of Naples and Pozzuoli. The processed Serapis P-wave travel-time collection, extended with an already acquired data set (MareVes97 project), allowed to compute the most comprehensive 3D P-wave velocity distribution in the bay of Naples down to about 6 km depth, including a small scale, high-resolution model in the Campi Flegrei caldera.
The three-dimensional image of the top of Mesozoic carbonate basement is reconstructed underneath the bay of Naples and the Mt. Vesuvius area. Its morphology is very complex due to the occurrence of fault escarpments and depressions, whose link with the volcanic activity is still to be fully understood.

Acknowledgments

Authors are grateful to people that, with an envaluable hard work in the field, contribute to the success of this project and to all participant institutions for providing seismic instruments.

References

Aster R. C., Meyer R. P. (1988). Three-dimensional velocity structure and hypocenter distribution in the Campi Flegrei caldera, Italy. *Tectonophysics*, 149, 195-218.

Aster R. C., Meyer R. P. (1989). Determination of shear- and compressional-wave velocity variations and hypocenter locations in a rapidly inflating caldera: the Campi Flegrei. *Phys. Earth Planet. Inter.*, 55, 313-25.

Ferrucci F., Gaudiosi G., Pino N. A., Luongo G., Hirn A., Mirabile L. (1989). Seismic detection of a major Moho upheaval beneath the Campanian volcanic area (Naples, Southern Italy). *Geophys. Res. Lett.* 16 ,1317-20.

Judenherc S., Zollo A. (2004). The Bay of Naples (southern Italy): Constraints on the volcanic structures inferred from a dense seismic survey. *J. Geophys. Res.*, 109, B10312, doi:10.1029/2003JB002876.

Vanorio T., Virieux J., Capuano P., Russo G. (2005). Three-dimensional seismic tomography from P wave and S wave microearthquake travel times and rock physics characterization of the Campi Flegrei Caldera. *J. Geophys. Res.*, 110(B03), doi:10.1029/2004JB003102.

Zollo A., Judenherc S., Auger E., D'Auria L., Virieux J., Capuano P., Chiarabba C., de Franco R., Makris J., Michelini A., Musacchio G. (2003). Evidence for the buried rim of Campi Flegrei caldera from 3-d active seismic imaging. *Geophys. Res. Lett.*, 30(19), 2002, doi:10.1029/2003GL018173.

Structure of Campi Flegrei caldera: new insights from the inversion of first P-arrival times of Serapis experiment

A. Zollo, D. Dello Iacono, S. Judenherc
Dipartimento di Scienze Fisiche, Università di Napoli, Italy

Introduction

The volcanic areas of Vesuvius and Campi Flegrei in the Naples volcanic region occupy the central part of the Campania Plain. The plain itself lies to the east of the Tyrrhenian Sea between a latitude of 40° and 41° North. It represents a large semi-graben from the Superior Pliocene (5.3 My) that was subjected to a pronounced sinking during the Quaternary (on average, over 1,000 m/My). The geological evolution of the Campania continental edge was marked by two orthogonal extension phases: the first was more ancient and was connected to the NW-SE-oriented faults, producing structures that have extended parallel to the Apennines; the second is connected to the NE-SW-oriented faults and has led to the formation within the plain of asymmetric horsts and grabens (Milia et al. 2003). The first volcanic products were disgorged around 400 ky BP at the end of the main extension phases, when the thinning of the crust of the continental edge resulted in the lower crust being more susceptible to fusion and to a rise in the magma. As a result of this Campi Flegrei activity, there were explosive eruptions throughout the entire Campania Plain and in the Bays of Naples and Pozzuoli at 315 ky, 205 ky, 184 ky, 157 ky, 39 ky, 18 ky, 12 ky BP (and more recently) (De Vivo et al., 2001, Milia et al., 2003).

The Gulf of Naples was instead explored in a seismic reflection study in the 1970s, conducted by the Experimental Geophysics Observatory (Osservatorio Geofisico Sperimentale), that identified a strong reflector dipping towards the WNW that has been interpreted as being the top of the Mesozoic carbonatic base (Finetti & Morelli 1974). More recently, Bruno et al. (1998) mapped the depth of the reflector around Vesuvius using the reflection data of AGIP.

The large urban centres that are inhabited by more than 2 million people, which will be immediately reachable by the volcanic products should there be an eruption, and the still-active magma systems of Vesuvius and Campi Flegrei represent a great risk to the population, as testified by the historic eruptions, the seismic-volcanic activity, the fumarolic activity, and the hot springs.

A definition of the structures that characterise the area and knowledge of their relationships to the volcanic activity represent key elements for an understanding of the system and an evaluation of the risk. For this reason, Vesuvius and Campi Flegrei have been subjected to intensive active-seismic studies over the past ten years, with the main aim of obtaining high resolution images of their internal structure for the identification and depth localisation of their magma-supply systems.

Dataset

Over these past ten years, there have been four data-acquisition investigations on land and at sea that have provided large databases of seismic traces that are widely distributed in the Vesuvius, Campi Flegrei and Gulfs of Naples and Pozzuoli areas (TomoVes94, TomoVes96, MareVes97 and Serapis 2001). In particular, the TomoVes94 and TomoVes96 investigations were designed according to a multiple 2D acquisition layout in the Vesuvius area, the MareVes97 investigations provided seismic coverage of the Gulf of Naples, and finally, the Serapis 2001 investigations extended the database to include the Gulf of Pozzuoli and the Campi Flegrei land area.
The last acquisition study, Serapis 2001, provided the 3D seismic coverage of the Gulf of Pozzuoli and of the Campi Flegrei land area, as well as a partial reacquisition of the Gulf of Naples. This project provided a database of more than 92,000 traces, recorded from 72 OBS positioned in the Gulfs of Naples and Pozzuoli, and from 62 3-component land stations in the Campi Flegrei. The shots totalled ca. 5,000 at 125 m distances, and they were produced with the 16 airguns mounted on the Nadir oceanographic ship of Ifremer, which covered a total of 620 km along dense grid-lines oriented N-S and E-W in the Gulf of Pozzuoli, and along a few grid-lines in the Gulf of Naples (Figure 1). Among the main results from this study, which also included part of the data from MareVes97, was the reconstruction of a regional structural model for the Gulfs of Naples and Pozzuoli through tomographic images, and the detailed imaging of the Campi Flegrei caldera structure.

Regional Tomography

SERAPIS experiment was a refraction/reflection seismic acquisition survey, carried out in the Golf of Pozzuoli and in the land area of the Campi Flegrei. This was designed to reconstruct the geometry of the Flegrei caldera for the identification of the presence and form of the potential reservoir of superficial magma, and for the definition of a regional structural model of the Bays of Naples and Pozzuoli.

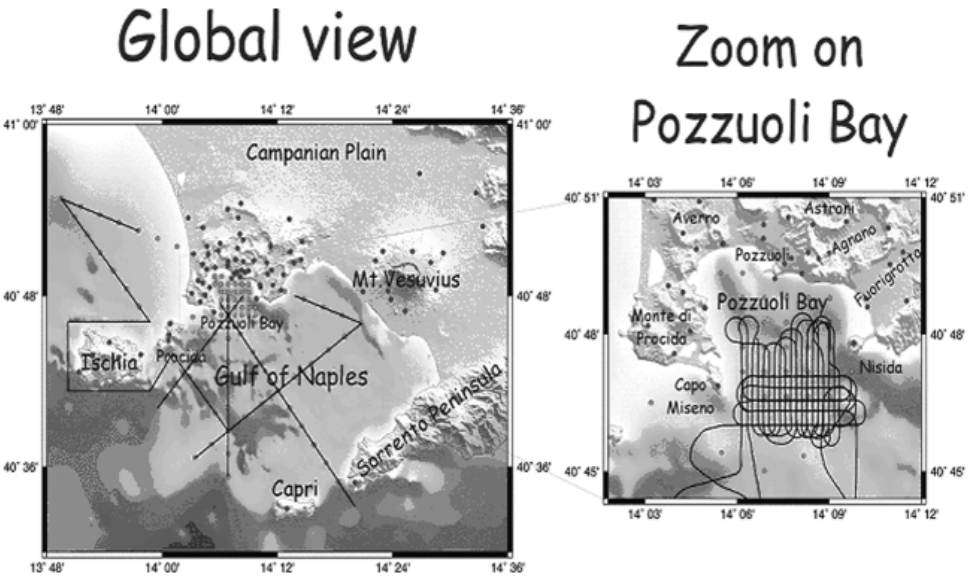

Fig. 1. The acquisition geometry of the Serapis 2001 active-seismic study (left). Enlargement of the Bay of Pozzuoli (right) (from Zollo et al. 2003).

The main background knowledge of the Flegrei area came from the active-seismic research conducted by the Experimental Geophysics Observatory (Finetti & Morelli 1974) and from the AGIP research in the 1980s. Finetti and Morelli (1974) revealed the presence of a strong reflector in the Gulf of Naples, dipping to the WNW, which was interpreted as being the top of the carbonatic bedrock, and of a NE-SW-oriented fault, which represented the off-shore continuation of the Torre del Greco fault (Figure 2).
The AGIP research was aimed at identifying areas in the Campi Flegrei that were potentially exploitable as geothermic sources, and it provided important information due to the deep boring and the extensive magnetic and gravimetric measurements. These last data, recently re-analysed by Capuano and Achauer (2002), revealed the presence of a ring-shaped relative gravimetric maximum centred on the Bay of Pozzuoli and characterised by an internal relative minimum (Figure 3).
The processing of the Serapis dataset provided 65,000 P-wave first arrivals from 300,000 wave forms recorded by the OBS, and 25,000 P-wave first arrivals from 400,000 wave forms recorded by the land stations.
In all, and considering also the integration of the data from the MareVes97 investigations, the dataset used included ca. 95,000 picks of P-wave first arrivals. In accordance with the source-receiver geometry used, a small-scale model of the 1D velocity distribution was constructed for the Gulf of

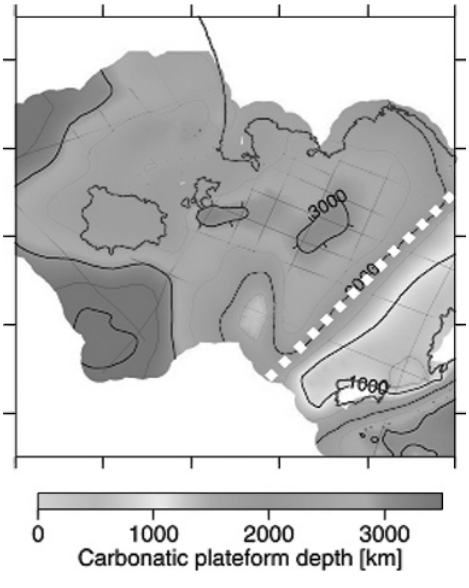

Fig. 2. Top of the Mesozoic basement deduced from the near-vertical seismic reflection survey data analysis carried out in 1970s in the area (Finetti and Morelli, 1974).
You can see this figure in color on page 211.

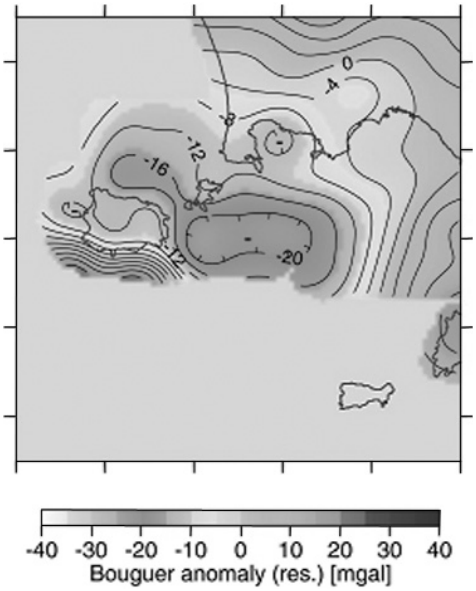

Fig. 3. Bouguer anomalies in the Gulfs of Naples and Pozzuoli (from Capuano & Achauer 2002).
You can see this figure in color on page 211.

Pozzuoli (PB) together with a large-scale model for the Gulf of Naples (NB) (Figure 4). The small-scale model was based on a dataset restricted to travel-times associated with the source-receiver pairs located in a 20-km-sided square centred on the Bay of Pozzuoli. The second, NB model contained all of the travel-times (see Zollo & Judhenerc 2004 for details).

The result obtained from the inversion of the P-wave travel-times of the large-scale model outlined a rather complex situation for the Bay of Naples (Figure 5). From the Sorrento Peninsula to the centre of the Bay of Naples the model showed two notable structural lines oriented NE-SW, that were interpreted as a two-step deepening of the carbonatic layer. The more southern step had already been seen by Finetti & Morelli (1974) and represented the off-shore continuation of the Torre del Greco fault. The vertical shift in the 1-2-km and 2-3-km horizontal tomographic sections was of ca. 1,000 m.

The north-west step had never been seen before, and it appeared to be parallel to that to the SE and to extend from the eastern limit of the Campi Flegrei caldera towards the SW for 35 km along the Posillipo-Banco di Fuori (PBF) segment. The vertical shift along this PBF fault was the same as that of the Torre del Greco fault: ca. 1,000 m (Figure 6).

The fault was evident in both the 3-4 km and 4-5 km horizontal tomographic sections and the vertical sections traced across the Gulf of Naples in a NW-

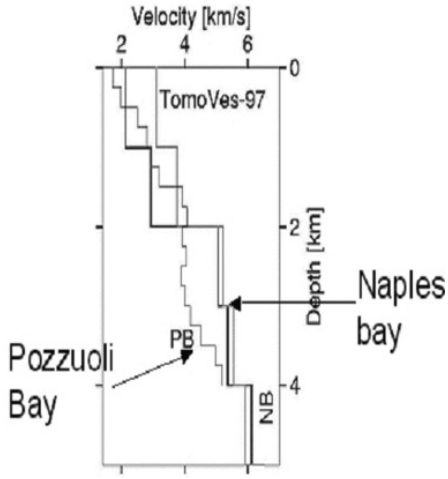

Fig. 4. One dimensional velocity models in the study area. The thick grey profile represents the TomoVes97-dataset-based model; the thick black profile is obtained with the whole dataset (NB) and the thin profile corresponds to the Bay of Pozzuoli subset (from Zollo & Judenherc 2004).

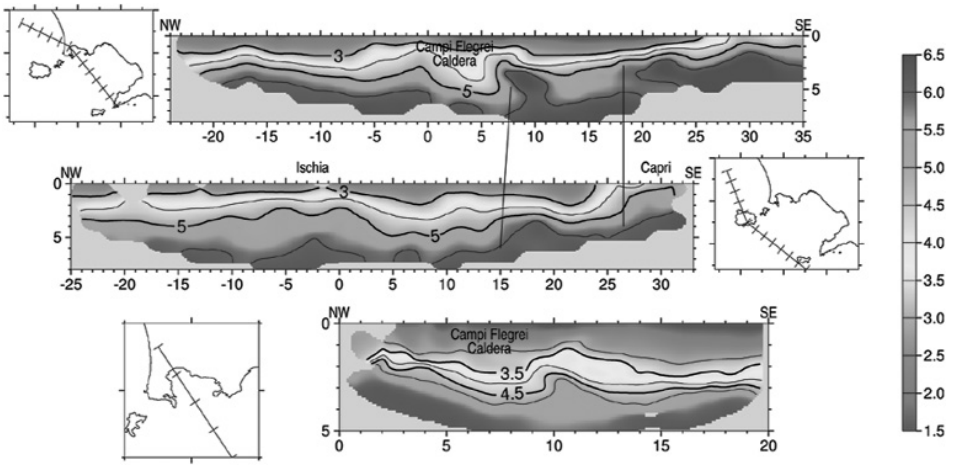

Fig. 5. Plane views of the NB velocity model. For each layer, the top and bottom depths of the layers are indicated, and the dots indicate the station locations; in the first layers they also represent the shot locations. The land topography is indicated with thin contour lines every 500 m. The iso-velocity lines are plotted at 3.0, 4.0 and 5.0 km/s (from Zollo & Judenherc 2004).
You can see this figure in color on page 212.

SE direction. In both cases, the velocity of the SE block (which was always >5.5 km/s) was ca. 1.0 km/s greater than that of the NW block. In agreement with numerous studies in the Vesuvius area, a Vp >5.5 km/s can be associated with the Mesozoic carbonatic bedrock. The two structural lines have been interpreted as faults that appeared in the carbonatic basement during the extension phase experienced by the Campania edge in the mid-Pleistocene.

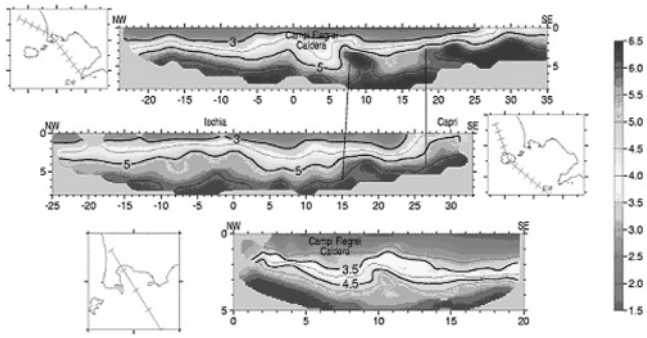

Fig. 6. Selected cross-sections of the NB (top and centre) and PB (bottom) models (with no vertical exaggeration). The small maps show the locations of the cross-sections, and the ticks are 5.0 km apart. The two NB cross-sections clearly show the normal faults affecting the carbonatic platform, with their locations indicated by the thick lines (from Zollo & Judenherc 2004).

Local Tomography: the buried rim of the CF caldera

The second tomographic inversion using the subset of 46,000 P-wave first arrivals allowed a more-detailed reconstruction of the Vp distribution of the Bay of Pozzuoli. The images revealed a sub-circular high-Vp anomaly extending from Capo Miseno to Nisida, while the central part of the Bay was characterised by a low Vp (Figure 7). The high-Vp anomaly was associated with the rim of the Flegrei caldera; it appeared in the 750-1,000 m horizontal tomographic sections and it was evident down to a depth of ca. 2.0 km. Below 2.0-2.5 km, the only remains of the upper structure was a high relative-velocity anomaly of an elliptical form that was traceable down to a depth of 3.5 km in the Bay of Pozzuoli. At a depth of 2.5-3.0 km, the images showed an increase in velocity due to the presence of the carbonatic layer.

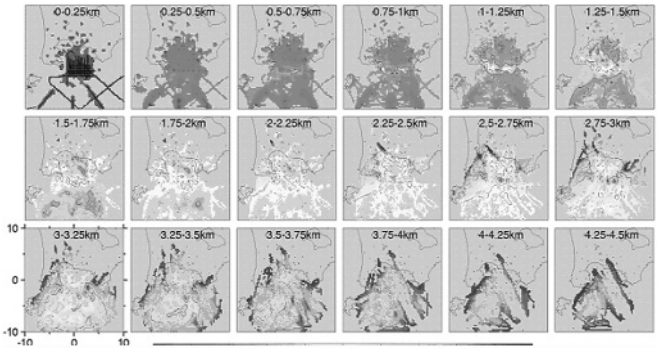

Fig. 7. Plane views of the PB velocity model. See legend of Figure 5 (from Zollo & Judenherc 2004).

The top of the carbonatic bedrock was revealed also in seismic sections passing across the bay, in which the refraction generated at the limit between the sedimentary-volcanic coverage of the Gulf of Pozzuoli and the carbonatic layer was seen (Figure 8).

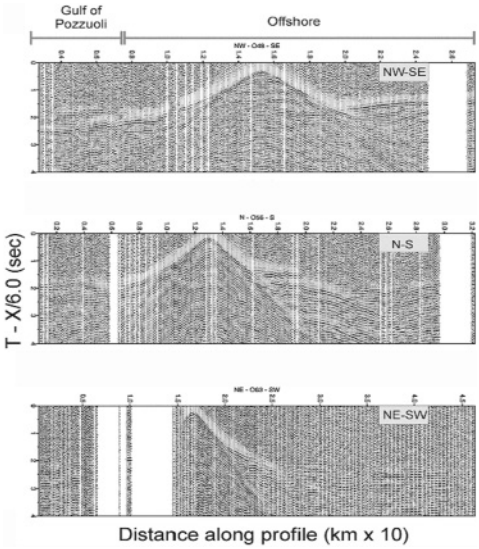

Fig. 8. Corresponding to the entry to the bay, the early arrival of the first P-waves can be related to the presence of the high-velocity caldera rim, which acts like a diffracting body by deflecting upwards the turning waves propagating in the superficial sedimentary layer. The second arrow points to the head-wave arrival generated at the limestone top discontinuity (from Zollo et al. 2003).

In this way, the images revealed the presence of the southern part of the rim of the Flegrei caldera, with a ca. 1-km thickness and ca. 1.0-1.5-km height limit. The north part of the caldera rim was scarsely sampled because of the distribution of the sources. Nevertheless, recent gravimetric measurements on land and at sea have revealed a cylindrical symmetry. In particular, the main character revealed by the Bouguer anomalies was a sub-circular relative minimum that correlated with the very low Vp of the Bay of Pozzuoli, bordered to the south by a gravimetric relative high that in turn confirmed the position of the high-Vp anomaly in the form of an arc (Figure 9).
In various 2D gravimetric models of the area that consisted of three layers of different densities (from the surface: first layer, d = 2.2 g/cm^3; second layer, d = 2.4 g/cm^3; third layer, d = 2.6 g/cm^3) (AGIP 1987, Rosi & Sbrana 1987), it was possible to correlate the forms of the 3.0-km/s and 3.5-km/s isolines with the depth and the form of the top of the structures at 2.2 g/cm^3 and 2.4

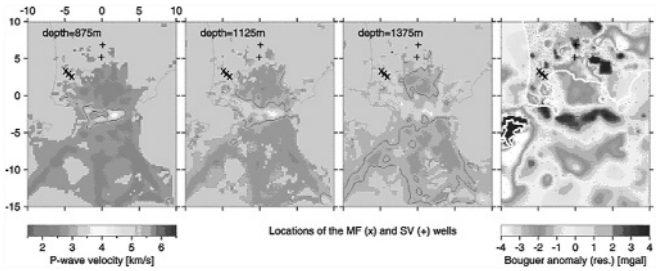

Fig. 9. P-velocity and Bouguer gravity anomaly images. The tomographic P-velocity images are displayed from the left to the right, at three different depths (875 m, 1,125 m and 1,375 m). The symbols "+" and "x" indicate the location of the S. Vito and Mofete wells, respectively, drilled by AGIP in the late 1970s for geothermal exploration purposes. The low-pass filtered map of the Bouguer gravity anomaly (reduction density: 2.4 g/cm^3) is shown on the left. (from Zollo et al. 2003).

g/cm^3, respectively. Furthermore, considering that the transition from 2.2 g/cm^3 to 2.4 g/cm^3 was associated with the transition from tuff-dominated units to lava-dominated units, the tomographic velocities <3.0 km/s were associated with the volcanic material that filled the bay (made up of loose pyroclastic rock, agglomerate tuff and chaotic tuff), while the velocities >3.5 km/s were associated with more coherent units (trachitic lava and/or tuff or tuff interlayered with lava) forming the rim of the caldera.

HIGH RESOLUTION TOMOGRAPHY

A final tomographic inversion used the P-wave first arrivals that were further restricted to the source-receiver pairs inside a square with 10-km sides centred in the Bay of Pozzuoli, and divided the model used for the inversion into 200x200x100m cell size sides. This resulted in very-high-resolution images of the Gulf of Pozzuoli down to a depth of ca. 1.1 km, which allowed the relationships between the deep structures and those more superficial to be investigated at the rim of the caldera (Figure 10).
The high-velocity anomaly in the form of an arc between ca. 0.7 and 2.0 km in depth corresponding to the rim of the Flegrei caldera was, as previously noted, associated with units of lava and tuff-interlayered lava, and showed a complex vertical development. Indeed, towards the surface it tended to divide into two sub-parallel branches that were visible on the horizontal tomographic sections to a depth of ca. 300-400 m. It was possible to correlate the position of dykes and volcanic mounds, and of off-shore fumaroles, as identified by surface seismic reflection research and direct observation, with the two branches (Mirabile et al. 1970, Pescatore et al. 1984, Milia 1998, Milia et al. 2003) (Figure 11).

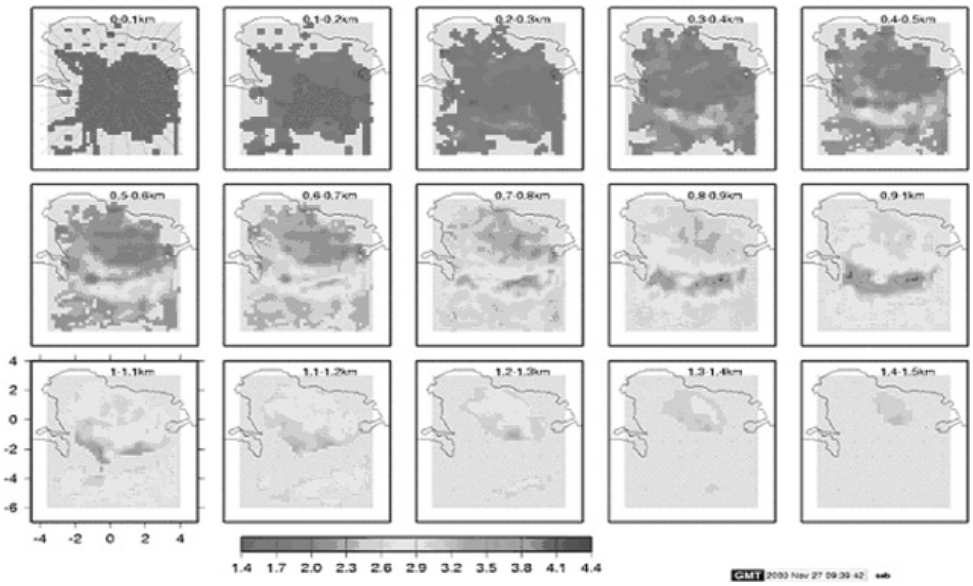

Fig. 10. The very-high-resolution seismic tomography for the Gulf of Pozzuoli, with the medium under investigation divided into 200x200x100m cell size sides. The red-based colours indicate the low velocities, and blue-based colours indicate the high velocities. For each layer, their top and bottom depths are indicated.
You can see this figure in color on page 213.

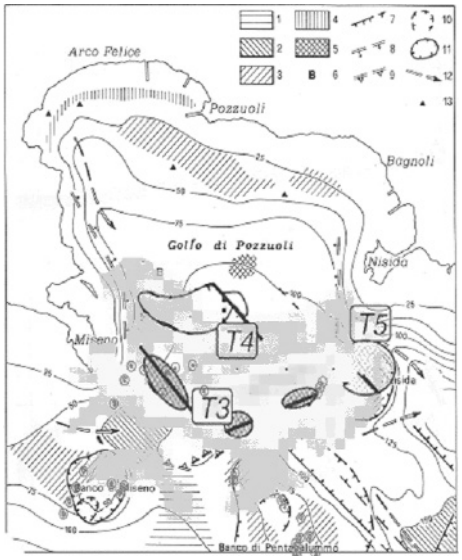

Fig. 11. The correlation between the position of the high-Vp anomaly in the form of a double arc and the position of the off-shore fumaroles of the Gulf of Pozzuoli, and of the dykes and volcanic mounds. T4: neapolitan yellow tuff; T5: Nisida complex volcanoes; T6: magmatic intrusion (dikes) (from Milia et al., 2003).

Conclusion

The Serapis investigations have therefore provided a regional-scale picture of the structural setting of the Gulf of Naples, which is characterised by carbonatic bedrock that dips towards the NW and is affected by two NE-SW-oriented faults of ca. 35 km, which give it a three-step structure. The northern-most fault stretching from the Posillipo Hill to Banco di Fuori could be linked to the two large ignimbric eruptions that characterise the volcanic history of Campi Flegrei and that promoted the rising of the magma towards the surface (Figure 12). Moreover, the tomographic images provide no evidence of the presence of a magma reservoir, down to a depth of 6 km.

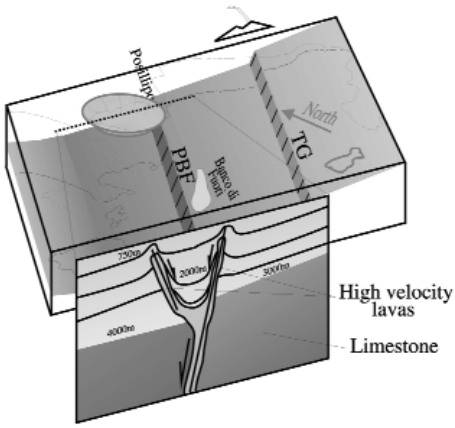

Fig. 12. Interpretative block diagram showing the main features identified in the tomographic models. The blue surface represents the carbonatic platform, dipping towards the northwest, with the two normal SW-NE Torre del Greco (TG) and Posillipo-Banco di Fuori (PBF) faults (from Zollo & Judenherc 2004).
You can see this figure in color on page 212.

On a local scale corresponding to the Bay of Pozzuoli, high- and very-high-resolution images have revealed the presence of an anomaly in the form of an arc that can be associated with the southern part of the Flegrei caldera rim. No tomographic evidence, however, could confirm the presence of two distinct concentric calderas that were reported to have formed following the eruptions of the Campania Ignimbrite and of the Napoletano Tufo Giallo (Orsi et al. 1996). Furthermore, it is possible to trace refractory waves of the carbonatic/sedimentary-volcanic layer limits in the seismic sections, which could confirm the presence of the Mesozoic carbonatic bedrock also in the Bay of Pozzuoli. Finally, the correlation between the position of minor volcanic structures (dykes, mounds and fumaroles) and the superficial high Vp

anomaly in the form of a double arc suggests that the post-caldera volcanic activity has been concentrated along the ring faults encircling the collapsed structure, both on land and under the sea. These faults could have functioned as preferential pathways for the rising of the gases and magma.

REFERENCES

Acocella V., Cifelli F., Funiciello R. (2000). Analogue models of collapse calderas and resurgent domes. *Journal of Volcanology and Geothermal Research*, 104, 81-96.

Agip. Geologia e Geofisica del Sistema Geotermico dei Campi Flegrei. *Servizi Centrali per l'Esplorazione, SERG-MMESG*, San Donato, 19 pp., 1987.

Aster R. C., Meyer R. P. (1988). Three-dimensional velocity structure and hypocentral distribution in the Campi Flegrei caldera, Italy. *Tectonophysics*, 149, 195-218.

Bartole R., Savelli D., Tramontana M., Wezel F. (1984). Structural and sedimentary features in the Tyrrhenian margin of Campania, Southern Italy. *Mar. Geol.*, 55, 163-180.

Benz H. M., Chouet B., Dawson P. B., Lahr J. C., Page R. A., Hole J. A. (1996). Three-dimensional P and S wave velocity structure of Redoubt volcano, Alaska. *J. Geophys. Res.*, 101, 8111-82.

Bruno P. G., Cippitelli G., Rampolla A. (1998). Seismic study of the Mesozoic carbonate basement around Mt. Somma-Vesuvius, Italy. *J. Geotherm. Volc. Res.*, 84, 311-22.

Capuano P., Achauer U. (2003). Gravity field modeling in the vesuvius and campanian area, in *TomoVes Seismic Project: Looking Inside Mt. Vesuvius*, edited by A. Zollo et al., Cuen, Napoli.

Cassano E., La Torre P. (1987). Geophysics, in R. Santacroce (ed.), Somma-Vesuvius. *CNR Quaderni della Ricerca Scientifica*, 114(8), 175-92.

D'Argenio B., Pescatore T., Scandone P. (1973). Schema geologico dell'Appennino meridionale. *Atti dell'Academia Nazionale dei Lincei,* 183, 49-72.

Dawson P. B., Chouet B. A., Okubo P. G., Villaseñor A., Benz H. M. (1999). Three-dimensional velocity structure of the Kilauea caldera, Hawaii. *Geophys. Res. Lett.*, 26(18), 2805-808.

De Bonatibus A., Latmiral G., Mirabile L., Palumbo A., Sarpi E., Scalera A. (1970). Rilievi sismici per riflessione: strutturali, ecografici (fumarole) e batimetrici del Golfo di Pozzuoli. *Boll. Soc. Nat. Napoli*, 79, 97-115.

De Vivo B., Rolandi G., Gans P. B., Calvert A., Bohrson W. A., Spera F. J., Belkin H. E. (2001). New constraints on the pyroclastic eruptive history of the Campanian volcanic plain (Italy). *Mineral Petrol*, 73, 47-65.

Finetti I., Morelli C. (1974). Esplorazione sismica a riflessione dei Golfi di Napoli e Pozzuoli. *Boll. Geof. Teor. Appl.*, 16(62/63), 175-222.

Gasparini P., Tomoves working group (1998). Looking Inside Mt. Vesuvius. *Eos Trans. AGU*, 79(229-230), 232.

Hole J. A. (1992). Nonlinear high-resolution three-dimensional seismic travel time tomography. *J. Geophys. Res.*, 97, 6553-62.

Ippolito F., Ortolani F., Russo M. (1973). Struttura marginale tirrenica dell'Appennino Campano: reinterpretazione di dati di antiche ricerche di idrocarburi. *Mem. Soc. Geol. It.*, XII, 227-50.

Judenherc S., Zollo A. (2004). The Bay of Naples (Southern Italy): constraints on the volcanic structures inferred from a dense seismic survey. *J. Geophys. Res.*, 109, B10312, doi: 10.1029/2003JB002876.

Lirer L., Luongo G., Scandone R. (1987). On the Volcanological Evolution of Campi Flegrei. *EOS, Trans. Am. Geophys. Union*, 68, 226-34.

Milia A. (1998). Le unità piroclastiche tardo-quaternarie nel Golfo di Napoli. *Geogr. Fis. Dinam. Quat.*, 21, 147-53.

Milia A. (1998). Stratigrafia, strutture deformative e considerazioni sull'origine delle unità deposizionale oloceniche del Golfo di Pozzuoli (Napoli). *Boll. Soc. Geol. It.*, 117.

Milia A., Torrente M., Russo M., Zappetta A. (2003). Tectonics and crustal structure of the campania continental margin: relationship with volcanism. *Mineralogy and Petrology*, 79, 33-47.

Milia A., Torrente M. (2003). Late-Quaternary volcanism and transtensional tectonics in the Bay of Naples, Campanian continental margin, Italy. *Mineralogy and Petrology*, 79, 49-65.

Orsi G., Scarpati C. (1989). Stratigrafia e dinamica eruttiva del Tufo Giallo Napoletano. *CNR-GNV Boll.*, 2, 917-30.

Orsi G., D'Antonio M., De Vita S., Gallo G. (1992). The Neapolitan Yellow Tuff, a large-magnitude trachytic phreatoplinian eruption: eruptive dynamics, magma withdrawal and caldera collapse. *Journal of Volcanology and Geothermal Research*, 53(1-4), 275-87.

Orsi G., De Vita S., Di Vito M. (1996). The restless, resurgent Campi Flegrei nested caldera (Italy): Constraints on its evolution and configuration. *J. Volc. Geotherm. Res.*, 74, 179-214.

Pescatore T., Diplomatico G., Senatore M. R., Tramutoli M., Mirabile L. (1984). Contributi allo studio del Golfo di Pozzuoli: aspetti stratigrafici e strutturali. *Mem. Soc. Geol. Ital.*, 27, 133-49.

Podvin P., Lecomte I. (1991). Finite difference computation of traveltimes in very contrasted velocity models: A massively parallel approach and its associated tools. *Geophysical Journal International*, 105, 271-84.

Rosi M., Sbrana A., Principe C. (1983). The Phlegraean Fields; Structural Evolution, Volcanic History and Eruptive Mechanisms. *Journ. Volc. Geoth. Res.* 17, 273-88.

Rosi M., Sbrana A. (Eds.). (1987). Phlegraean Fields. *CNR Quaderni della Ricerca Scientifica*, 114(9), 175.

Scarpa R., Tronca F., Bianco F., Del Pezzo E. (2002). High resolution velocity structure beneath Mount Vesuvius from seismic array data. *Geophys. Res. Lett.*, 29(21), 2040-4.

Scarpati C., Cole & Perrotta A. (1993). The Neapolitan Yellow Tuff: a large volume multiphase eruption from Campi Flegrei, Southern Italy. *Bull. Volcanol.*, 55.

Villasenor A., Benz H. M., De Luca G., Filippi L., Patane G., Scarpa R., Vinciguerra S. (1998). Three-dimensional P-wave velocity structure of Mt. Etna, Italy. *Geophys. Res. Lett.*, 25, 1975-8.

Wohletz K., Orsi G., de Vita S. (1995). Eruptive mechanism of the Neapolitan Yellow Tuff interpreted from stratigraphic, chemical and granulometric data. *J. Volcanol. Geotherm. Res.*, 67, 263-90.

Zollo A., Judenherc S., Auger E., D'Auria L., Virieux J., Capuano P., Chiarabba C., de Franco R., Makris J., Michelini A., Musacchio G. (2003). Evidence for the buried rim of Campi Flegrei caldera from 3-d active seismic imaging. *Geophys. Res. Lett.*, 30(19), 2002, doi:10.1029/2003GL018173.

2-D P velocity models and development of refraction data imaging techniques

R. de Franco, G. Caielli, R. Tondi
Istituto per la Dinamica dei Processi Ambientali, IDPA-CNR, Milano

Introduction

Objective of the work was to obtain 2-D P velocity models of Gulf of Naples and Pozzuoli area and in particular to define Campi Flegrei caldera structure from the inversion of the P first arrivals and obtain an image of the deeper refractor from the refraction convolution sections.

Data

In this report we present the result of the interpretation of the seismic refraction data acquired in the frame of SERAPIS seismic experiment in the Gulf of Naples, Phlegrean Field, Ischia and Vesuvius area. Our interpretation was made along three seismic lines: line1, line2 and line3; which present a different orientation in order to investigate the main structures of the Gulf of Naples and Phlegrean area. Along the line 1, 381 shots were recorded by 19 seismic stations: 9 OBS and 10 on land station. Line 2 consists in 175 shots recorded by 15 stations: 10 OBS and 5 on land stations. Along the line 3, 120 shots were recorded by 15 stations, with 13 OBS.
We analyzed the vertical component (z) and the p component recorded by the hydrophone of the OBS and the vertical component (z) of the on land stations. The on land stations were placed in a very noisly area and didn't have a good signal to noise ratio, for this reason we analyzed only few on land records. The lines utilized in our analyses are shown in Figure 1.

Methods

Our analyses consisted in:
– application of different inversion codes to first arrival data set to obtain 2D models along the three selected seismic lines;
– development of refraction data imaging techniques.

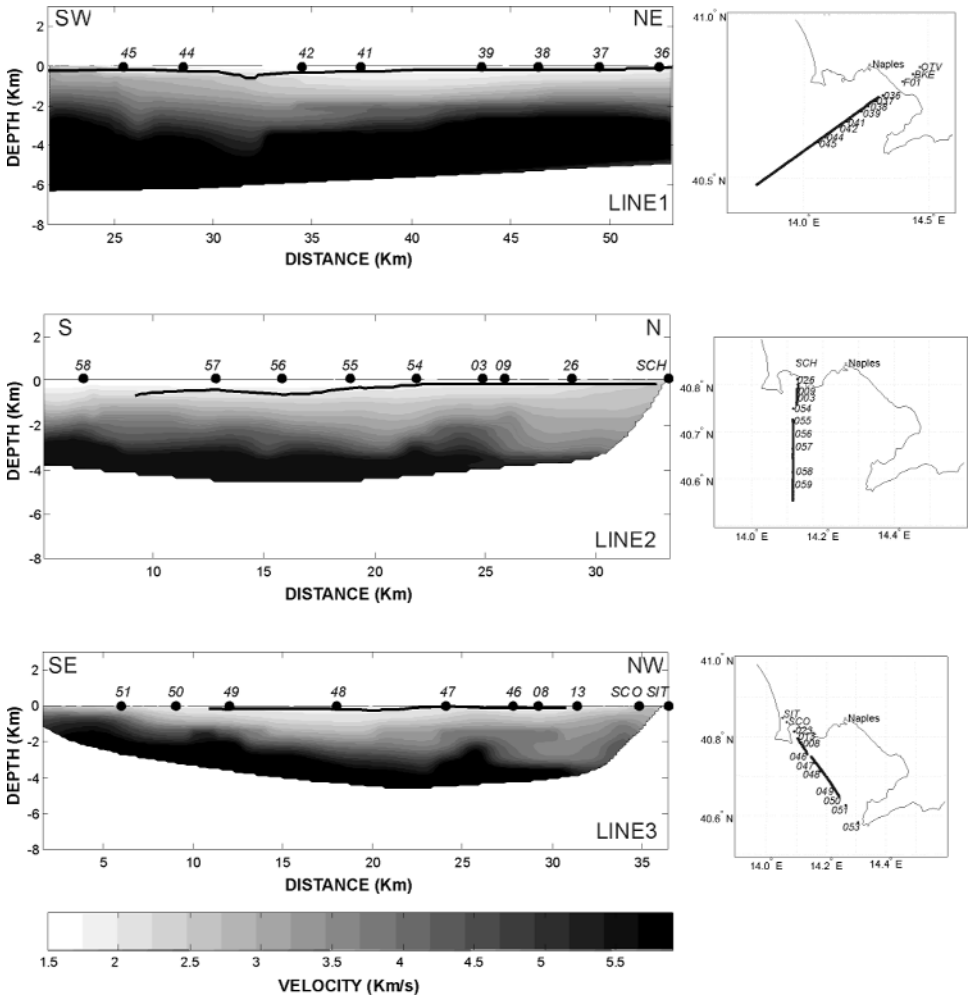

Fig. 1. Final velocity models for the three studied lines and location maps.

The first step consisted in the picking of the first P arrivals in the common receiver configuration, after a pre-processing dedicated to spectral analysis and data filtering.

The inversion codes utilized by our unit were: SEISOPT (Pullammanappallil and Louie, 1994) and CRT (Cerveny et al., 1988; Tondi and de Franco, 2004). The SEISOPT, uses a non linear annealing simulated optimisation approach and it is based on a Monte Carlo method for the model generation and eikonal solver for the travel-time calculation. In the SERAPIS data inversion we use 1-D and 2-D initial model obtained from the intercept time method applied to the cumulate travel time for the three studied lines.

The final velocity models obtained along the three analysed lines are shown in Figure 1. The seismic refraction data were analysed also using a tomographic approach CRT, based on a ray-tracing inversion procedure of the first arrivals of P waves (picking times).

To obtain an image of the refractors in the area a procedure was developed and applied to the data (de Franco, 2004). The refraction imaging involves three steps.

1) The convolution of two discrete time series $S_J(X_i,t_s)$ and $S_K(X_i,t_s)$, recorded at the *i*-th receiver with the two shots *J* and *K*, ($s=1,...,N$; *N* is the number of samples; $S_J(X_i,t_s)$ represents the seismic section from shot *J*), is given by equation 1, viz.,

$$C_{JK}(X_i,t_r) = S_J(X_i,t_s) * S_K(X_i,t_s) \qquad \text{for } i=f,...,l, \text{ and } r=1,...,2N-1 \qquad (1)$$

where * denotes the convolution operator. This operation is equivalent to sum the refracted arrival times at the receiver X_i located inside the offset range $[X_f,X_l]$ where refracted arrivals from a specified refractor are observed.

2) The cross-correlation of the convolved result obtained with equation 1 with $S_J(X_K,t_s)$ refracted traces recorded at the forward and reverse shot positions.

$$W_{JK}(X_i,t_m) = C_{JK}(X_i,t_r) \otimes S_J(X_K,t_s) \qquad \text{for } i=f,...,l;\ m=1,...,4N-3 \qquad (2)$$

where ⊗ denotes the cross-correlation operator. This operation perform the difference between the previous sum (eq. 1) and reciprocal time and is equal to the intercept time in the plus-minus sense. $W_{JK}(X_i,t_s)$ is the refractor image.

3) The stacking of convolved and cross-correlated traces for all shot *P* configurations:

$$\Sigma(X_i,t_r) = \sum_{J=1}^{P}\sum_{K=J}^{P}\left\{\left[S_J(X_i,t_s) * S_K(X_i,t_s)\right] \otimes S_K(X_J,t_s)\right\} \text{ for } i=J,...,K \qquad (3)$$

The procedure was applied to SERAPIS data line 1 and 3. Since we use a single reversed configuration for each line the processing was limited to the steps described by equation 2 and 3. For line 1 were used the common OBS data sections 42 e 36. The obtained image, reported in Figure 2 (left panel), covers the distance model range between 39-49 km. For line 3 the OBS 50 and OBS 13 data sections were used. The resulting image (Figure 2 right panel) covers the model distance range between 12-25 km. The processing evidenced the clear presence of a single refractor located at depth ranging respectively between 2 and 3 km for line 1 and between 2.5 and 4 km depth for line 3. This refractor is interpreted as the Mesozoic carbonatic basement.

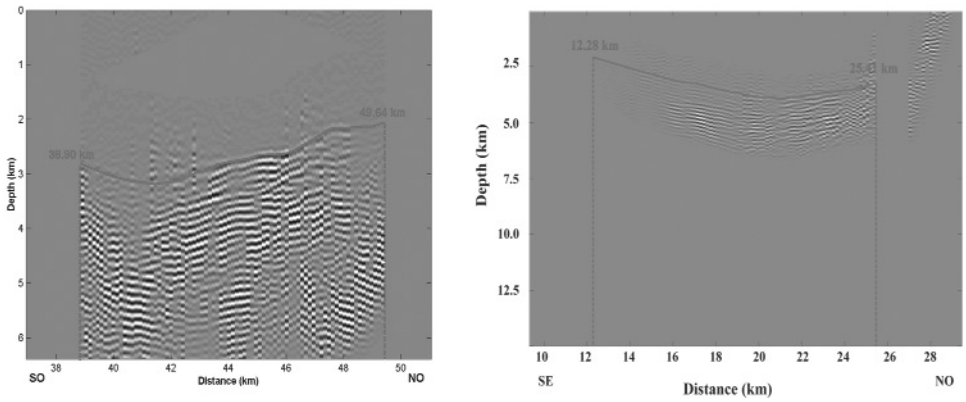

Fig. 2. Image of the deeper refractor along Line 1 (left) and Line 3 (right).
You can see this figure in color on page 214.

RESULTS

The 2D velocity models obtained along the three seismic lines allowed us to define the trend and the depth of the Mesozoic carbonatic basement in Gulf of Naples and Campi Flegrei area. This discontinuity, as evidenced by the refractor imaging analysis, constitutes the main refractor present in the studied area. The velocity is varying between 1.5 km/s and 6.4 km/s. The velocity values greater than 5.2 km/s are interpreted as the seismic basement.
The most prominent feature is the presence of a resurgent structure in the Campi Flegrei area observable along line 2 and line 3 (Figure 1). The top of this structure is found at about 1 Km depth and extends down to about 4-5 Km depth.

REFERENCES

Cerveny V., Klimes L., Psencik I. (1988). Complete seismic-ray tracing in three-dimensional structures, in *Seismological Algorithms*, edited by D.J. Doornbos. Academic Press, New York, 89-168.

de Franco R. (2005). Multi-Refractor Imaging With Stacked Refraction Convolution Sections. *Geophysical Prospecting*, 53, 335, doi:10.1111/j.1365-2478.2005.00478.x.

Pullammanappallil S. K., Louie J. N. (1994). A generalized simulated-annealing optimization for inversion of First-arrival times. *Bull. Seism. Soc. Am.*, 84(5), 1397-409.

Tondi R., de Franco R. (2005). Seismic travel times inversion for 3-D structures regularized with Sobolev norms. *Inverse Problems*, 21, 525-546, doi:10.1088/0266-5611/21/2/007.

4

Techniques for volcanic structure study

Part of the project was devoted to the development of procedures which make a joint use of active and passive source travel times and gravity measurements in order to reconstruct 3-D subsurface velocity and density models. This objective was performed by the extension of the procedure of Sequential Integrated Inversion to 3-D structures and comparing the observed gravity field with that computed by the passive source velocity model.
Understanding of the behavior of rocks forming subsurface structures is an important requisites to interpret seismological data in terms of both composition and state (saturation, pore pressure, etc.) of the earth's interior. Thus, laboratory measurements of physical properties (density, porosity, permeability, electrical and thermal conductivity, acoustic velocities, at standard conditions of pressure and temperature) on Campi Flegrei rock samples have been analyzed in comparison with available log data, and cross modeling using standard methodologies of rocks mechanics to understand the interrelationship between rock-, fluid- properties. Thermal modeling and static modeling of the stresses and deformations fields have been also performed.

Joint 3D seismo-gravity inversion (theoretical development)

R. de Franco[1], R. Tondi[1], T. Vanorio[2], J. Virieux[2]

[1] *Istituto per la Dinamica dei Processi Ambientali, IDPA-CNR, Milano*

[2] *Géosciences Azur, CNRS, Université de Nice, Sophie Antinopolies, Valbonne, France*

Introduction

Development of procedures which make a joint use of active and passive source travel times and gravity measurements in order to reconstruct 3-D subsurface velocity and density models.

Results

a) Extension of the procedure of Sequential Integrated Inversion (Tondi et al., 2000) to 3-D structures.
b) The vertical component of the gravity field produced by the passive source velocity model [recovered from the inversion of microevents (-1<M<4)] registered by the three-component temporary digital network installed by University of Wisconsin and Osservatorio Vesuviano during the last bradisism episode (1982-1984) with the TLR3 code (L. Lovisa et al., this issue) was calculated and compared to the observed field.

Methods

Aim of the procedure of Sequential Integrated Inversion is to make a joint use of active source P-wave travel times and gravity data in order to reconstruct accurate 3-D subsurface velocity and density models.
As the first demand of the procedure is a correct information deduced from the inversion of seismic travel times, an iterative technique (Tondi & de Franco, 2004) which regularizes the inversion problem with the use of the Sobolev norm of order two has been developed. In this way we can control the chaoticity of seismic rays during the iterations and obtain stable solutions with a weak dependence on the starting model and on the chosen discretization. Hence:

a) The velocity model is parametrized with tricubic B-splines specifying the distribution of the irregular velocity grid.
b) Seismic waves are modelled through a two-point ray tracing with a shooting procedure based on an accurate search for the subdomains of the ray take-off parameters, where the two-point rays may occur (Cervený et al., 1988).
c) The velocity parameter adjustement vector is obtained iteratively:

$$\Delta \mathbf{v} = [\mathbf{A}^T C_d^{-1} \mathbf{A} + s_{00}^2 \mathbf{S}_{00} + s_{11}^2 \mathbf{S}_{11} + s_{22}^2 \mathbf{S}_{22}]^{-1} \text{ x}$$
$$[\mathbf{A}^T C_d^{-1} \Delta \mathbf{t} + s_{00}^2 \mathbf{S}_{00} (\bar{\mathbf{v}} - \mathbf{v}^{M-1}) - s_{22}^2 \mathbf{S}_{22} \mathbf{v}^{M-1}] \quad (1)$$

with

– Δv the velocity parameter adjustment vector, of dimension N, the number of model parameters;
– Δt the traveltime residual vector of dimension J, the number of observations;
– C_d a chosen symmetric definite positive matrix of dimension JxJ, the data covariance matrix, the role of which is to calibrate, with respect to each other, the different travel times involved;
– **A** the ray characteristic operator (the Jacobian operator or the Fréchet derivative) of dimension JxN:

$$\mathbf{A(m)} = \frac{\partial t}{\partial \mathbf{m}} \quad (2)$$

which characterizes the sensitivity of travel times (t is the time integral from the source to the receiver) to slowness perturbations;

– $\mathbf{v}^{M-1}$ the velocity parameter vector resulting from the previous iteration of dimension N;
– $\bar{\mathbf{v}}$ the velocity parameter vector corresponding to the starting model of dimension N;
– s_{00}, s_{11}, s_{22}, the weighting factors associated with the minimization of the functions used for the velocity model parametrization and of the relative first and second derivatives;
– S_{00} the symmetric positive-definite matrix of L_2 scalar products of the functionals describing the velocity model parameters ; S_{11} and S_{22} the symmetric positive-semidefinite matrices of the isotropic Sobolev scalar products of the functionals describing the velocity model parameters.

d) The iteration process is stopped when:

$$\chi_{CALC} = \sqrt{\frac{(\Delta \mathbf{t})^T \mathbf{C}_d (\Delta \mathbf{t})}{J}} \quad (3) \quad \text{and} \quad \chi_{EST} = \sqrt{\frac{(\Delta \mathbf{t} - \mathbf{A}\Delta \mathbf{v})^T \mathbf{C}_d (\Delta \mathbf{t} - \mathbf{A}\Delta \mathbf{v})}{J}} \quad (4)$$

show similar values: this means that for that source-receivers configuration and that model parametrization the variance $\Delta\mathbf{v}$ to be brought to the model has become negligible.

e) To analyze the solution quality we choose to perform a Monte Carlo analysis of the covariance operator. Under this formalism, we invert K randomly perturbed data and model vectors for many nonlinear inversions until the posterior model covariance can be well approximated (Tarantola, 1987). In this way we can compute the *a posteriori* velocity mean vector over all the final $\mathbf{v}_k$ velocity models:

$$\mathbf{v}_{pos} = \frac{1}{K}\sum_{k=1}^{K}\mathbf{v}_k \tag{5}$$

and the *a posteriori* model covariance around the non perturbed solution $\mathbf{v}_\infty$:

$$C_V = \frac{1}{K}\sum_{k=1}^{K}(\mathbf{v}_k - \mathbf{v}_\infty)(\mathbf{v}_k - \mathbf{v}_\infty)^T \tag{6}$$

The *a posteriori* velocity mean vector is transformed in a density vector through a node dependent linear relationship (different coefficients *a* and *b*) on the basis of some a priori information on the structures represented by the model. The transformed grid of density values is then represented by a collection of rectangular prisms whose density is linearly dependent on the three coordinates. For each prism we define a point origin (the node in the external side, in the bottom on the left) that we call ρ_0 and three density gradients in the x,y,z directions with respect to this point (ρ_{1x}, ρ_{1y}, ρ_{1z}):

$$\begin{aligned}
&\rho_0 = \rho_{x,y,z}\\
&\rho_{1x} = (\rho_{x+1,y,z} - \rho_{x,y,z}) / \Delta x\\
&\rho_{1y} = (\rho_{x,y+1,z} - \rho_{x,y,z}) / \Delta y\\
&\rho_{1z} = (\rho_{x,y,z-1} - \rho_{x,y,z}) / \Delta z
\end{aligned} \tag{6}$$

The expression derived by Pohànka (1988) is used for the computation of the three components of the gravity field:

$$g(\mathbf{r}) = -\gamma \sum_{k=1}^{K}\sum_{l=1}^{l_1(k)}\left[\begin{pmatrix}(\rho_0 + \rho_1 \bullet \mathbf{r} + \rho_1 \bullet \mathbf{n}_k Z_k)\,\phi(u_{kl}, v_{kl}, w_{kl}, z_k, \varepsilon) + \\ \rho_1 \bullet v_{kl}\,\phi_2(u_{kl}, v_{kl}, w_{kl}, z_k, \varepsilon)\end{pmatrix} n_k - \frac{1}{2} Z_k\,\phi(u_{kl}, v_{kl}, w_{kl}, z_k, \varepsilon)\,\rho_1\right] \tag{7}$$

It is derived by substitution of $\rho(\mathbf{r'}) = \rho_0 + \rho_1(\mathbf{r'})(|\mathbf{r'} - \mathbf{r}|)$ in the integral of the field:

$$g(\mathbf{r}) = \gamma \iiint \nabla \frac{\rho(\mathbf{r'})}{|\mathbf{r'} - \mathbf{r}|}\, d\xi d\eta d\zeta \tag{8}$$

where $\mathbf{r'} = (\xi,\eta,\zeta)$ is referred to the system of Cartesian coordinates associated to the field, $\mathbf{r} = (x,y,z)$ is referred to the coordinates associated to the causative body, γ is the gravitational constant and

$$|\mathbf{r'} - \mathbf{r}| = \sqrt{(x-\xi)^2 + (y-\eta)^2 + (z-\zeta)^2} \tag{9}$$

The used parametrization leads to a perfect match between seismic and gravity modelling and allows to take in account: 1) bodies between which density contrasts are present and which therefore generate seismic reflections at their interfaces; 2) bodies across which there are linear density variations, but between which the densities are continuous. This avoids artificial density contrasts across the interfaces of homogeneous polyhedra.
The flow chart of the whole SII procedure is represented in Figure 1.

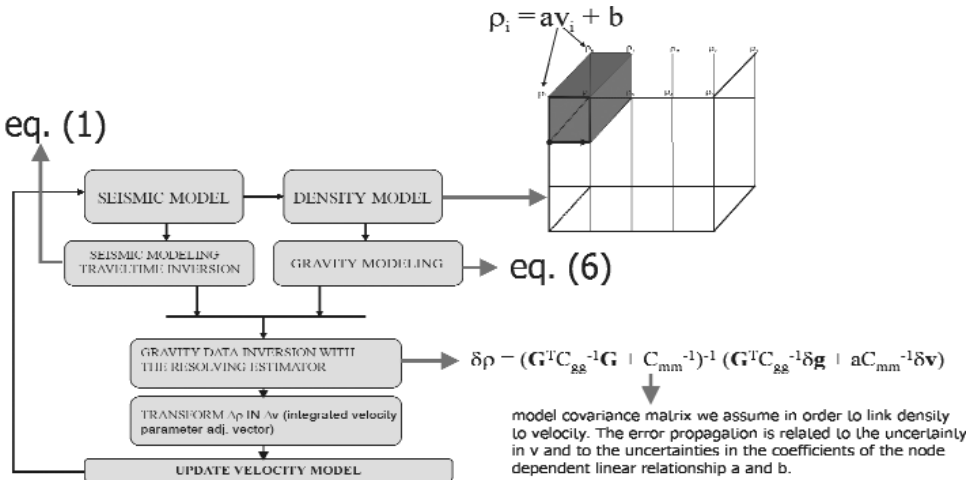

Fig.1. Flow chart of the whole Sequential Integrated Inversion procedure for 3-D structures.

Application: the gravity field of the passive source velocity model

The grid of 29 x 29 x 19 velocity nodes, regularly spaced with a spatial resolution of 500 m x 500 m x 500 m, recovered by inversion of 5886 passive

events with the TLR3 code (L. Lovisa et al., this issue) is transformed in a density grid using the empirical formula of Ludwig et al. (1970):

$$\rho = -0.7 + 2.23*v - 0.598*v^2 + 0.0704*v^3 - 0.00283*v^4 \quad (10)$$

with ρ the density in g/cm^3 and v the P-wave velocity in km/s (Figure 2).

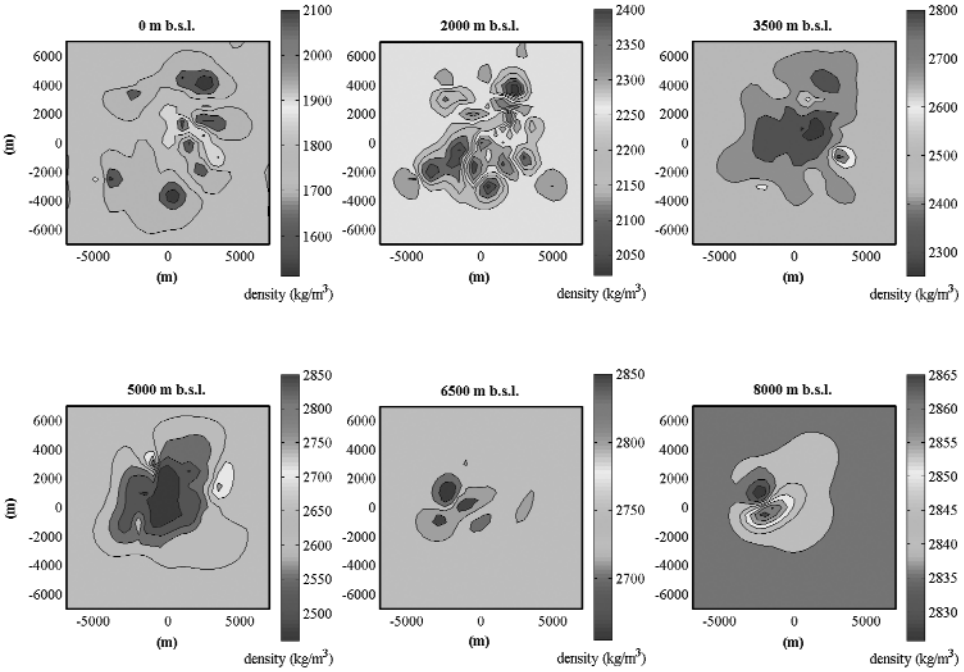

Fig. 2. Density model recovered from passive source velocity model.
You can see this figure in color on page 215.

Hence, following the above procedure the density grid is partitioned in 14112 regular rectangular prisms and the vertical component of the gravity field is calculated using the formula derived by Pohànka (Figure 3a). The calculated field is compared to the observed field extracted from the gravity map of the area which covers all the Campanian plain and the Gulf of Naples (Berrino et al., 1998). The estimated gravity residuals (Figure 3b) evidence that the reconstructed model induces a slight misplacement toward west, of the gravity minimum produced by the Phlegrean caldera.

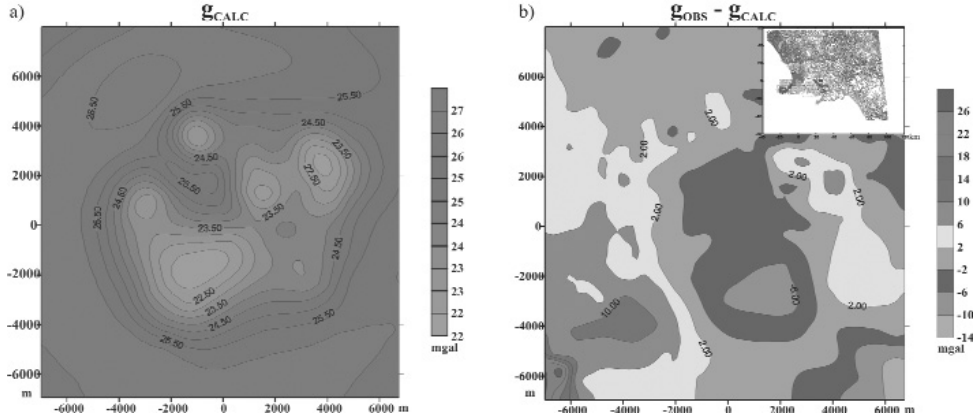

Fig. 3. a) The calculated gravity field produced by the density model in Figure 2 (bkg. = 2480 kg/m^3) and b) the related gravity residuals with respect to the observed field (792 measurement points extracted from the gravity map which covers all the Campanian plain and the Gulf of Naples (Berrino et al., 1998) shown in the inset.
You can see this figure in color on page 216.

References

Berrino G., Corrado G., Riccardi U. (1998). Sea gravity data in the gulf of Naples: a contribution to delineating the structural pattern in the Vesuvian area. *Journal of Volcanology and Geothermal Research*, 82, 139-50.

Cervený V., Klimeš L., Pšencik I. (1988). Complete seismic ray-tracing in three dimensional structures, in *Seismological Algorithms*, D.J. Doornbos Academic, 89-168, S. Diego Calif.

Pohànka V. (1998). Optimum expression for computation of the gravity field of a polyhedral body with linearly increasing density. *Geophysical Prospecting*, 46, 391-404.

Ludwig W. J. J., Nafe E., Drake C. L. (1970). Seismic refraction, in *The Sea*, edited by A.E. Maxwell, pp. 53-84, Wiley Intersc. Hoboken N.J.

Tondi R., de Franco R. (2004). Accurate assessment of 3D crustal velocity and density parameters: application to Vesuvius data sets, *Geophysical Journal International*, under revision.

Tondi R., de Franco R. (2005). Seismic travel times inversion for 3-D structures regularized with Sobolev norms. *Inverse Problems*, 21, 525-546, doi:10.1088/0266-5611/21/2/007.

Thermo-mechanical modeling of the Campi Flegrei volcanic area (Italy)

G. Giberti[1], G. Russo[1], T. Vanorio[2], B. Yven[3], M. Zamora[3]

[1] *Dipartimento di Scienze Fisiche, Università Federico II, Napoli, Italia*

[2] *Géosciences Azur, CNRS, Université de Nice, Sophie Antinopolies, Valbonne, France*

[3] *IPGP, University VI-VII, Paris, France*

Abstract: The themes afforded during the years of the activity of the Project refer essentially to two items: 1) laboratory measurements on Campi Flegrei rock samples, analysis of their physical properties, comparison with available log data, and cross modeling using standard methodologies of rocks mechanics; 2) unsteady thermal modeling and static modeling of the stresses and deformations fields. The main results obtained are shortly resumed here.

Introduction

Campi Flegrei project included the modeling of the thermal and mechanical behavior of the caldera. Unsteady numerical thermal models were developed to asses the relative importance of different factors in influencing the temperature field. Numerical models of the displacement field generated by different reservoir under pressure were also developed. For all these models, it is important to know the physical properties of the hosting medium. Moreover, physical properties of the caldera rocks are relevant for the interpretation of the experimental results of geophysical surveys. For these reasons, laboratory measurements on Campi Flegrei rock samples were both performed and collected from the existing literature. In the following the main results obtained from modeling and laboratory measurements are described.

Laboratory measurements, log data, models of physical properties

Measurements of physical properties (density, porosity, permeabilities, electrical and thermal conductivity, acoustic velocities, at standard conditions of pressure and temperature) of rocks sampled on surface and at depth has been carried out. These measurements were performed as a PhD research at IPGP by Yven (Yven, 2001) under the supervision of Prof. Zamora. The results have

been analysed and compared with other similar data from literature and those measured by Vanorio (Vanorio, 2003) on the same samples, to verify the consistencies and the differences (Giberti et al., this issue).
The dependence on temperature, within the range (0-1200 °C), of the elastic and thermal properties of superficial volcanic rocks is an item that could be important for thermo mechanical modelling. As it was impossible, for technical reasons, to study experimentally this dependence on the Campi Flegrei samples, a detailed bibliographic research has been conducted to extrapolate the aimed relationship. Experimental and theoretical models have been considered. It resulted that sensible variations of the parameters are attained only at temperatures near the solidus-liquidus transition. These temperatures could be attained only near a magmatic intrusion. The whole set of geophysical data measured in the area deny the possibility of this occurrence at shallow depth (first 5-6 km). Consequently, the surface deformations and stress field models have been developed without taking into account the effect of the temperature (internal report, unpublished, Vanorio).
Finally, the inter-relationships among physical properties of Campi Flegrei rocks measured with different methods (laboratory and wells-log-data) and at different pressure conditions have been analyzed with standard methodologies of rock physics. In particular, the digitalization of the whole set of the available Agip logs referring to the area has been carried out, and the analysis of these data together with the analysis of laboratory measurements under in situ pressure conditions have provided signatures on how petrophysical properties would affect seismic response (Vanorio et al., 2002). The cross-disciplinary methodology of analysis of the measured physical properties has revealed fruitful in determining over-pressurized horizons. As an example, an inferred pore fluid pressure, mainly exerted by water, of about 15 MPa in rock formations, at 1000-1600 m depth, at the Mofete1 well was inferred (see Figure 1). Data plotted in Figure 1 were obtained by models that relate the elastic moduli of a rock formation to porosity, pore fluid compressibility, mineralogy and effective pressure. In particular, it has been modeled: 1) the elastic moduli of the dry rock frame both at zero porosity and at the critical porosity by the Hertz-Mindlin contact theory, to compute the effective bulk (K_{HM}) and shear (μ_{HM}) moduli of a dry mixture of volcanic rock and clay at critical porosity (Φ_c) under a given effective pressure; 2) the upper (HS+, stiffer rock) and lower (HS-, softer rock) Hashin-Shtrikman bounds between the two end points at zero porosity (K_S, μ_S) and at the critical porosity (K_{HM}, μ_{HM}) for the two-component mixture of volcanic rock and clay; 3) the elastic moduli of the water and steam saturated mixture using Gasmann's fluid substitution equation; 4) density of water and steam saturated rock as function of pressure and temperature of fluids to obtain velocity (Vp, Vs) and Poisson's ratio data. In Figure 1 the comparison between log data and the model of Vp versus Poisson's ratio for a depth interval ranging from 1000 m to 1600 m is shown. Data are grey graded as a function of depth. According to the model, the best fit of the data is obtai-

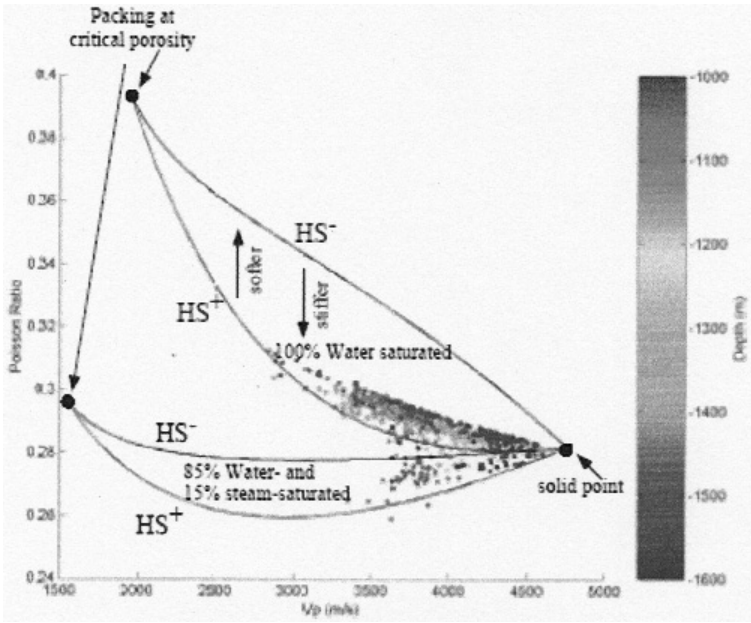

Fig. 1. Comparison between log data and the model of Vp/Vs. Poisson's ratio for a depth interval ranging from 1000 m to 1600 m.
You can see this figure in color on page 214.

ned for an effective pressure of 20MPa. Since at 1300 m the confining pressure is estimated to be about 35 MPa, the pore fluid pressure is about 15MPa.

MODELS

Thermal models

3D and 2D axially symmetric thermal modeling in conductive non-stationary regime has been developed. The models have been solved numerically considering the heterogeneity of the medium, the dependence of the thermal and physical properties of rocks on temperature, different hypothesis on the volcanological history of the area (one or more magmatic intrusion episodes, the effect on the temperature field of caldera collapses, the role of fluids, etc.). An estimate of the role of a possible stationary natural convection induced by difference in temperature in potential aquifers or in a porous medium has been carried out developing the necessary numerical codes. The simulations have been carried out both using finite difference and commercial finite element codes. The results of these studies, which have been the subject of two graduating theses, are till now unpublished (Caponetto and Giberti, 1996, Mercogliano and Giberti, 2000).

Modeling of the deformation and stress field induced by shallow and deep sources of overpressure has been performed. This modeling is carried out using a commercial element finite code and under the hypothesis of linear elasticity. The heterogeneity of the medium is taken into account, and the model is schematically based on the results of the two seismic tomographies based on data acquired during the SERAPIS active seismic survey (this project, various UR) and by the inversion of the data of earthquakes measured in the area during the 1982-84 bradyseismic crisis (Vanorio et al., 2003). One of the schematic model developed in this context is show in Figure 2.

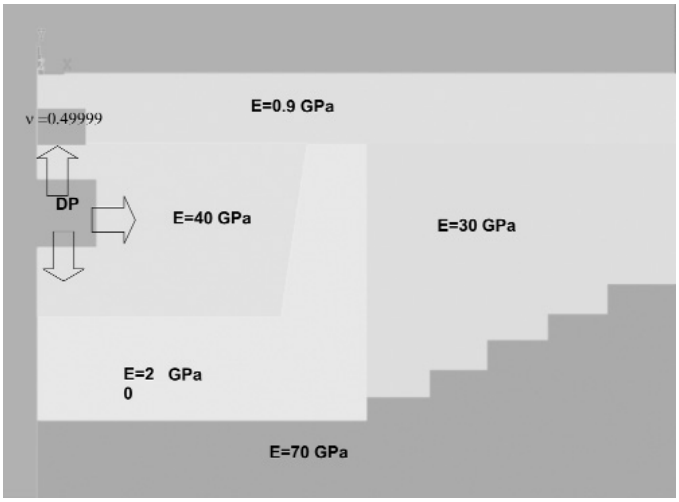

Fig. 2. Cartoon of one of the models utilized to find displacements on surface due to a shallow overpressure source. See text for more comments.

Deformation

The model is axis-symmetric, the different grey zones refer to different lithologies and different elastic properties (E is the Young Modulus, ν is the Poisson's Ratio). The arrows indicates that at shallow depth (1.5 km in the figure) an uniform (1 km in height and 1 km in radius) source of overpressure (a thermo-metamorphic trapped gas?) is acting. It corresponds to a cylindrical volume of about 3 km^3. The zone above the source with the indication ν=0.4999 would simulate the elastic response of a zone containing prevalently water or vapour. As an example of the preliminary results obtained with such a configuration with an overpressure of 15 MPa, we found that a maximum vertical uplift of about 1 m is obtained; that almost doubles when the radius of the source is taken as 1.25 km, all the other parameters being unchanged.

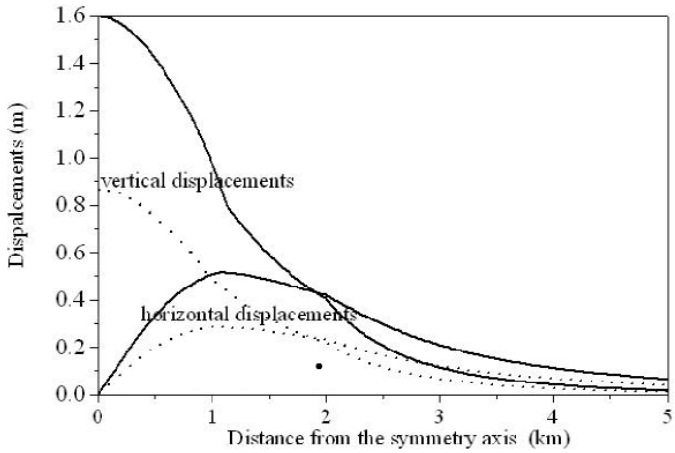

Fig. 3. Vertical and horizontal surface displacements versus the distance from the symmetry axis.

DISCUSSIONS

Lab and log data

The whole set of lab and log data and the analysis on them has been fruitful to better characterize the physical properties of rocks of this area, but there is a bias that do not allow to use them directly in modeling. It has in fact to be pointed that the whole set of data (lab and log measures) refer to very specific sites of the Campi Flegrei area. In fact the wells, to which samples and logs refer, are situated on the border of the caldera and out of the area interested by the two recent (1970-72,1982-84) bradyseismic crises. These sites were chosen by the Agip Oil Company almost exclusively because good candidates for geothermal exploitation and until now no other wells inside the area has been drilled. In this condition, basing on what is found on few local points, all localized on the border of the caldera, only guesses on the physical properties and structures of the internal area can be done. Fortunately, more insights on this subject has come from two tomographic studies (Vanorio et al, 2005, and Zollo et al., 2004).

Thermal modeling

The results of thermal models indicates that, in conductive regime, the models will able in reproducing the temperature data measured in wells only making unrealistic and unmotivated hypothesis on the time, volume and depth of big magmatic intrusions. High temperature gradients, as those locally measured in geothermal wells, could be explained as due to the effect of some local and

recent (some thousand of years old) shallow small intrusion, whose conductive effect at shallower depth are visible now, given the times scales of thermal conduction in volcanic rocks. Moreover the presence of trapped aquifers, which promptly acquire and homogenise thermal energy, but very slowly loose this energy, will be of aid in explaining the specific features measured in the wells.

Deformations

The preliminary results of deformation models indicate that the essentials parameters that determine uplifts of the order of magnitude of those measured during the bradyseismic crises are surely the heterogeneities of the rocks, and a shallow oblate source of overpressure. The associated horizontal deformations do not appear have the trend and the value of the measured ones, and this is attributed to the assumed symmetry of the model. 3D modeling are on schedule.

References

Caponnetto D., Giberti G. (1996). Thermal modeling of volcanic areas, Degree thesis, Università Federico II Napoli.

Mercogliano P., Giberti G. (2000). Thermal modeling of phlegrean Fields volcanic area, Degree thesis, Università Federico II Napoli.

Vanorio T., Prasad M., Nur A. (2002). Petrophysical properties of volcanic samples: a contribution to studying ground deformation in Campi Flegrei volcanic area, Italy, poster presented at the XXVII General Assembly, EGS.

Vanorio T. (2003). Physical properties of volcanic rocks from the Campanian Plain. *TOMOVES: The Internal Structure of Mt. Vesuvius: A Seismic Tomography Investigation.* Edited by P. Capuano et al., Liguori Editore, 553-580.

Vanorio T., Virieux J., Capuano P., Russo G. (2003). New inferences on the Campi Flegrei Caldera structure from microearthquakes P and S delay time tomography, presented at 2003 Fall Meeting, AGU.

Vanorio T., Virieux J., Capuano P., Russo G. (2005). Three-dimensional seismic tomography from P wave and S wave microearthquake travel times and rock physics characterization of the Campi Flegrei Caldera, *J. Geophys. Res.*, 110, B03201, doi:10.1029/2004JB003102.

Yven B. (2001). Minéralogie, microstructure et propriétés physiques des roches volcaniques des Champs Phlégréens (Italie), PhD thesis, IPGP.

Zollo A., Judenherc S., Auger E., D'Auria L., Virieux J., Capuano P., Chiarabba C., de Franco R., Makris J., Michelini A., Musacchio G. (2003). Evidence for the buried rim of Campi Flegrei caldera from 3D active seismic imaging. *Geophys. Res. Lett.*, 30(19), 2002, doi:10.1029/2003GL018173.

Mechanical properties of volcanic rocks and their relations to transport properties

M.L. Bernard[1,2], M. Zamora[1]

[1] *Dept. of Geomaterials, Institut de Physique du Globe, Paris, France*

[2] *Dept. of Physics, University of Naples, Italy*

Introduction

Presently, seismic methods are extensively used to image volcanic structures. But, the mechanical properties of a great variety of volcanic rocks still be poorly known. Moreover, the interest in developing interrelationships between petrophysical properties of rocks is well documented in the literature, at least for petroleum reservoir rocks. Established relationships between parameters, whether obtained by laboratory studies or from well logs, are effectively employed by oil companies in the interpretation of their geophysical well log data and show an important potential to extract more information from geophysical field measurements.
Consequently, it is necessary to study seismic properties of volcanic rocks (at different scale) and to establish if and how they are related to their other physical properties in order to make full use of seismic investigations or any other geophysical data. To this end, we present a laboratory study on dependences of mechanical properties (velocity and attenuation of P and S waves) on transport properties (thermal conductivity, air permeability and electrical formation factor) in a selection of volcanic rocks.

The samples

Two rock collections were used to lead this study:

Set 1: the first one is composed of 48 samples coming from Mount Pelée (Martinique, French West Indies), an explosive volcano mainly composed of andesitic pyroclastic materials. The sampling takes in account the different products usually find on this volcano (pumices, non-porous and porous blocks of "nuées ardentes" deposits, scoria, lava-dome, lava-flow, consolidated and unconsolidated ash, …) (Figure 1) and presents a large range of porosity (between 1 and 65%) (Bernard, 1999; Jouniaux et al., 2000).

Previous studies show that the chemical composition of Mount Pelée products remains relatively constant (Bourdier et al., 1985; Fichaut et al., 1989; Gourgaud et al., 1989; Vincent et al., 1989; Villemant et al., 1996): their bulk composition is generally acid andesitic (59-60% SiO_2). For more details about Mt Pelée products see, for example, Bourdier et al. (1989), Vincent et al. (1989) or Boudon (1993)[1].

Set 2: the second one is composed of 5 cores coming from the geothermal well "Trecase", a deep borehole drilled on the slopes of Vesuvius (Italy), and 9 samples collected in Somma-Vesuvius outcrops (Figure 2).

Trecase well reaches the Mesozoic carbonatic rocks at a depth of 1700 m b.s.l. The 3 shallower drilling-samples (T1: 727m ; T3: 730 m; and T5: 1223 m) come from the large Pleistocene volcano-sedimentary sequence; samples T1

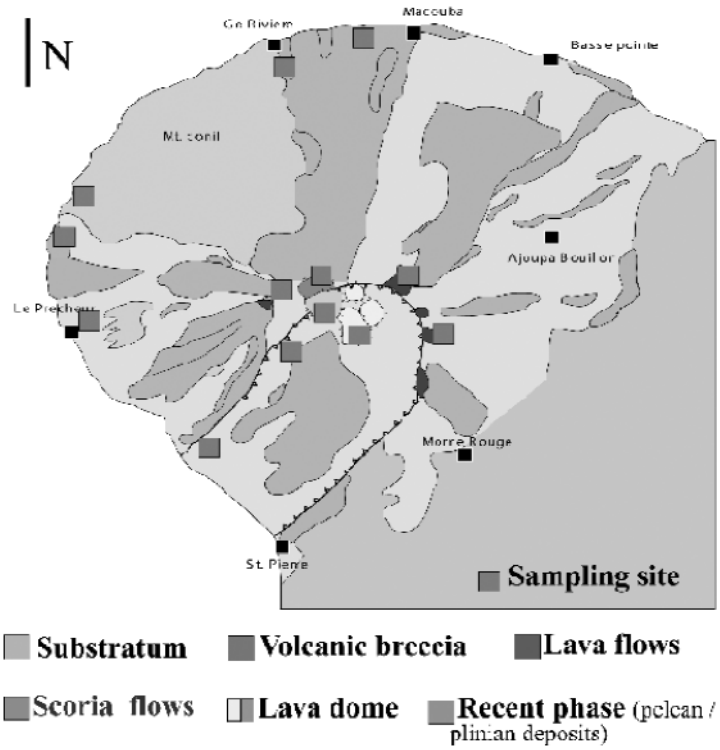

Fig. 1.

[1] Note that the mineralogical/chemical composition of these samples remaining relatively constant, any variation in their mechanical properties will be mainly linked to the differences in their pore space (volume and geometry).

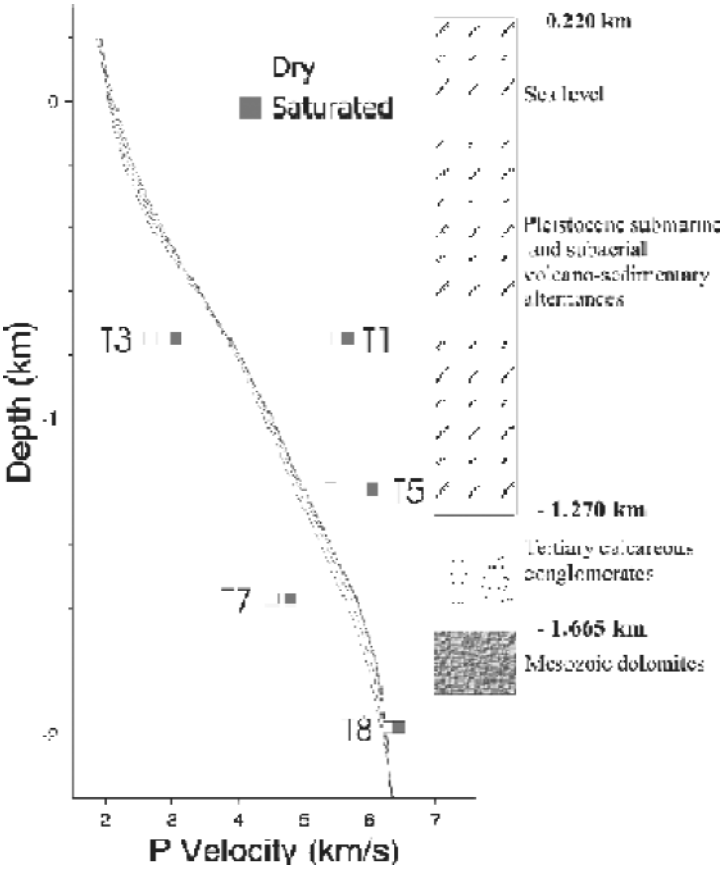

Fig. 2.

and T5 are phonolitic-tephritic lava and T3 is a tuffite. The 4rd sample (T7: 1557 m) is a Tertiary calcareous conglomerate non well-consolidated whereas the deeper sample (T8: 1968 m) is a dolomite. The subsurface samples are mainly lavas representative of the recent Vesuvius activity (from 1796 to 1944) but two samples come from the Somma dome.

The chemical composition of the Somma-Vesuvius volcanic rocks ranges largely, from phonolites to phonolitic tephrites and leucite-trachybasalts. For more details, see Santacroce (1987) and specially Principe et al. (1987)[2].

Two of the drilling samples studied are sedimentary rocks (T7, T8). This second set presents a larger range of mineralogical/chemical composition than the first one.

[2] Note that two of the drilling samples studied are sedimentary rocks (T7, T8). This second set presents a larger range of mineralogical/chemical composition than the first one.

The measurements

Porosity (volume of the connected pores) is measured using the triple weighing method.

Transport Properties

Three parameters characterizing transport properties have been study:

1. Air Permeability: using a falling head permeameter.
2. Electrical formation factor: by measuring electrical conductivity of core-sample saturated successively with 10 electrolytes. Formation factor is calculated by nonlinear inversion of the electrical conductivities measured, using the Revil and Glover (1998) model. Formation factor describes the effect of the geometry of the porous medium on the macroscopic fluid or electrical flow.
3. Thermal conductivity: on dry samples, using the divided bar technique (Beck, 1988).
   The measurements have been done on core-samples (23 or 25 mm diam.) extracted from the cubic samples used for velocity and attenuation measurements.

Mechanical Properties

1. Velocity of P and S waves were measured using an ultrasonic pulse-transmission method, at 1 MHz. The measurements were performed at atmospheric pressure and room temperature, on successively dry and full-water-saturated cubic samples (50 mm on edge generally). The uncertainty in measurements is less than 2% for dry samples and less than 4% for water saturated samples.
2. Attenuation coefficient of P and S waves (inversely proportional to quality factor Q) were measured using the spectral-ratio method (Toksoz et al., 1979). In this method, the amplitude spectrum of the first seismic pulse transmitted by the sample is compared with this one of a reference sample with very low attenuation (aluminium). The uncertainty in measurements is about 10% for $5<Q<50$. For each sample, the measurements were performed in their 3 directions (cubic samples) and the averaged values are reported in the figures.

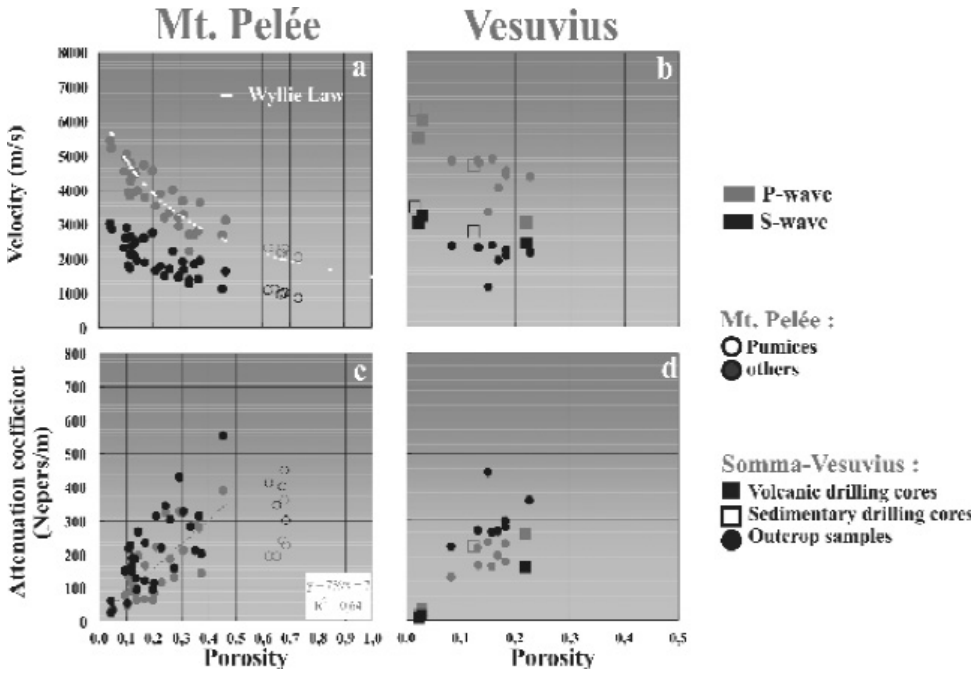

Fig. 3.

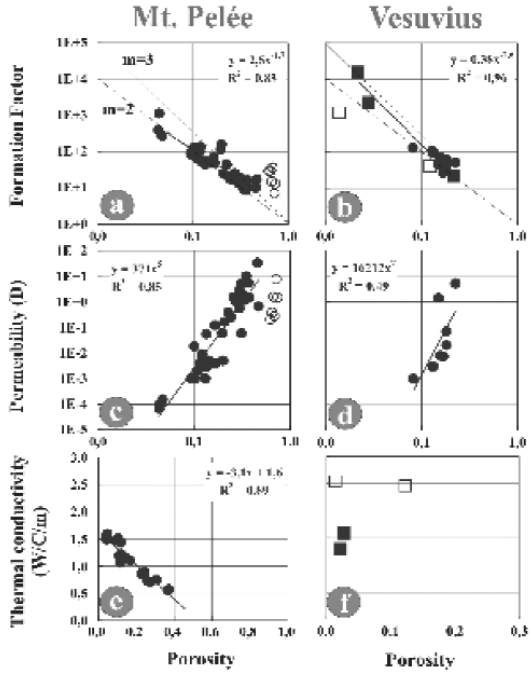

Box 1

Archie empirical equation (Archie, 1942) : $F = \phi^{-m}$
Carmen-Kozeny model (Carman, 1956) : $k = A \cdot \phi^{n}$

where ϕ is porosity, F, formation factor and k, permeability. A, n, and m depend on the geometry of porous network.

Fig. 4.

Velocity, Attenuation and Transport Properties

Thermal conductivity (Figure 5)

The Mt. Pelée dataset indicates clearly a linear increase of velocity with increasing thermal conductivity whereas a dependence of attenuation upon thermal conductivity is less evident. For Vesuvius samples, the scarcity of thermal measurements (TW-cores only) and lithology differences (volcanic and sedimentary rocks) do not allow any conclusion. Indeed, thermal conductivity of rocks is primarily controlled by variations in mineral content.
Anyway, a linear relation between thermal conductivity and velocity is in agreement with elementary Deby theory – as observed in silicates (Horai and Simmons, 1969) and in sandstones (Zamora et al., 1993) – and results from the common dependence of velocity and thermal properties on porosity (Figures 3 a, b and 4 e, f).
A linear correlation exists between thermal conductivity and velocity in volcanic samples presenting similar lithology: velocity investigations can be an indirect method to predict thermal behavior of volcanic area. A relationship between thermal and attenuation properties remains less evident.

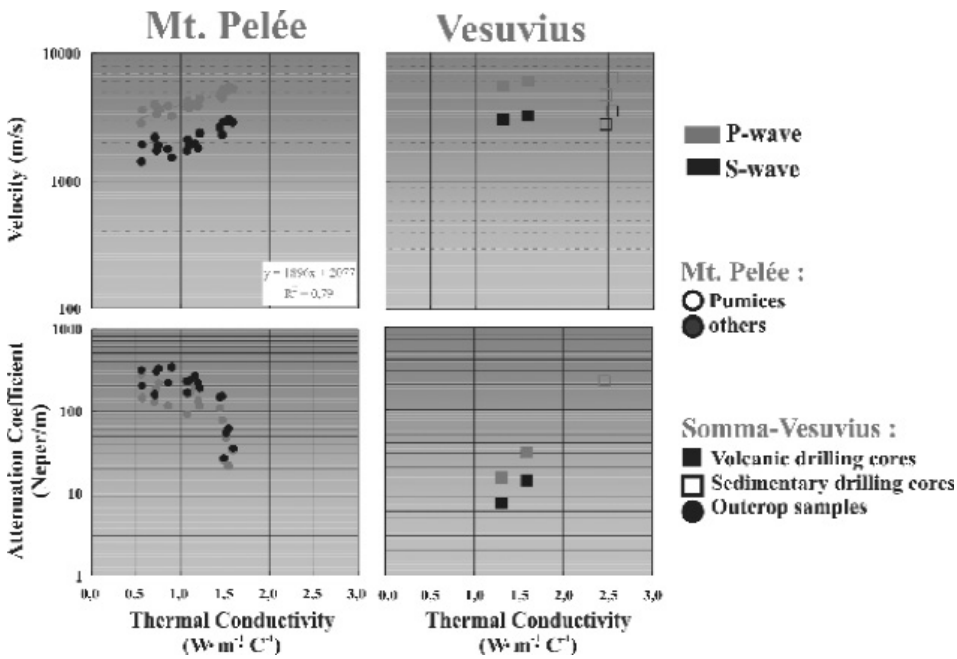

Fig. 5.

Air Permeability (Figure 6)

For both Mt. Pelée and Vesuvius dataset (only outcrop samples), velocity decreases weakly with increasing permeability. This can be explain by the dependence observed between velocity and porosity (Figure 3 a, b) and the upward trend of permeability with increasing porosity (Figure 4 c, d). But the effect of permeability on velocity is small compared to that of porosity.
In contrast, a strong dependence of attenuation upon permeability is observed (specially in the Mt. Pelée dataset where permeability covers 6 orders of magnitude). Such result is comprehensible since it is well established that the most likely mechanisms for energy loss in fluid-saturated rocks are based on fluid flows (solid/fluid relative displacements) and then related to the "local" or "global" permeability of rocks (Akbar et al., 1993; Dvorkin and Nur, 1993).
Attenuation rather than velocity is strongly correlated with permeability since both permeability and attenuation are intimately linked to the process of fluid motions in the rock.

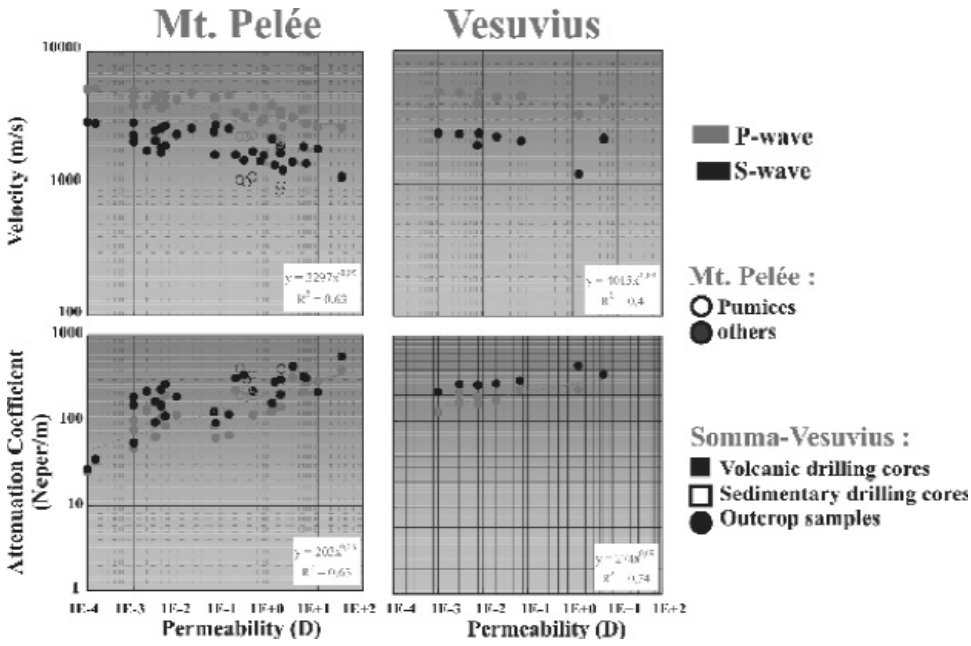

Fig. 6.

Formation factor (Figure 7)

For both Mt. Pelée and Vesuvius dataset, strong correlations are obtained between velocity, attenuation and formation factor. Velocity increases with increasing formation factor whereas attenuation decreases with increasing formation factor. High formation factors indicate well-consolidated media which are generally characterized by high velocity and low attenuation.
The dependency is slightly stronger for attenuation (and P-waves) (correlation coefficient $R > 0.8$). The effect of differences in lithology is negligible since both attenuation and formation factor are weakly dependent upon the mineral composition (in comparison to the effect of the pore space).
Such strong dependency between attenuation and formation factor reflects surely the fact that both formation factor and attenuation are controlled mainly by the geometry of conductive paths. According to Brown (1980), formation factor is closely link to the coupling coefficients taking part in Biot theory (high frequency domain).
The correlations observed are better for formation factor than for permeability. Permeability measurements reflect the "global" permeability of the sample. Moreover, formation factors are measured on water-saturated samples whereas permeabilities on dry samples.
Velocity and more specially attenuation are closely linked to formation factor.

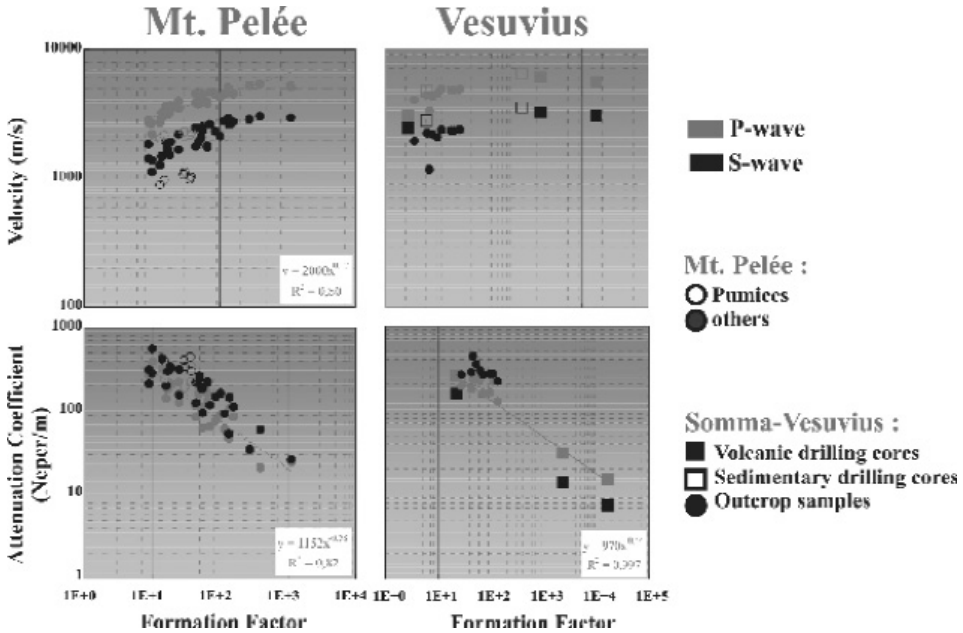

Fig. 7.

Conclusion

Volcanic rocks (presenting similar lithology) show significant relations among their seismic properties (velocity and attenuation) and transport properties (air permeability, electrical and thermal conductivity). Better correlations are generally obtained for P waves (on 100% water-saturated samples). Electrical properties are specially efficient in predicting seismic properties. Attenuation measurements can be studied as a significant indicator of rock permeability in volcanic rocks, at least at laboratory scale.

Remarks:

1) Unfortunately, standard theoretical models describing physical properties of rocks are largely based on observations and measurements in sedimentary rocks. They could not be well adapted to volcanic rocks given the fundamental differences in their pore structure (vesicular/granular). Then it is quite difficult to go past to empirical correlations. New models describing physical properties of volcanic rocks must be developed.
2) The problem of representativeness of laboratory measurements compared to in situ physical properties of rock formations remains a question under debate. But, these new laboratory measurements of physical properties of volcanic rocks, and specially those accomplished in the framework of TomoVes project on Vesuvius rocks, provide a base for a quantitative comparative study of rock mechanical properties at micro- and macro-scopic scales. For example, Figure 2 shows that P-wave velocities measured in laboratory on the borehole samples (Vesuvius dataset) are consistent with velocity profile inferred from the tomographic study (TomoVes).

References

Abkar N., Dvorkin J., Nur A. (1993). Relating P-wave attenuation to permeability. *Geophysics*, 58, 20-9.

Archie G. E. (1942). The electrical resistivity log as aid in determining some reservoir characteristics. *Trans. Americ. Inst. Mineral. Met.*, 146, 54-62.

Beck A. E. (1988). Methods of determining thermal conductivity and thermal diffusivity (Chap. 4), *Handbook of Terrestrial Heat-flow Density Determination*, Kluwer-Academic Publishers.

Bernard M. L. (1999). Étude expérimentale des propriétés physiques des roches pyroclastiques de la Montagne Pelée. Thèse de Doctorat de l'Université Paris VII-Denis Diderot, 315 p.

Boudon G. (1993). La Montagne Pelée, Martinique: évolution volcanologique, dans: "Pleins Feux sur les Volcans", *Mém. Soc. Géol. F ance, APBG Numéro Spécial*, 163, 231-8.

Bourdier J. L., Gourgaud A., Vincent P.M. (1985). Magma mixing in a main stage of formation of Montagne Pelée: The Saint-Vincent type scoria flow sequence (Martinique, F.W.I). *J. Volcanol. Geotherm. Res.*, 25, 309-32.

Bourdier J. L., Boudon G., Gourgaud A. (1989). Stratigraphy of the 1902 and 1929 nuée ardente deposits, Mount Pelée, Martinique. *J. Volcanol. Geotherm. Res.*, 38, 77-96.

Brown R. J. S. (1980). Connection between formation factor for electrical resistivity and fluidsolid coupling factor in Biot's equations for acoustic waves in fluid-filled porous media. *Geophysics*, 45, 1269-75.

Carman P. C. (1956). Flow of gases through porous media. *Academic Press Inc., Butterworth Sc. Publ., London*.

Dvorkin J., Nur A. (1993). Dynamic poroelasticity : A unified model with the squirt and the Biot mechanisms. *Geophysics*, 58, 524-33.

Fichaut M., Maury R. C., Traineau H., Westercamp D., Joron J. L., Gourgaud A., Coulon C. (1989). Magmatology of Mount Pelée (Martinique,F.W.I.). III: Fractional crystallization versus magma mixing. *J. Volcanol. Geotherm. Res*, Mount Pelée special Issue, 38,189-212.

Gourgaud A., Fichaut M., Joron J. L. (1989). Magmatology of Mt Pelée (Martinique, F.W.I.), I: Magma mixing and triggering of the 1902 and 1929 Pelean nuées ardentes. *J. Volcanol. Geotherm. Res*, Mount Pelée special Issue, 38(1-2),143-70.

Horaï K., Simmons G. (1969). An empirical relationship between thermal conductivity and DEBYE temperature for silicates. *J. Geophys. Res.*, 75(5), 978-82.

Jouniaux L., Bernard M. L., Zamora M., Pozzi J. P. (2000). Streaming potential in volcanic rocks from Mount Pelée. *J. Geophys. Res.*, 105, 8391-401.

Principe C., Rosi M., Santacroce R., Sbrana A. (1987). Explanatory notes to the Geological Map, in Somma-Vesuvius, edited by R. Santacroce, *CNR Quad. Ric. Sci.*, 1987, 114(8), 11-52.

Santacroce R. (ed.). Somma-Vesuvius. *CNR Quad. Ric. Sci.*, 114(8), 251 p.

Revil A., Glover P. W. J. (1998). Nature of surface electrical conductivity in natural sands, sandstones, and clays. *Geophys Res. Lett.*, 25, 691-4.

Toksöz M. N., Johnston D. H., Timur A. (1979). Attenuation of seismic waves in dry and saturated rocks: I Laboratory measurements. *Geophysics*, 44, 681-90.

Villemant B., Boudon G., Komorowski J. C. (1996). U-series disequilibrium in arc magmas induced by water magma interaction. *Earth Planet. Sci. Lett.*, 140, 259-67.

Vincent P. M., Bourdié J. L., Boudon G. (1989). The primitive volcano of Mount Pelée: its construction and partial destruction by flank collapse, edited by G. Boudon, A. Gourdon, Mount Pelée. *J. Volcanol. Geotherm. Res.*, 38, 1-15.

Wyllie M. R. J., Gregory A. R, Gardner L. W. (1956). Elastic wave of velocities in hetereogeneous and porous media. *Geophysics*, 21, 41-70.

Zamora M., Vo-Thanh D., Bienfait G. (1993). An empirical relationship between thermal conductivity and elastic wave velocities in sandstone. *Geophys. Res. Lett.*, 20, 1679-82.

Three dimensional Q_P and Q_S tomographic images of the Campi Flegrei caldera

S. de Lorenzo[1], A. Zollo[2], M. Trabace[1], T. Vanorio[3]

[1] *Dipartimento di Geologia e Geofisica, Università degli Studi di Bari, Italy*

[2] *Dipartimento di Scienze Fisiche, Università degli Studi di Napoli Federico II, Italy*

[3] *Géosciences Azur, CNRS, Université de Nice, Sophie Antinopolies, Valbonne, France*

Abstract: New tomographic 3D Q_p and Q_s images of the Campi Flegrei have been built by inverting the whole data set of the microearthquakes recorded during the 1984 seismic crisis. In both the inversions the uppermost crust (between 0 and 3 km of depth) was subdivided in 189 cells having a volume of 1*1*1 km^3. The residual reduction is statistically significant in both the cases, but the relative error on Q, as inferred by using the random deviates technique, is generally high. This indicates that a future effort has to be made to better constrain the obtained images by inserting an additional grid layer between 3 and 4 km of depth and/or using irregular grids to account for the higher spatial resolution in the central eastern part of the caldera. The inferred 3D Q_p images substantially confirm the result of a previous tomographic study in the area (de Lorenzo et al., 2001 a&b). The 3D Q_s maps show some interesting new features, such as a surface positive anomaly located slightly south of Monte Nuovo where the last eruption (1538 a.d) took place.

INTRODUCTION

Many tomographic attenuation studies have been carried out in volcanic areas (see e.g. Sanders and Nixon, 1995 and references therein). This is because the attenuation Q_p and Q_s parameters are extremely sensitive to variations in the temperature of the rocks and can assume extremely low values in presence of magma reservoir and/or fluid filled or partially saturated cracks. (for a thorough discussion see Sato and Sacks, 1989). Starting from these grounds, in a previous study (de Lorenzo et al., 2001 a&b) a three-dimensional Q_p image of the Campi Flegrei caldera has been obtained by an inversion technique which inverts the characteristic durations (rise time and pulse width) of first arrival P waveforms (Zollo & de Lorenzo, 2001) to obtain source and attenuation parameters. The analysis was based only on a small subset of the events recorded during the 2nd bradiseismic crisis (87 events). Since the entire dataset of the microearthquake occurred in the area is now available, in this article we describe the results of:

1) a new 3D tomographic reconstruction of Q_p by using the same technique but a more robust dataset of 272 events, selected from the entire dataset of the microearthquakes recorded during the second bradiseismic crisis.
2) the first 3D tomographic reconstruction of Q_s from the inversion of first arrival S wave spectra of 226 microearthquakes recorded during the same crisis.

Q_P INVERSION

Data and technique

We selected 2674 P waveforms, extracted form the entire dataset of the 1984 seismic crisis. On each first arrival P waveform we measured the rise time τ (the time interval between the onset of the wave and its first zero crossing time) and the pulse width ΔT (the time interval between the onset of the wave and its second zero crossing time) (Figure 1). Rise times and pulse widths have

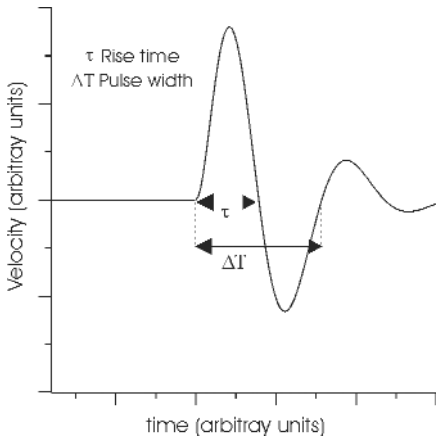

Fig. 1. Schematic picture of rise time and pulse width on a velocity seismogram.

been plotted as a function of the identification number of the event at each station (Figure 2). It is worth noting that, owing to the peculiar position of the microearthquakes, some stations recorded a high number of readable P waves, whereas only a limited number of data was available from the other stations. The procedure of data selection was carried out manually owing to the need of defining the quality of each datum. In particular six categories have been

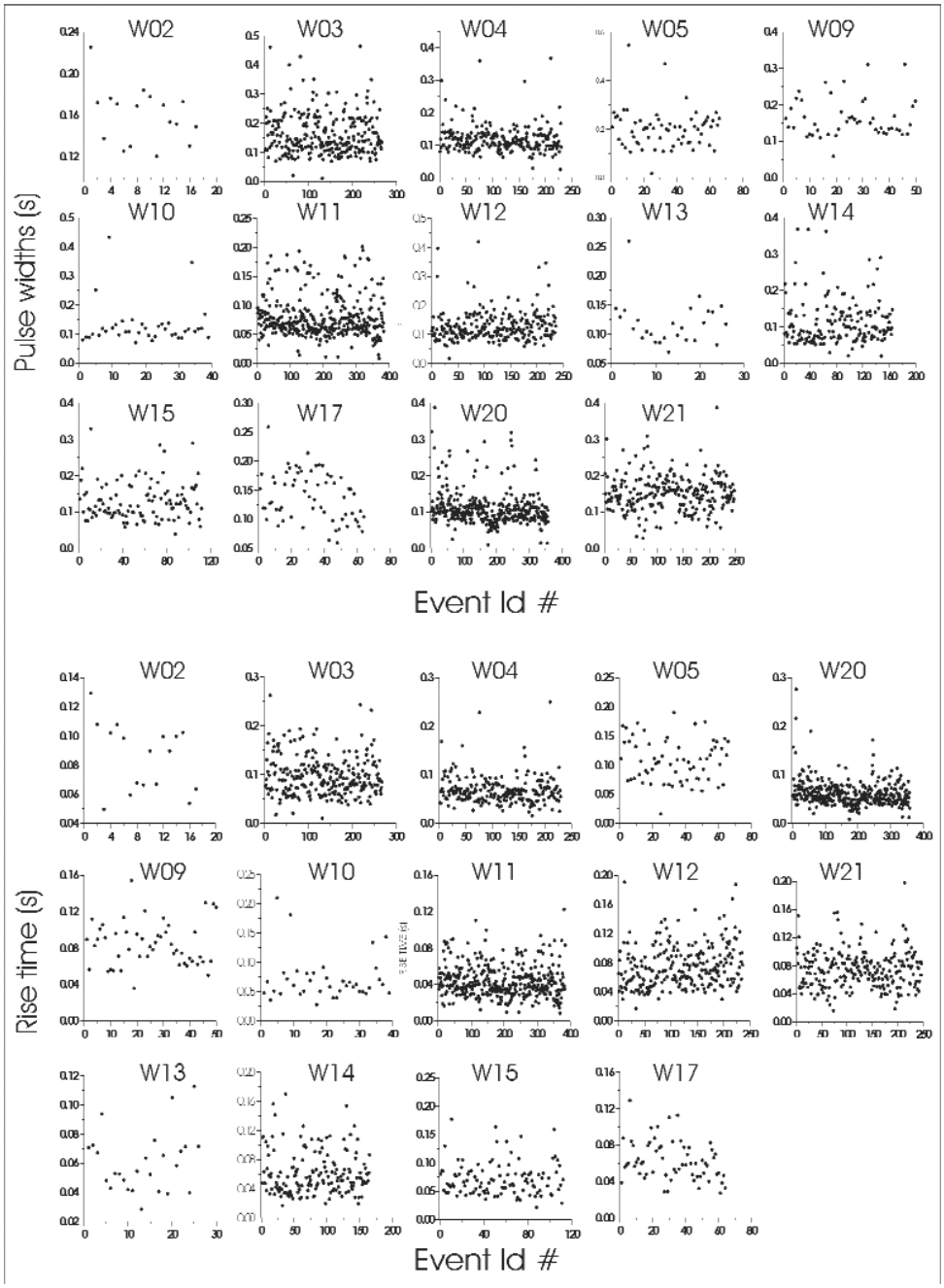

Fig. 2a. a) Pulse widths of the 226 events considered in this study. Data are ordered per station. b) Rise times of the 226 events considered in this study. Data are ordered per station.

defined, as shown in Figure 3. Only data which have a quality less or equal to 4 have been considered in the inversion. In particular for data having quality 3 and 4 we have considered only rise time data.

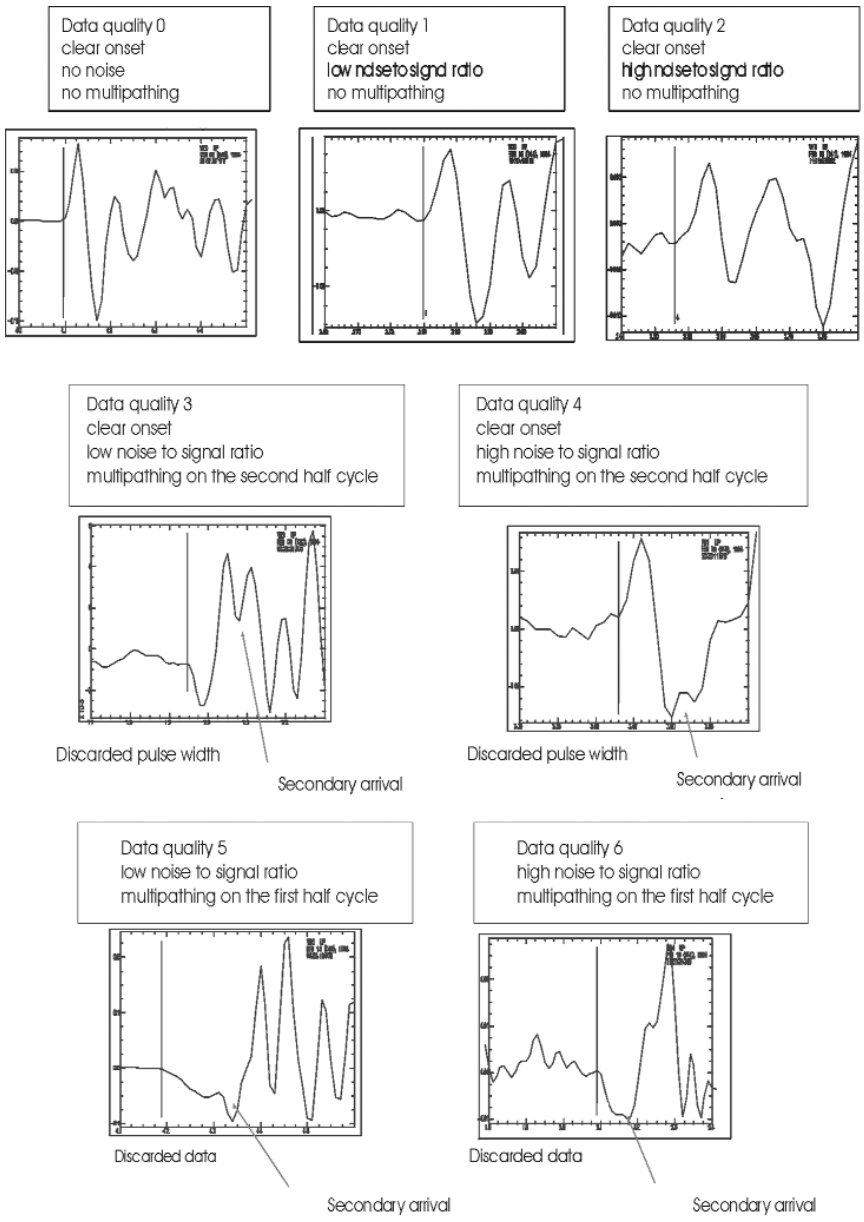

Fig. 3. Example of different data quality of recorded P waves.

The inversion technique is based on two numerically built non linear relationships relating rise times and pulse widths to source (fault radius L, dip δ and strike ϕ of the fault plane) and attenuation (Q_p) parameters. Owing to the non linear form of the inverse problem, the inversion strategy is based on the use of the Simplex Downhill method (Press et al., 1989) to retrieve the best fit model parameters through a robust exploration of the model parameters space (Zollo & de Lorenzo, 2001).

Results

At the first step of the inversion we determined the source and apparent Q_p parameters for each event. The apparent Q_p of an event represents the geometrical average of Q_p values along the ray path available for that event. The source radii (generally ranging from 0.1 and 0.2 km) inferred from the inversion are represented in Figure 4. As in the previous study (de Lorenzo et al.,

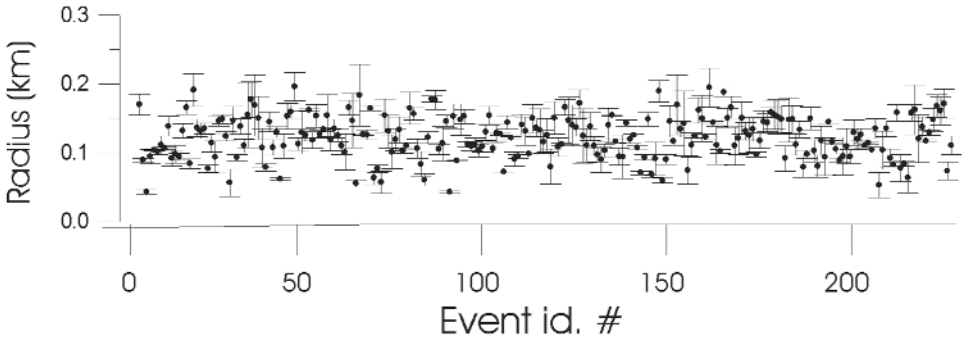

Fig. 4. Source radii obtained from the inversion of rise times and pulse widths data

2001a) the source radius is the parameter better constrained by the inversion, with an average error of about 15 m. Fault dip is better constrained than strike (average error on dip = 9°). The fault strike is very poorly constrained. This is caused by the limited azimuthal coverage and the low number of data for each studied event (for a thorough discussion see de Lorenzo & Zollo, 2003). In order to obtain the 3D Q_p image we subdivided the ray sampled volume in a 3D grid constituted by 189 cells of 1 x 1 x 1 km^3. The grid is represented by three layers having a thickness of 1 km. Each layer has been subdivided in 9 x 7 = 63 blocks. In order to obtain an "a priori" information on resolution we built the hit count maps (Figure 5a). These clearly indicate that the resolution

in the central-eastern part is higher than in the western part, owing to the relative position of the acquisition layout and the hypocenters of the dataset.
By using the iterative technique given in Zollo & de Lorenzo (2001), after three steps no further variance reduction was observed. A residual reduction of about 15% was obtained with respect to the homogenous case (average residual on rise time= 0.028 s; average residual on pulse width = 0.048 s). The inferred 3D Q_p image is shown in Figure 8a. By using the random deviates technique (Vasco and Johnson, 1998) an image of errors on the retrieved Q_p (error map) was obtained (Figure 8b).

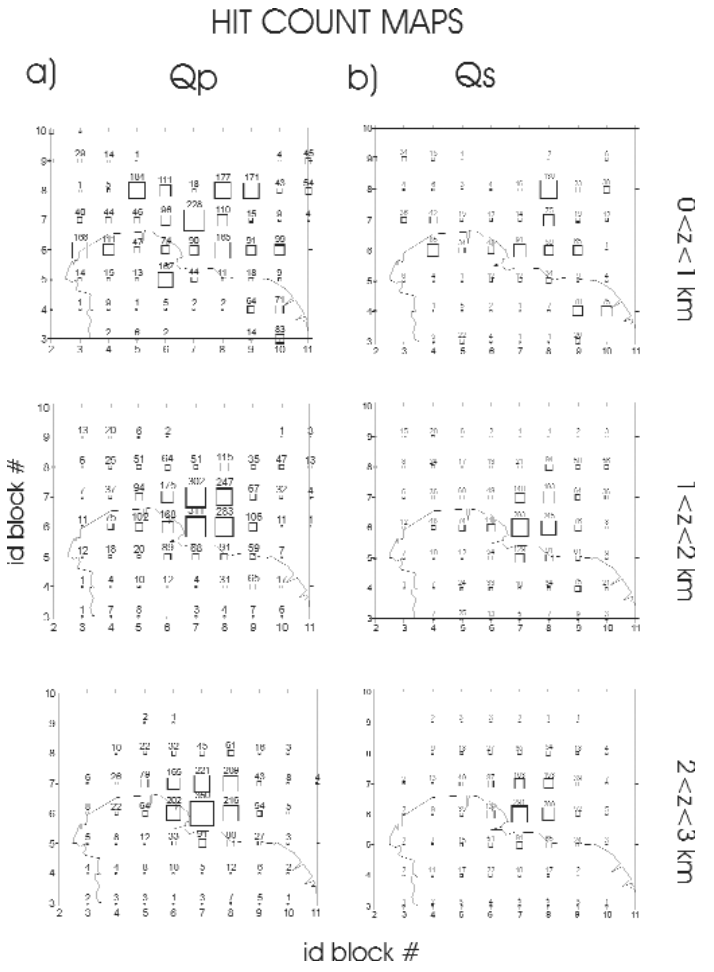

Fig. 5. a) Hit count maps representing the number of rays crossing each cell available for the Qp inversion; b) Hit count maps representing the number of rays crossing each cell available for the Qs inversion.

Q_S INVERSION

Data and technique

We selected 226 events of the dataset. For each of these events at least two S waves at two different stations have been clearly recorded. The data considered in the study are represented by the spectra of the S velocity waves, obtained by averaging the S wave spectra on the two horizontal components.
The technique used to obtain the 3D Q_s image of the Campi Flegrei caldera uses an iterative inversion technique based on three steps, as described by Scherbaum (1990).
Since S waves are contaminated by secondary arrivals, it is very difficult, if not impossible, to define the onset of the S wave and its duration by using an automated procedure. For this reason the data selection was based on the following criteria:

1) selection of a time window with a length of 0.5 s containing the S waveform;
2) application of a cosine taper with a fraction equal to 10%;
3) calculation of the fast Fourier transform;
4) smoothing of the spectra with an average moving window of 4 points (Press et al., 1989).

The modeling of spectra was based on the simplified assumption that the source time function has a simple shape with a single corner frequency in the spectrum and decaying as an inverse omega square function (Brune, 1970). Moreover we assumed that the attenuation term is represented by a constant Q attenuation operator. Under these assumptions the following expression for the theoretical velocity spectrum is obtained (Scherbaum, 1990):

$$\Omega^{teo} = 2\pi f \Omega_0 \frac{\exp(-\pi f t / Q)}{1 + \left(\frac{f}{f_c}\right)^2} \qquad (1)$$

In equation (1) f is the frequency, Ω_0 is the low frequency spectral level and f_c is the corner frequency in the spectrum.
As demonstrated by Scherbaum (1990), a tradeoff among Q and f_c is usually observed when inverting a single spectra. For this reason, at least two spectra for each event are required to search to better constrain the corner frequency of the event.
The iterative inversion procedure is based on three inversion steps (Figure 6). At the first step we retrieve, for each event, the best fitting values of Ω_0, Q and f_c. Clearly, the retrieved Q for each event is a geometrical average of the Q_s along the ray-paths considered for each source-receiver couple. The inferred Q_s may be then back-projected along each ray-path. This procedure is very

useful in that a first Q_s image may be obtained by geometrically averaging the intersecting Q values of each block in which the ray-sampled volume has been subdivided (Scherbaum, 1990). At the second step of the procedure, we fix Ω_0 and f_c at the values previously inferred and assume that the misfit among the observed and the theoretical spectra is caused by a poor knowledge in the Q structure. Under this assumption the observed spectrum will be given by:

$$\Omega^{obs} = 2\pi f \Omega_0 \frac{\exp\left(-\pi f t / \left(Q^1 + \Delta Q\right)\right)}{1 + \left(\frac{f}{f_c}\right)^2} \tag{2}$$

where Q^1 is the Q value estimated at the first inversion step. By comparing (1) and (2) we obtain:

$$\Omega^{obs} = \Omega^{teo} \exp\left(-\pi f t / \left(\Lambda Q\right)\right) \tag{3}$$

By taking the natural logarithm we have:

$$\frac{-\ln \Omega^{obs} + \ln \Omega^{teo}}{\pi f} = t / \left(\Delta Q\right) \tag{4}$$

By indicating with M_{blo} the number of blocks in which the ray-sampled volume has been subdivided, equation (4) is the starting point for the formulation of a linear inverse problem:

$$\sum_{i=1}^{M_{blo}} t_{i,j} m_i = d_j \tag{5}$$

where:

$$m_i = \frac{1}{\Delta Q_i} \tag{6}$$

and:

$$\frac{-\ln \Omega^{obs,j} + \ln \Omega^{teo}}{\pi f} = d_j \tag{7}$$

where the index j represents one of the spectra belonging to the dataset *(1≤j≤N)*. By indicating with:

$$\overline{G} = \begin{bmatrix} t_{1,1} & \cdots & \cdots & t_{1,M_{blo}} \\ \cdot & & & \\ \cdot & & & \\ t_{N,1} & \cdots & \cdots & t_{N,M_{blo}} \end{bmatrix} \tag{8}$$

the matrix constituted by the travel time of the rays in each of the blocks of the considered volume and with:

$$\bar{d} = [d_1 \ldots . d_N] \tag{9}$$

the data vector, the linear inverse problem can be written as:

$$\overline{G}\overline{m} = \bar{d} \tag{10}$$

where:

$$m = \begin{bmatrix} m_1 \\ \\ \\ m_{Mblo} \end{bmatrix} \tag{11}$$

Usually the solution to this problem in L_2 norm is given by (Menke, 1989):

$$m = \left(G^T G\right)^{-1}\left(G^T d\right) \tag{12}$$

In a first attempt we used this solution, but we obtained physically unreasonable results, caused by the singularity in the inverse matrix. In fact, even if one reduces the problem only to the search of the Q values in the blocks really traveled by at least one ray, the main problem with this approach is that it does not admit to impose the physical constraints (in our case $Q_s>0$) to the inferred solution. For this reason the solution to the equation (5) has been searched by adapting a perturbative technique to our problem, as described by Ho-Liu et al. (1989). This consists of searching the solution to equation (5) by an iterative approach. At the k+1 iteration the solution to the linear problem (5) is approximated by:

$$\begin{aligned} m_i^{k+1} &= m_i^k + \frac{\sum_j d_j^k G_{ji}}{\mu + \sum_j G_{ji}} \\ d_j^k &= d_j^0 - \sum_j G_{ji} m_j^k \end{aligned} \tag{13}$$

The equation (13) allows us to impose, step by step, the positivity constraint to our problem without any difficulty.
In equation (13) the parameter μ is used as a damping factor to reduce the effect of less constrained model parameters and to stabilize the solution (we assumed $\mu = 0.001$).
At the third step of the inversion we fix the Q structure to that previously inferred and search for new estimates of Ω_0 and f_c. The procedure is then stopped when no further variance reduction is observed (Figure 6).

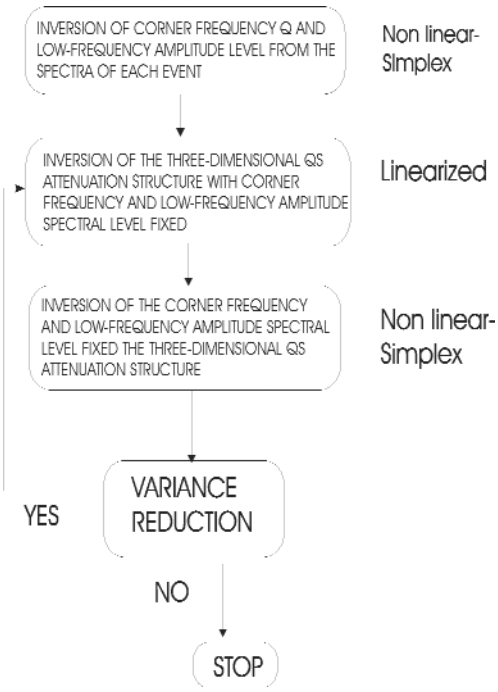

Fig. 6. Flowchart of the inversion scheme used for imaging the Qs structure.

Results

At the first inversion step we determined an apparent Q_s ranging from 10 to 250, with an average value of $Q_s = 83 \pm 60$. The high value of the standard deviation may be caused by a strong heterogeneity in the Q_s structure. An example of fitting is shown in Figure 7a. As expected, a residual trade-off among Q_s and f_c is inferred after the first inversion step (Figure 7b) (Scherbaum, 1990). This is another indication that the Q_s structure has not been constrained after the first inversion step. To quantify the misfit-level, at each inversion step we compute the residual distribution quantified by equation (7). The absolute average residual after the first step was equal to 8 s (Figure 7c).

In order to obtain a tomographic Q_s image we subdivided the ray sampled volume in a 3D grid constituted by 189 cells of 1 x 1 x 1 km^3. The grid is represented by three layers having a thickness of 1 km. Each layer has been subdivided in 9 x 7 = 63 blocks. In order to obtain an "a priori" information on resolution we built the hit count maps (Figure 5b). These clearly indicates that the resolution in the central-eastern part is higher than in the western part, owing to the position of the hypocenters of the dataset. By using the iterati-

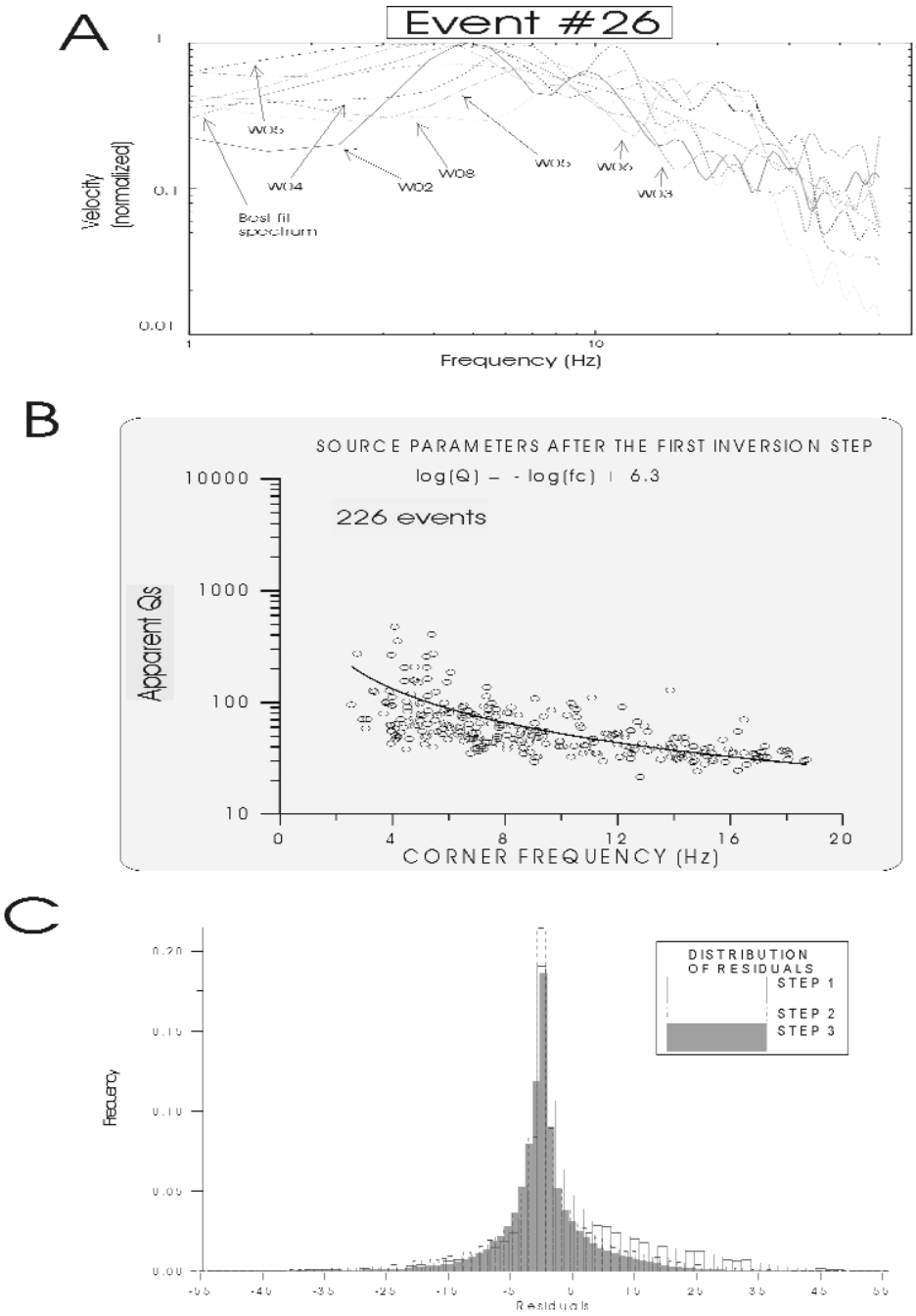

Fig. 7. a) Velocity spectra for the event #26 together with the best fit theoretical spectra at the first inversion step. b) Apparent Qs as a function of the corner frequency after the first inversion step. It is worth nothing the correlation among the two parameters. c) Distribution of residuals after three steps of the inversion technique.

ve technique described in section 1, after two inversion steps we obtained a residual reduction of ca 45% and the 3D Q_s map shown in Figure 4b. By using the random deviates technique (Vasco and Johnson, 1998) the error map was computed (Figure 8d).

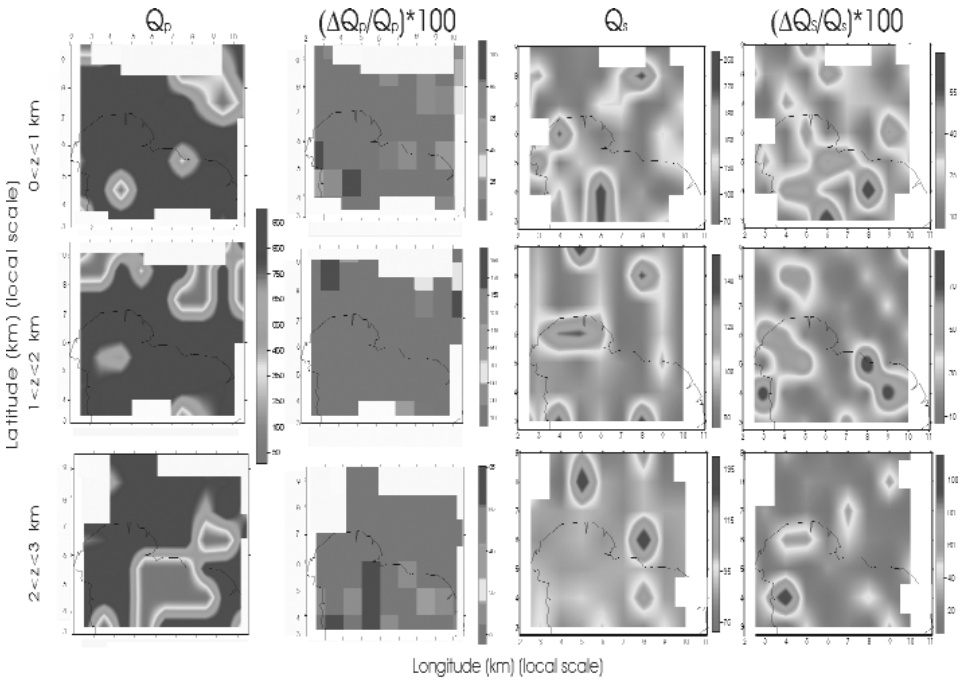

Fig. 8. a) 3D Qp map of the Campi Flegrei caldera; b) 3D Qp error map of the Campi Flegrei caldera; c) 3D Qs map of the Campi Flegrei caldera; d) 3D Qs error map of the Campi Flegrei caldera. You can see this figure in color on page 217.

Discussion and conclusion

It is worth noting the similarity of the 3D Q_p image obtained in this study and the previously inferred 3D Q_p image (de Lorenzo et al., 2001 a&b). This study confirms the presence of a low Q_p anomaly at high depth (between 2 and 3 km) located in the central-eastern part of the caldera (Agnano-Solfatara). Moreover, the previously inferred surface low Q_p anomaly (between 0 and 1 km of depth) is newly retrieved by the inversion, even if it seems to extend at greater depths (until to 2 km of depth). The most interesting and new result is the presence of an extended low Q_p anomaly at depth between 2 and 3 km offshore, south of Pozzuoli bay. This anomaly was not recovered in the previous study, for the lack of resolution in the southern part of the ray crossed volume. In this study, the increase in the number of available data allows for

a higher resolution in the deeper layer (between 2 and 3 km of depth). The retrieved anomaly lies now in a part of the caldera crossed by seismic rays. It is located near the same zone where the most important deformation effects occurred during the last bradiseismic crisis.
We are not able, at the present, to evaluate if this anomaly represents the effect of a magma body located at depth in the area. Since no magma body down to 6 km of depth has been inferred form SERAPIS active seismic tomography (Zollo et al., 2003; Judenherc & Zollo, 2004) we can hypothesize that this anomaly is due to the joint effect of an increase of temperature with depth (de Lorenzo et al., 2001) and the presence of hot pressurized fluids as hypothesized by Vanorio et al. (2005).
Let us consider now the Q_s maps. The first observation concerns the general low Q_s values in the area. This result indicates that the piroclastic products are probably characterized by high shear attenuation. However, since we don't selected a specific phase but a fixed window (1.28 s) we cannot be sure, as in the time duration methods, that we are analyzing the intrinsic Q_s. Therefore, probably, these low Q_s values may also reflect the contribution of additional scattering attenuation.
It is worth nothing that a positive Q_s anomaly is present at middle depth ($1<z<2$ km) in the central western part of the area, including Mt. Nuovo, where the last eruption occurred (in 1538). Therefore this anomaly may be correlated with the presence of a solidified volcanic dome surrounded by the above said more incoherent products. Another interesting result, that would require a further interpretation, is represented by the high Q_s anomaly located in the north-eastern part of the caldera and inferred both in the surface ($0<z<1$ km) and in the middle ($1<z<2$ km) layer. The average Q_s in the deeper layer ($2<z<3$ km) is lower than in the other two layers. This is probably caused by the joint effect of an increase of the temperature with depth (de Lorenzo et al., 2001 a) and the presence of hot pressurized fluids (de Lorenzo et al., 2001b, Vanorio et al., 2005), whereas the smoother image of Q_s in this layer may be an effect of the inversion and be caused by a lower ray crossing. The residual reduction is statistically significant in both the inversions, but the relative error on Q, as inferred by using the random deviates technique, is generally enough high. Therefore a future effort has to be made to better constrain the obtained images. Two attempts have to be realized in a future work. The first will consist in adding a grid layer between 3 and 4 km of depth to take advantage of the spatial distribution of the rays with the depth. The second will consist in the use of irregular grids to take advantage of the higher spatial resolution in the central eastern part of the caldera.

Acknowledgments

Many thanks to Edoardo Del Pezzo for very enlightening suggestions.

REFERENCES

Brune J. N. (1970). Tectonic stress and the spectra of seismic shear waves from earthquakes. *J. Geoph. Res.*, 75, 4997-5009.

de Lorenzo S., Zollo A. (2003). Size and Geometry of Microearthquake Seismic Ruptures from P and S Pulse Width Data. *Geoph. J. Int.*, 155, 422-42.

de Lorenzo S., Zollo A., Mongelli F. (2001). Source parameters and three-dimensional attenuation structure from the inversion of microearthquake pulse width data: Qp imaging and inferences on the thermal state of the Campi Flegrei caldera (southern Italy). *J. Geophys. Res.*, 106, 16265-86.

de Lorenzo S., Gasparini P., Mongelli F., Zollo A. (2001). Thermal state of the Campi Flegrei caldera inferred from seismic attenuation tomography. *Journal of Geodynamics*, 32(4), 467-87.

Ho-Liu, Kanamori H., Clayton R.W. (1988). Applications of attenuation tomography to Imperial valley and Coso-indian wells region, southern California . *J. Geophys. Res.*, 93 (B9), 10501-10520.

Judenherc S., Zollo A. (2004). The Bay of Naples (southern Italy): Constraints on the volcanic structures inferred from a dense seismic survey. *J. Geophys. Res.*, 109, B10312, doi:10.1029/2003JB002876.

Menke W. (1984). Geophysical data analysys: discrete inverse theory. *Academic, New York*.

Press W. H., Flannery B. P., Teukolsky S. A., Vetterling W. T. (1989). Numerical Recipes. *Cambridge University Press, New York*.

Sanders C. O., Nixon L. D. (1995). S wave attenuation structure in Long Valley caldera, California, from three component S-to-P amplitude ratio data. *J. Geophys. Res.*, 100, 12395-404.

Sato H., Sacks I. S. (1989). Anelasticity and thermal structure of the oceanic upper mantle: temperature calibration with heat flow data. *J. Geoph. Res.*, 94, 5705-15.

Scherbaum F. (1990). Combined inversion for the three-dimensional Q structure and source parameters using microearthquakes spectra. *J. Geophys. Res.*, 95 (B8), 12423-12428.

Vanorio T., Virieux J., Capuano P., Russo G. (2005). Three-dimensional seismic tomography from P wave and S wave microearthquake travel times and rock physics characterization of the Campi Flegrei Caldera. *J. Geophys. Res.*, 110, B03201, doi:10.1029/2004JB003102.

Vasco D. W., Johnson L. R. (1998). Whole earth structure estimated from seismic arrival times. *J. Geophys. Res.*, 103, 2633-72.

Zollo A., Judenherc S., Auger E., D'Auria L., Virieux J., Capuano P., Chiarabba C., de Franco R., Makris J., Michelini A., Musacchio G. (2003). Evidence for the buried rim of Campi Flegrei caldera from 3-d active seismic imaging. *Geophys. Res. Lett.*, 30(19), 2002, doi:10.1029/2003GL018173.

Zollo A., de Lorenzo S. (2001). Source parameters and three-dimensional attenuation structure from the inversion of microearthquake pulse width data: Method and synthetic tests. *J. Geophys. Res.*, 106, 16287-306.

Full-waveform modelling in 3D visco-elastic structures

P. Klinc, G. Seriani, E. Priolo

Istituto Nazionale di Oceanografia e Geofisica Sperimentale, Trieste, Italy

Introduction

The numerical simulation of seismic wave fields in three-dimensional large-scale complex models is computationally demanding and requires high performance parallel machines. The use of a Fourier pseudo-spectral method (FPSM) for solving 3D problems (Reshef et al., 1988) results in a coarser spatial sampling and improves the computational efficiency. The accuracy of the method is highly improved by evaluating the spatial derivatives on staggered grids, i.e. on separate grids which are shifted in space half a grid step along the direction of differentiation (Özdenvar and McMechan, 1996).
Since the precise description of the macroscopic physical behavior of the earth medium does not allow independent consideration of the elastic response and of the attenuation properties (Minster, 1980), the generalized standard linear solid model (Zener, 1948) has been adopted for the description of the phenomenology of the earth medium and it has been embedded in the time domain computational scheme, by using memory variables (Carcione et al., 1988). In order to minimize the wasted computational volume for the non-reflecting absorbing layers at the model boundaries, the Perfectly Matching Layers (PML) technique (Chew and Liu, 1996) has been adopted. The free surface condition at the top boundary of the model has been introduced using an original approach designed for the FPSM.

Method

The evolution of the seismic wavefield is computed in time domain, and is based on the equation of the momentum conservation, which is time stepped using the linearized form:

$$v_i(t+\Delta t) = v_i(t) + \frac{\Delta t}{\rho}\left(f_i^{ext.}(t+\frac{\Delta t}{2}) + \sum_{k=1,3} \sigma_{ik,k}(t+\frac{\Delta t}{2}) \right) \qquad (1)$$

where v is particle velocity, ρ is density, $f_{ext.}$ is the external force density, **σ** is the stress tensor and Δt is the time sampling interval. The stress tensor evolution is time stepped using:

$$\sigma_{ij}(t+\frac{\Delta t}{2}) = \sigma_{ij}(t-\frac{\Delta t}{2}) + \dot{\sigma}_{ij}(t) \tag{2}$$

where the time derivative of the stress at time t has to be obtained from the spatial derivatives of the particle velocity field v*(t)* by applying a stress-strain relation.

The Fourier pseudo-spectral method requires a discretization of the spatial domain (a rectangular box) in a structured grid. The accuracy of the wave propagation modeling is highly improved by evaluating the spatial derivatives on separate grids of points which are shifted in space half a grid step along the direction of differentiation. Denoting the spatial Fourier transform along the p-th direction with F_p, the used differential operator can be expressed as:

$$D_p^{\pm} = F_p^{-1}\left[k_p \exp\left(\pm i k_p \frac{\Delta x_p}{2} \right) F_p \right] \tag{3}$$

The operators D_p^+ and D_p^- are applied alternately in order to avoid the drifting of the computational domain, but producing the stagger instead. Different components of the particle velocity field and of the stress field are therefore evaluated on different grids of points that are shifted in space half a grid step, as shown in Figure 1. As a drawback of the adoption of the pres-

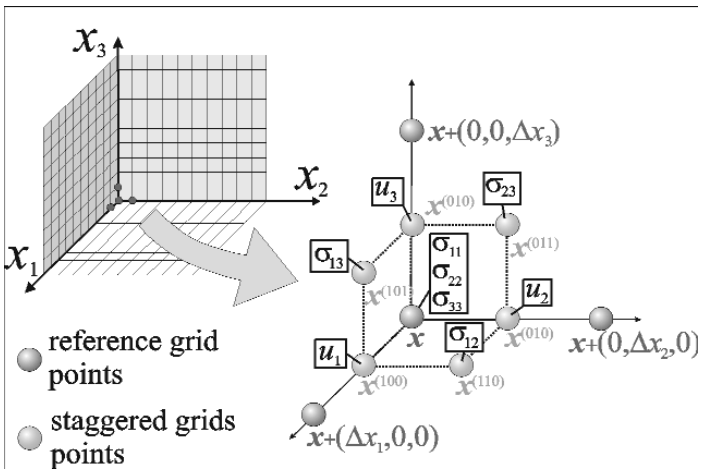

Fig. 1. The staggered grids scheme.

ent scheme, it is impossible the direct evaluation of the three components of the ground motion at the same point in space. In order to extract all the components of the ground motion at a receiver located in a reference grid node, we need to average the components evaluated in the nearest staggered grid points. The same applies for the perturbations of the stress field which are used to introduce the source.

MODELING THE ATTENUATION

The stress response of a visco-elastic medium is characterized by the fading memory of the past strain states. With this concept in mind it is easy to overcome the awkwardness of the stress-strain relation for an isotropic visco-elastic solid which is usually written as:

$$\sigma_{ij} = \delta_{ij}\dot{\psi}_{\lambda} * \theta + 2\dot{\psi}_{\mu} * \varepsilon_{ij} \tag{4}$$

where δ_{ij} is the Kronecker's delta, δ_{ij} is the strain tensor, $\theta = \varepsilon_{11}+\varepsilon_{22}+\varepsilon_{33}$ is the dilatation and ψ_{λ} and ψ_{μ} are independent relaxation functions playing the role of the Lamé constants, and * is the convolution operator. Introducing $\psi_{\pi} = \psi_{\lambda}+\psi_{\mu}$ as the P-wave relaxation function, we can rewrite eq. (4) as

$$\sigma_{ij} = \delta_{ij}\left(\dot{\psi}_{\pi} - 2\dot{\psi}_{\mu}\right) * \theta + 2\dot{\psi}_{\mu} * \varepsilon_{ij} \tag{5}$$

and we can describe the behavior of each of the P- and S- waves using the generalized standard linear (SLS) model:

$$\begin{cases} \psi_{\pi}(t) = \left(\lambda + 2\mu\right)\left(1 - \frac{1}{L}\sum_{l} a_{l}^{P} \exp\left(\frac{-t}{\tau_{\sigma l}^{P}}\right)\right) H(t) \\ \psi_{\mu}(t) = \mu\left(1 - \frac{1}{L}\sum_{l} a_{l}^{S} \exp\left(\frac{-t}{\tau_{\sigma l}^{S}}\right)\right) H(t) \end{cases} \tag{6}$$

where *H(t)* is the Heavyside function, λ and μ are the "static" values of the Lamé constants, and a_l^S, $\tau^S\sigma_l$, a_l^S and $\tau^S\sigma_l$ are parameters to be evaluated separately from the desired frequency independent Q^P and Q^S using procedures which are not described here. The form of eq. (6) allows to rewrite eq. (5) as:

$$\sigma_{ij} = \delta_{ij}\left(\pi_0 - 2\mu_0\right)\theta + 2\mu_0\varepsilon_{ij} + \frac{1}{L}\sum_{l} R^{(l)}{}_{ij} \tag{7}$$

where $\pi_0 = \psi_{\pi}(0)$, $\mu_0 = \psi_{\mu}(0)$ and where $R^{(l)}{}_{ij}$ are the memory variables, which describes the stress contribution due to the past strain states. Thanks to the

form of eq. (6) it is possible to implement a linearized time stepping scheme for the memory variables:

$$R_{ij}^{(l)}(t+\Delta t)=\left(1-\frac{\Delta t}{\tau_{\sigma l}}\right)R_{ij}^{(l)}(t)+\Delta t\left(\delta_{ij}\left(\pi_l-2\mu_l\right)\theta+2\mu_0\varepsilon_{ij}\right) \tag{8}$$

with $\pi_l = (\lambda+2\mu)d_l^{\mathrm{P}}/\tau_{\sigma l}$ and $\mu_l = \mu a_l^{\mathrm{S}}/\tau_{\sigma l}$, having chosen $\tau_{\sigma l} = \tau_{\sigma l}^{\mathrm{P}} = \tau_{\sigma l}^{\mathrm{S}}$. The described approach allows to model correctly the seismic waves propagation in media where the intrinsic attenuation of the compression waves is different from that of the shear waves, as demonstrated in Figure 2.

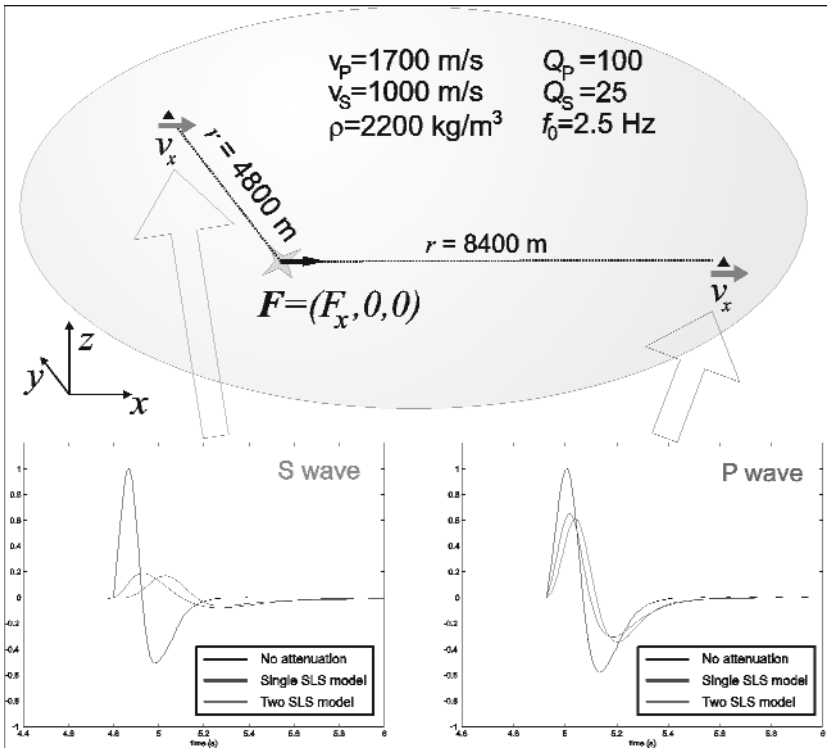

Fig. 2. Effectiveness of the attenuation mechanism.

Implementation of the parallel algorithm

The stress-velocity time advancing scheme is suitable for a parallel implementation. The huge amount of data to be passed to the Fourier differential operators calls for a parallelization of the procedure following the data decomposition approach. The computational domain is evenly split into horizontal slices which are assigned to single processors. Each processor perform all the computations on the sub-domain that has been allocated to it except for the differentiation in the vertical direction. In order to compute the derivative in the vertical direction the computational domain is *pro tempore* re-organized in vertical slices (Figure 3). This step can be easily achieved in a Message Passing Interface (MPI) framework using the apposite MPI subroutine. Since the vertical derivatives have to be computed twice in a time step, a noticeable amount of communication between processors is required. This means that the speed-up given by the parallelization may not grow above the value it reaches when the effective computational time becomes comparable to the communication latency. Tuning tests are therefore required to optimize the efficiency of the scheme and exploit at the best the computing power of the available multi-processor device. For the structural model hypothized beneath the Campi Flegrei area with grid size 240 x 280 x 160 plus absorbing boundaries (Lovisa et al., 2004), the maximum speed-up was reached by splitting the domain among 32 processors, on an IBM-SP4 parallel supercomputer. In that case, one cycle of the stress-velocity loop required less than 4 seconds of wall-clock time.

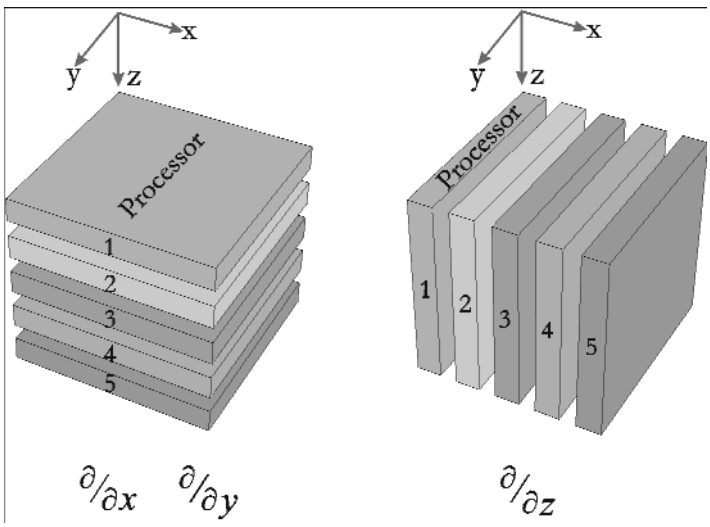

Fig. 3. Domain decomposition approach.

MODEL BOUNDARIES

Perfectly matching absorbing layers

In order to prevent the wrap-around effect – in the Fourier PSM the wavefield propagates through the model borders periodically and comes back in the computational domain from the opposite side –, the model must be surrounded by suitable absorbing layers. In 3D problems, the increase of the overall dimensions of the computational domain due to the application of classical sponge layers (Cerjan et al., 1985) may be meaningful. On the other hand, the implementation of perfectly matched-layer – PML absorbing belts (Chew and Liu, 1996; Collino and Tsogka, 2001; Festa and Nielsen, 2003), reduces the wasted computational domain to about 20% of that of the classical method. The basic principle of the PML method is to surround the model with an unphysical damping medium which produces no reflections at the interface with the model. This can be achieved by forcing an anisotropic attenuation in the absorbing layer, and setting it maximum for the waves entering perpendicularly the interface. See referenced works for theoretical details. In practice the wavefield in the absorbing layer is split in two parts: one propagating along the direction normal to the interface between the absorbing layer and the interior of the model, and the second one propagating in directions which are parallel to that interface. The PML method consists in an explicit damping of the normal part alone, whereas the other part evolves following the scheme adopted within the model.

Free surface

Often, geo-models in which wave propagation is simulated are bounded by a free surface on their top (x_3=0). The x_3-derivatives of both the displacement and stress field at free surface are to be evaluated as left derivatives (for x_3 increasing with depth). In order to simulate the value of the left x_3 derivative at x_3=0 using the Fourier global differential operator, we need to define virtual particle velocity and stress fields above the free surface, i.e. in an additional layer below the bottom absorbing strip (consider the periodicity of the computational domain). The free surface condition:

$$\begin{cases} \sigma_{q3} = 0 \\ R_{q3} = 0 \end{cases} \qquad \text{for } x_3=0 \qquad (9)$$

can be efficiently simulated by some virtual σ_{q3} fields which are anti-symmetric around the free surface plane, according to the so-called image method

(Levander, 1988). On the other hand, the virtual particle velocity field in the region above the free surface must verify the condition:

$$\begin{cases} v_{1,3} = -v_{3,1} \\ v_{2,3} = -v_{3,2} \\ v_{3,3} = -\frac{\pi_0 - 2\mu_0}{\pi_0}\left(v_{2,2} + v_{3,3}\right) \end{cases} \qquad \text{for } x_3=0 \qquad (10)$$

which is somewhat harder to impose. In the presented procedure the virtual particle velocity field above the free surface is described with a third degree polynomial with the four coefficients determined by imposing the continuity with the particle velocity field below the free surface and imposing the value of its derivative at x_3=0 using equation (10).
The effectiveness of both the free surface and PML absorbing boundaries is illustrated in Figure 4. The creation of the Rayleigh wave and the vanishing of the wave-field at the external boundaries of the computational domain as well as that of the wave-field wrapped around are clearly seen.

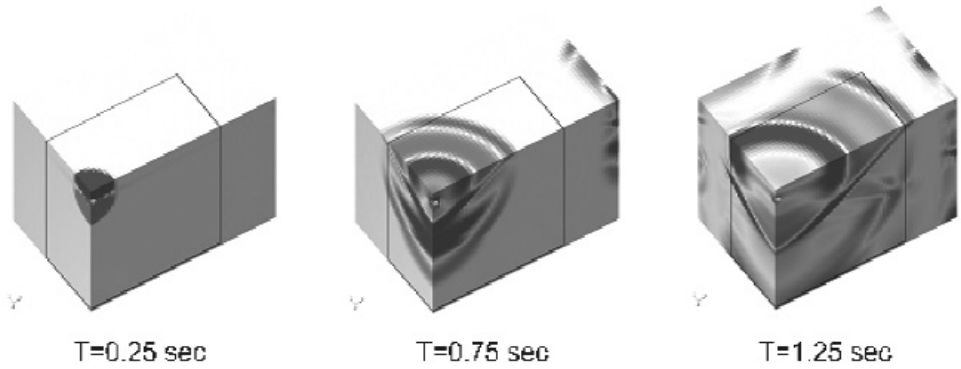

Fig. 4. Effectiveness of the absorbing layers and free surface conditions.
You can see this figure in color on page 208.

Implementation of the reciprocity principle

In grid methods, such as the pseudo-spectral method, the wavefield is computed at all grid nodes and, if required, stored in a subset of nodes. In principle, each source needs one run. Thus the creation of a set of synthetics for a large number of sources requires running a large number of simulations.

However, the wavefield is often is "recorded" only at a small number of receivers. This is the case, for instance, of several earthquakes recorded by permanent stations during a long period. In that case the application of the reciprocity principle (Eisner and Clayton, 2001), provides a useful way to reduce the number of simulations dramatically.
Formally, given two arbitrary points x and x' located anywhere in the medium volume or on its boundary, their reciprocal relation is written as:

$$G_{ij}(\boldsymbol{x},\boldsymbol{x}',t) = G_{ji}(\boldsymbol{x}',\boldsymbol{x},t) \tag{11}$$

where $G_{ij}(x_a, x_b, t)$ is the *j*-th component of the displacement response at point x_a to the application of an unit force in the *i*-th direction at point x_b.
Since seismic sources in volcanic areas exhibits mechanism with varying orientation, the method has been used for the computations of the Green's functions spatial derivatives for the given set of hypocenter-receiver pairs, while the effective waveforms need to be extracted using the relation (Burridge and Knopoff, 1964):

$$u_q(x_R) = G_{pq,r}(x_R, x)\Big|_{x=x_S} M_{pr}(x_S) \tag{12}$$

where $G_{pq,r}$ is the Green's function gradient, M_{pr} is the moment tensor representation of the source, and u_q is the wavefield at receiver R. x_S and x_R are the coordinates of the source and receiver, respectively. The spatial differentiation of the Green's function is intended at source location x_S.
An efficient approach for the calculation of the waveforms for all possible source mechanisms consists in the evaluation of a data-set of Green's functions spatial derivatives at the location of the formal sources (actual receivers) for a number of elementary mechanisms (e.g.: three directional forces aligned with the Cartesian axes), and then to recompute the wavefield for the appropriate source mechanism during post-processing. The spatial derivatives are computed runtime by the Fourier pseudospectral method at no additional cost.
The validity of the reciprocity principle applied to the Fourier staggered pseudo-spectral method is demonstrated in Figure 5, which shows the comparison among the components of the Green's function computed by the Fourier pseudo-spectral method in the two reciprocal cases, i.e. for a source in point A and a receiver in point B, and for a source in point B and a receiver in point A. The structural model used for the wavefield propagation represents the structure beneath the Campi Flegrei area and has been described in Section 1.5. In particular, receivers A and B are located at the surface of incoherent pyroclastics material, and within the layer of solidified magma at depth of 2.5 km, respectively. The waveform fitting is excellent.

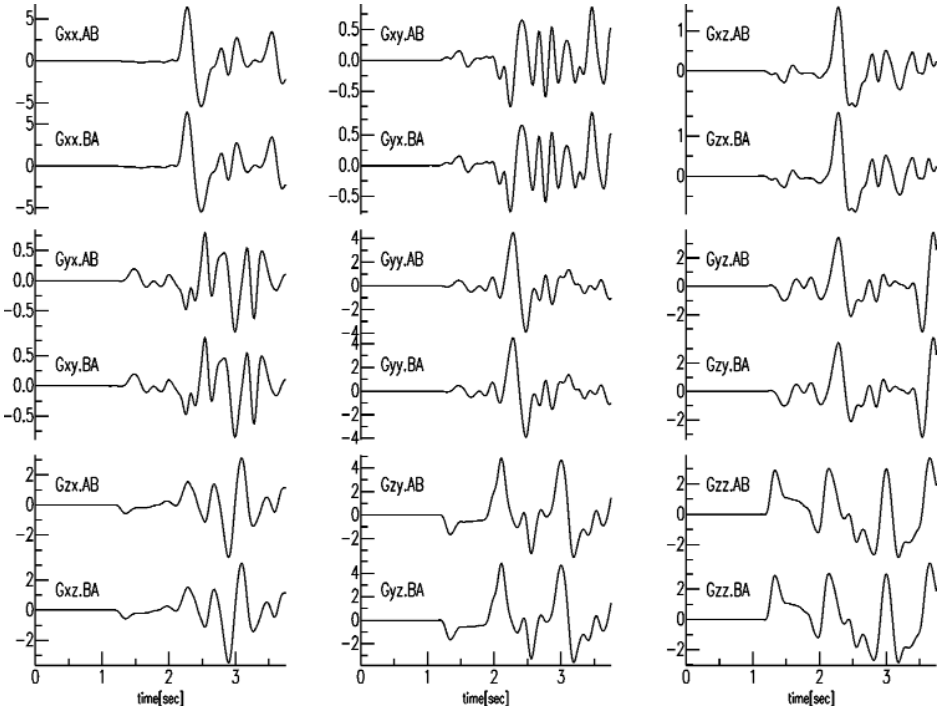

Fig. 5. Validation of the reciprocity principle. Seismograms computed using the Fourier staggered pseudospectral method by exchanging the source-receiver position. See text for details.

Conclusions

A procedure for the modelling of seismic waveforms in complex 3D media with visco-elastic properties has been developed. It is based on the stress-velocity time marching scheme and the space derivatives are performed using the Fourier differential operators on staggered grids. The effects of viscosity are taken in account by means of the standard linear solid model. The implementation of the procedure in a parallel algorithm is required in order to perform the computations in reasonable wall-clock times. The simulations for a realistic case are performed with a rate of about 1000 cycles of the marching scheme per wall-clock hour, using 32 processors of an IBM-SP4 computer. The modelling of several events in the same receiver location may be performed in a single run thanks to the exploitation of the reciprocity principle.

REFERENCES

Carcione J. M., Kosloff D., Kosloff R. (1988). Wave propagation in a linear viscoelastic medium. *Geophys. J. Int.*, 95, 597-611.

Cerjan C., Kosloff D., Kosloff R., Reshef M. (1985). A nonreflecting boundary condition for discrete acoustic and elastic wave equations. *Geophysics*, 50, 705-8.

Chew W., Liu Q. H. (1996). Perfectly matched layer for the elastodynamics: a new absorbing boundary condition. *J. Comp. Acoust.*, 4, 341-59.

Collino F., Tsogka C. (2001). Application of the perfectly matched absorbing layer model to the linear elastodynamic problem in anisotropic heterogeneous media. *Geophysics*, 1, 294-307.

Festa G., Nielsen S. (2003). PML Absorbing Boundaries. *Bull. Seismol. Soc. Am.*, 93, 891-903.

Kennet B. L. N., Furumura T. (2002). The influence of 3-D Structure on the Propagation of Seismic Waves Away from Earthquakes. *Pure Appl. Geophys.*, 159, 2113-31.

Levander A. R. (1988). Fourth-order finite-difference P-SV seismograms. *Geophysics*, 53, 1425-36.

Lovisa L. et al. (2004). The Campi Flegrei blind test. *Gruppo Nazionale di Vulcanologia, Open File Report*: OFR_ISMACF_A5.1.

Minster J. B. (1980). Wave propagation in viscoelastic media, in *Physics of the Earth's Interior*, edited by A.M. Dziewonski, E. Boschi, Proceedings of the International School of Physics "Enrico Fermi", Course 78, 152-212.

Olsen K. B., Archuleta R. J. (1996). Three dimensional Simulation of Earthquake on the Los Angeles fault System. *Bull. Seismol. Soc. Am.*, 86, 575-96.

Özdenvar T., McMechan G. A. (1996). Causes and reduction of numerical artifacts in pseudo-spectral wavefield extrapolation. *Geophys. J. Int.*, 126, 819-28.

Reshef M., Kosloff D., Edwards M., Hsiung C. (1988). Three-dimensional modeling by the Fourier method. *Geophysics*, 53, 1184-93.

Zener C. (1948). *Elasticity and Anelasticity of Metals*. Univ. of Chicago Press, Chicago (USA).

Full-wave simulation of a Serapis seismic section

P. Klinc, E. Priolo

Istituto Nazionale di Oceanografia e Geofisica Sperimentale, Trieste, Italy

Introduction

The staggered, 3D Fourier pseudo-spectral method developed within this project has been applied to the computation of one of the seismic profiles acquired during the SERAPIS experiment. In particular, a 2D common receiver seismic section corresponding to receiver OBS48 has been reproduced in the low frequency band (f_{max} = 6 Hz). The use of a 3D method for simulating the full-wave propagation through a 2D model – more properly, it is a 2.5 D model – is motivated by the fact that this is an easy way to take into account the attenuation effects due to geometrical (spherical) spreading exactly. At this stage, this work demonstrates mainly the effectiveness of the numerical method developed as a tool for interpreting active seismic data. Therefore, the results must still be considered demonstrative.

Setting of the numerical experiment

The presence of a buried caldera rim beneath the Campi Flegrei bay area has been suggested by a tomographic study based on the SERAPIS seismic experiment dataset (Zollo et al, 2003). In order to assess the effective signature of the interpreted structural features on the recorded seismic profiles, we perform a numerical simulation of a common receiver seismic section. The specific profile crosses the Pozzuoli bay with NW-SE orientation from point (40.842N, 14.051E) to point (40.568N, 14.321E), and goes through the location of receiver OBS48, at coordinates (40.712N, 14.179E).
The 2D structural model across the profile is composed by five structural units (Table 1). Within the units the velocity features with a vertical gradient of increase with the depth. At the surface a thin water layer is present (Figure 1), which is simulated by an anelastic layer with a strong attenuation for the shear waves.
Since the wave propagation is solved through a 3D method, the model is "extruded" in the transversal direction maintaining the same structure. The "vector" model is then discretized into a structured grid with constant spatial

Tab. 1. Physical parameters of the 2D model

Layer	V_{P0} (m/s)	dV/dz (s^{-1})	V_P/V_S	z_0(m)	ρ(g/cm^3)
Sea	1500	0	2.20	0	1.0
1	2000	0.60	2.20	800	2.0
2	2700	0.32	1.80	750	2.2
3	3500	0.15	1.75	1000	2.5
4	4500	0.15	1.75	3000	2.5
5	6000	0.10	1.72	0	2.6

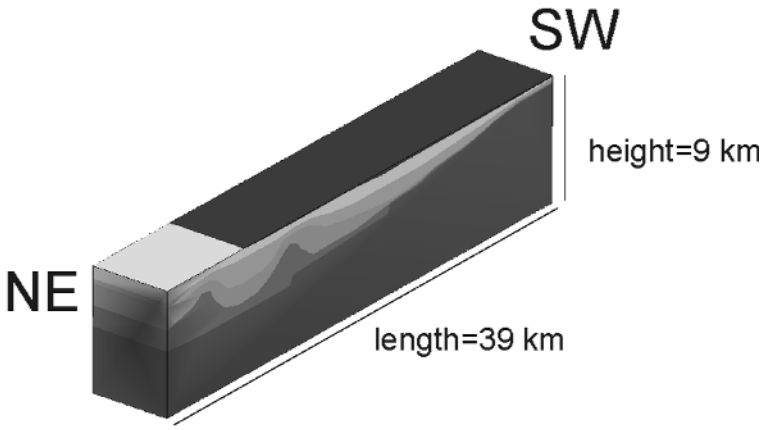

Fig. 1. The "2.5D" structural model used in the seismic numerical experiment.

step Δx=50m, which allows accurate seismogram computation up to the maximum frequency f_{max} = 6 Hz. Here, the high accuracy of the staggered, Fourier pseudo-spectral method have been exploited, for which a minimum number of two grid points per wavelength (G=2) can be used for accurate wave propagation (Klinc et al., 2004). A total number of 360 sources are defined at the model surface in the longitudinal direction (i.e. model length) from km 6 to km 24. From the practical point of view the sources correspond to contiguous grid points. The receiver simulates OBS48 station; it is located at coordinate 18 km and depth of approximately 250 m. A reciprocal source-receiver configuration has been used to perform the whole set of simulations, exploiting the reciprocity principle (Klinc et al., 2004). The computational time required to compute the seismic section has been 30 hours on 16 processors of an IBM-SP4 computer.

RESULTS

The results consist of 360 two component (vertical and horizontal-radial) time series. The Figure 2 shows the common receiver seismic sections for the vertical and horizontal-radial components, respectively, plotted with a gain proportional to the source-receiver distance. The third component, corresponding to SH waves is not considered, since the source is a pure explosion. In order to correlate better the simulated section to the real one, the data have been cut-off out of a 4 s-wide time window with slope (i.e. wave velocity) of 6 km/s, which corresponds to the speed wave refracted by the limestone basement.

The synthetic section reproduces several features present in the real section (Zollo et al., 2003), however it also contains a number of artifacts that must be removed in the future. In particular in the vertical component, the high-velocity head waves refracted by the limestone basement can be clearly recognized. Among them, the early arrival of the direct P-waves, diffracted by the caldera rim, might also be recognized at large offset, although a more thorough interpretation of the section still has to be performed. On the other hand, the low velocity signature of the ground roll dominates the wave-field at small offset. This wave is not present in the real section and is due to the

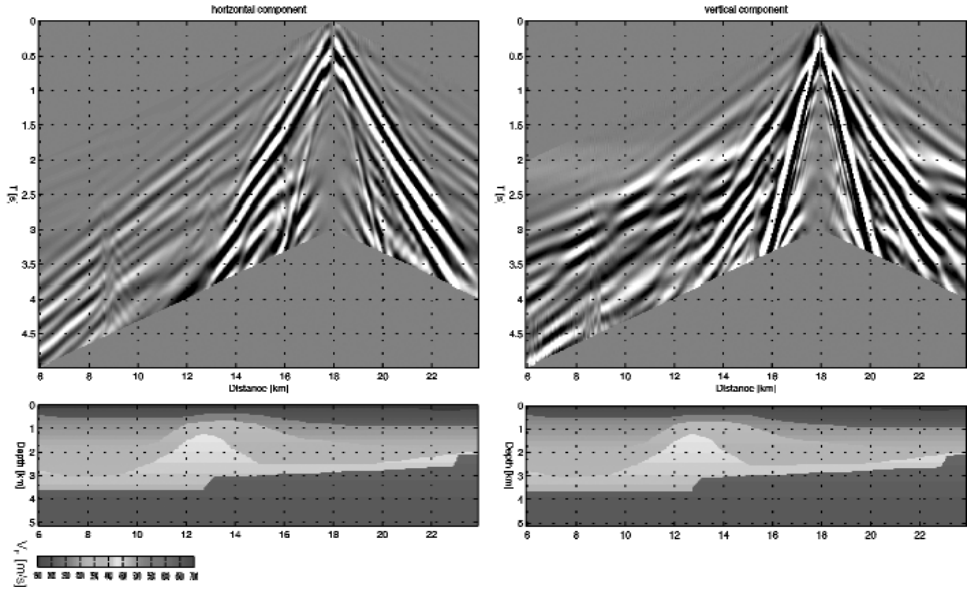

Fig. 2. Common receiver seismic section for station OBS48 (top) and the input structural model (bottom). Horizontal (left) and vertical (right) and components.
You can see this figure in color on page 218.

particular physical properties defined for the water level. In this simulation, in fact, instead of the theoretical $V_S = 0$ km/s, a value of $V_S = 680$, $Q_S = 10$ has been tested for the water.

Conclusions

The aim of this study is to help the interpretation of the sections recorded during the SERAPIS experiment, and in particular to define the seismic signature of a buried high-velocity caldera rim in the structure beneath the Campi Flegrei bay area. The full-wave propagation has been solved through the staggered, 3D Fourier pseudo-spectral method developed within this Project along a 2.5D model.
The synthetic seismic section here presented has mainly demonstrative purposes, since it "explores" the low frequency band. Within this limit, a number of signatures common to both the synthetic and real section seem to confirm the interpretation made through the proposed model about the presence of a buried high-velocity caldera rim beneath the Pozzuoli Gulf. However, a rigorous comparison of the synthetic section to the real data will be meaningful only after further improvement.

Acknowledgements

The 2D structural model along the simulated profile has been kindly provided by S. Judenherc.

References

Klinc P., Seriani G., Priolo E. (2004). Full-Wavefield Forward Modelling. *Gruppo Nazionale di Vulcanologia, Open File Report*: OFR_ISMACF_A7.1.

Zollo A., Judenherc S., Auger E., D'Auria L., Virieux J., Capuano P., Chiarabba C., de Franco R., Makris J., Michelini A., Musacchio G. (2003). Evidence for the buried rim of Campi Flegrei caldera from 3-d active seismic imaging. *Geophys. Res. Lett.*, 30(19), 2002, doi:10.1029/2003GL018173.

Morphology and depth of reflectors from 2D non-linear inversion of seismic data

M. Vassallo[1], V. Nisii[2], A. Zollo[1], G. Iannaccone[2]

[1] *Dipartimento di Scienze Fisiche, Università Federico II di Napoli*

[2] *Osservatorio Vesuviano, INGV, Napoli*

Abstract: We present here two methods to obtain reflection images of upper crust seismic reflectors. The techniques are based on migration and waveform coherence analysis of reflected seismic phases recorded in local earthquake seismograms and in active seismic data.

The first method is a move-out and stack of reflected seismic phases in local earthquake recordings. The theoretical travel times of reflected/converted phases in a 1D medium for a given interface depth and velocity model are used to align the recordings in time. The locations and origin times of events are initially estimated from the P and S arrival times. Different seismic gathers are obtained for each reflected/converted phase at the interface under consideration, and the best interface depth is chosen as that which maximizes the value of a semblance function computed on moved-out records. This method has been applied to seismic records of microearthquakes that have occurred at the Mt. Vesuvius volcano, and it confirms the reports of an 8- to 10-km-deep seismic discontinuity beneath the volcano that was previously identified as the roof of an extended magmatic sill.

The second is a non-linear 2D method for the inversion of reflection travel times aimed at the imaging of a target upper-crust reflector. This method is specifically designed for geophysical investigations in complex geological environments (oil investigations, retrieving of images of volcano structures) where the presence of complex structures makes the standard velocity analysis difficult and degrades the quality of migrated images. Our reflector is represented by nodes of a cubic-spline that are equally spaced at fixed horizontal locations. The method is based on a multiscale approach and uses a global optimization technique (genetic algorithm) that explores the whole of the parameter space, i.e. the interface position nodes. The forward problem (the modelling of reflection travel times) is solved using the finite-difference solver of Podvine & Lecomte (1991) and using an *a priori* known background velocity model. This non-linear method allows the automated determination of the global minimum (or maximum) without relying on estimates of the gradient of the objective function in the starting model and without making assumptions about the nature of the objective function itself. We have used two types of objective functions. The first is a least-squares L2 norm, defined as the sum of the squared differences

between the observed and the calculated travel times. The second is based on coherence measures (semblance). The main advantage of using coherence measures is that they do not require travel-time picking to assess the degree of fit to the data model. Thus, the time performance of the whole procedure is improved and the subjectivity of the human operators in the picking procedure is removed.
The methods are tested on synthetic models and have been applied to a subset of data that was collected during the active seismic experiments performed in September 2001 in the gulfs of Naples and Pozzuoli in the framework of what is known as the SERAPIS project.

Introduction

Reflected and/or converted phases from crustal discontinuities have been frequently observed on microearthquake records (Iyer, 1992). The analysis of secondary arrivals using different techniques has proven to be valuable for the definition of the position and physical characteristics of reflecting interfaces. The modelling of reflected and/or converted waves is widely used for the retrieving of other physical parameters of the propagation medium in seismic exploration (P-to-S impedance contrast, anisotropy, P-to-S velocity ratio, and others) (Yilmaz, 1987; Sheriff and Geldart, 1982).
Recently, several studies of wave amplitudes and arrival times of secondary wave trains on earthquake recordings have been used to study the crustal structure (James et al., 1987) and to delineate the geometry and extension of a magmatic body in various volcanic regions. For example, the use of travel-time and amplitude analyses for the location and interpretation of S-to-S and P-to-S reflected phases from a local seismic network in the area of Socorro, Rio Grande Rift (New Mexico, USA), allowed the identification of a sharp crustal discontinuity at a depth of approximately 18 km, which was interpreted as the top of a thin, extended magma layer (Sanford et al., 1973; Rinehart et al., 1981; Balch et al., 1997). Other evidence for mid-crust discontinuities of magmatic origin have been found in Japan, at the Nikko-Shirane volcano (Matsumoto and Hasegawa, 1996) and in California, at the Long Valley caldera (Stroujkova and Malin, 2000) through the analysis of S-to-S and S-to-P waves observed on microearthquake records.
In the present study, we first search for deeper discontinuities beneath Mt. Vesuvius by using the move-out and stacking method that is usually applied in exploration seismology and that is known as a coherency stack (Naess and Burland, 1985). Based on an *a priori* known background velocity model, the optimal interface depth is determined by maximizing the semblance function, which is calculated from the converted and reflected phase signals extracted from the microearthquake records (Nisii et al., 2004).
Determination of geological discontinuities from active seismic data is usually carried out by migration techniques (Yilmaz and Chambers, 1984; Yilmaz,

1987; Sheriff and Geldart, 1982) that require prior knowledge of the velocity. Conventional velocity analysis methods, such as semblance analysis (Toldi 1989), focusing analysis (Yilmaz and Chambers, 1984), and migration move-out analysis (Al-Yahya, 1989), are carried out interactively. However, in complex geological environments, the presence of complex structures makes the standard velocity analysis difficult and degrades the quality of migrated images. Another approach is to use the inversion of reflection data: first, a high resolution velocity model is determined by first-arrival travel time inversion, and then this model is used as the background reference medium for an interface inversion that is aimed at imaging a target reflector (Amand & Virieux 1995, Improta 2002).

In this study, we examine the use of a non-linear optimization method to obtain the localization and morphology of a seismic reflector by using active seismic data. The inversion method is designed to image rough reflectors that are embedded in an *a priori* known, laterally inhomogeneous velocity model. This method is based on the simulation of seismic wave propagation in a given media, and it employs a scheme of non-linear optimisation for the determination of the interface model. For a given interface model, the data are calculated with numerical techniques (forward problem) and the reliability of the model is evaluated by means of a cost-function value that is defined by the difference between the observed and the calculated data. Then, the interface model determination becomes a numerical determination of the minimal-cost model (optimization). The method is specifically designed for geophysical investigations in complex geological environments, for the obtaining of the morphology and the positions of embedded discontinuities.

We envision that these kinds of techniques will be appropriate as part of much more comprehensive investigations where the crustal velocities and regional structures can be determined by a variety of methods that involve controlled as well as natural sources.

Modelling of reflected/converted arrival time phases in local earthquake recordings. Application to the Mt. Vesuvius data

Method 1

The proposed method to model the reflected/converted arrival times follows the approach usually used in reflection seismology for the determination of the morphology of reflecting interfaces by means of the post-stack migration of seismic sections.

Assuming a horizontal reflector in a medium with a given 1D background velocity model, the theoretical arrival times of the four possible reflected/con-

verted phases are calculated (P-to-P, S-to-P, S-to-S, P-to-S) for any source and receiver pair of the analyzed waveform data set. For each considered wave type, a time window on the seismic records is centred on the theoretical arrival time. The semblance function is calculated in the selected time windows for all of the records along the entire seismic section. The semblance, S_T, is defined as the ratio of the total energy of the stacked trace in the time interval ($t+\Delta t$) to the sum of the energies of the individual traces in the same time interval (Neidell and Taner, 1971):

$$S_T = \frac{1}{N} \frac{\sum_{t}^{t+\Delta t} \left(\sum_{i=1}^{N} g_{ti} \right)^2}{\sum_{t}^{t+\Delta t} \sum_{i=1}^{N} (g_{ti})^2} \qquad (1)$$

where g_{ti} is the amplitude of trace *i* at time *t*. The semblance range of variability is between 0 and 1. The semblance is a measure of the wave-form similarity between different seismic records. For very coherent events in different records, this function assumes values close to 1. Prior to the computation of the semblance, the seismic records were normalized to minimize the differences arising from varying source magnitudes.

The semblance is evaluated for a given range of interface depths, and for each interface depth, different time windows are selected on the seismograms according to the newly computed phase arrival times. The optimal interface depth is selected as the one which maximizes the semblance for each of the analyzed reflections and converted events.

Assuming that the background velocity model is correct, a well-identified reflection/conversion event must generate pulses aligned at the zero time value in a moved-out seismic section. The alignment can be quantitatively verified by computing the stack function versus time (i.e. the sum of the amplitude at any time along the seismograms in the entire seismic section). The presence of reflected/converted arrivals in the section will correspond to a peaked stack function, with its maximum at time zero.

The method can be applied to the search of different secondary waves (P-to-P, P-to-S, S-to-P, S-to-S) on three-component seismograms. The comparisons of the semblance and stack plots calculated for the different phases allows for better constraint of the interface depth. The method assumes an *a priori* knowledge of the earthquake hypocentres and the background velocity model, which is assumed to be one dimensional. The uncertainty of these parameters may strongly affect the phase identification in seismograms and the correct positioning of the depth of the interface. In addition, other effects can bias the interface location, such as station statics (including topographical effects), and possible 3D heterogeneity of the propagation medium and an irregular morphology of the interface.

Application

We have applied this described method to the interpretation of the vertical component records from 24 local seismic events that occurred between July and December of 1999 and that were recorded by the surveillance network operated by Osservatorio Vesuviano, INGV. The duration magnitudes ranged from 0.4 to 3.0. A total number of 205 vertical component recordings were selected for the present study. The events were located in a 3D velocity model (Lomax et al., 2001) using the non-linear technique proposed by Lomax et al. (2000). The resulting hypocentres lie along the axial zone of the volcano edifice in the depth range of 1-4 km. The final epicentral distances between events and stations vary between a few hundred meters to 17 km (Figure 1). The calculated travel-time RMS values are smaller than 0.1 s.

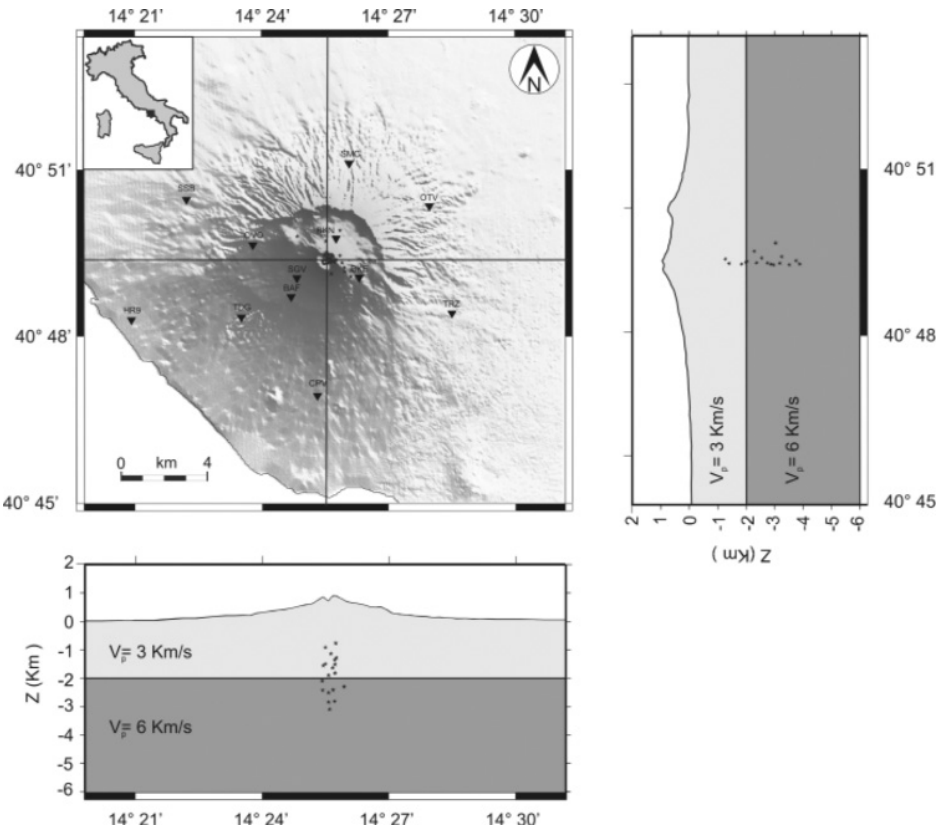

Fig. 1. Topographical map showing Mt Vesuvius and some of the seismic stations of the surveillance network owned by Osservatorio Vesuviano, INGV (solid triangles). The North-South and East-West vertical cross-sections show the 24 local event positions (stars) selected, and the assumed 1D velocity models.

The study of the converted/reflected waves was carried out considering a reflector depth ranging from 4 to 15 km with 0.2-km depth intervals. The minimum depth value was chosen as being deeper than the discontinuity between the alluvial and the recent volcanic sediments and the Mesozoic limestone formations, the average depth of which was determined to be 2 km (Zollo et al., 2002b).
The assumed background velocity model is composed of one layer over a half space (Zollo et al., 2002a; Lomax et al., 2001) (Figure 1). The calculation of the arrival times of the reflected phases was carried out by a two-point ray-tracing technique in the layered velocity model. Only the P-to-P and S-to-P wave types were considered for the analysis, since they are the most readable on the vertical component seismograms. A time window of 0.2 s centred at the theoretical arrival time of the reflected/converted phase was chosen. For more details of the data pre-processing adopted to reduce uncertainties associated with the use of local earthquake recordings, see Nisii et al. (2004).
The analysis of the semblance as a function of the interface depth for the P-to-P phase showed a major coherence value at about 9 km. A similar depth was obtained from the S-to-P phase analysis. The P-to-P phases identified by the semblance method are clearly visible in seismograms arranged as a common shot gathered in a conventional seismic reflection section (Figure 2). The records were moved-out according to the theoretical arrival times of a P-to-P phase for an interface depth of 9 km. The reflected wave pulses align around time zero on the moved-out section in Figure 2. The records of the stack and semblance as a function of time confirm the evidence of a secondary arrival

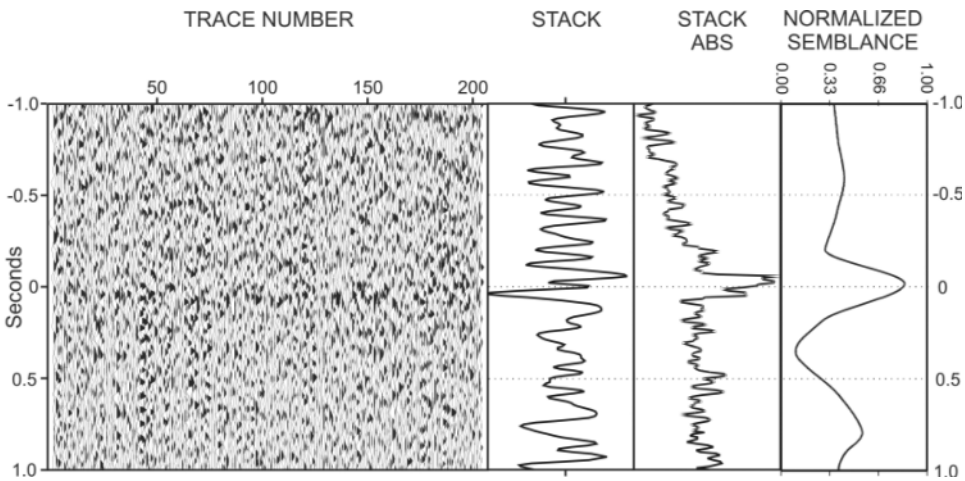

Fig. 2. An example of the seismograms showing clear secondary arrivals. The zero time is the origin time of the microearthquakes. The solid markers indicate the theoretical arrival times of the direct S wave and of the reflected/converted P-to-P and S-to-P phases from an interface at about 9 km in depth. The traces have been normalized to the integral of ABS.

with the presence of a marked peak at time zero. A quantitative estimation of the interface depth was provided by the time width of the semblance function around zero time in Figure 2. A total time width of about 0.3 s was measured for the P-to-P phases, which assumes a velocity of 6 km/s above the interface, suggesting an uncertainty of about 1 km for the interface depth.
The main sources of error affecting the width of the semblance can be the uncertainty in the earthquake location (hypocentral coordinates and origin time), a non-planar shape of the reflecting interface, and lateral heterogeneity of the velocity model. In the case of the Mt. Vesuvius earthquakes, assuming a realistic variability for all of these unknown parameters, the observed variation in the arrival time of reflected/converted phases is much smaller than the average wave travel time from sources to the receivers (tenths of seconds vs several seconds). This is the reason that despite the simplicity of the propagation model, a satisfactory alignment of the reflected/converted phases can be obtained, with a small dispersion around the zero time value in the seismic section.

MORPHOLOGY AND DEPTH OF REFLECTORS FROM 2D NON-LINEAR INVERSION OF ACTIVE SEISMIC DATA

Method 2

This method is based on the same concept as the previous one, but it is applied to active seismic data to obtain the depth and the morphology of an interface embedded in 2D heterogeneous media.
The reflection travel times are calculated by a three-step procedure. Initially, the first arrival travel times from each source and receiver to the nodes of a regular grid are calculated by the fast-time estimator of Podvin & Lecomte (1991). These travel times are calculated for a velocity model that has the same velocity values as the background model up the interface, and a velocity of zero below the interface (Figure 3); in this mode, only the reflected travel times are considered in the process. Then, the one-way travel times for each source/receiver to each point of the interface are calculated through an interpolation among the nearest four grid nodes (Figure 3). Finally, according to Fermat's principle, the reflection point for a source-receiver pair and for a given interface will be that which provides the minimum total travel time.
The reflector is represented by a cubic-spline function where the control points are equally spaced in the horizontal direction at fixed horizontal locations, and they can move vertically with continuity within a given depth range. The inversion is based on the numerical optimization of two possible cost functions. The first is a least squares L_2 norm, defined as the sum of the squared differences between the observed and the theoretical travel times. The second cost function is based on the value of the semblance (Neidell and Taner, 1971) that is evaluated along the calculated travel-time curves. For any source-

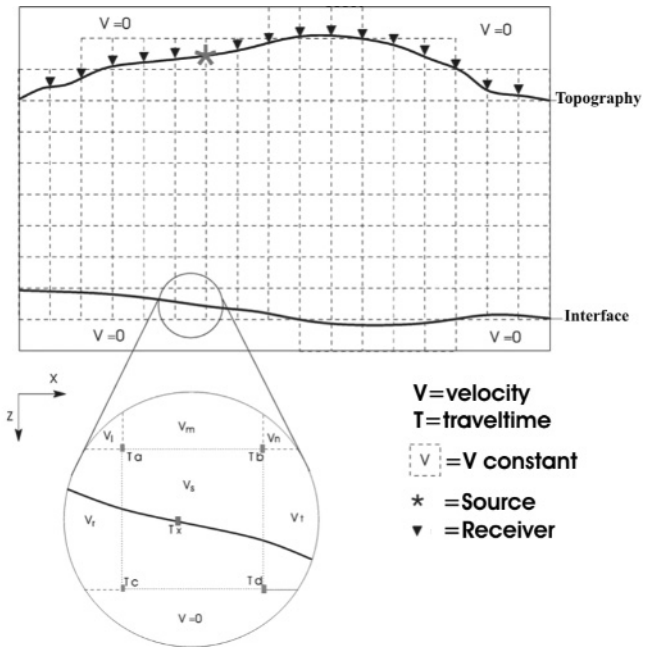

Fig. 3. Scheme followed for the resolution of the forward problem. The velocity model is divided into constant velocity boxes with a regular grid. In the grid nodes, the travel times are calculated by the Podvine & Lecomte (1991) finite differences method. The large circle shows a magnification of the Figure: the travel time in a fixed interface point (dots on the curve) is evaluated by performing an interpolation among the nearest four grid nodes (dots on the square).

receiver pair, a time window that is centred at the theoretical arrival time is selected on the seismic records. The semblance function (1) is computed in the selected time windows for all of the records along the entire seismic section (Figure 4). The semblance is a measure of the reflection/conversion waveform similarity. The main advantage of using wave-form coherence is that it does not require travel-time phase picking, thus improving the time performance of the whole procedure and removing the effects caused by the subjectivity of the human operators in the picking procedure.

The inversion strategy follows a multiscale approach (Lutter & Nowack, 1990): a series of inversions is run by progressively increasing the number of interface nodes. The strategy is described by the following steps:

1. With a minimal number of parameters fixed, the interface model is determined without putting ties on the dimension of the parameter space;
2. A model characterized from a greater number of parameters is searched for in the neighbourhood of the solution previously found;
3. The successive inversion run uses the same technique: the model, defined from a greater number of parameters is searched in the neighbourhood of the model previously determined.

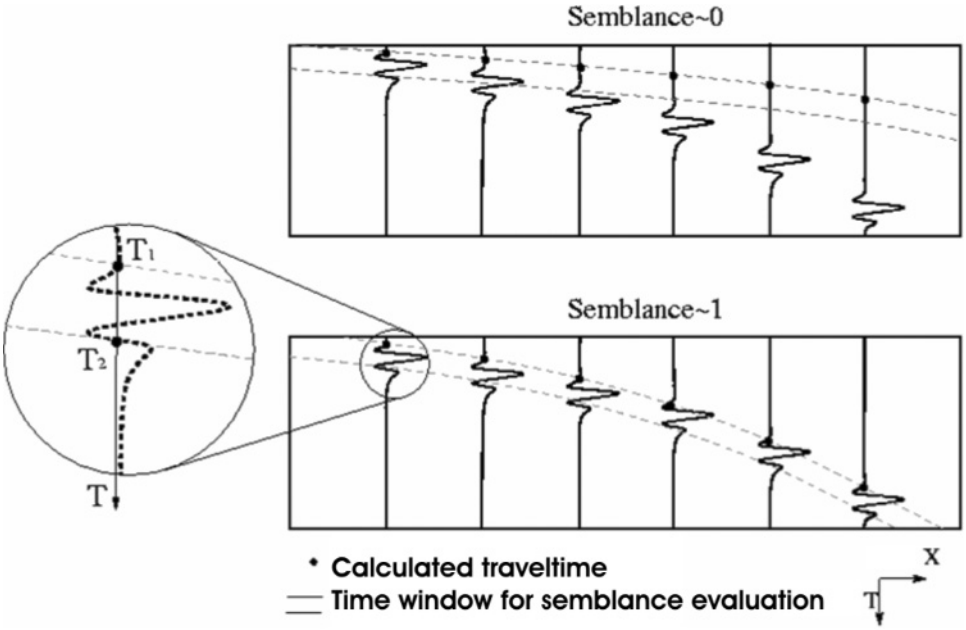

Fig. 4. Semblance evaluation along two different travel-time curves. For the calculation of the semblance, we extract the waveform contents in the windows given by the calculated travel times (in the large circle, the window is between the times T_1 and T_2). In the upper box, a bad travel time curve is shown (low semblance value), while the lower panel shows a travel-time curve that followed a coherent phase (high semblance value).
You can see this figure in color on page 219.

In this way, the passage from one step to the successive step improves the small wavelength characteristics of the final reflector model.
The search for the model parameter vector that minimizes the cost function (or maximizes the semblance function) is performed through the technique of the genetic algorithm (GA; Goldberg 1989; Whitley 1994) optimization method. Among the different non-linear optimization methods (Monte Carlo, simulated annealing), the GA has been shown to be very efficient and fast for the wide exploration of a multi-parametric model space and for the bracketing of the region containing the absolute minimum (Boschetti et al., 1996; Sambridge and Drijkoningen, 1992).

Application to simulated data

In this section, we present the results of our trials of the non-linear inversion on the synthetic models. The inversion of numerical simulated data is very important because it provides information about the ability of the method for the retrieval of the fixed geometrical features used to obtain the synthetic

dataset. We have performed two different simulated inversions. The first is based on the optimization of the L_2 norm, where the simulated data are the reflected travel times calculated on a fixed propagation media width of a given reflector. In the second, the inversion is based on the maximization of the semblance function, where the simulated data are the seismogram-calculated width numerical method on a fixed propagation model.

L_2 TESTS

To obtain the synthetic reflected travel times, a 20-km long and 10-km deep model was used (Figure 5). The P-velocity (Vp) model is divided into two different sections by a curved reflector surface, with depths ranging from 5 km to 6 km. Between the topographic and reflector surfaces, the Vp increases with the depth; under the interface, the velocity is constant. Along the top of the model there are six sources and 14 receivers, thus resulting in 84 calculated travel times (Figure 5).

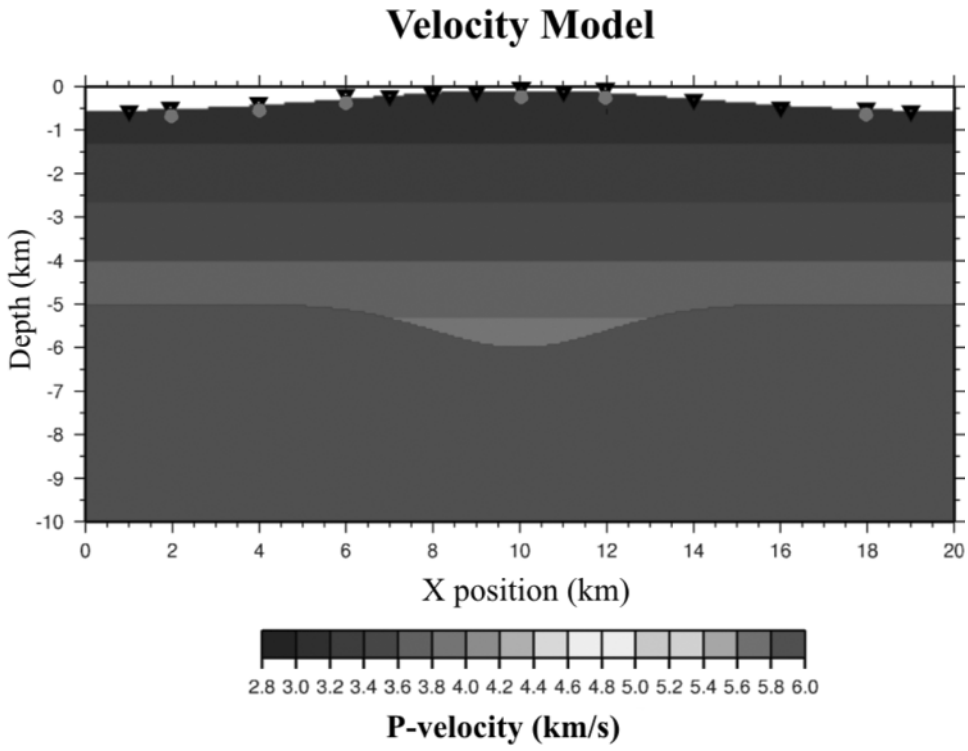

Fig. 5. Adopted model for the determination of synthetic travel times. The triangles show the locations of the receivers and the stars show the positions of sources.
You can see this figure in color on page 219.

For the first run, we allowed the node depth to vary from 0.5 km to 8.5 km. A succession of four interface models parametrized by 2, 3, 5 and 9 nodes were progressively inverted (Figure 6). Moving from a small to a larger number of interface position nodes, we always observed a decrease in the final cost function values and an increase in the agreement between the synthetic and the retrieved interface models. The RMS decreased from 0.14 s with the two-node model to 0.053 s for the final model (17-node model).

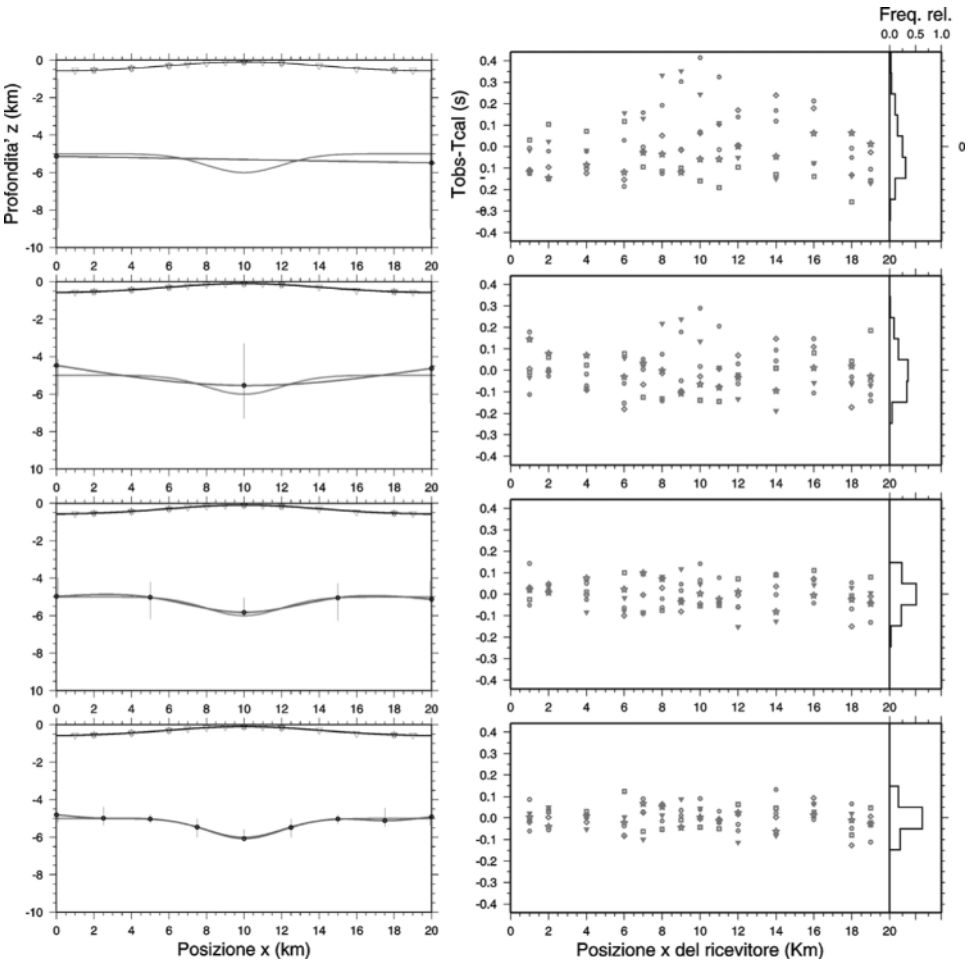

Fig. 6. The results of inversions of synthetic travel times. The final interface models are obtained by performing a succession of four inversion runs with an increasing number of interface nodes (solid circles). The line without nodes shows the real position of the reflector (Figure 5) and the vertical bars are the intervals of search of the nodes. In the panels on the right, the residual distributions and the histograms associated with determined models are displayed.
You can see this figure in color on page 220.

SEMBLANCE TEST

To test the inversion based on the waveform coherency criterion, we generated 150 synthetic seismograms that were obtained by the discrete wave-number method (Coutant, 1989). The seismograms were calculated using a propagation model formed of parallel and plane layers (Figure 7). In the first layer, the Vp was 3.5 km/s and the S velocity (Vs) was about 2.0 km/s; in the second layer, the Vp was 5 km/s and the Vs was 2.9 km/s. The interface that separates the two layers was located at 5 km of depth. Along the top of the model, there were two explosive sources and 75 receivers (Figure 7).

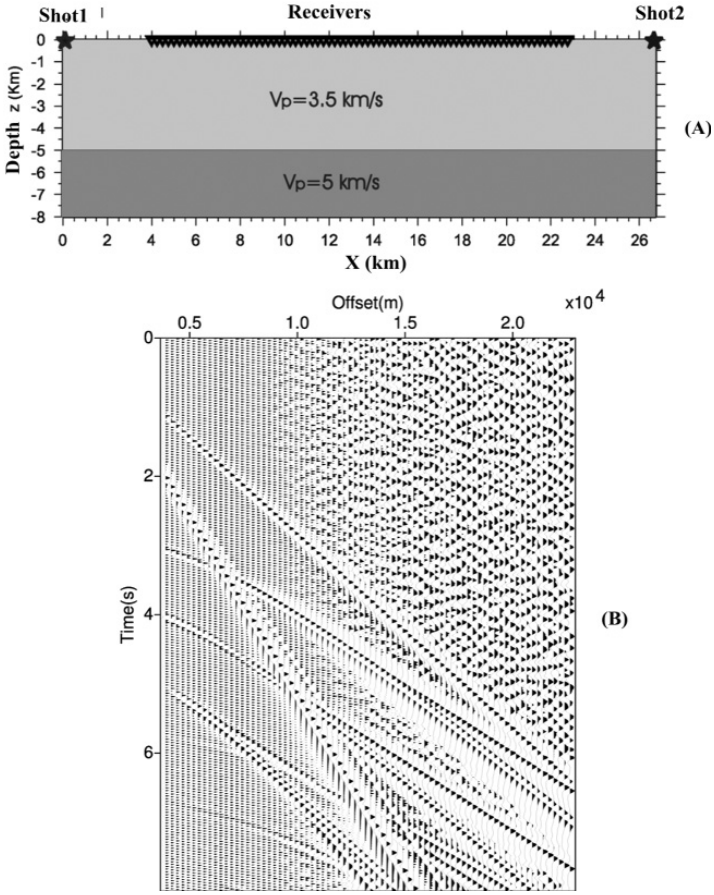

Fig. 7. Adopted model (A) for generation of synthetic seismograms (B). The triangles show the locations of the receivers and the stars show the positions of the sources (A). The synthetic common source gather section (B) shows only the first 10 s of the simulated traces relative to shot 1. The traces are normalized for the maximum trace values and they are filtered with an AGC filter on a window of 0.5 s. No filters were applied to the traces during the inversions.
You can see this figure in color on page 200.

The retrieved interface models are shown in Figure 8. Following the multiscale strategy, the inversion begins with the position search of the model defined from two single nodes, these are searched for in depths ranging from 2 km to 6 km. All of the obtained interfaces are horizontal and are approximately located at 5.1 km in depth. The retrieved depth interface locations are very close to the real depth of the interface (5 km; Figure 8). The possible cause of the discrepancy between these two values could be the Vp value assumed during

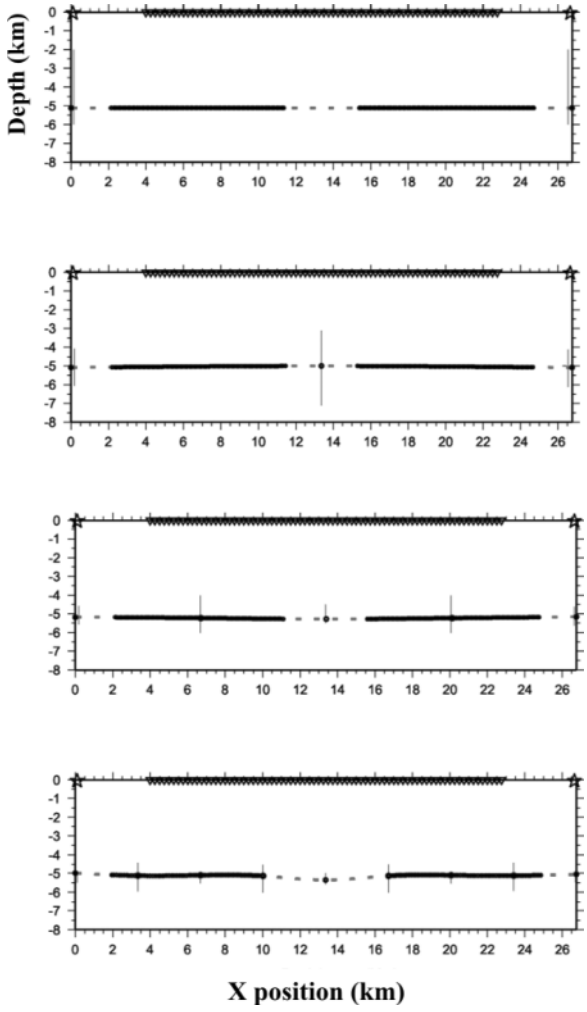

Fig. 8. Interfaces obtained with inversions of synthetic traces. The interface models (dotted line) were obtained performing a succession of four inversion runs with an increasing number of interface nodes (solid circles). The dots on the interface model are the impact points of seismic rays; the vertical bars are the intervals of search of the nodes.

the inversion; this was obtained on the basis of a normal move-out analysis that was performed on the synthetic section and it is greater than 0.1 km/s with respect to the real Vp value. The models obtained in the different singular steps (increasing the number of nodes; Figure 8) are very similar, and they are all in the same position. This is due to the simplicity of the propagation model adopted: only two nodes are enough to represent the complexities of the real interface.

The reliability of the retrieved model can be verified with the construction of the seismic panels obtained by the seismograms that are corrected for the calculated reflection travel times. With no error in the location and shape of the interface, the modelled reflection events should align at 0 s and should show a lateral coherence on the panels. Therefore, the reliability of the determined interface can be verified by measuring the alignment of the reflection events on the panel by the semblance value assumed on the traces corrected for the estimated travel times. Figure 9 shows an example of the time move-out panel that was obtained by correcting the traces for the retrieved nine-node model. The alignment and the wave-form coherence of the reflected phase are excellent in all of the panels. The phase alignment and the coherence are given by the semblance trace, which clearly shows a high peak at 0 s.

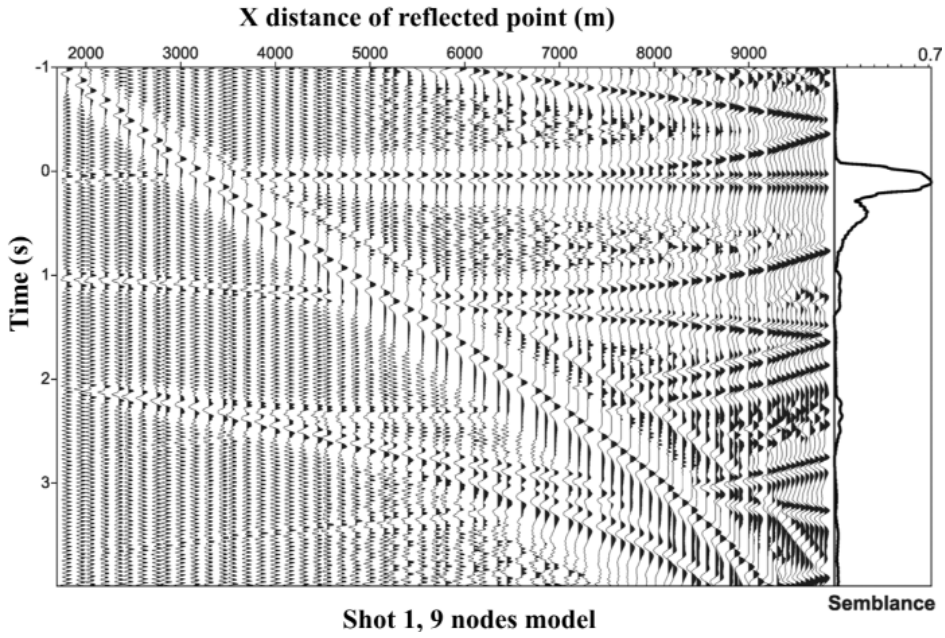

Fig. 9. Time moved-out section. The traces are corrected for the estimated travel times of the modelled reflected phase by the 17-node interface show in Figure 8. The horizontal semblance value of the traces allows the measuring of the alignment and coherence of the modelled phase.

Application to real active seismic data

The 2D non-linear inversion method was applied to a subset of data collected during the active seismic experiments performed in September 2001 in the gulfs of Naples and Pozzuoli in the framework of the SERAPIS project (Judenherc and Zollo, 2004) (Figure 10). The data (475 seismograms) used for the inversions were recorded by ocean-bottom system (OBS) O48 for the shots situated in a band of 250 m centred at the QUR line (Figure 10).

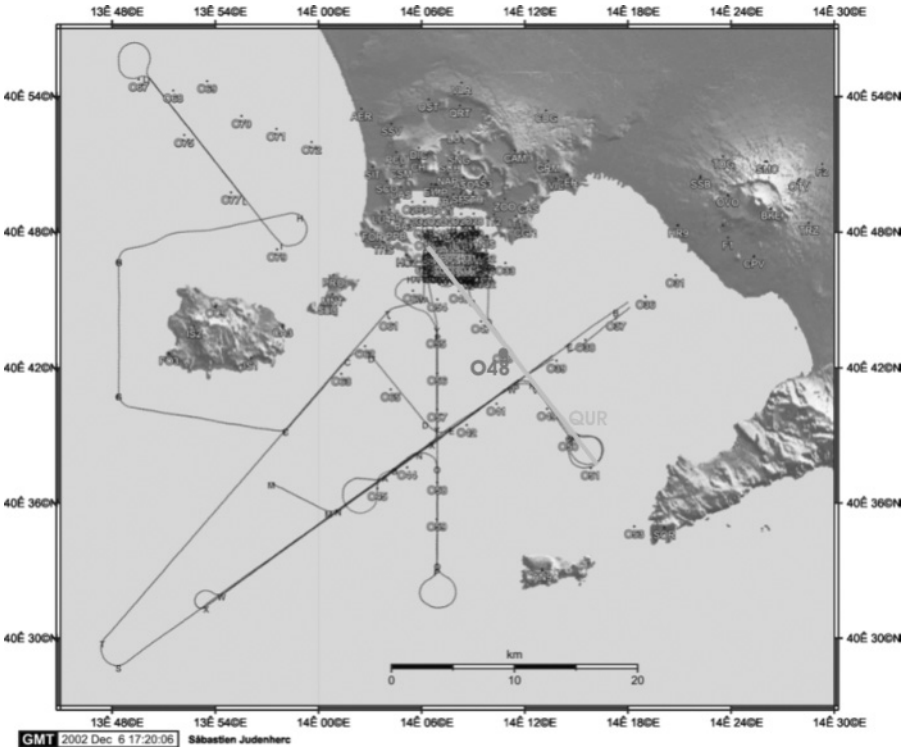

Fig. 10. Station and shot map of the SERAPIS experiment. The lines show the positions of the shots (more than 5,000 air-gun shots at spacings of about 125 m). The dots show the position of the stations (60 on-land stations, and 72 ocean-bottom seismographs).
You can see this figure in color on page 200.

The assumed background velocity model is composed of one layer over the half space. The upper layer extends from 0 to 1.1 km (b.s.l.) with a Vp of 1.9 km/s. The half-space Vp is assumed to be 3.4 km/s. These velocities were assigned following the NMO correction on the CRG section (Figure 11).

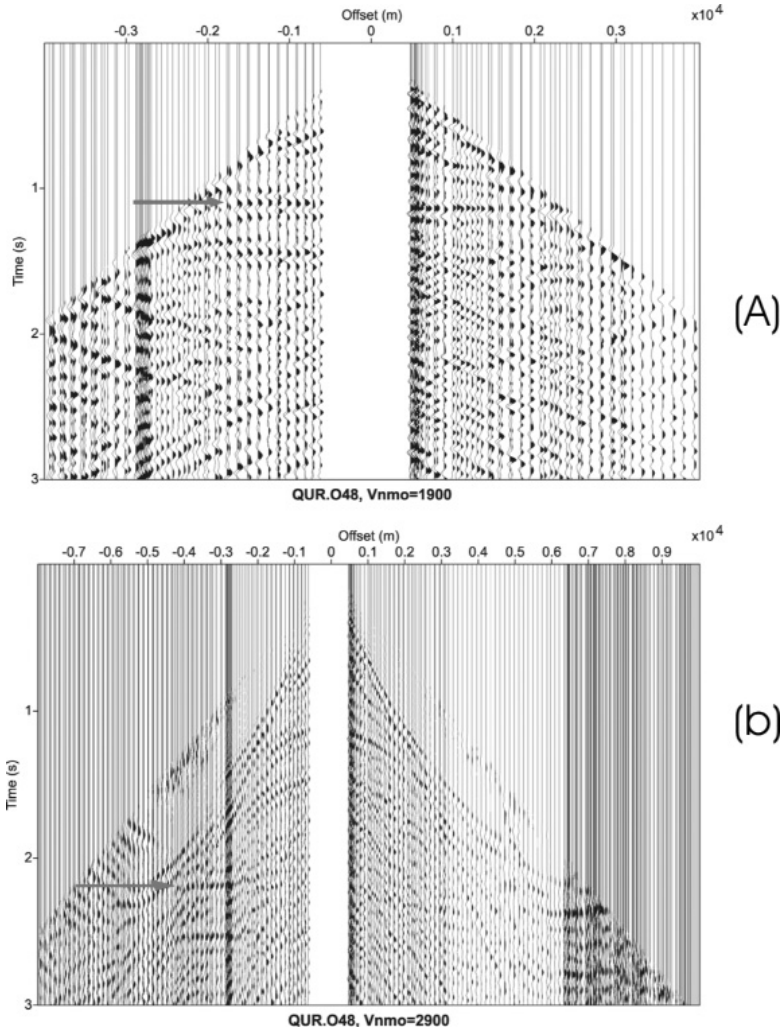

Fig. 11. Normal move-out corrections on traces recorded by OBS 048. The correction shows two clear phases: the first is well corrected by an NMO velocity of 1,900 m/s [indicated with arrows in (a)], and the second is flat for a velocity of 2,900 m/s [arrows in(b)].

A succession of five interface models parametrized by 2, 3, 5, 9 and 17 nodes were progressively inverted (Figure 12). Moving from a small to a larger number of interface position nodes, we always observed an increase in the final value of the semblance function. The semblance plot (Figure 13) shows a CRG section that was corrected for the estimated travel times on the maximum semblance interface with 17 nodes. The phase alignment and coherence are shown by the high horizontal semblance values of the traces, which clearly show a coherent signal at 0 s.

The determined maximum semblance interface (17-node interface model) is interpreted as the top of a carbonatic platform. This result is consistent with the tomographic sections obtained from the tomographic inversion of the first arrivals (Judenherc, 2004).

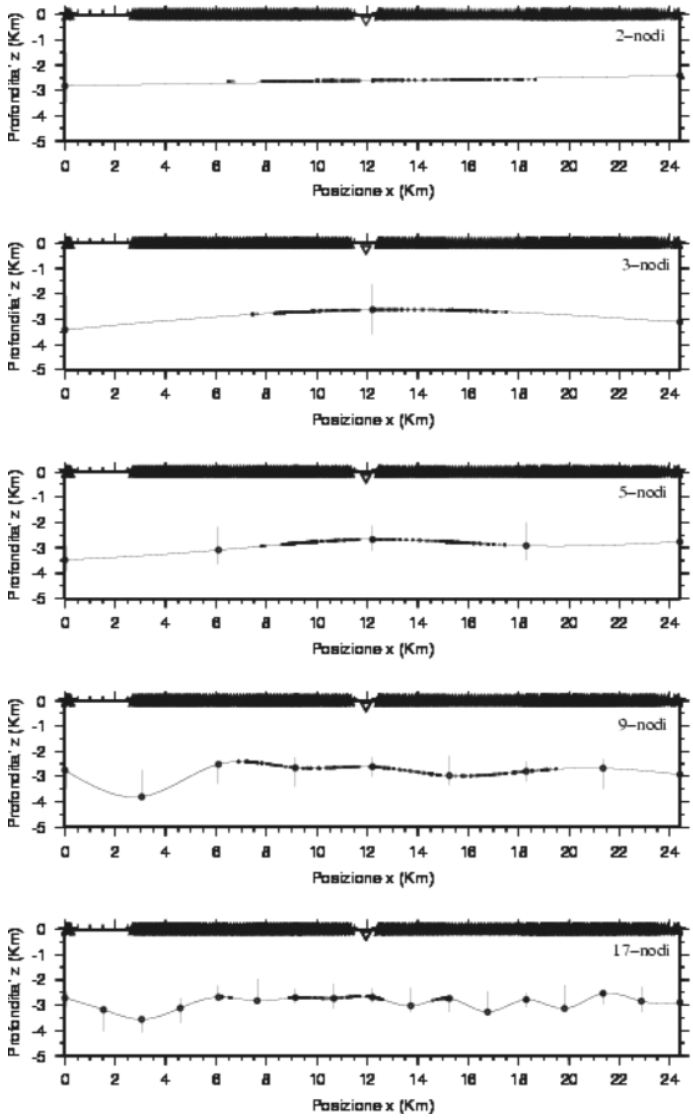

Fig. 12. Maximum semblance interface models obtained by performing a succession of five inversion runs with an increasing number of interface nodes (solid circles). The interface inversion technique is applied to over 475 seismograms recorded by the O48 receiver (triangle) for shots (stars) by QUR profile (Figure 10).

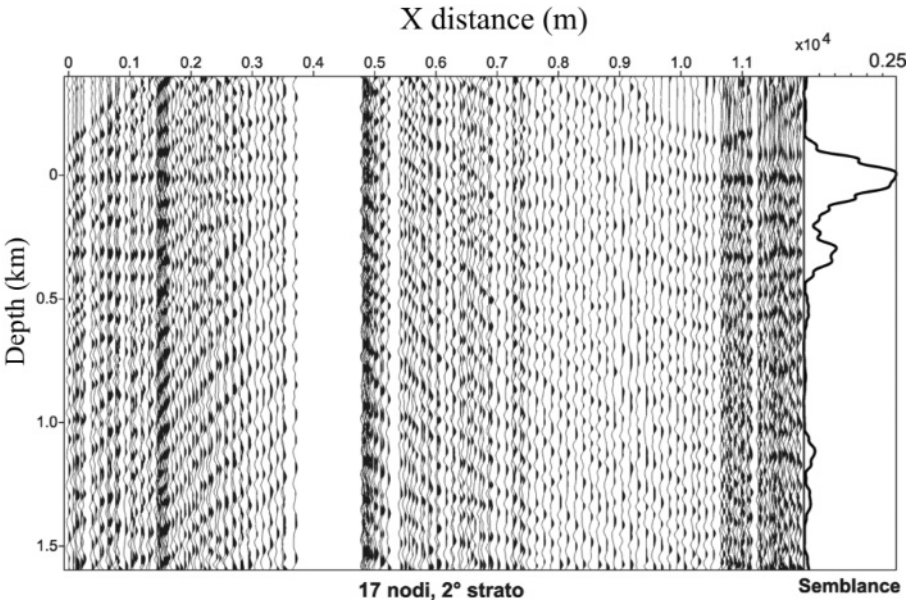

Fig. 13. Time moved-out section. The traces are corrected for the estimated travel times of the modelled reflected phase by the 17-node interface show in Figure 4. The horizontal semblance value of the traces allows the measurement of the alignment and coherence of the modelled phases.

Discussion and conclusions

We have presented two methods to invert the passive (the first method) and active (the second method) seismic reflection data. The described methodologies can be considered as useful tools for the identification and location of the depths of shallow crustal discontinuities when microearthquake records or active seismic data are used. Working with earthquake sources offers the advantage that unlike conventional reflection seismics, the sources are located within the investigated medium and they have larger and more strongly coupled energies than active sources, probing into the deeper crust. Furthermore, earthquakes can provide a much broader frequency bandwidth and represent far more efficient generators of shear waves than controlled sources. The main drawback is that the uncertainties of the estimates of source parameters (origin time, source location, fault mechanism) can influence the quality of the stack, thus affecting the accuracy of the interface depth. There are ways of minimizing these inherent difficulties, by considering some additional corrections and by selecting an appropriate earthquakes data set (James et al., 1987) and using active and passive seismic data at the same time.
Despite the assumed simplicity of the propagation medium, this technique has been proven to be robust and efficient for the search and first-order model-

ling of secondary arrivals on microearthquake records. The shape and width of the semblance function peak is a measure of the uncertainty of the interface depth, since a narrow semblance curve indicates a well-constrained interface depth. It also provides an estimate for the phase-timing error, which is related to unknown path and source effects. We applied this methodology to P-to-P and S-to-P waves observed on local earthquake records acquired by the surveillance seismic network operating on the Mt. Vesuvius volcano. Recent studies using reflected/converted wave fields of crustal discontinuities beneath the Mt. Vesuvius volcano were reported by Auger et al. (2001) using an active seismic data set. Based on the modelling of wave amplitudes as a function of the incidence angle, this study identified a major seismic discontinuity at about 8 km in depth, characterized by a negative velocity contrast (from 6 km/s to less than 4 km/s for P waves, and from 3.5 km/s to less than 1.0 km/s for S waves).

Our analysis of microearthquake records confirms this evidence, although it provides a slightly greater value for the interface depth (9 km) beneath the volcanic complex. This discrepancy can be attributed to the use of a simplified crustal model, whereas in the Auger et al. (2001) study, accurate static corrections were applied to the data to account for the lateral variation of the shallow velocity structure. Based on the measured velocity contrast, Auger et al. (2001) interpreted the reflector as the top of a midcrust, sill-like magmatic reservoir beneath the volcanic complex, with a lateral extent of at least 400 km^2.

This result, and the P and S velocities estimated by Auger et al. (2001), suggest a partially molten body, consistent with highly fractured rock with diffusive melt. Several observations of midcrust discontinuities associated with magmatic reservoirs beneath volcanoes have been made worldwide, based on seismic-data modelling. Beneath the Nikko-Shirane volcano (the Northeast Japanese arc), a midcrust reflector was identified at 8-15 km in depth with a lateral extension of about 15x15 km^2, which is interpreted as the top of a low-velocity thin layer of partially melted material (Matsumoto and Hasegawa, 1996). In the volcanic area of Casa Diablo, Long Valley, California, USA, seismic reflections from a 1.5-2-km^2 curved surface have been interpreted as being produced by the roof of a magma chamber at about 7.8 km in depth (Sanders, 1984). The presence of magmatic sills in the depth range of 8-20 km beneath different volcanoes worldwide is attributed to a neutral condition of the magma buoyancy force with the surrounding crust. The uprising of magma from the mantle in an extensional tectonic regime can give rise to thin and wide sill reservoirs in the upper crust (Ryan, 1994; Iyer et al., 1990). The discovery of a deep, sill-like magmatic reservoir beneath Mt. Vesuvius is relevant for the understanding and modelling of possible future eruptive scenarios.

The method presented using inverted active seismic data is tested on synthetic data and it has been used to image the location of a carbonatic platform

under the gulf of Naples. The method is specifically designed for geophysical investigations in complex geological environments where the presence of complex structures makes the standard velocity analysis difficult and degrades the quality of migrated images. Inversion based on coherence measures (semblance) does not require the picking of reflections, thus improving the time performance of the whole procedure and removing the subjectivity of the human operators in the picking procedure.
Our inversion that is based on the maximization of the semblance or on the minimization of the cost function demonstrates with synthetic data that the method is stable and efficient when it is used coupled to a multistep strategy. The interface model that is obtained by application of this inversion method on the SERAPIS data is interpreted as the top of a carbonatic platform, and this result is consistent with the tomographic studies recently published by Judenherc (2004).

References

Amand P., Virieux J. (1995). Non linear inversion of synthetic seismic reflection data by simulated annealing. *65th Ann. Internat. Mtg: Soc. Expl. Geophy. Expanded Abstracts*, 612-5.

Auger E., Gasparini P., Virieux J., Zollo A. (2001). Imaging of a mid-crust high to low seismic discontinuity beneath Mt. Vesuvius. *Science*, 204, 1510-2.

Al-Yahya K. (1989). Velocity analysis by iterative profile migration. *Geophysics*, 54, 718-29.

Balch R. S., Hartse H. E., Sanford A., Lin K. (1997). A new map of the geographic extent of the Socorro mid-crustal magma body. *Bull. Soc. Seism. Am.*, 87, 174-82.

Bernard M.-L., Zamora M. (2000). Mechanical properties of volcanic rocks and their relations to transport properties. *EOS, Trans. Am. Geophys. U.*, 81, Fall Meet. Suppl., Abstract V71A-33.

Boschetti F., Dentith M. C., List R. D. (1996). Inversion of seismic refraction data using genetic algorithms. *Geophysics*, 61, 1715-27.

Coutant O. (1989). Programme de simulation numerique AXITRA. *Res. Report LGIT*, Grenoble.

Gasparini P., Tomoves Working Group (1998). Looking inside Mount Vesuvius. *EOS, Trans. Am. Geophys. U.*, 79, 229-32.

Goldberg X. (1989). Genetic Algoritm in Search, Optimization and Machine Learning. *Addison-Wesley Pub. Co., pp. 432*.

Improta L., Zollo A., Herrero A., Frattini R., Virieux J., Dell'Aversana P. (2002). Seismic imaging of complex structures by nonlinear traveltime inversion of dense wide-angle data: application to a thrust belt. *Geophys. J. Int.*, 151, 264-8.

Iyer H. M. (1992). Seismological detection and delineation of magma chambers:Present status with emphasis on the Western USA, in *Volcanic Seismology*, edited by P. Gasparini, R. Scarpa, K. Aki, Springer-Verlag, pp. 299-338.

Iyer H. M., Evans J. R., Dawson P. B., Stauber D. A., Achauer U. (1990). Differences in magma storage in different volcanic environments as revealed by seismic tomography: silicic volcanic centers and subduction-related volcanoes, in *Magma transport and storage* edited by M.P. Ryan, Wiley, pp. 293-316.

James D., Clarke T., Meyer R. (1987). A study of seismic reflection imaging using microearthquake sources, *Tectonoph.*, 140, 65-79.

Lomax A., Zollo A., Capuano P., Virieux J. (2001). Precise, absoute earthquake location under Somma-Vesuvius volcano using a new 3D velocity model. *Geophys. J. Int.*, 146, 313-31.

Lomax A., Virieux J., Volantand P., Berge C. (2000). Probabilistic earthquake location in 3D and layered models: Introduction to a Metropolis-Gibbs method and comparison with linear locations, in *Advances in seismic event location*, edited by C.H. Thurber, N. Rabinowitz, Kluwer, Amsterdam, pp. 101-134.

Matsumoto S., Hasegawa A. (1996). Distinct S wave reflector in the midcrust beneath Nikko-Shirane volcano in the northeastern Japan arc. *J. Geoph. Res.*, 101, 3067-83.

Naess O. E., Bruland L. (1985). Stacking methods other than simle summation, in *Developments in Geophysical Methods*, 6, 189-223, edited by A.A. Fitch, Elsevier Applied Science Publishers, London.

Neidell N. S., Taner M. S. (1971). Semblance and other coherency measurements for multichannel data. *Geophysics*, 36, 482-97.

Nisii V., Zollo A., Iannaccone G. (2003). Depth of a mid-crustal discontinuity beneath Mt Vesuvius from the stacking of reflected and converted waves on local earthquake records. *Bull. Soc. Seism. Am.*, 94(5), 1842-9.

Podvin P., Lecomte I. (1991). Finite difference computation of traveltimes in very contrasted velocity models: a massively parallel approach and its associated tools. *Geophys. J. Int.*, 105, 271-84.

Ryan M. P. (1994). Neutral-Buoyancy Controlled Magma Transport and Storage in Mid-ocean Ridge Magma Reservoirs and Their Sheeted-Dike Complex: A Summary of Basic Relationships. in *Magmatic Systems*, vol. 2, edited by M.P. Ryan, Academic Press, London, pp. 97-138.

Rinehart E., Sanford A. R. (1981). Upper crustal structure of the Rio Grande Rift near Socorro, New Mexico, from inversion of microearthquake S-wave reflections. *Bull. Soc. Seism. Am.*, 71, 437-50.

Toldi J. L. (1989). Velocity analysis without picking. *Geophysics*, 34, 191-9.

Sambridge M., Drijkoningen G. (1992). Genetic algorithms in seismic waveform inversion. *Geophys. J. Int.*, 109, 323-42.

Sanders C. O. (1984). Location and configuration of magma bodies beneath Long Valley, California, determined from anomalous earthquake signals. *J. Geophys. Res.*, 89, 8287-302.

Sanford A. R., Alptekinand O., Toppozada T. R. (1973). Use of reflection phases on microearthquake seismograms to map an unusual discontinuity beneath the Rio Grande Rift. *Bull. Seism. Soc. Am.*, 63, 2021-34.

Sheriff R. E., Geldart L. P. (1982). Exploration Seismology. *Cambridge University Press*, New York.

Stroujkova A. F., Malin P. E. (2000). A magma mass beneath Casa Diablo? Further evidence from reflected seismic waves. *Bull. Seism. Soc. Am.*, 90, 500-11.

Yilmaz O. (1987). Seismic Data Processing, in *Investigations in Geophysics*, edited by B. Nictzel, Vol. 2, Society of Exploration Geophysicists, Tulsa, Oklahoma.

Yilmaz O., Chambers R. (1984). Migration velocity analisis by wavefield extrapolation. *Geophys.*, 49, 1664-74.

Zollo A., Gasparini P., Virieux J., Le Meur H., De Natale G., Biella G., Boschi E., Capuano P., de Franco R., Dell'Aversana P., De Matteis R., Guerra I., Iannaccone G., Mirabile L., Vilardo G. (1996). Seismic evidence for a low-velocity zone in the upper crust beneath Mount Vesuvius. *Science*, 274, 592-4.

Zollo A., D'Auria L., De Matteis R., Herrero A., Virieux J., Gasparini P. (2002). Bayesian estimation of 2D P-velocity models from active seismic arrival time data: Imaging of the shallow structure of Mt. Vesuvius (Southern Italy). *Geophys. J. Int.*, 151, 556-82.

Zollo A., Marzocchi W., Capuano P., Lomax A., Iannaccone G. (2002). Space and time behaviour of seismic activity al Mt. Vesuvius volcano, Southern Italy. *Bull. Seism. Soc. Am.*, 92(2), 625-40, doi: 10.1785/0120000287.

Database on laboratory measured data on physical properties of rocks of Campi Flegrei volcanic area (Italy)

G. Giberti[1], B. Yven[2], M. Zamora[2], T. Vanorio[3]

[1] *Dipartimento di Scienze Fisiche, Università Federico II di Napoli, Italy*

[2] *Institute de Physique du Globe, Universitè de Paris 6/7, Paris, France*

[3] *Géosciences Azur, CNRS, Université de Nice, Sophie Antinopolies, Valbonne, France*

Excepts from the (unpublished) PhD Thesis of Dr Beatrice Yven, carried out at IPGP Lab (Paris, France) under the supervision of Prof. M. Zamora.

Contents

1) Samples and their gross volcanic characteristics
2) Porosity
3) Permeability
4) Density
5) Electrical conductivity
6) Thermal conductivity
7) Acoustic parameters

1) Samples

The measures were made on 9 surface samples and 11 samples collected by the AGIP Oil Company -Italy. In the following table the first column refer to the name given to the sample, the second and third column, respectively, to the depth and in situ temperature (°C) at which the sample has been collected, the fourth to the gross volcanic characteristics (PREC and POSTC refer to a gross estimate of the time of deposition, and mean before or after the Campanian Ignimbrite caldera formation).
Legenda for surface samples: NYT1, NYT2 , sampled on the caldera's border; N1, N2: Nisida; B: Baia; SV10, SV30 (sampled on surface at San Vito 1 and San Vito 3 wells, respectively); MF10, MF20 (sampled at Mofete 1 and Mofete 2 wells). The others refer to well samples.

Samples	Depth (m)	Temperature °C (in situ)	Gross characterization
NYT1	0	-	Yellow tuff
NYT2	0	-	Yellow tuff
N1	0	-	Yellow tuff
N2	0	-	Yellow tuff
B	0	-	Yellow tuff
SV10	0		Yellow tuff
SV11	810	130	Consolidated tuff Deposition under sea level POSTC
SV12	1420	260	Chaotic Tuff Deposition under sea level POSTC
SV13	2130	300	Chaotic Tuff Aerial deposition POSTC
SV15	2860	390	Metamorphic tuff Deposition under sea level POSTC
SV30	0	-	Yellow tuff
SV31	1320	225	Lava Deposition under sea level PREC
SV32	1950	305	Tuffites alterated at high temperature Deposition under sea level PREC
MF10	0	-	Yellow tuff
MF11	680	240	Clayey tuffs Deposition under sea level POSTC
MF12	1047	260	Solid lava Aerial deposition PREC
MF13	1600	325	Volcano- sediment Deposition under sea level PREC
MF20	0	-	Yellow tuff
MF21	1960	345	lava -latite Aerial deposition PREC
MF51	2490	340	Tuffites Alterated at high temperature Deposition under sea level PREC
MF52	2700	360	latite Deposition under sea level PREC

2) Porosity

Measured on samples with different volumes (third column; 125 cm^3, fourth column: 12 cm^3) saturated with distillate water. Some of the measurements were made with Helium. The correspondence among the two measures indicates the homogeneity in the porosity of the samples. Depth and Temperature refer to depth and temperature at which rocks were sampled. The exceptions (grey in the table) are: SV31 (lava, this sample appear to have a 3% of unconnected porosity), MF51 (lava, and unconnected porosity (4%)).

Samples	Depth (m)	Temperature °C	Porosity (%) 125 cm^3	Porosity (%) 12 cm^3	He Porosity (%) 12 cm^3
NYT1	0		0,483	0,463	
NYT2	0		0,493	0,485	
N1	0		0,486	0,481	
N2	0		0,453	0,438	
B	0		0,479	0,467	
SV10	0		0,420	0,405	
SV11	810	130	0,340	0,329	0,351
SV12	1420	260	0,234	0,219	0,233
SV13	2130	300	0,224	0,219	0,223
SV15	2860	390	0,146	0,151	0,154
SV30	0	20	0,445	0,435	
SV31	1320	225	0,102	0,059	0,146
SV32	1950	305	0,201	0,203	0,206
MF10	0	20	0,492	0,471	
MF11	680	240	0,397	0,398	0,424
MF12	1047	260	0,177	0,154	0,161
MF13	1600	325	0,129	0,177	0,175
MF20	0	20	0,516	0,503	
MF21	1960	345	0.068	0.049	0.049
MF51	2490	340	0,058	0,079	0,079
MF52	2700	360	0,049	0,045	0,048

Notes

* The depth-decreasing porosity is attributed more to the presence of clay minerals than to compaction.
* The lab data are compatible with those measured in the wells (Agip Logs).
* The atypical increase of porosity in the San Vito1 at 2900 m depth and San Vito 3 at 2300 m depth is attributed to carbonate dissolution at the metamorphic limit.
* Mofete wells: The atypical value of the Mofete 51 sample indicates a metamorphic limit and the carbonate dissolution is at around 2500-2700 m depth.

3) PERMEABILITY

Measured with air. Errors around 1% for values that are greater than 01.mD=0,9869E-15 m^2). The measures have been done with two different methods. Beams method for the surface samples and permeameter at variable charge for the wells samples.
The data have been corrected to take into account the KlinKeberg effect to have the permeability to liquids. These values have to be considered estimates, as the true values depend on the parameter b, that depends on the rocks properties. Here a averaged value for b was considered).
Law for the Klinkeberg effect:

$$k_l = k_a\left(1 + \frac{b}{P_f}\right)^{-1}$$

Note that, theoretically, the permeability, as given through the Darcy law, is only dependent on the properties of the rocks and equal for gas or liquid permeants.

Samples	Depth (m)	Temperature °C	k_a permeability (mD)	k_l permeability (mD)	k_l permeability (E-14m2)
NYT1	0	-	73,7	50,00	4,93
NYT2	0	-	239,4	200,00	19,7
N1	0	-	-	nd	nd
N2	0	-	446,5	400,00	39,5
B	0	-	43,8	31,00	3,06
SV10	0	-	139,1	110,00	10,9
SV11	810	130	0,36	0,25	0,0247
SV12	1420	260	0,26	0,17	0,0168
SV13	2130	300	1,18	0,80	0,0790
SV15	2860	390	0,79	0,50	0,0493
SV30	0	-	45,1	33,00	3,26
SV31	1320	225	<0,1	<0,1	<1.E-16
SV32	1950	305	1,98	1,30	0,0128
MF10	0	-	717,0	610,00	60,2
MF11	680	240	1,51	1,00	0,0987
MF12	1047	260	<0,1	<0,1	<1.E-16
MF13	1600	325	1,45	0,95	0,0938
MF20	0	20	884,5	750,00	74,0
MF21	1960	345	<0,1	<0,1	<1.E-16
MF51	2490	340	0,53	0,33	0,0326
MF52	2700	360	0,19	0,11	0,0109

Notes and comments

– Relationships between porosity and permeability.
  * SV1: No clear evidence (see also figures on the previous pages on porosity) with the exceptions of two small section: 803-812 m, yellow tuffs, and 2860-2865 m, metamorphic tuffs. The connected porosity or network of micro pores left void by clay minerals appear very complex and does not seem to be suitable for the fluid circulation
– Relationships between depth and permeability.
  * SV1: Till to 1400 m depth the permeability is very low 0,1-1mD (impermeable cover of a possible geothermal zone?) The same hypothesis is suggested for the SV3 zone at 1400 m of depth.
  * The greater permeability at greater depth (in particular at Mofete and in lava samples) is attributed to fissures (following a suggestion given by Rosi and Sbrana, Campi Flegrei, Quaderni del CNR).
  * The low values of permeability at depth are attributed essentially to the presence of clay minerals, only in part to compaction.
  * At Mofete, during the perforations, 3 zones of water reservoirs have been identified: between 550-900 m (MF1), 1800-2000 m(MF2) and 2550-2700m (MF5). Given the low values of permeabilities it is suggested that here the fluid circulations is through fractures or faults.

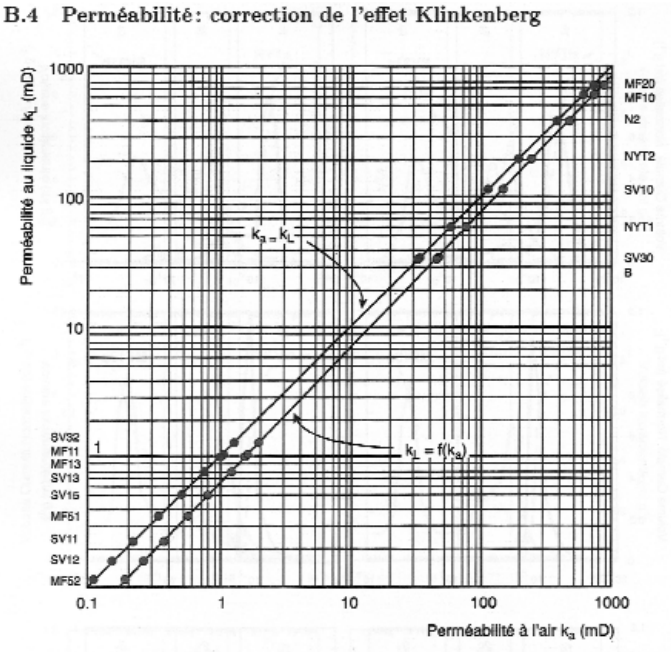

FIG. B.3 – *Perméabilités mesurées et corrigées de l'effet Klinkenberg (modifié d'après l'abaque de Corelab Inc).*

4) Density

Measured: M_{dry} = dry mass, M_{arc} =Archimedean mass, M_{sat} = water saturated mass to obtain

$$\rho_{app} = \frac{M_{dry}}{(V_t - V_c)} = \frac{M_{dry}}{(M_{dry} - M_{arc})}\rho_f \quad \rho_t = \frac{M_{dry}}{(V_t)} = \frac{M_{dry}}{(M_{sat} - M_{arc})}\rho_f \quad \rho_m = \frac{M_{dry}}{(V_m)}$$

where: $\rho_f = 0.0092$ g/cm^3 (distilled water), V_t total volume, V_c volume of connected pores, V_{nc} volume of unconnected pores, V_m volume of rock matrix: $V_t = V_m + V_c + V_{nc}$.
To measure M_{arc} the fully saturated sample is immersed in a bath of distilled water.
From $M_{sat} = M_{dry} + \rho_f V_c \Rightarrow V_c$ and $M_{arc} = M_{dry} - \rho_f (V_m + V_c)$, ρ_m is measured through the measure of the mass of pulverized sample filling up a volume of 125 cm^3).

Samples	Depth (m)	Temperature °C	bulk density (gr/cm^3)	apparent density (gr/cm^3)	matrix density (gr/cm^3)
NYT1	0	-	1,16	2,25	2,30
NYT2	0	-	1,14	2,25	----------
N1	0	-	1,27	2,33	----------
N2	0	-	1,27	2,33	----------
B	0	-	1,20	2,31	----------
SV10	0	-	1,29	2,23	2,23
SV11	810	130	1,63	2,47	2,51
SV12	1420	260	1,95	2,54	2,57
SV13	2130	300	2,08	2,68	2,72
SV15	2860	390	2,29	2,69	2,72
SV30	0	-	1,30	2,34	
SV31	1320	225	2,25	2,50	2,59
SV32	1950	305	2,29	2,87	2,92
MF10	0	-	1,17	2,31	2,33
MF11	680	240	1,54	2,55	2,61
MF12	1047	260	2,30	2,69	2,70
MF13	1600	325	2,20	2,70	2,76
MF20	0	-	1,11	2,29	2,33
MF21	1960	345	2,60	2,79	2,79
MF51	2490	340	2,53	2,72	2,81
MF52	2700	360	2,52	2,66	2,70

Notes

* In general $\rho_m \geq \rho_{app}$ (within experimental errors (1,2%)). If unconnected pore volumes are present. These data confirm this rule (within experimental errors (1,2%)). In particular this is true for SV31 and MF51: for the SV31 sample attributed to incomplete saturation, to unconnected pore volume for MF51.
* The changes of density with depth are attributed to the different mineralogical rock and crystals properties. For SV1, it has inferred the law ρ_t=2,52+0,48 log z, 800<z<2865, attributed to compaction and different conditions of pressure and temperature after the sinking of this zone.

5) Electrical conductivity

Preliminary note: essentially surface conductivity (σ_s), due to the presence of minerals on the surfaces of the connected pore network. That determines currents (cations) when in presence of fluids (with conductivity σ_f) flowing in the pores. The estimate on the matrix conductivity (which would determine the volume conductivity σ_v) brings to a value 10^{-4} times smaller with respect to the surface conductivity.
The effective conductivity σ_r, when the surface conductivity is low, is determined essentially from the fluid conductivity (Archie law $\sigma_r=\sigma_f/F$, where F is the form factor), but this condition is satisfied if the relation among σ_r and σ_f, both at high and low salinity, is linear. For the here measured samples, at low salinity, the relationship between σ_r and σ_f **is not** linear.
The relationship between F and porosity is given by $F=\phi^{-m}$, where the value of *m,* cementification coefficient, indicates the electrical connectivity of the pore volume (m>1, decrease of connectivity).
For some of these measures two samples (denoted a and b) were available.

Samples	Depth (m)	Temperature °C	Porosity (%)	frequency (kHz)	F	error	Surface conductivity (10-3Sm-1)	error	m
NYT1	0	-	0,444	100	8,70	0,90	42,70	16,80	2,67
NYT2a	1	-	0,465	100	5,30	0,20	38,60	6,50	2,21
NYT2	0	-	0,465	100	5,30	0,20	0,71	5,00	2,18
N1	0	-	0,481	100	6,70	0,10	21,60	1,00	0,13
N2	0	-	0,430	100	9,50	0,30	36,60	4,70	2,67
Ba	1	-	0,451	100	7,70	0,30	80,90	8,90	2,57
B	0	-	0,469	100	6,60	0,20	80,90	7,40	2,48
SV10	0	-	0,395	100	11,30	0,40	50,30	6,60	2,61
SV11	810	130	0,329	20	16,70	0,80	25,60	2,40	2,53
SV12	1420	260	0,231	20	21,200	0,70	7,60	0,60	2,09
SV13	2130	300	0,219	20	24,90	0,70	7,60	0,60	2,09
SV15	2860	390	0,15	20	31,40	1,30	1,90	0,20	1,82
SV30a	0	-	0,445	100	6,50	0,30	36,30	4,50	2,32
SV30b	0	-	0,424	100	6,60	0,30	42,80	5,00	2,20
SV31	1320	225	0,059	1	451,90	4,40	1,20	0,00	2,16
SV32	1950	305	0,203	10	31,10	1,10	2,00	0,10	1,16
MF10	0	-	0,459	100,00	6,10	0,20	75,00	7,50	2,33
MF11	680	240	0,398	20,00	8,10	0,30	36,30	3,40	2,27
MF12	1047	260	0,154	1,00	118,30	8,80	5,00	0,50	2,55
MF13	1600	325	0,177	10,00	28,20	0,70	1,70	0,10	1,93
MF20	0	-	0,485	100,00	5,40	0,20	70,90	8,30	2,33
MF20b	0	-	0,470	100,00	5,20	0,20	65,30	4,40	2,18
MF21	1960	345	0,049	1,00	214,91	9,10	0,30	0,00	1,80
MF51	2490	340	0,079	10,00	118,00	3,00	1,00		1,88
MF52	2700	360	0,079	1,00	381,00	10,00	0,80		1,92

Comments

* Environment with a low conductivity: the conductivity increases only in presence of fluids which activate the surface conductivity (on surface this conductivity is due to zeolites and at depth to clay minerals).
* Value of the coefficient *m*: 2.5 on average on surface, 1.8 in wells. It has to be noted that, as the porosity decreases with depth, the *m* value in wells indicates there a better electrical conductivity.
* The values for the SV31 sample are attributed to saturation problems.

6) THERMAL CONDUCTIVITY

Preliminary notes: measured only on wells samples, in steady conditions and at room temperature. At the end of this section some relationships to extrapolate the values at every temperature are given.

Samples	Depth (m)	Temperature °C	Porosity (%) 125 cm^3	Thermal conductivity ($Wm^{-1}K^{-1}$) DRY	error	Thermal conductivity ($Wm^{-1}K^{-1}$) SAT	error	DRY/SAT
SV10	0							
SV11	810	130	0,34	0,62	0,01	1,14	0,01	1,83
SV12	1420	260	0,23	1,00	0,00	1,46	0,00	1,46
SV13	2130	300	0,22	0,22	1,03	1,43	0,03	1,39
SV15	2860	390	0,15	1,10	0,02	1,51	0,01	1,37
SV30	0							
SV31	1320	225	0,102	1,290	0,010	1,410	0,010	1,090
SV32	1950	305	0,201	0,203	2,290	1,000	1,340	1,340
MF10	0							
MF11	680	240	0,400	0,710	0,010	1,470	0,080	2,080
MF12	1047	260	0,160	1,120	0,080	1,530	0,040	1,370
MF13	1600	325	0,180	1,580	0,040	1,790	0,030	1,133
MF20	0		0,516					
MF21	1960	345	0,050	2,690	0,010	3,690	0,050	1,370
MF51	2490	340	0,080	1,540	0,000	1,940	0,040	1,260
MF52	2700	360	0,050	1,620	0,010	1,810	0,020	1,120

Comments

* The thermal conductivity decreases with the porosity. It does not appear however a precise relationships between dry and saturated values, in particular at low porosity, where the influence of the microstructure is important.
* Dry thermal conductivity is low, smaller (or almost of the same order of magnitude) of that of other similar pyroclastic or sedimentary rocks.
* In porous rocks, the saturated conductivity is two times greater with respect to the dry conductivity, but in the lava or metamorphic rocks the saturation does not change the conductivity value.
* The value of the thermal conductivity of matrix is estimated to be around a 2 $Wm^{-1}K^{-}$.
* The high conductivity for some sample of Mofete and San Vito at depth is attributed to fissures.

* Taking into account that fluids that can occupy the pores and that the air conductivity is λ_{air}=0.026 $Wm^{-1}K^{-1}$ and the water conductivity is (at room temperature) λ_{water} 0,06 $Wm^{-1}K^{-1}$, a law that fits the saturated data is given by

$$\lambda_{sat} = 0{,}64^{\varphi}(\lambda_{water})^{\varphi}(\lambda_{matrice})^{1-\varphi}$$

* From this and from the relationships that rules the changes with temperature of the thermal conductivity of the water and of a typical pyroclastic rock, the values of the thermal conductivity at different temperature can be extrapolated.

$$\lambda_{water}(T) = \lambda_{water}(T_0)\left[1 + 2.38E-03(T-T_o) + 9.97E-6(T-T_o)^2\right] \quad T - T_0 \text{ in } °C$$

$$\lambda_{matrix}(T) = \lambda_{matrix}(T_0) * 293\left[1 + 273 * T\right]^{-1} \quad T \text{ in } °C$$

On these basis, the thermal conductivities at different temperatures have been evaluated and compared with those measured by Agip during the drilling. The agreement is quite good.

7) Acoustic properties

Preliminary notes: The frequency of the measures was 1MHz on samples of height of 5 and 8 cm.

Samples	Depth (m)	Temperature °C	VP (m/s) DRY	Error VP DRY	VP (m/s) SAT	Error VP SAT	VS (m/s) DRY	Error VS DRY	VS (m/s) SAT	Error VS SAT	VP/VS DRY	VP/VS SAT
NYT1	0		1908	76	2540	51	1508	42	1002	20	1,81	2,53
NYT2	0		1611	102	2234	45	935	75	779	55	1,72	2,87
N1	0		1840	74	2406	48	973	39	920	18	1,89	2,62
N2	0		2223	89	2501	50	1338	54	1102	22	1,66	2,27
B	0		2396	192	2419	96	1465	108	1103	40	1,64	2,41
SV10	0		2332	93	2762	55	1366	55	1185	24	1,71	2,33
SV11	810	130	2983	119	3068	61	1866	75	1555	31	1,60	1,97
SV12	1420	260	3231	129	3552	71	2059	82	1799	36	1,57	1,97
SV13	2130	300	3916	157	3974	49	2296	92	2152	43	1,71	1,87
SV15	2860	390	4020	161	3936	79	2383	95	2101	42	1,69	1,87
SV30	0		2298	92	2435	49	1364	100	987	61	1,68	2,47
SV31	1320	225	4722	189	4815	96	2655	106	2611	52	1,78	1,84
SV32	1950	305	4567	186	4460	89	2667	107	2493	50	1,75	1,79
MF10	0	20	1892	76	2260	45	1152	46	914	18	1,64	2,47
MF11	680	240	2559	102	2426	49	1489	60	1116	22	1,72	2,17
MF12	1047	260	4271	171	4405	88	2470	99	2313	46	1,73	1,90
MF13	1600	325	4368	175	4320	86	2564	103	2442	49	1,70	1,77
MF20	0	20	1779	71	2136	43	1052	42	731	15	1,69	2,92
MF21	1960	345	3602	144	4966	99	2323	93	2589	52	1,55	1,92
MF51	2490	340	4256	170	5247	105	2615	105	2734	55	1,63	1,92
MF52	2700	360	4713	189	5403	108	2859	114	2890	58	1,65	1,87

Comments

* The error is 5% (on average) on dry rocks, 2% on saturated.
* The values with grey background in the table indicates an atypical behaviour: in fact, usually VP DRY < VP SAT (as the bulk modulus more than the density is influenced by fluid pressure in pores), and VS DRY ≥ VS SAT (as the shear or rigidity modulus does not change with saturation). The atypical values for the SV31 is attributed to partial saturation, those for MF21, MF51, MF52 to fissures in samples, for the other samples to partial saturation or presence of clay minerals.
* Surface samples: for same sample, the values of VP SAT are more than 40% greater than VP DRY values. As all the sample have almost the same porosity and density, the differences could be due to differences in the network of pores.

Elastic parameters (derived)

Definitions: ρ total density.

Poisson Modulus $\nu = \frac{v_p^2 - 2v_s^2}{2\left(v_p^2 - v_s^2\right)}$ Young Modulus $E = 2\rho v^2_S(1+\nu)$

Bulk modulus $K = 4\rho(v^2_P - (4/3)\, v^2_S)$ Shear or rigidity modulus $\mu = \rho v^2_S$

Samples	Depth (m)	Temperature °C	Poisson SAT	Poisson DRY	E (Gpa) DRY	E (Gpa) SAT	K (Gpa) DRY	K (Gpa) SAT	μ (Gpa) DRY	μ (Gpa) SAT
NYT1	0		0,28	0,41	3,30	5,20	2,00	8,50	1,30	1,70
NYT2	0		0,25	0,43	2,50	4,10	1,60	6,90	1,00	1,00
N1	0		0,31	0,41	2,00	2,80	2,40	7,60	1,10	1,40
N2	0		0,22	0,40	5,60	8,60	3,30	8,10	2,30	2,10
B	0		0,20	0,40	6,30	10,10	3,50	7,60	2,60	1,70
SV10	0		0,24	0,39	6,00	8,90	3,80	9,90	2,40	2,40
SV11	810	130	0,18	0,33	13,40	18,40	6,90	12,40	5,70	4,80
SV12	1420	260	0,16	0,33	19,10	24,80	9,30	18,30	8,20	7,10
SV13	2130	300	0,24	0,29	27,20	31,80	17,30	22,50	11,00	10,80
SV15	2860	390	0,23	0,30	32,00	36,50	19,70	23,70	13,00	10,90
SV30	0		0,23	0,40	6,00	9,10	3,70	8,10	2,40	1,70
SV31	1320	225	0,27	0,29	40,20	44,20	29,00	34,20	15,80	16,60
SV32	1950	305	0,26	0,27	40,90	45,60	29,20	27,90	16,30	15,60
MF10	0		0,21	0,37	3,80	6,20	2,10	6,70	1,60	1,40
MF11	680	240	0,24	0,40	8,50	11,90	5,50	8,30	3,40	2,50
MF12	1047	260	0,25	0,27	35,00	38,40	23,10	29,50	14,00	12,80
MF13	1600	325	0,24	0,43	35,70	40,40	22,70	26,00	14,40	14,50
MF20	0		0,23	0,31	42,00	48,60	1,90	6,30	1,20	0,90
MF21	1960	345	0,14	0,30	50,10	55,60	15,00	42,00	14,00	17,90
MF51	2490	340	0,20	0,31	42,00	48,60	23,50	47,50	17,50	20,20
MF52	2700	360	0,21	0,30	50,10	55,60	28,70	47,30	20,70	21,90

Vanorio T. (2003). Physical properties of volcanic rocks from the Campanian Plain. *TOMOVES: The Internal Structure of Mt. Vesuvius: A Seismic Tomography Investigation*. Edited by P. Capuano et al., Liguori Editore, 553-580.

Conclusive remarks and future research perspectives

Aldo Zollo

Coordinator of the Serapis Project, Dipartimento di Scienze Fisiche, Università di Napoli Federico II

The original main project goals were:
- detailed imaging of the caldera structure;
- integrate and compare seismic models with other geophysical information (gravity, thermal data, rock physical properties);
- construct a passive data bank for Campi Flegrei caldera;
- development of innovative techniques for seismic data modeling and inversion.

All of these have been achieved although with different levels of completion, and can be summarized as follows.
The very high resolution tomographic inversion of active seismic data from the SERAPIS experiment has revealed the buried rim of the Campi Flegrei caldera is clearly detected at about 800-2000 m depth, which presents as an anular high P-velocity and high density body. It has a diameter of about 8-12 km and a height of 1-2 km. According to stratigraphic and sonic log data from deep boreholes and tomographic P velocities, the rim is likely formed by solidified lavas and/or tuffs with interbedded lava. This study confirms the existence for a depressed limestone basement beneath the caldera at less than 4 km depth, while no evidence are found for shallower magmatic bodies.
The SERAPIS and microearthquake data sets have been analyzed for modeling reflections/conversions using standard and new techniques. The move-out and stack analysis of microearthquake records occurring at Mt.Vesuvius confirmed the evidence for a 8-10 km deep seismic discontinuity underneath the volcano, which has been previously identified by migration of active seismic data and interpreted as the roof of an extended magmatic sill. This result can have important implications also for the search and expected depth of the magma chamber beneath Campi Flegrei caldera. 2D velocity models along profiles oriented respectively about N-S and SE-NW and crossing the Campi Flegrei area were obtained using different inversion codes to Serapis data sets. The inferred models show the presence of a resurgent structure in the Campi Flegrei area, consistently with results from 3D high resolution imaging by seismic tomography. The top of this structure is found at about 1 Km depth and extends down to about 6 Km depth.

The joint interpretation of the velocity distribution (as inferred from 3D seismic tomography of SERAPIS data) together with both the available gravity measurements and models and the geothermal drilling information has allowed to locate and map lithological units at depths under the bays of Napoli and Pozzuoli. A model of the Campi Flegrei caldera in relation to the underlying Mesozoic limestone unit is proposed. In this model, no evidence for an extended magma chamber exists in the upper 6 km beneath the Bay of Naples. The feeding system of the Campi Flegrei caldera appear to be directly controlled by the tectonic structures affecting the limestone unit beneath the Bay of Naples. Two NE-SW normal faults run beneath the Vesuvius volcano and Campi Flegrei, which are related to the pre-Pleistocene Apenninic tectonics.
The structure of the caldera and the role of hydrothermal fluids on velocity changes, has been explored through a multidisciplinary approach using 3-D delay-time earthquake tomography and rock physics characterization. The main results from this study reveal a flat and low Vp/Vs anomaly at a 4-km depth under the city of Pozzuoli, above which the earthquakes are located. This anomaly implies the presence of fractured, over-pressured, gas-bearing formations, and excludes the presence of melted rocks. At a shallow depth, a high Vp/Vs anomaly located at 1 km suggests the presence of rocks that contain fluids in the liquid phase. Finally, the maps of the Vp*Vs product show a high Vp*Vs horse-shoe-shaped anomaly located at a 2-km depth. This is consistent with gravity and well data, and might constitute the on-land remainder of the caldera rim, which has been detected below the sea level by tomography using active-source seismic data. The preliminary integration of active and passive data sets has been performed, using a standard 3D tomographic method which includes interfaces. The inferred Vp/Vs model shows, at surface, high anomalies around the caldera rim and a low anomaly at depth, consistent with a gas enriched volume, as discovered by the inversion of passive data only.
Source parameters of microearthquakes recorded during the 1982-1984 crisis have been estimated by the non-linear inversion of first P pulse durations. This work provides moment and stress drop scaling laws of earthquakes in the volcanic area to be used for seismic hazard analyses and strong motion simulations. The avalaible 3D model of P-wave attenuation (Qp) has been refined using the new earthquake data sets acquired during the project.
Highly informative data banks are among the main project outcomes and can be made available for Civil Protection and scientific purposes. The project has implemented the complete database of 3-component waveforms containing several hundreds of microearthquake recorded at Campi Flegrei, during the last unrest episode (1983-84). Pickings of first P and S arrival times for the microearthquakes in the database to be used for subsequent interpretation. The whole waveform data base have been re-picked, measured P and S arrival times have been checked and validated trough self-consistency tests and analyses. Active seismic waveforms and related P-picks (more than 90000 data)

from the SERAPIS experiment are also available. Both data banks are available on the CD-Rom enclosed.
A numerical blind test has been built-up and carried out to estimate the effective resolution power of the station network that recorded the seismic sequence of 1983-84 and constrain the potential of the existing database for the purposes of local earthquake tomography. It is provided a rigorous validation of the various utilized tomographic techniques. The 3D geological model, in digital GoCad format, represents a permanent representation of the structure, and it can be used and easily improved in the future.
A number of innovative methodologies for geophysical exploration of volcanoes have been developed, tested and applied during the present project and can be fully exported to the study of other volcanic areas:

– Sequential Integrated Inversion for joint modeling of seismic and gravity data;
– 3-D, visco-elastic, staggered, pseudo-spectral Fourier method (SPSFM3D) which solves the full- wave propagation of seismic waves in complex 3D media;
– 3D tomographic method based on an accurate finite difference travel-time computation which simultaneously inverts P- and S- first-arrival times for both velocity model parameters and hypocenter locations;
– a method for kinematic migration of reflected/converted arrivals from microearthquake records aimed at identifying and locating at depth the reflecting interface;
– 2D non linear method (multi-scale approach, global optimization) based on waveform coherence of reflected seismic phases from active seismic data.

The technological innovations of this project are related to the design and equipment used during the SERAPIS experiment.
The first one is the use of a dense array of sea-bottom seismographs for seismic exploration of volcanoes and the second is the experiment design.
The advanced array of sea-bottom instruments has been installed and operated during three weeks, demonstrating that sub-marine seismic (but not only seismic) monitoring of volcanic activity is feasible and should be implemented in the future with permanent systems, linked to the on-shore monitoring networks.
The experiment design was 2-D and 3D, with receivers installed at the sea bottom and on-land, source spacing smaller than 100m and energised with battery of 16 litres airguns (6 to 12 cannons).
We have nearly reproduced the typical acquisition lay-out of industrial surveys for oil research. The high quality and density of acquired seismic information suggest the experiment design can be exported to investigate the structure of other coastal volcanoes (Etna, Stromboli, …).
From the methodological point of view we mention the "Blind Test" approach used to validate local earthquake tomographic methods for a given acquisition lay-out. This approach allows to quantitatively assess limits and

advantage of different adopted methodologies when applied to a common acquisition geometry framework.
A number of relevant issues directly raise from the present project and need to be addressed in future can be summarised as follows:

– **Magma chamber location, geometry and size beneath Campi Flegrei caldera.** Results from the present project exclude the presence of a large magmatic body within the upper 5-6 km of the crust beneath the caldera. This calls in question previous hypotheses for the magma chamber depth at 4-5 km, based on earthquake locations, thermal data and sporadic observations of teleseismic records.
  The evidence for a down-faulted Mesozoic basement layer beneath the caldera, whose top occurs at a depth of 4-5 km, indicate that the magma chamber has to be well inside the limestone layer. The problems of identifying and locating the magma reservoir beneath Campi Flegrei caldera and investigating its connections to the deep Mt. Vesuvius feeding system have to be addressed by the analyis and modeling of reflection/conversion arrivals recorded during the SERAPIS experiment. This research activity is still on going at RU1 and providing very promising results. Possibly another seismic reflection experiment could be planned after getting first results from the analyis of serapis data.
– **Structure and lithology of the buried caldera rim.** Seismic and gravity data show that it is a high velocity, high density body, likely related to solidified lavas and/or tuffs with interbedded lava, as inferred from borehole observations on land. What mechanisms do control the resurgency phenomena and the ring-shaped form of the caldera rim? Is the imaged rim the site for magma up-rising during recent eruptions, as the location of recent volcanoes, the presence of fumeroles and dome structures at sea, seem to indicate?
– **Evidence of regional faults and relation with volcanoes.** Two extended NE-SW normal faults are imaged by 3D active seismic tomography affecting the Mesozoic basement. Both can be related to the 700 Ky extensional regime. The normal fault affecting the carbonatic basement in correspondence with the Campi Flegreis cadera rim, can provide an upward route for the molten material that is located in a deeper magma chamber, lying within or beneath the carbonatic basement. The more recent NW-SE normal fault system is contemporary with the Campanian Ignimbritic eruption [Milia and Torrente, 1999]. It may have had a trigger role, by locally reactivating the middle Pliocene SW-NE system. It is also suggested that a similar geometric relation between the Vesuvius volcano and an analogous normal fault with the same orientation exists. The Torre de Greco normal fault controls the magma displacements toward the surface in a way similar to the Posillipo-Banco di Fuori fault beneath Campi Flegrei. The link between regional faulting and volcanism of the Neapolitan volcanic district is a major research issue to be addressed in the future.

– **Origin, presence and roles of hydrothermal fluids.** Our project reveals a flat and low Vp/Vs anomaly at a 4-km depth under the city of Pozzuoli, above which the earthquakes are located. This anomaly implies the presence of fractured, over-pressured, gas-bearing formations, and excludes the presence of melted rocks.
  The modeling of the physical properties of the rock and the reversal trends encountered along velocity profiles leads to interpret the low Vp/Vs anomaly at 4 km in depth as the top of formations that are enriched in gas that is under supercritical conditions. The 1982-1984 earthquake locations are mostly distributed on the top of velocity reversals and within the low Vp/Vs anomaly. Since these signatures were interpreted as being caused by gas under supercritical conditions, it is speculated that the seismicity is induced by over-pressured fluids. Further seismicity analysis have to be made with regard to this issue. Nevertheless, the phenomenological correlation among the uplift rate, the seismicity and the increase in the H_2O/CO_2 ratio in fumaroles as a function of time [Chiodini et al., 2001; 2003] would suggest that the observed phenomena may have a common origin.
– **Thermo-mechanical modelling of caldera mechanisms.** High resolution tomography does not provide evidence for two nested calderic structures, as was previously proposed for the CI (Campanian Ignimbrite) and NYT (Neapolitan Yellow Tuff) eruptions. The revealed buried rim is probably related to both the CI and NYT collapses. This would imply that both eruptions can be associated to a single caldera rim. Tomographic images have allowed the estimation of a collapse of about 1,200m. The corresponding volume of the erupted material (50km^3) is compatible with the estimation for the NYT eruption only, indicating that a deep feeding system must exist, below 6km.
  Surface geological evidence and analyses of distribution of volcanic products contrast these deep observations, showing at least two caldera borders, presumably associated with two different eruption episodes. How is the model of a single caldera mechanically compatible with surface geological and volcanological evidences? Can post-eruptive mechanical stress readjustments at the earth surface produce en-echelon, double ring-like fracturing associated to a resurgency caldera episode? And also, is a deep magma reservoir (z> 6-7 km) linked to the surface by a depth-extended fracturing system compatible with borehole data (thermal, lithostratigraphy, rock physical properties, …) and present thermal state of the caldera?

Appendix

1984 Campi Flegrei P- and S- phase picking

G. Russo[1], T. Vanorio[2], P. Capuano[3,4], E. Auger[1], M. Bonagura[1], G. Caielli[5], V. Convertito[1], N. Damiano[4], L. D'Auria[1], A. Emolo[1], L. Lovisa[6], M. Moretti[7]

[1] *Dipartimento di Scienze Fisiche, Università Federico II, Napoli, Italy*

[2] *Géosciences Azur, CNRS, Université de Nice, Sophie Antinopolies, Valbonne, France*

[3] *Dipartimento di Scienze e Tecnologie per l'Ambiente ed il Territorio, Università del Molise, Isernia, Italy*

[4] *Osservatorio Vesuviano, INGV, Napoli, Italy*

[5] *Istituto per la Dinamica dei Processi Ambientali, CNR, Milano, Italy*

[6] *Istituto Nazionale di Oceanografia e Geofisica Sperimentale, Trieste, Italy*

[7] *Centro Nazionale Terremoti, INGV, Roma, Italy*

Introduction

After the checking and verification of some possible inconsistency of data-set picking, we obtain about 4583 P-phase picking and about 3321 S-phase picking. We define the picking weight p, taking into account the reading time error, to give an idea of picking quality. We obtain 80% of P-picking with $p \leq 1$ and 70% of S-picking with $p \leq 2$.
The following table resume P- and S- phase picking clustered for each event. Table is written in HYPO format.

```
W03   IPU0 84 116 33321.50          22.79ES+0
W04   IP+0 84 116 33321.36          22.50IS-1
W02   IP+2 84 116 33321.51          22.60ES-2
W05   IP+1 84 116 33322.65          24.49IS-2
W15  EP+2 84 116 33321.99           23.30ES+1
W06  EP+0 84 116 33322.23           23.94ES+1
W08   EP-3 84 116 33321.88          23.26ES-2
                    10
```

Col 1-4: Station ID
Col 5-8: Impulse ID; phase ID, polarity; weight
Col 10-15: year; mounth; day
Col 16-24: hour;minute; second
Col 32-36: second of S-phase
Col 37-40: Impulse ID; phase ID, polarity; weight

The full list is available in the enclosed CD-Rom.

P-phase picking of Serapis experiment

J. Battaglia, D. Dello Iacono, S. Judenherc
Dipartimento di Scienze Fisiche, Università Federico II di Napoli

First P-arrival times have been manually picked on pre-processing common receiver sections. the used P-picks for seismic tomography consist of about 65.000 data relative to sea-bottom stations and 25.000 data from on-land stations.
Data are organized in TLR3 format.

```
40.782500 14.132300    0.000   2.466190 1.000  1 ANF  3386 3    P
40.782500 14.132300    0.000   2.493647 1.000  1 BA1  3386 3    P
40.782500 14.132300    0.000   2.405794 1.000  1 BA3  3386 3    P
40.782500 14.132300    0.000   2.691651 0.600  1 BAI  3386 3    P
40.782500 14.132300    0.000   2.879643 0.600  1 CAS  3386 3    P
40.782500 14.132300    0.000   2.715721 0.600  1 FOR  3386 3    P
```

Each column including info for the different picks and comes as follows:
- longitude and latitude of the shot
- 0.000 for a time origin shift
- travel time
- weight
- not used
- station ID
- shot number
- code to indicate the type of the source (required by TLR3 program)
- type of wave

The full list is available in the enclosed CD-Rom.

Colour reproduction of selected figures

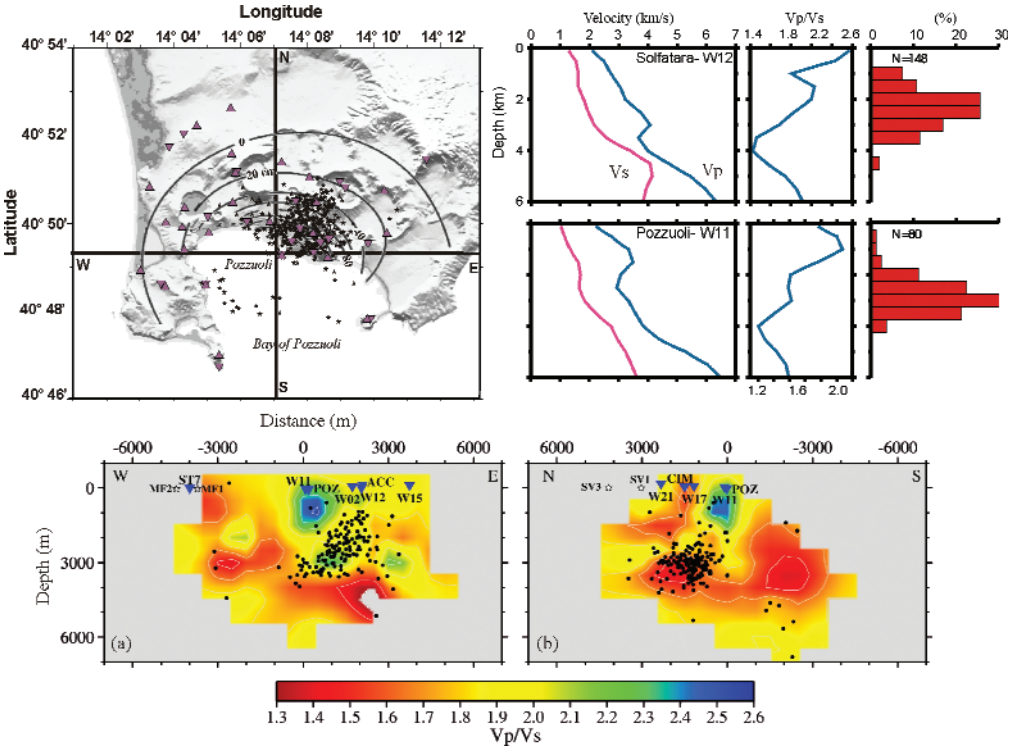

Fig. 1.2.2. *Top left panel* – Map of the CF caldera showing seismometer stations (triangles) and final earthquake locations (stars). The map also reports the elevation contours (black lines) for the 1982-1984 uplift. *Top right panel* – Reversal trends on vertical velocity profiles, Vp/Vs and, histograms showing earthquake distribution along profiles (radius equal to 0.5 km). *Bottom* – Vp/Vs vertical cross-sections and earthquake distribution (black points) along the directions reported in the map. Stars and triangles indicate wells and stations, respectively. You can see this figure on page 31.

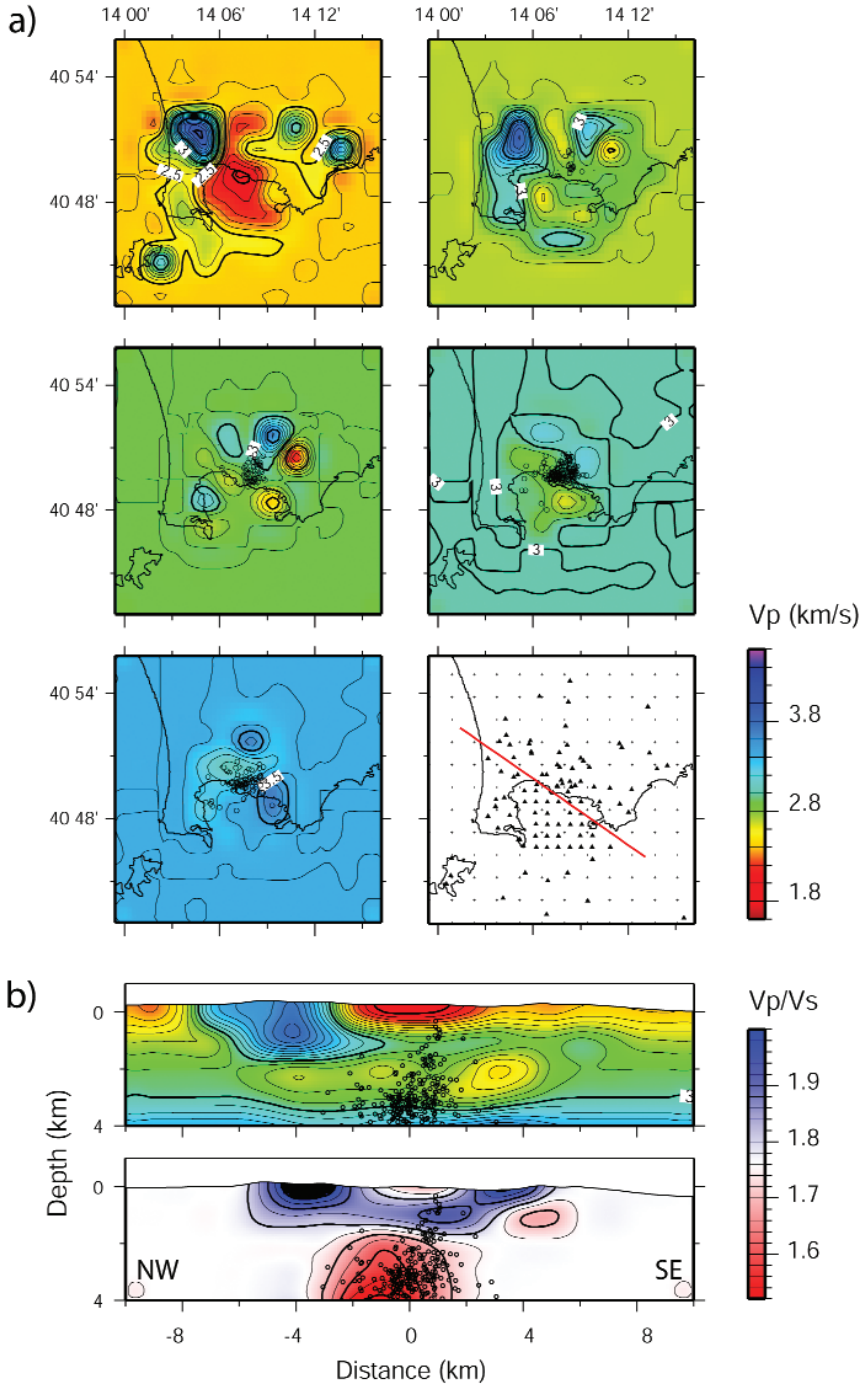

Fig. 1.3.2. (a) P wave velocity model in the five layers. (b) Vertical sections across the caldera of Vp (top) and Vp/Vs (bottom) models. Relocated earthquakes are plotted on sections. You can see this figure on page 36.

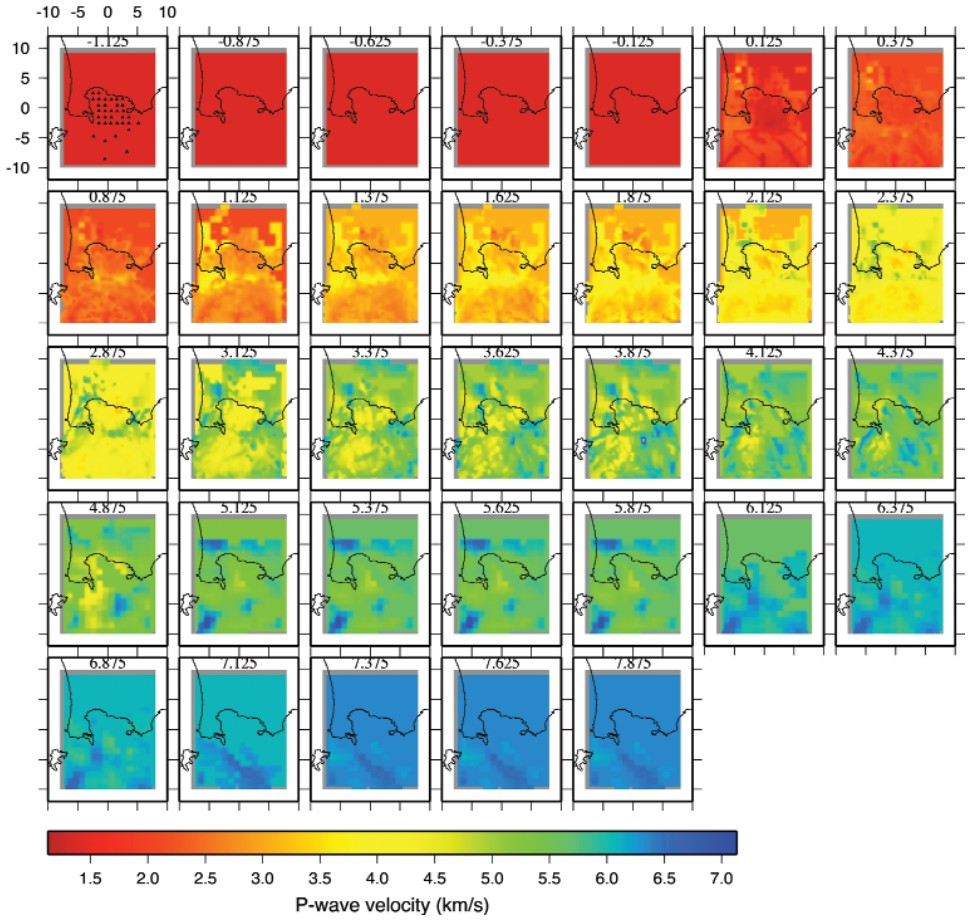

Fig. 1.4.1. 3D P-wave velocity filtered model resulting from the integration of two tomographic images of the CF area from the SERAPIS experiment (Zollo et al., 2003; Judenherc and Zollo, 2004). The first slice also shows the position of the OBS used for the location of the SERAPIS shots in the Pozzuoli bay. You can see this figure on page 40.

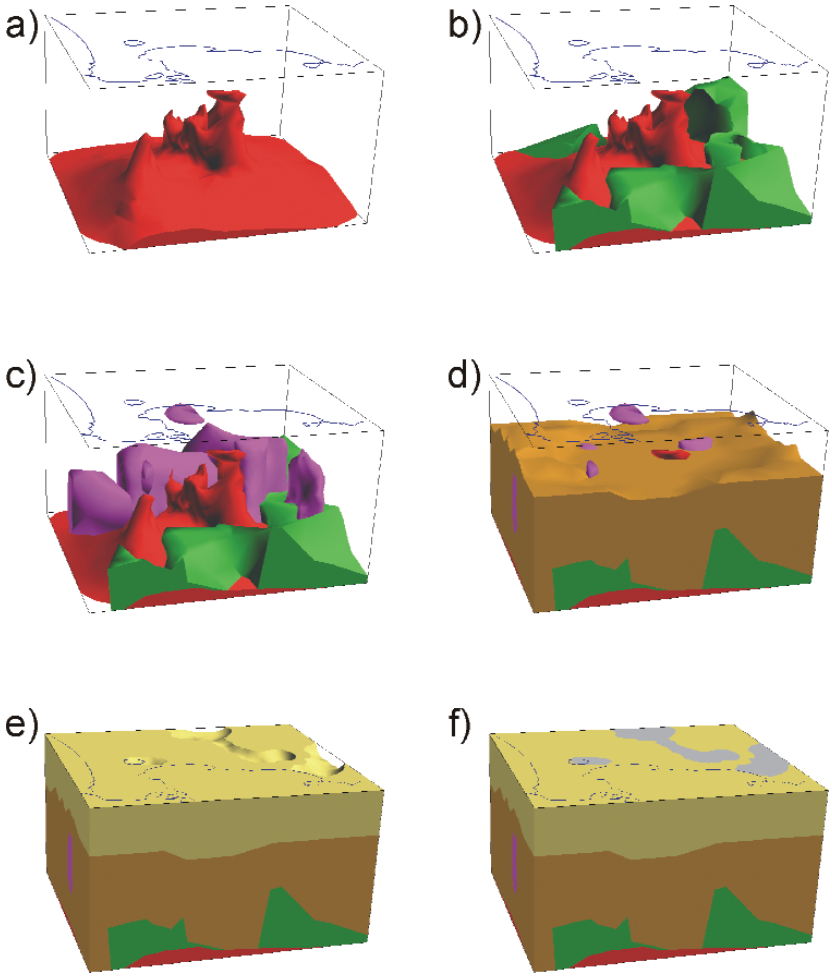

Fig. 2.1.2. Structure of the digital model. You can see this figure on page 56.

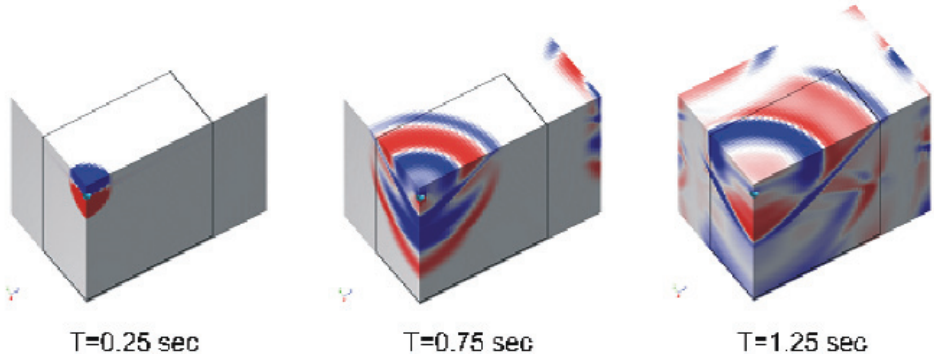

Fig. 4.5.4. Effectiveness of the absorbing layers and free surface conditions. You can see this figure on page 149.

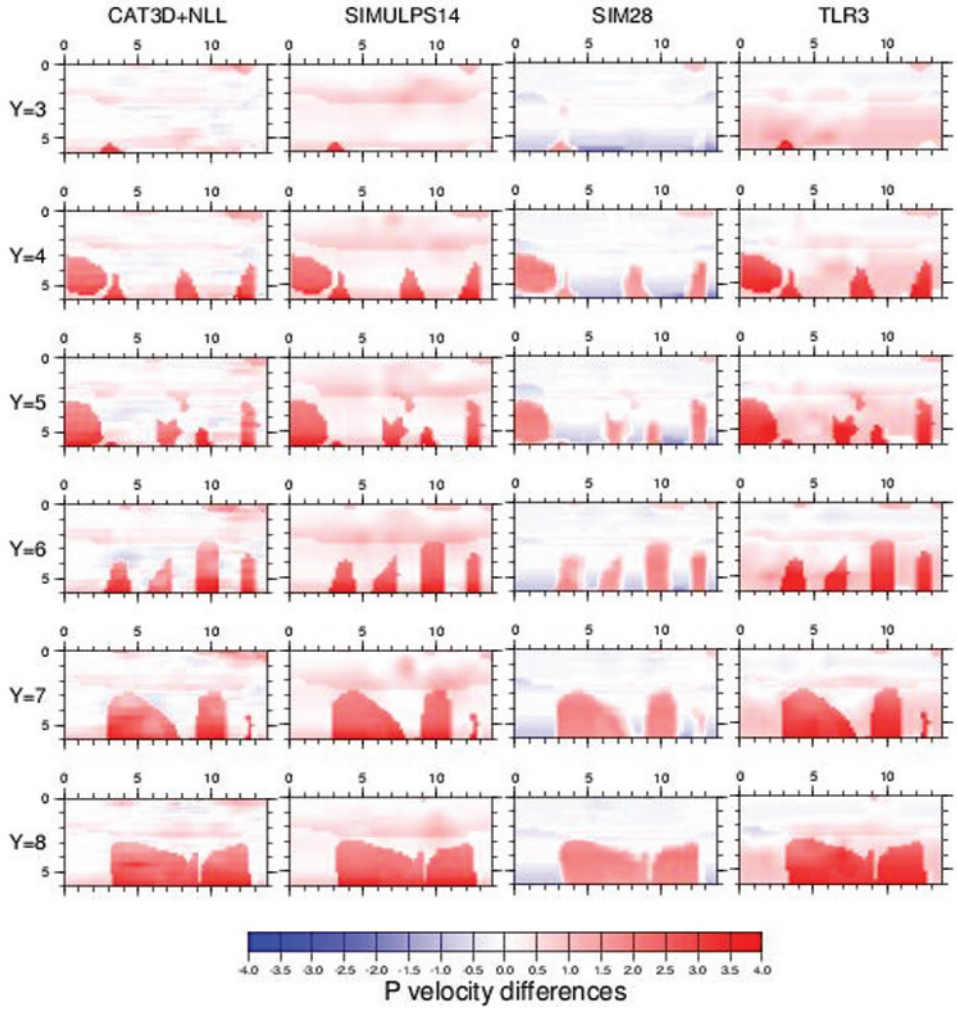

Fig. 2.2.6. Difference between Vp synthetic and inverted models along Y sections. Blue/red areas indicate negative/positive misfit. White areas correspond to good fit. You can see this figure on page 73.

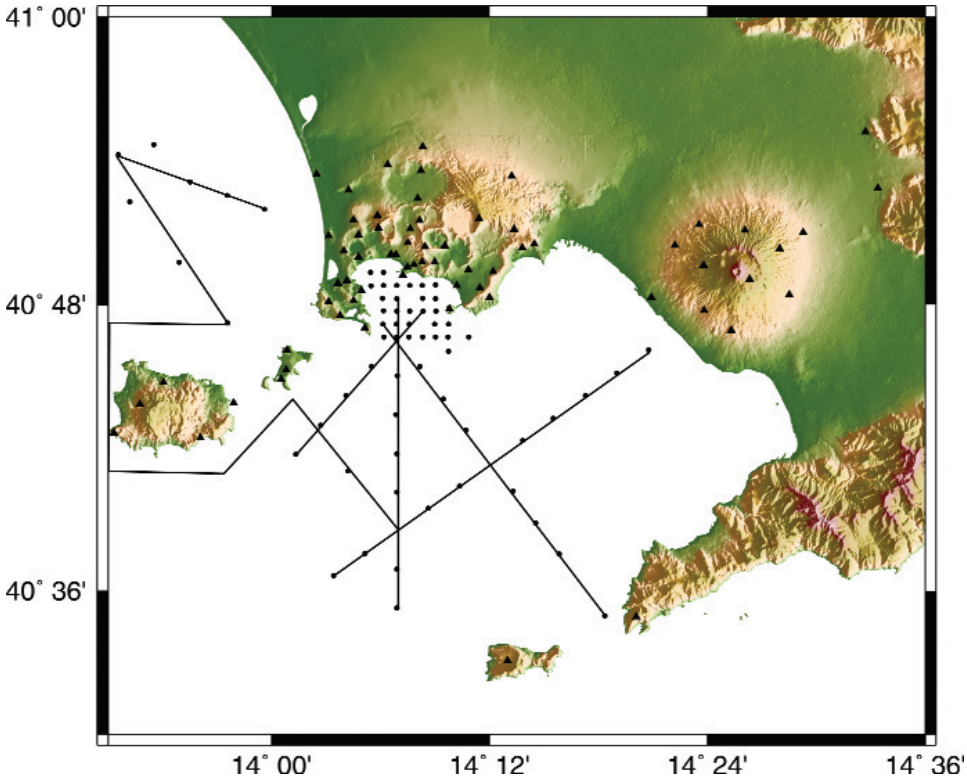

Fig. 3.1.1. Map of the area investigated during the SERAPIS experiment. Black lines traces the path of the vessel during the campaign. Red and blue circles display the position of OBS and seismograph during the experiment. You can see this figure on page 81.

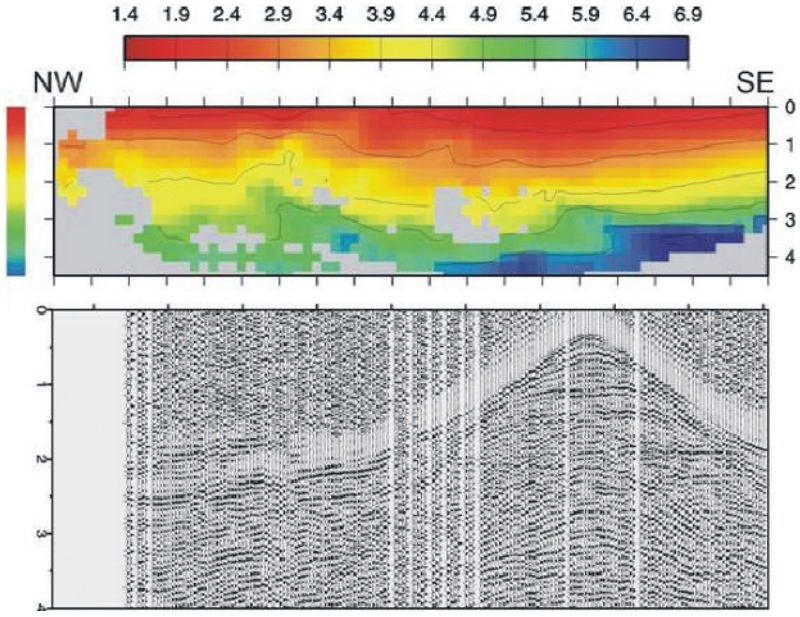

Fig. 3.1.4. Example of P-velocity depth section in the Campi Flegrei bay area. You can see this figure on page 84.

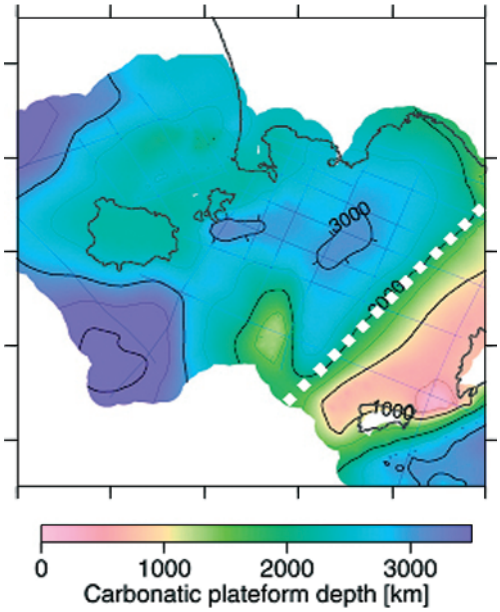

Fig. 3.2.2. Top of the Mesozoic basement deduced from the near-vertical seismic reflection survey data analysis carried out in 1970s in the area. You can see this figure on page 91.

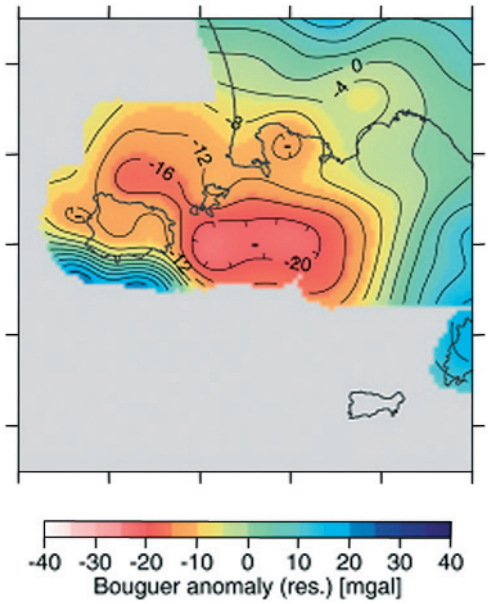

Fig. 3.2.3. Bouguer anomalies in the Gulfs of Naples and Pozzuoli (from Capuano & Achauer 2002). You can see this figure on page 91.

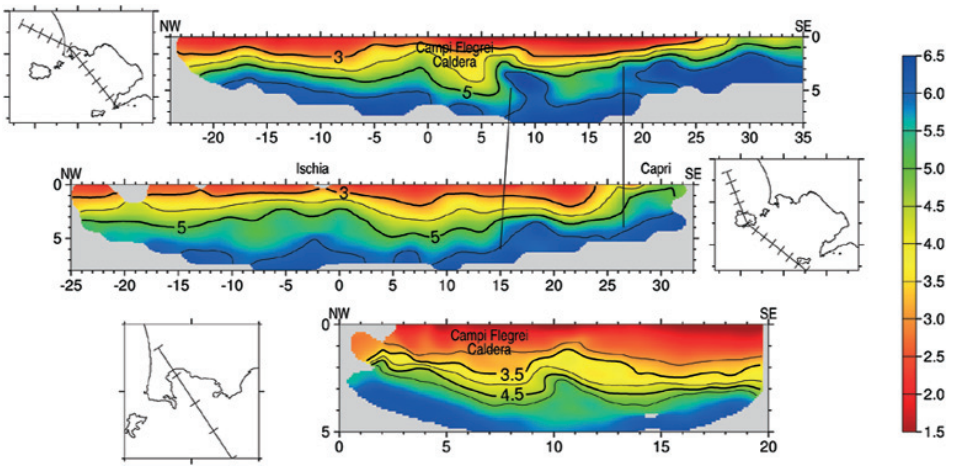

Fig. 3.2.5. Plane views of the NB velocity model. For each layer, the top and bottom depths of the layers are indicated, and the dots indicate the station locations; in the first layers they also represent the shot locations. The land topography is indicated with thin contour lines every 500 m. The iso-velocity lines are plotted at 3.0, 4.0 and 5.0 km/s (from Zollo & Judenherc 2004). You can see this figure on page 92.

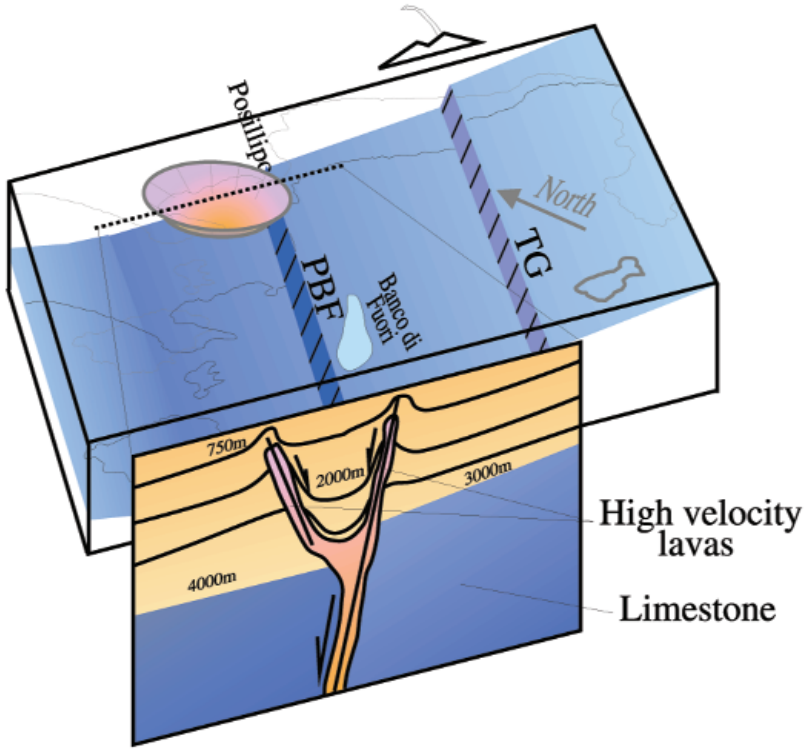

Fig. 3.2.12. Interpretative block diagram showing the main features identified in the tomographic models. The blue surface represents the carbonatic platform, dipping towards the northwest, with the two normal SW-NE Torre del Greco (TG) and Posillipo-Banco di Fuori (PBF) faults (from Zollo & Judenherc 2004). You can see this figure on page 97.

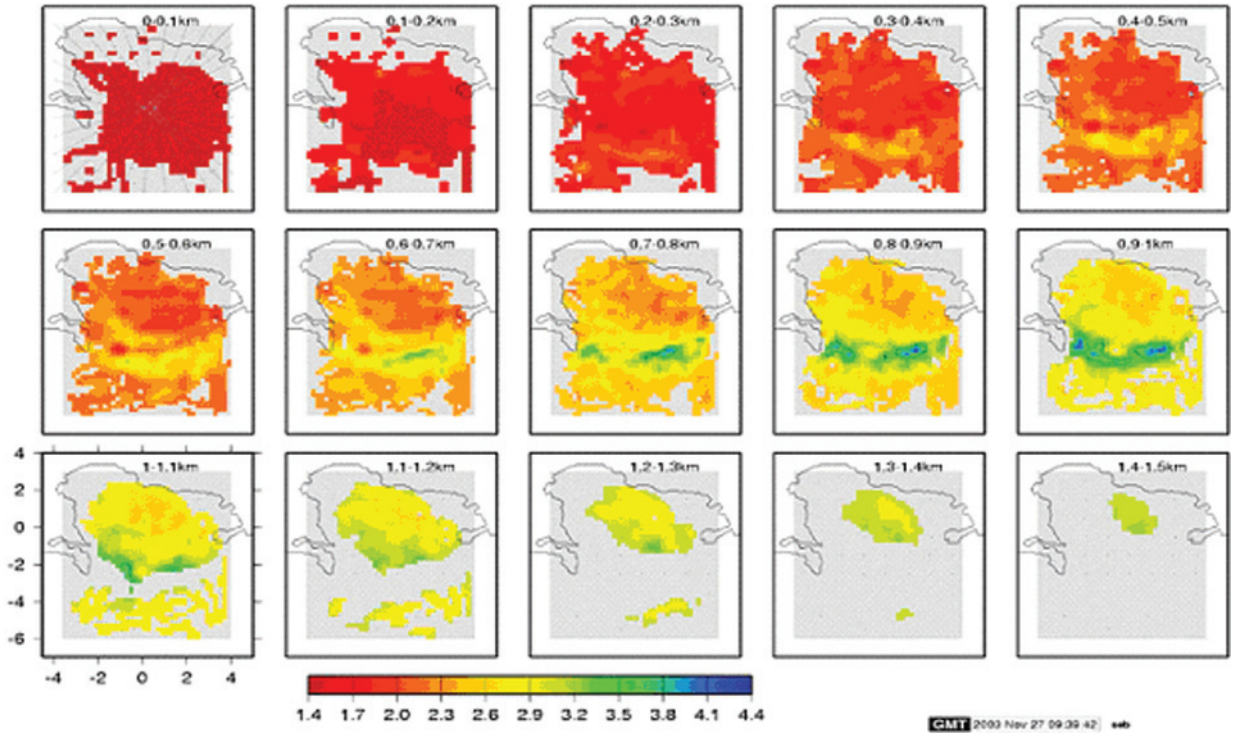

Fi.g 3.2.10. The very-high-resolution seismic tomography for the Gulf of Pozzuoli, with the medium under investigation divided into 200x200x100m cell size sides. The red-based colours indicate the low velocities, and blue-based colours indicate the high velocities. For each layer, their top and bottom depths are indicated. You can see this figure on page 96.

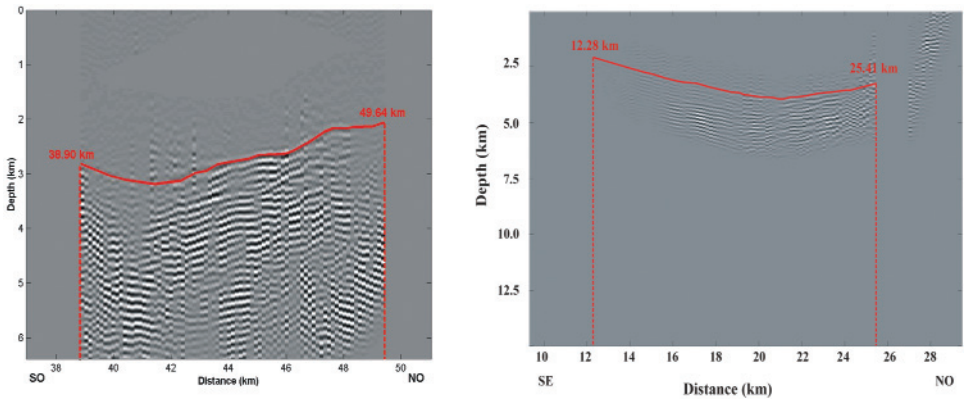

Fig. 3.3.2. Image of the deeper refractor along Line 1 (left) and Line 3 (right). You can see this figure on page 103.

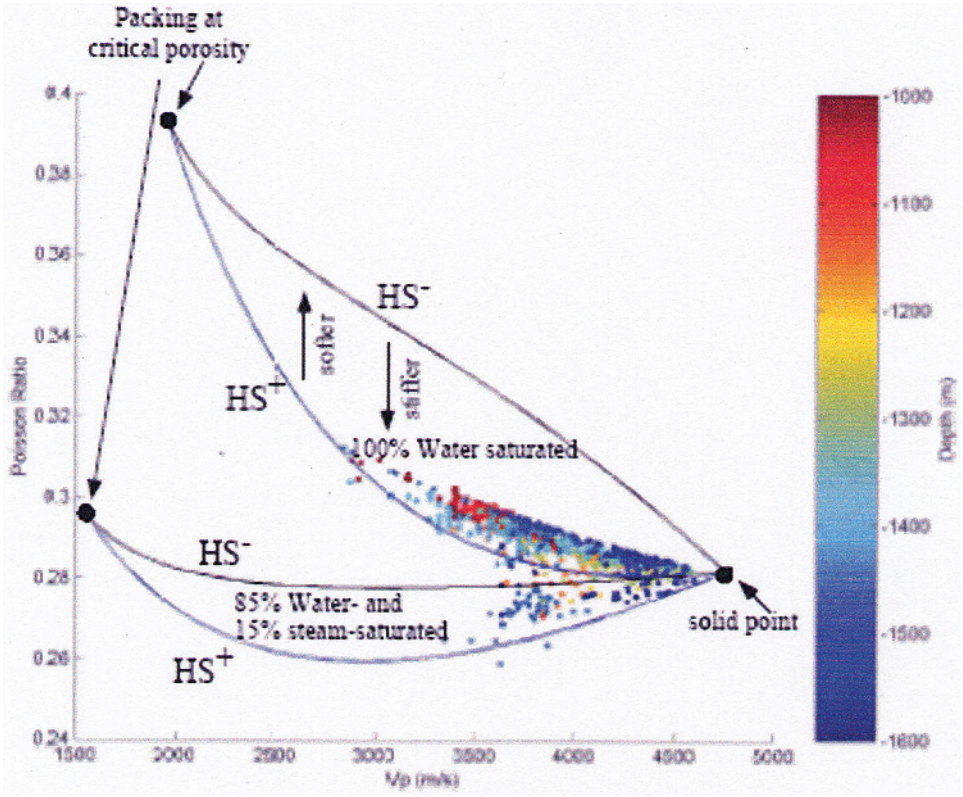

Fig. 4.2.1. Comparison between log data and the model of Vp/Vs. Poisson's ratio for a depth interval ranging from 1000 m to 1600 m. You can see this figure on page 115.

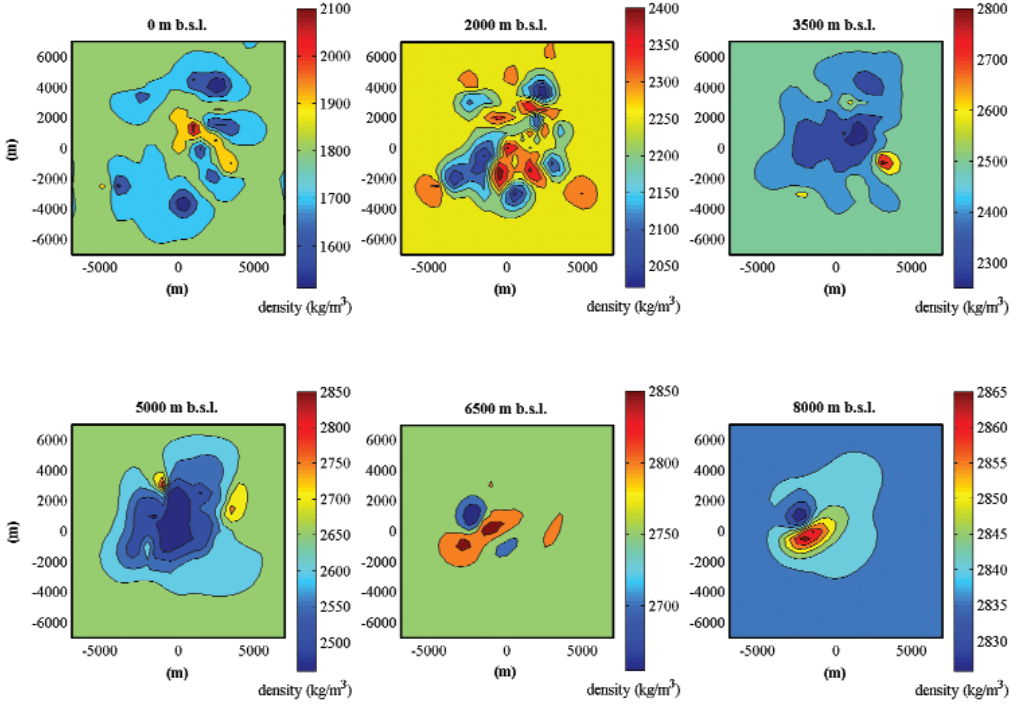

Fig. 4.1.2. Density model recovered from passive source velocity model. You can see this figure on page 111.

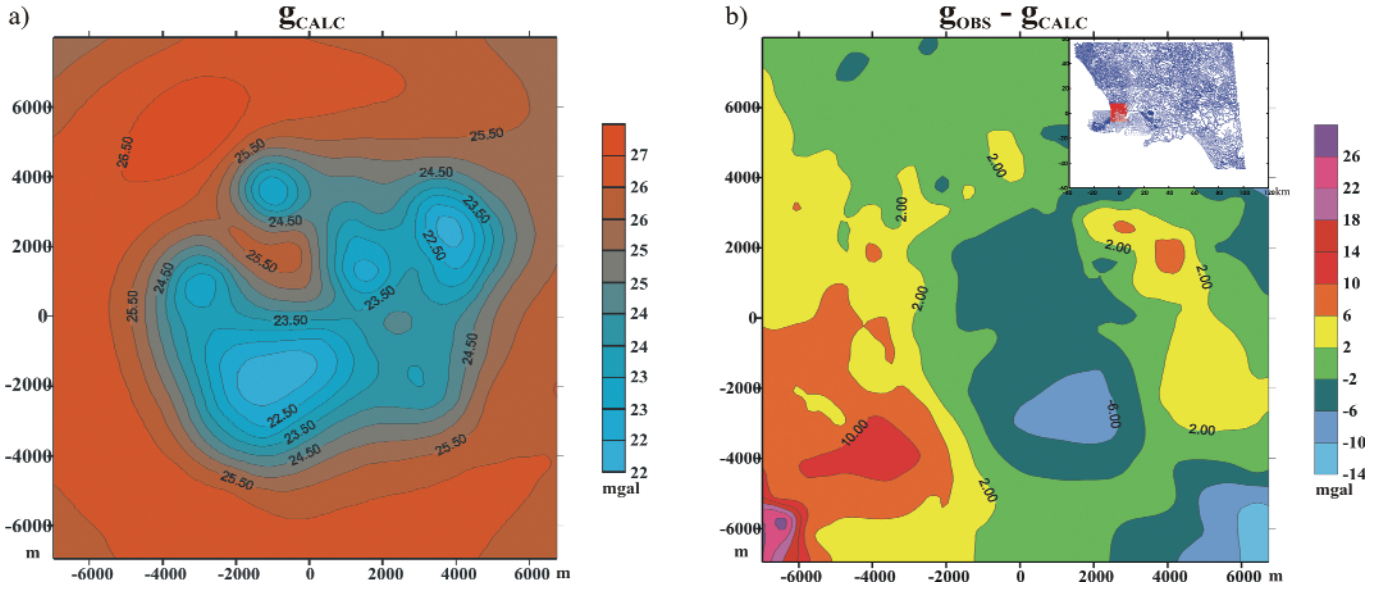

Fig. 4.1.3. a) The calculated gravity field produced by the density model in Figure 2 (bkg. = 2480 kg/m^3) and b) the related gravity residuals with respect to the observed field (792 measurement points extracted from the gravity map which covers all the Campanian plain and the Gulf of Naples (Berrino et al., 1998) shown in the inset. You can see this figure on page 112.

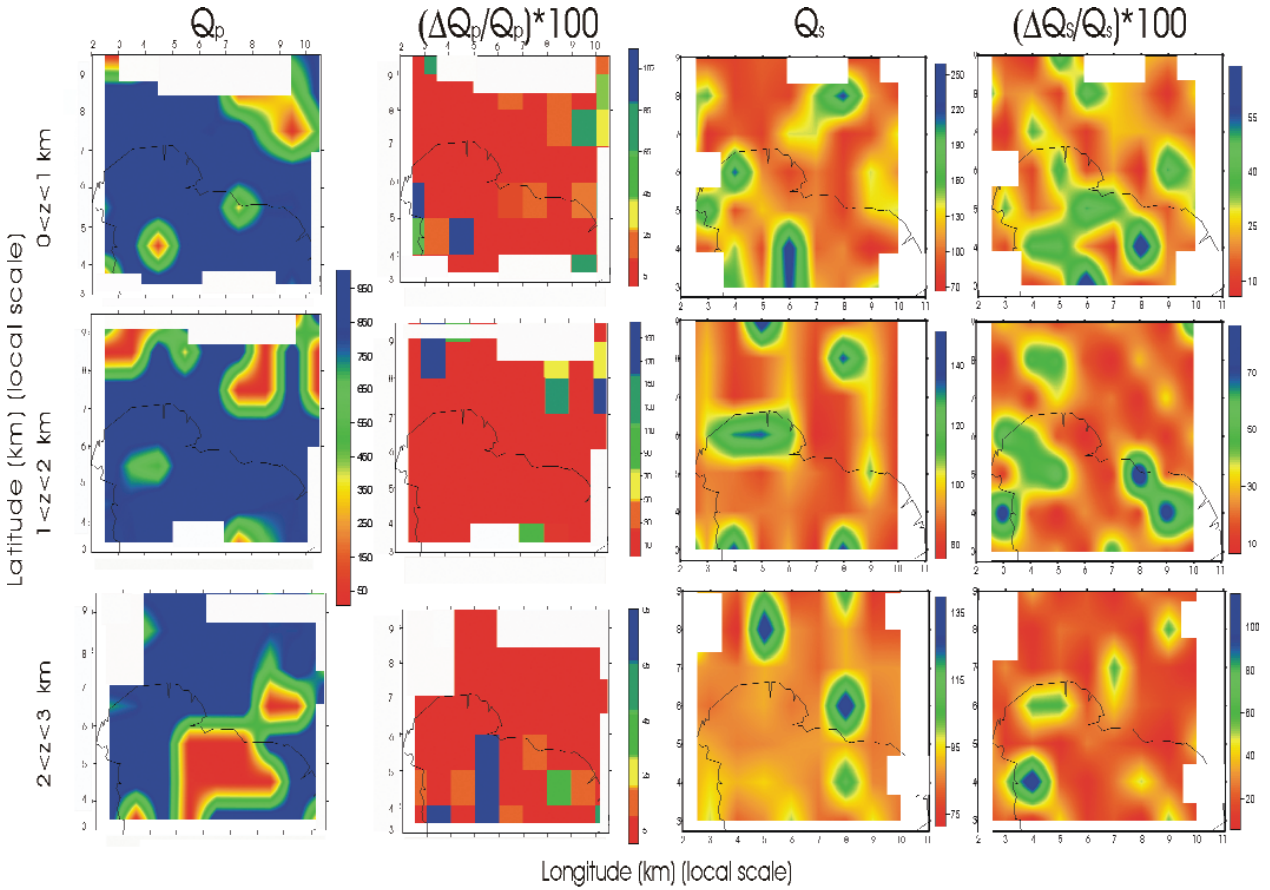

Fig. 4.4.8. a) 3D Qp map of the Campi Flegrei caldera; b) 3D Qp error map of the Campi Flegrei caldera; c) 3D Qs map of the Campi Flegrei caldera; d) 3D Qs error map of the Campi Flegrei caldera. You can see this figure on page 140.

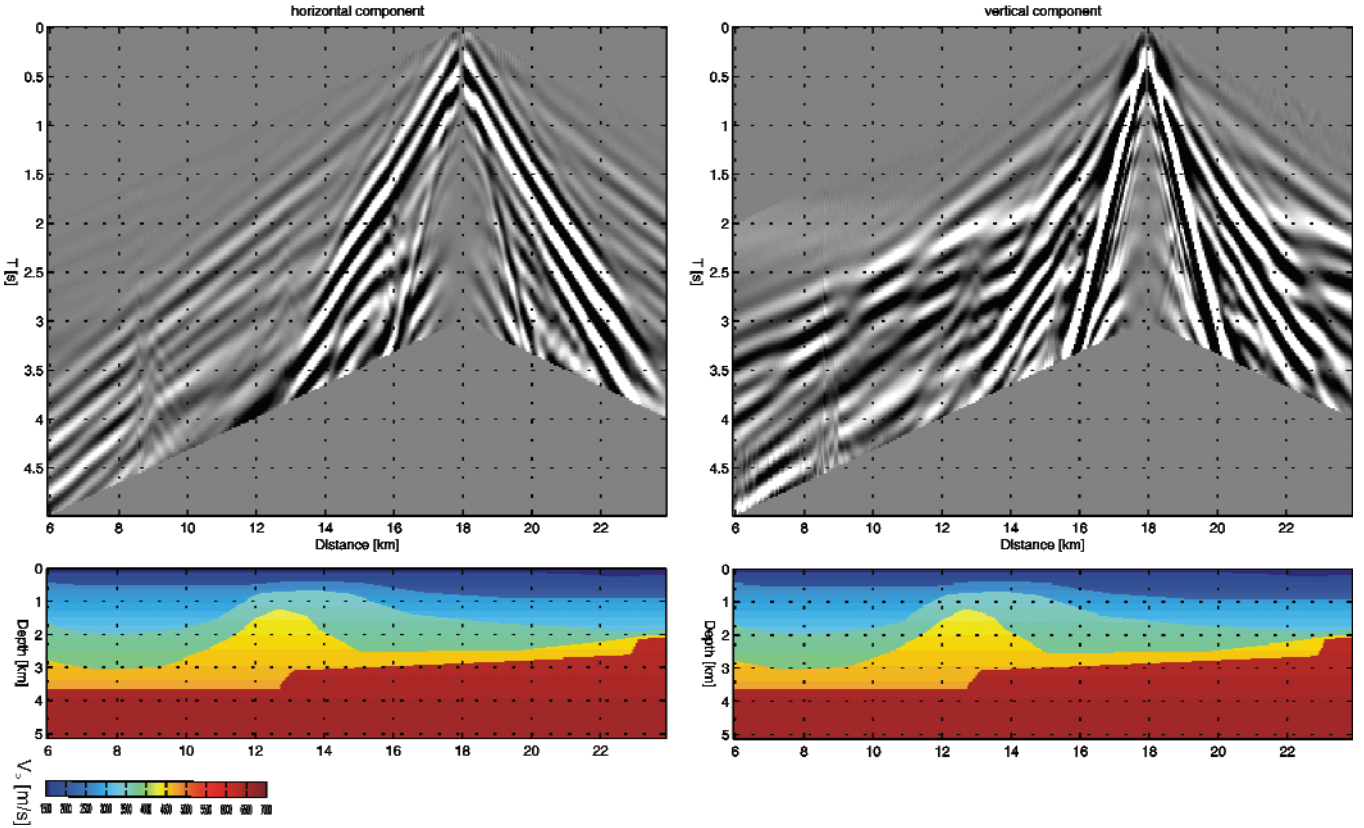

Fig. 4.6.2. Common receiver seismic section for station OBS48 (top) and the input structural model (bottom). Horizontal (left) and vertical (right) and components. You can see this figure on page 155.

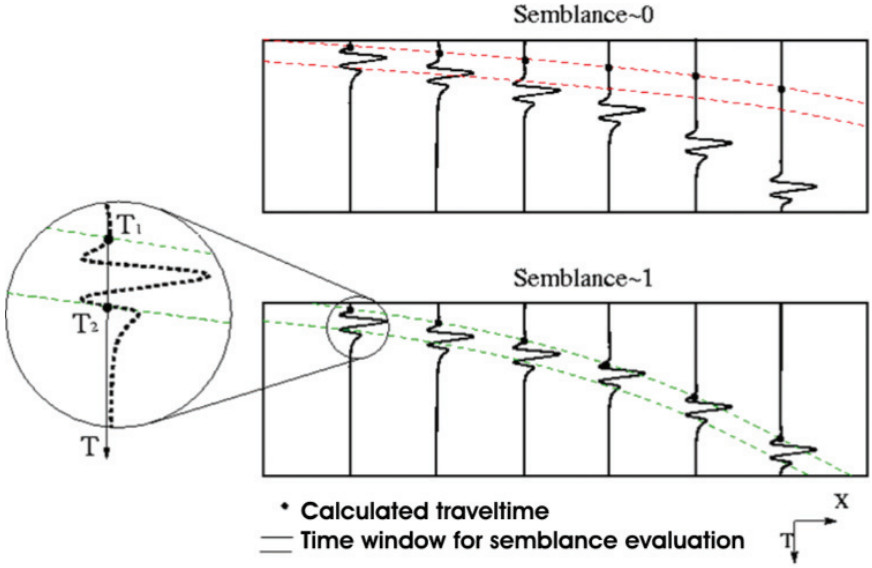

Fig. 4.7.4. Semblance evaluation along two different travel-time curves. For the calculation of the semblance, we extract the waveform contents in the windows given by the calculated travel times (in the large circle, the window is between the times T_1 and T_2). In the upper box, a bad calculated travel time is shown (low semblance value), while the lower panel shows a travel-time curve that followed a coherent phase (high semblance value). You can see this figure on page 165.

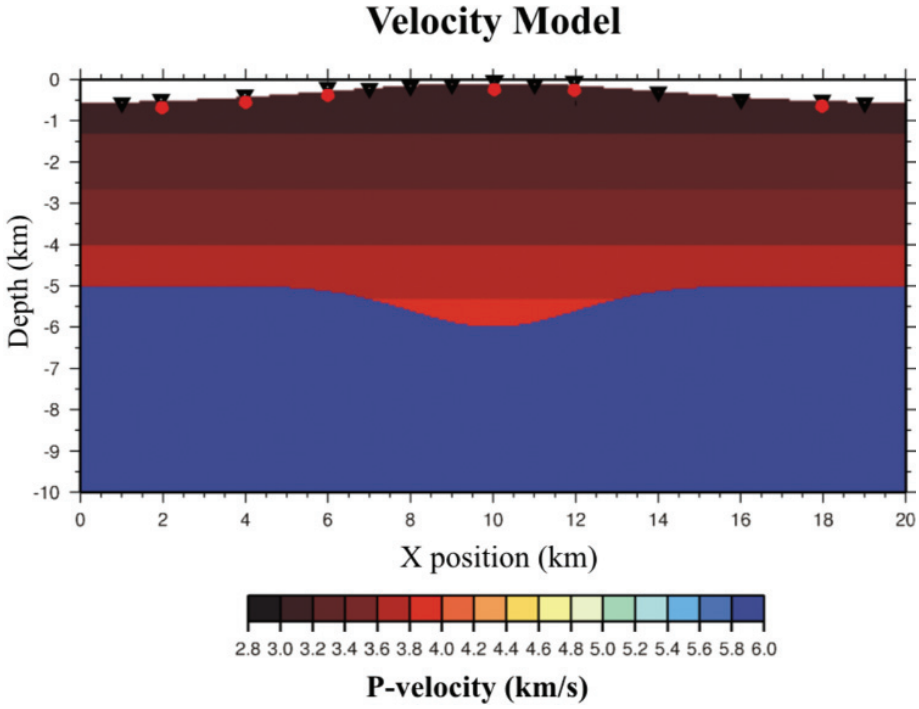

Fig. 4.7.5. Adopted model for the determination of synthetic travel times. The triangles show the locations of the receivers and the stars show the positions of sources. You can see this figure on page 166.

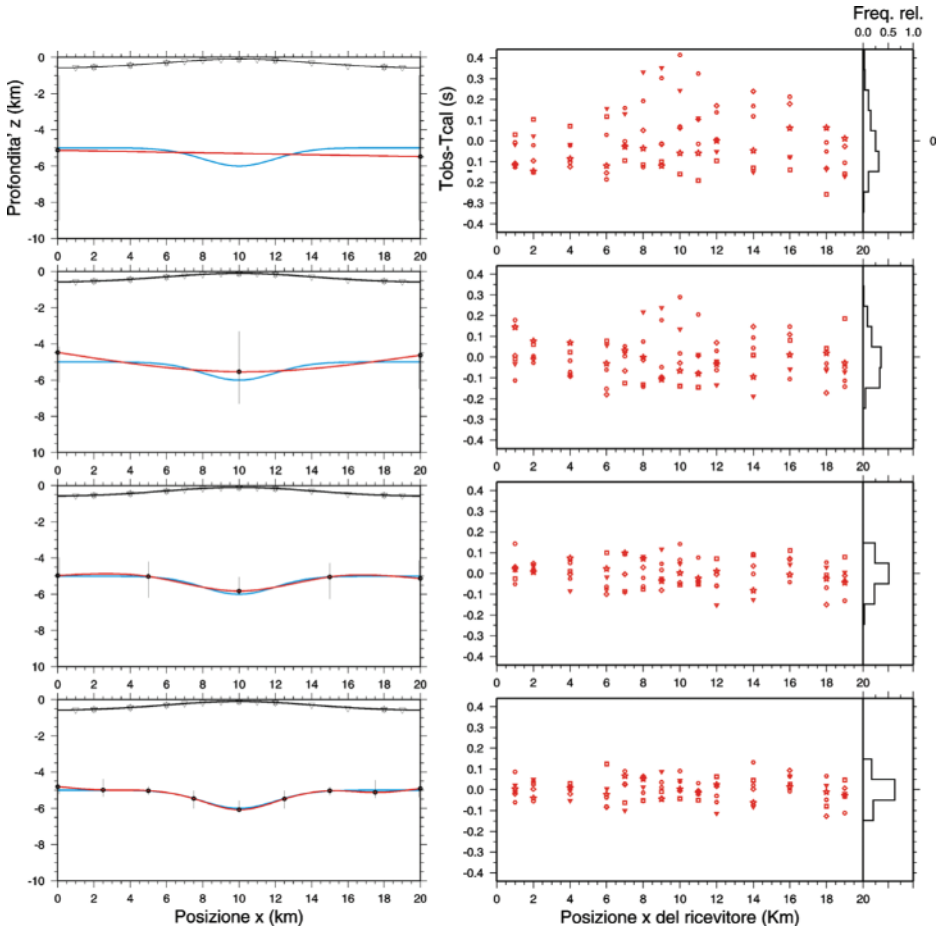

Fig. 4.7.6. The results of inversions of synthetic travel times. The interface models obtained are obtained by performing a succession of four inversion runs with an increasing number of interface nodes (solid circles). The line without nodes shows the real position of the reflector (Figure 5) and the vertical bars are the intervals of search of the nodes. In the panels on the right, the residual distributions and the histograms associated with determined models are displayed. You can see this figure on page 167.

Finito di stampare nel mese di giugno 2006
presso Officine Grafiche Francesco Giannini & Figli S.p.A. – Napoli

ISBN-10: 88-89972-04-1
ISBN-13: 978-88-89972-04-5